FEW-FERMION SYSTEMS UNDER A MATTERWAVE MICROSCOPE

VINCENT M. KLINKHAMER

Dissertation
submitted to the
Combined Faculties of the Natural Sciences and Mathematics
of the Ruperto-Carola University of Heidelberg, Germany
for the degree of
Doctor of Natural Sciences

Put forward by
Vincent Mirou Klinkhamer
Born in Berkeley, CA, USA
Oral examination: January 25th, 2018

FEW-FERMION SYSTEMS UNDER A MATTERWAVE MICROSCOPE

Referees:	Prof. Dr. Selim Jochim Prof. Dr. Matthias Weidemüller

ABSTRACT

This thesis presents correlation measurements in two different few-fermion systems of ultracold ^{6}Li atoms. The measurements have been performed with a new spatially and spin-resolved imaging method with single-atom sensitivity, with which we can probe coherences of the initial system as correlations in the momenta. First, we study attractively interacting atoms in a single microtrap, which serves as a basis for understanding the expansion dynamics of strongly interacting Fermi gases. We observe correlation features in the relative coordinate for different interaction strengths. We explain several of these features theoretically by calculating the initial interacting state in the microtrap and projecting it on a molecular bound state and scattering waves. Next, we study a small number of repulsively interacting particles in the ground state of a double-well potential. This system constitutes the fundamental building block of the Hubbard model. We observe interference patterns in the coordinates of the individual particles and in their relative coordinates. From the amplitude and phase of these patterns, we extract off-diagonal density matrix elements of the state, which we use to directly show coherence and entanglement in our system.

ZUSAMMENFASSUNG

In dieser Dissertation werden Korrelationsmessungen an zwei fermionischen Systemen ultrakalter ^{6}Li-Atome vorgestellt, die mit einem neuen orts- und spinaufgelösten Einzelteilchen-Abbildungsverfahren durchgeführt wurden. Mit diesem Verfahren können wir Kohärenzen des Ausgangssystems als Korrelationen der Teilchenimpulse nachweisen. Zunächst untersuchen wir attraktiv wechselwirkende Atome in einer Mikrofalle. Dieses System dient als Verständnisgrundlage für die Expansion stark wechselwirkender Fermigase. Wir beobachten Korrelationen in der Relativkoordinate für verschiedene Wechselwirkungsstärken. Einige dieser Merkmale erklären wir theoretisch durch die Projektion des Anfangszustandes auf Molekül- und Streuzustände unter Berücksichtigung der Wechselwirkung. Weiterhin untersuchen wir Wenigteilchensysteme bei verschiedenen abstoßenden Wechselwirkungen im Grundzustand eines Doppelmuldenpotentials, welches den Grundbaustein des Hubbard-Modells darstellt. Wir beobachten Interferenzmuster in den Einzelteilchen- und Relativkoordinaten, anhand derer Amplitude und Phase wir Nebendiagonaleinträge der Dichtematrix bestimmen. Mit diesen Dichtematrixeinträgen können wir unmittelbar die Kohärenz und Verschränkung unseres Systems nachweisen.

CONTENTS

1 INTRODUCTION 1

2 MANY-BODY QUANTUM THEORY 5
- 2.1 Many-Body Quantum States 5
  - 2.1.1 Constructing Many-Body Quantum States 5
  - 2.1.2 Density Matrix 7
  - 2.1.3 Operators on Many-Body Quantum States 8
- 2.2 Correlation Functions 10
  - 2.2.1 General Correlation Functions 10
  - 2.2.2 Correlation Functions in Quantum Optics 11
  - 2.2.3 Applications of the Hanbury Brown and Twiss Effect 14
- 2.3 Entanglement 17
  - 2.3.1 Definition and Properties of Entanglement 18
  - 2.3.2 Entanglement Witnesses and Entanglement Entropy 19
- 2.4 Hubbard Model 22
  - 2.4.1 Hubbard Model Hamiltonian 22
  - 2.4.2 Limiting States of the Fermi-Hubbard Model 24
  - 2.4.3 Correlations in the Hubbard Model 26

3 ATOMIC PHYSICS 29
- 3.1 Dipole Trapping of Neutral Atoms 29
- 3.2 Scattering Theory and Feshbach Resonances 32
  - 3.2.1 Scattering at Low Energies 32
  - 3.2.2 Zero-Energy Scattering Resonances 37
  - 3.2.3 Feshbach Resonances 38
  - 3.2.4 Feshbach Molecules 40
  - 3.2.5 Contact Interaction 41

4 EXPERIMENTAL SETUP AND PREPARATION 43
- 4.1 Properties of Lithium 43
  - 4.1.1 Internal States and External Magnetic Fields 43
  - 4.1.2 Optical Properties 45
  - 4.1.3 Collisional Properties 47
- 4.2 Cooling a Fermi Gas 49
- 4.3 Preparing Few-Fermion Systems 53
  - 4.3.1 Spilling Technique 53
  - 4.3.2 Optimization of the Preparation Fidelity 54
- 4.4 Transfer to Multiple Microtraps 56
  - 4.4.1 Double Well 58
  - 4.4.2 Multiple Wells 59

4.5 Intensity Stabilization of Multiple Microtraps 60
4.5.1 Optical Setup and Camera 61
4.5.2 RF Setup 63
4.5.3 Feedback Software 64
4.5.4 First Results 65

5 SINGLE-ATOM DETECTION 67
5.1 Detection in a Magneto-Optical Trap 68
5.2 Spatial Resolution 69
5.2.1 Optical Resolution Limit 69
5.2.2 Quantum Gas Microscopes 70
5.2.3 Matterwave Microscope 71
5.3 Momentum Imaging 74
5.4 In-Situ Imaging 77
5.5 Spin Resolution and Photon Number 78
5.5.1 Photon Scattering Process 78
5.5.2 Rapid Spin-Resolved Imaging 81
5.6 Single Photon Detection 82
5.6.1 Noise Sources of CCDs 83
5.6.2 Electron-Multiplying CCDs 84
5.7 Image Processing 85
5.8 Summary 87

6 STRONGLY INTERACTING FERMIONS IN A SINGLE WELL 89
6.1 Description of the Experiments 90
6.2 Experimental Results for Two Particles 90
6.3 Theoretical Interpretation 94
6.3.1 Interacting Atoms in an Axially-Symmetric Microtrap 95
6.3.2 Interacting Atoms in an Isotropic Microtrap . . 97
6.3.3 Free Expansion with Contact Interactions 98
6.3.4 Free Expansion of Isotropic Trapped States . . . 99
6.4 Summary 104

7 EXPERIMENTS WITH A DOUBLE WELL 105
7.1 Double-Well Hubbard Hamiltonian 105
7.1.1 One Particle in a Double Well 106
7.1.2 Two Particles in a Double Well 107
7.2 In-Situ Measurements 109
7.2.1 Occupation Number Measurements 109
7.2.2 Spectroscopic Measurements 110
7.3 Singlet-Triplet Oscillations 112
7.4 Momentum-Space Measurements 116
7.4.1 Two Non-Interacting Particles 116
7.4.2 Two Indistinguishable Particles 118
7.4.3 Two Repulsively-Interacting Particles 120
7.5 Entanglement in the Double Well 122

7.5.1 Entanglement Witnesses 122
7.5.2 Entanglement Entropy 125

8 CONCLUSION 129
8.1 Summary 129
8.2 Outlook 132

A DERIVATION OF THE TWO-POINT CORRELATION FUNCTION 135

B ERROR ESTIMATES FOR SINGLE-WELL MEASUREMENTS 137

C SCATTERING LENGTHS FOR THE SINGLE-WELL EXPERIMENTS 139

D CORRELATION MEASUREMENTS WITH A SINGLE WELL 141

E ENTANGLEMENT ENTROPIES AND WITNESSES 151

REFERENCES 153

LIST OF FIGURES

Figure 2.1 Double-slit experiment 12
Figure 2.2 Setup of the Hanbury Brown and Twiss experiment 13
Figure 2.3 Hanbury Brown and Twiss correlations 14
Figure 2.4 Sketch of the Hanbury Brown and Twiss geometry 15
Figure 2.5 Entanglement Witness 20
Figure 2.6 Limiting states of the Hubbard model 24
Figure 2.7 Schematics of superexchange 26
Figure 2.8 Phases of the Bose-Hubbard model after TOF . 27
Figure 3.1 Two-level atom with light shift 31
Figure 3.2 Visualization of the scattering length 36
Figure 3.3 Scattering length and phase shift in a square potential 37
Figure 3.4 Wavefunction close to a zero-energy resonance 38
Figure 3.5 Open- and closed-channel potentials 39
Figure 4.1 Hyperfine splitting of ^{6}Li 44
Figure 4.2 Zeeman splitting of ^{6}Li 45
Figure 4.3 Polarizability of ^{6}Li 46
Figure 4.4 Feshbach resonances of the three lowest hyperfine states 49
Figure 4.5 Experimental sequence for high-field evaporation 50
Figure 4.6 Range of experimentally accessible states . . . 52
Figure 4.7 Spilling technique 53
Figure 4.8 Stufenplot 55
Figure 4.9 Tunnel times 56
Figure 4.10 Microtrap optical setup 58
Figure 4.11 Double-well preparation scheme 58
Figure 4.12 Energy levels during the preparation of a double well 59
Figure 4.13 Four-well preparation schemes 60
Figure 4.14 RF setup for multiple microtraps 63
Figure 4.15 Structure of the feedback software 64
Figure 5.1 Fluorescence detection with the imaging setup 70
Figure 5.2 Flashing beam setup 73
Figure 5.3 Imaging with an optical dipole trap 74
Figure 5.4 Momentum and in-situ imaging 75
Figure 5.5 Photon number distributions 80
Figure 5.6 Photon number probability 81
Figure 5.7 Schematic of the imaging laser lock 82
Figure 5.8 Histogram of the EMCCD signal 85

Figure 5.9 Image processing of single-atom image 86
Figure 5.10 Histogram of maxima of LP-filtered images . . 87
Figure 6.1 Example of the imaging procedure for correlation measurements 91
Figure 6.2 Correlated densities for two particles in a single well. 92
Figure 6.3 Fringe spacing after T/4 94
Figure 6.4 Energy of two particles in a harmonic trap . . 96
Figure 6.5 Wavefunction of two atoms in a harmonic trap 97
Figure 6.6 Busch wavefunction overlap 100
Figure 6.7 Busch wavefunction overlap components . . . 101
Figure 6.8 Busch wavefunction momentum components . 103
Figure 7.1 Occupation measurement of the double well . 110
Figure 7.2 Spectroscopic measurement of the double well 111
Figure 7.3 Energy spectrum of the double well 112
Figure 7.4 Bloch Sphere of two singly-occupied sites . . . 113
Figure 7.5 Singlet-triplet oscillations in a double well . . 115
Figure 7.6 Density of a single particle after TOF 117
Figure 7.7 Correlated density of non-interacting particles in a double well 118
Figure 7.8 Correlations of two indistinguishable fermions 120
Figure 7.9 Basis for fitting correlated density 122
Figure 7.10 Fitted correlated densities in the double well . 123
Figure 7.11 Entanglement witnesses measured in the double well 124
Figure 7.12 Entanglement entropy in a double well 125
Figure 7.13 Entanglement entropy measurements in a double well 127
Figure 8.1 Correlation measurements with one and two wells 130

LIST OF TABLES

Table 4.1 Properties of ^{6}Li 47
Table 4.2 Spilling times 57
Table 7.1 States and Hamiltonian of the double well . . 106
Table C.1 Scattering lengths for the single-well experiments 139
Table E.1 Purities and entanglement entropies 152
Table E.2 Entanglement witnesses 152

ACRONYMS

ADC	analog-to-digital converter
AO	analog-output
AOD	acousto-optic deflector
AOM	acousto-optic modulator
CHSH	Clauser-Horne-Shimony-Holt, eponymous discoverers of the CHSH inequality
CIC	clock-induced charge
COM	refers to center-of-mass coordinates
DAC	digital-to-analog converter
ECDL	external-cavity diode laser
EM	electron-multiplying
EMCCD	electron-multiplying CCD
HBT	Hanbury Brown and Twiss
LR	likelihood ratio
MOT	magneto-optical trap
NA	numerical aperture
ODT	optical dipole trap
PHC	Peres-Horodecki criterion
PID	proportional-integral-derivative controller
PSF	point spread function
QE	quantum efficiency
QGP	quark-gluon plasma
REL	refers to relative coordinates
RF	radio frequency
TOF	time-of-flight
VDW	Van der Waals
VI	virtual instrument, a subroutine of a LabVIEW program
WKB	Wentzel-Kramers-Brillouin

1

INTRODUCTION

Since its development approximately 100 years ago, quantum theory has been hugely successful at describing microscopic processes of all kinds. It expresses the states of particles not directly by their coordinates in configuration space, but by their probability amplitudes, the wavefunctions. A notable feature of quantum mechanics is that a particle can be in a superposition of states. If these states have a well-defined phase relation to each other, they are said to be a coherent superposition, as opposed to a statistical mixture. Coherence can lead to interference patterns when measuring an observable of a quantum particle or correlations between observables. These interference patterns are similar to the interference effects found in classical wave mechanics.

Another distinct feature of quantum mechanics is entanglement. It can occur when two (or more) independent quantum objects are combined into a single system. The system is entangled if it can only be described by one common wavefunction, and not by separate wavefunctions for the individual particles. This was famously shown with the Bell test [Bel64], where entanglement leads to correlations between two particles which cannot be explained by classical theory (or, more precisely, a local realist theory). Interestingly, entanglement is a property which can be created and destroyed, for example when two particles interact. It is an essential resource in applied fields such as quantum cryptography or quantum computing.

Naturally, coherence and entanglement both play an important role when adding more and more quantum particles to a system. Both phenomena can lead to strong correlations between a large number of particles, for example, in strongly coupled quantum fluids. A wide range of systems of current interest falls into this category, including unitary atomic quantum gases, electrons in strongly correlated materials such as strange metals, nuclear matter, and the quark-gluon plasma in a heavy-ion collisions [Ada+12]. While these systems exist in wholly different environments, with temperatures ranging between 10^{-8} K and 10^{12} K, their common dependence on strong correlations makes it possible to describe all of them with low-viscosity hydrodynamics.

Long-range correlations also play a prominent role in quantum phase transitions. This type of phase transitions typically occurs at zero temperature when a coupling constant of a Hamiltonian is tuned. Close to the quantum critical point, the characteristic length scale of the fluctuations in the system diverges, and the correlations decay algebraically decay with the distance [Sac11]. While directly observing a quantum critical point at 0 K may be impossible, one can still detect the effects of these correlation fluctuations near a quantum critical point at finite temperatures in the quantum critical region.

In both cases, correlations caused by the quantum nature of a system have a strong influence on its properties. In the case of strongly correlated quantum fluids, for example, the viscosity is affected. It describes how momentum is dissipated and governs the transport properties of the fluid. Close to a critical point, it has been conjectured that the ratio of viscosity over entropy-per-particle, η/s, is close to a universal bound [KSS05]. First examinations of this prediction have been performed by looking at the expansion dynamics of an ultracold quantum gas [Cao+11] and via momentum correlations in heavy-ion collisions, which probe a strongly coupled quark-gluon plasma (see [Mar11; Bec14] for overviews).

A simple example for a correlated system close to a quantum phase transition is a dimerized lattice of Heisenberg spins [Sac08]. If the coupling of the spins within a dimer dominates over the coupling between dimers, each dimer can be treated separately. There will be correlations between the spins within a dimer, but not on larger scales. If the inter- and intra-dimer coupling is similar, an antiferromagnetic Néel-state with long-range spin order may form. One can reveal this ordered phase by looking at the magnetic properties of such a material, e.g., the magnetic susceptibility [MAH76]. One can also study its excitations, whose energy separation from the ground state is predicted to vanish at the critical point. This effect produces a characteristic excitation spectrum, which has been measured in certain alloys with neutron scattering [Rüe+08]. A more direct measure of the correlations in the material, albeit averaged over the entire sample, can be obtained from the structure factor of scattering experiments [SSW51].

In the last couple of decades, it has become possible to create artificial quantum many-body states with ultracold gases. Due to the high level of experimental control over the system's parameters, one can use such experiments to simulate different aspects of existing strongly correlated systems, or even to create new systems which do not occur naturally. To analyze ultracold quantum gases, many of the aforementioned measurement techniques have been adapted and applied to atomic systems: Instead of using neutrons for scattering experiments, one has been able to measure magnetic ordering from the Bragg scattering of light [Har+15]. Correlations in the momenta of particles have been probed by letting the gas expand and correlating the resulting density distribution ([Föl+05; Rom+06], and more recently [Hod+17]). With a novel imaging technique, it has even been possible to directly measure long-range correlations of fermions in a lattice atom by atom [Maz+17], which provides an observable which cannot be obtained, e.g., from condensed matter systems.

In the Heidelberg few-fermion experiment, we have developed a unique approach to study correlated quantum systems. One ingredient is the deterministic preparation of few-fermion systems with very low entropy, first developed in [Ser^{+}11; Ser11]. The other ingredient is an efficient imaging method to obtain as much information as possible from these systems, called the *matterwave microscope*. This imaging method, which we have developed over the last two years [Bec16; Ber17], combines spatially resolved single-atom detection with a time-of-flight expansion.

In short, we first release the atoms from our initial system into a large external harmonic potential, in which the atomic density distribution expands. Afterward, we optically detect the resulting density distribution. Depending on how we apply our harmonic potential in the first step, we can perform different transformations on the initial density distribution [Mur^{+}14] and thereby probe different observables. In this thesis, we approximately perform a Fourier transform on our initial spatial distribution, which means that we probe the initial momentum distribution.

Our optical detection has been optimized to be able to resolve each atom spatially, as well as its hyperfine state. This maximizes the information that we can extract from the spatial distribution of atoms. We use a custom-built microscope objective with a large numerical aperture [Ser11], which can collect a large fraction of the scattered photons and provides spatial resolution. Together with our photon-counting EMCCD camera, this allows us to use a short exposure time for each image and still obtain a clear signal. This keeps the heating rate and diffusive motion of the atoms small during imaging[1], and we can image the position of individual atoms in free space with spin resolution.

In this thesis, we have used our new imaging method to study the correlations of systems containing a small number of interacting fermionic particles. In the first experiment, we prepared a "bulk" system of two atoms in a tight optical trap with strong attractive interactions near a Feshbach resonance. We use this minimal system to study the role of interactions for the time-evolution during the expansion of a Fermi gas. This understanding is crucial if we want to perform experiments with larger numbers of particles in the future, for example to study strongly coupled quantum fluids.

In the second experiment, we prepared small systems of repulsive atoms in a double-well potential. This is a minimal realization of spatially discretized quantum systems, in particular the Hubbard model. The system contains two of the major competing elements which can drive phase transitions in the Hubbard model, the inter-site hopping

---

[1] This means that we do not have to cool the atoms during imaging or to fix their position. It makes our imaging scheme easier to implement technically and is similar to the light-sheet imaging developed by [Büc^{+}09].

and the on-site interactions. With the matterwave microscope, we were able to perform complementary measurements to our previous experiments with this system [Mur⁺15b]. By measuring the correlations between the atoms, we were able to directly show the coherence of our system and to detect entanglement between the particles, depending on the interaction strength.

In the future, we can also use our imaging method on systems containing more particles, thanks to its single-atom detection capability. In particular, our measurements on paired particles in a double well indicate the potential for studying larger systems, which may, for example, support elaborate bound states like resonating valence [And87; ADL04; PB08].

2

MANY-BODY QUANTUM THEORY

This thesis covers several experiments performed on systems containing a small number of ^{6}Li atoms. As the atoms have been cooled well below the Fermi temperature, they behave as quantum particles. Even though these small systems are no true many-body systems, it makes sense to introduce quantum many-body formalisms already for just two particles. Therefore, this chapter will explain the fundamental concepts related to many-body quantum theory, which are important to fully appreciate our experiments.

First, we will revisit the methods needed to express arbitrary states and operators in a many-body system. We will focus on one operator in particular, the correlation function, which measures the correlations within a quantum state. By studying a few examples of how correlation functions have been used in different areas of physics, for example in quantum optics, we will find results which are instructive for understanding our experiments.

Also, we will briefly introduce entanglement, a property which is absent in classical systems and characteristic for quantum systems. In our experiments described in Chapter 7, we can use the properties derived in this section together with the correlation function to show the quantum nature of our systems.

Finally, we will look at the Hubbard model, which is widely used in the fields of condensed matter and ultracold atoms to describe systems of interacting particles on a lattice. Using the concepts introduced in the earlier sections, we will demonstrate some of its phases and observables which appear for many different lattice configurations, including the double well. Theoretical results which are specific to the double well will not be presented in this chapter, but will be presented together with the experimental results in Chapter 7.

2.1 MANY-BODY QUANTUM STATES

2.1.1 *Constructing Many-Body Quantum States*

In general, quantum systems can be described with states of a Hilbert space. The state of a single particle can be described by a set of numbers containing information about all its properties (quantum numbers), for example, its position, momentum, polarization, spin, etc. The values of these quantum numbers denote the mode that the particle occupies. Often, it is possible to separate the total Hilbert space into independent subspaces for the different quantum numbers. For example, the electron in a hydrogen atom can be approximately described by its principle quantum number n, its angular momentum quantum numbers l and m_l, and its spin quantum number m_s. Note that the choice of these quantum numbers is not unique, as one could also use the spatial wavefunction $\psi(r)$ of the electron, together with its spin, to describe its state. However, the nlm_lm_s-space is often more convenient.

Now, we want to see how to describe a quantum system composed of many particles. Suppose that we have a system containing N two-level qubits (Hilbert space dimension of each qubit $d = 2$). If we want to build a combined Hilbert space using tensor products, we find from combinatorics that the combined space will have 2^N, or, in general, d^N basis states. This exponential increase of the size of the Hilbert space is one of the reasons why it can be difficult to exactly solve quantum many-body problems.

If the system is composed of *identical* fermions (bosons), its total many-body state must obey the antisymmetrization (symmetrization) requirement. By expressing generic fermionic states using the Slater determinant

$$\Phi(l_1, l_2, \ldots, l_N) = \frac{1}{\sqrt{N!}} \begin{vmatrix} \phi_{l_1}(x_1) & \cdots & \phi_{l_N}(x_N) \\ \vdots & \ddots & \vdots \\ \phi_{l_1}(x_N) & \cdots & \phi_{l_N}(x_N) \end{vmatrix}, \tag{2.1}$$

one can conveniently take into account this requirement. For bosonic states, one has to use a permanent instead of a determinant. The l_i express the specific value of the quantum numbers n of the i^{th} particle, i.e., which of its M modes it occupies.

A simplified notation for the basis states is called the *Fock basis*. It counts the occupation of all the single-particles modes,

$$\Phi(l_1, l_2, \ldots, l_N) = |n_1, n_2, \ldots, n_M\rangle \equiv |\mathbf{n}\rangle, \tag{2.2}$$

where n_1 counts the number of particles in the first single-particle mode, n_2 counts the number of particles in the second mode, and so forth. $\mathbf{n}$ is the vector containing the occupation numbers of all modes. For example, if we have two identical fermions with four modes each, then we can express the state $\Phi(2,4) = (\phi_2(x_1)\phi_4(x_2) - \phi_2(x_2)\phi_4(x_1))/\sqrt{2}$ as $|0, 1, 0, 1\rangle$.

This notation is much simpler, because it only counts the number of identical particles per mode and does not label them. Therefore, the need for explicit (anti-)symmetrization is avoided. This is equivalent to stating that Fock states intrinsically have the correct (anti-)symmetry, as each Fock state represents a determinant/permanent. Together with the Fock states, we have also introduced the braket notation to denote the states of the Hilbert space.

Using the Fock states as defined above, we can thus express a general pure N-body state as a superposition of all possible Fock basis states,

$$|\Psi\rangle = \sum_{\mathbf{n}} c_{\mathbf{n}} |\mathbf{n}\rangle \,, \tag{2.3}$$

where the sum runs over all possible $\mathbf{n}$ with $\sum_{i=1}^{M} n_i = N$ and contains normalized complex coefficients $c_{\mathbf{n}}$. In the picture of eq. (2.1), the sum runs over all possible ways of combining N modes l_j.

2.1.2 *Density Matrix*

In reality, no system will remain in a pure state indefinitely due to interactions with its environment. Therefore, as every realization of a system may result in different states, one has to understand how the statistical ensemble of this system looks like. Such an ensemble can be written as a *density matrix*, which is defined as

$$\hat{\rho} = \sum_{mn} \rho_{mn} |m\rangle \langle n| \,, \tag{2.4}$$

where m and n label basis states, which, for example, may be Fock states. The coefficients of the sum are defined as $\rho_{mn} = \langle m| \hat{\rho} |n\rangle$. They can be conveniently used to define a matrix, hence the name of ρ. The diagonal terms correspond to populations and must add up to 1, i.e., $\mathrm{Tr}\,\hat{\rho} = 1$. The off-diagonal terms can be seen as coherences which couple two of the basis states[1]. Their magnitudes are limited to

$$|\rho_{mn}|^2 \leqslant |\rho_{mm}| |\rho_{nn}| \,, \tag{2.5}$$

i.e., they cannot be larger than the populations in the corresponding states. If this equation is an equality for all m and n, the density matrix describes a pure state.

Using the density matrix, one can calculate the expectation value of any observable $\langle \hat{A} \rangle = \mathrm{Tr}(\hat{\rho}\hat{A}) = \sum_i \langle i|\hat{\rho}\hat{A}|i\rangle$. In general, one therefore needs to know all entries of the density matrix, which requires a number of measurements in conjugate measurement bases, e.g., with quantum tomography. However, if one is interested in only certain observables, it may be enough to know only parts of the density matrix.

---

[1] If one chooses the correct basis $|\psi_j\rangle$, it can also be expressed as a diagonal matrix $\hat{\rho} = \sum_j p_j |\psi_j\rangle \langle \psi_j|$. If this sum contains more than one term, the state is an incoherent mixed state.

2.1.3 *Operators on Many-Body Quantum States*

Now that we have seen how many-body states can be expressed and which role they play in the measurement of observables, it makes sense to look at how (many-body) observables have to be treated in the formalism of Fock states. In principle, any observable can be expressed as an operator, which acts on a Hilbert space and maps a state to another state. Operators are marked by a caret, e.g. $\hat{A}$, to recognize them easily[2]. In this section, I will list a few useful operators and how they can be expressed in Fock space.

First, let us consider how particles can be added to or removed from Fock states. This can be done with *creation* and *annihilation operators*. With these operators, we can construct any many-body state starting from a state without any particles, the vacuum state $|0\rangle = |0, \dots, 0\rangle$. For bosons, the creation and annihilation operators are defined as

$$\begin{aligned} \hat{a}_i^\dagger \left|\dots, n_i, \dots\right\rangle &= \sqrt{n_i + 1} \left|\dots, n_i + 1, \dots\right\rangle \\ \hat{a}_i \left|\dots, n_i, \dots\right\rangle &= \sqrt{n_i} \left|\dots, n_i - 1, \dots\right\rangle . \end{aligned} \tag{2.6}$$

They obey the commutation relations

$$\begin{aligned} \left[\hat{a}_i, \hat{a}_j^\dagger\right] &= \delta_{ij} \\ \left[\hat{a}_i, \hat{a}_j\right] &= 0 \\ \left[\hat{a}_i^\dagger, \hat{a}_j^\dagger\right] &= 0. \end{aligned} \tag{2.7}$$

For fermions, the creation and annihilation operators are defined as

$$\begin{aligned} \hat{a}_i^\dagger \left|\dots, n_i, \dots\right\rangle &= (-1)^{\sum_{j<i} n_j} \left(1 - n_i\right) \left|\dots, n_i + 1, \dots\right\rangle \\ \hat{a}_i \left|\dots, n_i, \dots\right\rangle &= (-1)^{\sum_{j<i} n_j} n_i \left|\dots, n_i - 1, \dots\right\rangle . \end{aligned} \tag{2.8}$$

The fermionic definition already takes into account that there can be no more than one particle per mode, as the state would otherwise be impossible to antisymmetrize. The sign comes from the anticommutation relations,

$$\begin{aligned} \left\{\hat{a}_i, \hat{a}_j^\dagger\right\} &= \delta_{ij} \\ \left\{\hat{a}_i, \hat{a}_j\right\} &= 0 \\ \left\{\hat{a}_i^\dagger, \hat{a}_j^\dagger\right\} &= 0. \end{aligned} \tag{2.9}$$

---

[2] Other symbols are typically scalar values or functions, or, if written in bold face, (Euclidean) vectors.

For both bosons and fermions, a occupation *number operator* can be defined to count the number of particles n_i in the i^{th} mode,

$$\hat{n}_i \left|\ldots, n_i, \ldots\right\rangle = \hat{a}_i^\dagger \hat{a}_i \left|\ldots, n_i, \ldots\right\rangle = n_i \left|\ldots, n_i, \ldots\right\rangle . \tag{2.10}$$

For fermions, it has the property that $\hat{n}_i^2 = \hat{n}_i$ and therefore also that $\hat{n}_i\,(1 - \hat{n}_i) = 0$, of which we will make use later. With the number operator, we can also define an operator which counts the total number of particles in the system, $\hat{N} = \sum_{i=1}^{M} \hat{n}_i$.

In general, any operator $\hat{T}$ on N-particle Fock space which consists of single-particle operators $\hat{t}$ can be expressed using creation and annihilation operators [Sch08],

$$\hat{T} = \sum_{i,j} t_{ij} \hat{a}_i^\dagger \hat{a}_j, \tag{2.11}$$

where $t_{ij} = \left\langle l_i \right| \hat{t} \left| l_j \right\rangle$ is the matrix element of the single-particle operator for modes l_i and l_j. Similarly, one can define general two-particle operators on Fock space as

$$\hat{F} = \frac{1}{2} \sum_{i,j,k,l} f_{ijkl} \hat{a}_i^\dagger \hat{a}_j^\dagger \hat{a}_k \hat{a}_l \tag{2.12}$$

with matrix elements

$$\begin{aligned} f_{ijkl} &= \left\langle l_i, l_j \right| \hat{f} \left| l_k, l_l \right\rangle \\ &= \int\!\!\int dx_1 dx_2\, \phi_{l_i}^*(x_1) \phi_{l_j}^*(x_2) f(x_1, x_2) \phi_{l_k}(x_1) \phi_{l_l}(x_2). \end{aligned} \tag{2.13}$$

An important operator which relates the Fock states back to real space is the *field operator*. It creates or annihilates a particle at a specific location $\mathbf{r}$,

$$\hat{\Psi}^\dagger(\mathbf{r}) \left|0\right\rangle = \left|\mathbf{r}\right\rangle . \tag{2.14}$$

The state $\left|\mathbf{r}\right\rangle$ is an eigenvector of the position operator $\hat{\mathbf{r}} \left|\mathbf{r}\right\rangle = \mathbf{r} \left|\mathbf{r}\right\rangle$. It creates this state by adding all modes in Fock space,

$$\hat{\Psi}^\dagger(\mathbf{r}) \left|0\right\rangle = \sum_i \psi_i^*(\mathbf{r})\, \hat{a}_i^\dagger \left|0\right\rangle \tag{2.15}$$

and is thus closely related to the basis wavefunctions of the modes in position space $\psi_i(\mathbf{r})$. Its (anti-)commutation relations are

$$\begin{aligned} &\left[\hat{\Psi}(\mathbf{r}_1), \hat{\Psi}^\dagger(\mathbf{r}_2)\right] = \delta(\mathbf{r}_1 - \mathbf{r}_2) && \left\{\hat{\Psi}(\mathbf{r}_1), \hat{\Psi}^\dagger(\mathbf{r}_2)\right\} = \delta(\mathbf{r}_1 - \mathbf{r}_2) \\ &\left[\hat{\Psi}(\mathbf{r}_1), \hat{\Psi}(\mathbf{r}_2)\right] = 0 && \left\{\hat{\Psi}(\mathbf{r}_1), \hat{\Psi}(\mathbf{r}_2)\right\} = 0 \\ &\left[\hat{\Psi}^\dagger(\mathbf{r}_1), \hat{\Psi}^\dagger(\mathbf{r}_2)\right] = 0 && \left\{\hat{\Psi}^\dagger(\mathbf{r}_1), \hat{\Psi}^\dagger(\mathbf{r}_2)\right\} = 0 \end{aligned} \tag{2.16}$$

for bosons and fermions, respectively.

One can also define a *particle density operator*[3] which counts the number of particles at a position $\mathbf{r}$, $n(\mathbf{r}) = \sum_{k=1}^{N} \delta(\mathbf{r} - \mathbf{r}_k)$. Using field operators, it can be expressed as [FW71]

$$\begin{aligned} \hat{n}(\mathbf{r}) &= \hat{\Psi}^\dagger(\mathbf{r})\hat{\Psi}(\mathbf{r}) \\ &= \sum_{ij} \psi_i^*(\mathbf{r})\psi_j(\mathbf{r})\, \hat{a}_i^\dagger \hat{a}_j. \end{aligned} \tag{2.17}$$

The expectation value of the particle density operator for a given pure state $|\Psi_0\rangle$ can be understood as the total probability of finding (annihilating) a particle at position $\mathbf{r}$,

$$\begin{aligned} \langle \hat{n}(\mathbf{r}) \rangle &= \langle \Psi_0 | \hat{\Psi}^\dagger(\mathbf{r})\hat{\Psi}(\mathbf{r}) |\Psi_0\rangle \\ &= \sum_f \langle \Psi_0 | \hat{\Psi}^\dagger(\mathbf{r}) |f\rangle \langle f| \hat{\Psi}(\mathbf{r}) |\Psi_0\rangle \\ &= \sum_f \left| \langle f| \hat{\Psi}(\mathbf{r}) |\Psi_0\rangle \right|^2 . \end{aligned}$$

If we want to know the expectation value for a general state described by a density matrix $\hat{\rho}$, we obtain

$$\begin{aligned} \langle \hat{n}(\mathbf{r}) \rangle &= \sum_{iklmn} \psi_k^*(\mathbf{r})\psi_l(\mathbf{r})\, \rho_{mn}\, \langle i \mid m\rangle \langle n| \hat{a}_k^\dagger \hat{a}_l |i\rangle \\ &= \sum_{klmn} \psi_k^*(\mathbf{r})\psi_l(\mathbf{r})\, \rho_{mn}\, \langle n| \hat{a}_k^\dagger \hat{a}_l |m\rangle . \end{aligned} \tag{2.18}$$

2.2 CORRELATION FUNCTIONS

2.2.1 *General Correlation Functions*

As mentioned before, a system can be fully characterized by determining all entries of the density matrix. However, as the number of basis states scales exponentially with the size of the system, this can become challenging for systems with large numbers of particles [Cra$^+$10]. Instead of trying to measure all entries of the density matrix, we will focus on measuring just the correlations in the system. This is a natural approach, because the correlations are what gives a system a many-body character — If the particles in a many-body system show no correlations, it can be described by a product of individual, independent single-particle systems. We therefore want to find an observable which describes the correlations between $2, 3, \ldots, n$ particles

---

[3] Note the difference in notation, the particle number operator counts the particles in mode i, whereas the particle density operator counts the particles at position $\mathbf{r}$.

in the system, with increasing complexity. In general, we do this with the *n-point correlation function*, which is the expectation value for applying an operator $\hat{O}$ at n points:

$$\tilde{G}^{(n)}(x_1, x_2, \ldots, x_n) = \left\langle \hat{O}(x_1)\hat{O}(x_2)\ldots\hat{O}(x_n) \right\rangle, \tag{2.19}$$

where, in general, the x_i stand for points in space-time.

If we look again at the particle density, it is clear that it is a lowest-order correlation function,

$$\langle \hat{n}(x_1) \rangle = \tilde{G}^{(1)}(x_1). \tag{2.20}$$

Recalling the definition of the density operator (2.17), we can also write it as a correlation function of two field operators,

$$\langle \hat{n}(x_1) \rangle = \left\langle \hat{\Psi}^\dagger(x_1)\hat{\Psi}(x_1) \right\rangle \Leftrightarrow G^{(1)}(x_1, x_1). \tag{2.21}$$

This expression can be generalized to Glauber's definition of the *field correlation function* [Gla63b; Gla06]

$$\begin{aligned} G^{(n)}(x_1, \ldots, x_{2n}) &= \left\langle \hat{\Psi}^\dagger(x_1)\ldots\hat{\Psi}^\dagger(x_n)\hat{\Psi}(x_{n+1})\ldots\hat{\Psi}(x_{2n}) \right\rangle \\ &= \mathrm{Tr}\Big(\hat{\rho}\hat{\Psi}^\dagger(x_1)\ldots\hat{\Psi}^\dagger(x_n)\hat{\Psi}(x_{n+1})\ldots\hat{\Psi}(x_{2n})\Big) \end{aligned} \tag{2.22}$$

for arbitrary even numbers of field operators.

In this notation, the correlation describes the overlap of a state with n particles removed in positions $x_1, \ldots, x_n$ with a state where n particles have been removed in positions $x_{n+1}, \ldots, x_{2n}$. Alternatively, it is the overlap of the initial state with a state where n particles have been moved[4] from $x_1, \ldots, x_n$ to $x_{n+1}, \ldots, x_{2n}$.

Intuitively, if one knows all correlation functions to N^{th} order, one can fully describe an N-particle state, as one then knows the overlap of the state with all other possible states. However, already the lower-order correlation functions can contain information about the state. As they are more easily accessible in experiments, we will mainly use the first- and second-order correlation function from here on.

2.2.2 *Correlation Functions in Quantum Optics*

Although correlation functions are essential in many fields in physics and science in general, we will first study their role in quantum optics, as many of its concepts can also be applied to ultracold atomic

---

[4] This interpretation is evoked in quantum field theory, where the correlation functions are called propagators [PS95].

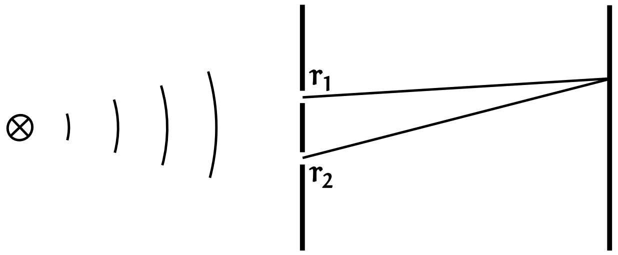

Figure 2.1: Double-slit experiment. The point source on the left ensures that the observer at $\mathbf{r}$ sees a coherent superposition of the fields emitted at $\mathbf{r}_1, \mathbf{r}_2$.

systems. In quantum optics, correlation functions are used to characterize the coherence properties of light [Sud63; Gla63a]. This involves studying the light's intensity distribution, which depends on the electric field[5] as $I(x,t) = |E(x,t)|^2$. If we decompose the electric field in positive and negative frequency components, $E = E^{(+)} + E^{(-)}$, we can quantize it and treat the $(\pm)$-components as the field operators $\Psi^{(\dagger)}$ introduced before.

A familiar example of a correlation measurement on a light field comes from the double-slit experiment: When illuminating a double slit with a single light source (Figure 2.1), we can observe an interference pattern in the intensity on a screen behind the double slit. The intensity at position x on the screen is given by the square of the electric field $E(x)$, which in turn is a superposition of the two fields originating from the slits, $E(x_1) + E(x_2)$. Using the electric field operators, we can express the time-averaged[6] intensity as

$$\begin{aligned}
\langle I(x) \rangle &\propto \left\langle \left| E^{(+)}(x_1) + E^{(+)}(x_2) \right|^2 \right\rangle \\
&= \left\langle E^{(-)}(x_1) E^{(+)}(x_1) \right\rangle + \left\langle E^{(-)}(x_2) E^{(+)}(x_2) \right\rangle \\
&\quad + \left\langle E^{(-)}(x_1) E^{(+)}(x_2) \right\rangle + \left\langle E^{(-)}(x_2) E^{(+)}(x_1) \right\rangle \\
&= G^{(1)}(x_1, x_1) + G^{(1)}(x_2, x_2) + G^{(1)}(x_1, x_2) + G^{(1)}(x_2, x_1).
\end{aligned} \tag{2.23}$$

In the last line, the terms were identified with the correlation functions from eq. (2.20) and (2.22). Hence, the intensities measured at one point can be expressed by using only first-order field correlation functions, regardless of which field is being probed. The last two terms in the sum contain oscillatory terms which can give rise to the interference pattern.

We can also study higher-order correlation functions by correlating the intensities at different points on the screen. If we measure at two

---

[5] Without loss of generality, we assume that the electric field is linearly polarized, such that we can describe it just with its magnitude E.

[6] While $I(t) = |E^{(+)}(t) + E^{(-)}(t)|^2$ contains the fast oscillations of the electric field, the time-averaged intensity can be described by just $\langle I \rangle = \langle |E^{(+)}|^2 \rangle$.

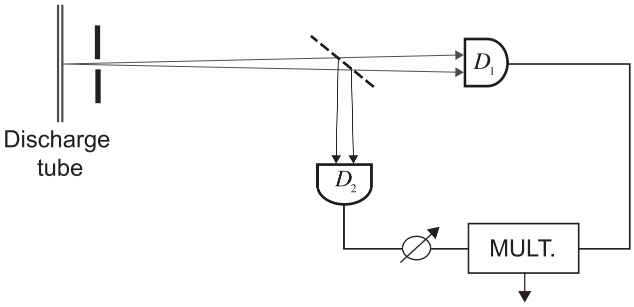

Figure 2.2: Simplified setup of the Hanbury Brown and Twiss experiment [HT56b]. Photons are emitted from the discharge tube and pass a half-silvered mirror on their way to the detectors. From [Gla07]

points, we essentially perform the Hanbury Brown and Twiss (HBT) experiment [HT56b]. In its most condensed realization (Figure 2.2), it measures the intensity of a light field in two locations in time by shifting the detectors forward or backward along the beam. The observable one obtains is the two-point field correlation function

$$G^{(2)}(x_1, x_2, x_2, x_1) = \left\langle E^{(-)}(x_1) E^{(-)}(x_2) E^{(+)}(x_2) E^{(+)}(x_1) \right\rangle . \tag{2.24}$$

What one observes as a function of x_1, x_2 depends on the state $|\Psi_0\rangle$ that is measured. Let us first consider the case where the system is in a pure, coherent state. The states are by definition eigenstates of the annihilation operator, i.e., $E^{(+)}(x)\,|\Psi_c\rangle = \mathcal{E}(x)\,|\Psi_c\rangle$, where $\mathcal{E}(x)$ is the eigenvalue. For this state, the two-point correlation function reduces to

$$\begin{aligned} G^{(2)}_{\text{coh}}(x_1, x_2, x_2, x_1) &= \mathcal{E}^*(x_1)\mathcal{E}^*(x_2)\mathcal{E}(x_2)\mathcal{E}(x_1) \\ &= G^{(1)}(x_1, x_1)\, G^{(1)}(x_2, x_2), \end{aligned} \tag{2.25}$$

which is the product of the uncorrelated intensities measured at the two points independently.

If the source is not coherent, the correlation function evaluate differently. To compare this correlation function to the coherent case, we can normalize it to the values of the independent intensities. This quantity is called the *normalized n-point correlation function,*

$$g^{(n)}(x_1, \ldots, x_n) = \frac{G^{(n)}(x_1, \ldots, x_n, x_n, \ldots, x_1)}{G^{(1)}(x_1, x_1) \ldots G^{(1)}(x_n, x_n)} . \tag{2.26}$$

For the special case of a chaotic light source, e.g., a discharge tube as it was used by Hanbury Brown and Twiss, the two-point correlation function becomes [Gla06; Gla07]

$$g^{(2)}_{\text{chaotic}}(x_1, x_2) = 1 + \frac{\left|G^{(1)}(x_1, x_2)\right|^2}{G^{(1)}(x_1, x_1)\, G^{(1)}(x_2, x_2)} . \tag{2.27}$$

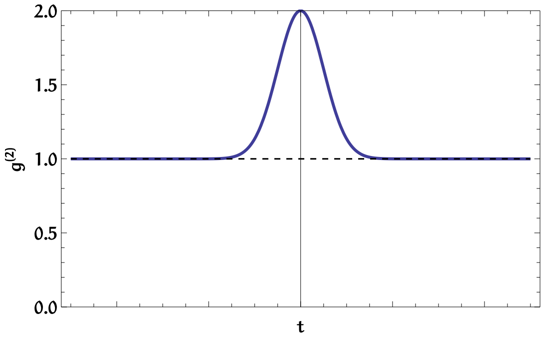

Figure 2.3: Ideal two-point correlation of a chaotic photon source versus delay time between the two detectors. Zero delay time corresponds to placing both detectors at the same distance x_1. If the photons are indistinguishable, their coincidence rate is enhanced.

For measurements at $x_1 = x_2$, i.e., when the photons are in the same mode, the value of the correlation function is enhanced, as shown in Figure 2.3. This is also what Hanbury Brown and Twiss had observed in their original experiment [HT56b]. It shows us that indistinguishability alone will already introduce correlations to our many-body system, due to the (anti-)symmetrization requirement for identical particles.

2.2.3 *Applications of the Hanbury Brown and Twiss Effect*

Because the HBT effect only requires the detection of indistinguishable particles at two locations and no special initial conditions, it is broadly used in many different fields of physics, of which I will present three applications (in parts following the review [HJ99]): The first is the original idea that Hanbury Brown and Twiss had had, namely the determination of the size of astronomical objects from intensity correlations in their light field [HT54; HT56a]. A second, similar application has been developed for particle physics, where the correlations detected in the products of a high-energy collision convey information about the collision process itself (see for example [Gol+60; Koo77; Zaj+84]).

The third application involves ultracold atoms in optical potentials which can be probed with optical measurements of the density (see for example [Föl+05; Föl08; Rom+06; Rom09], or [Föl14] for a review). It will serve as an example of how HBT correlations, which are caused by the symmetry requirement for the wavefunction of indistinguishable particles, can be linked back to the more general correlations which we started with in the beginning. For example, interactions between distinguishable ultracold atoms may give rise to similar correlations, as we will also see in our experiments. As this application of the HBT effect requires some background knowledge specific to

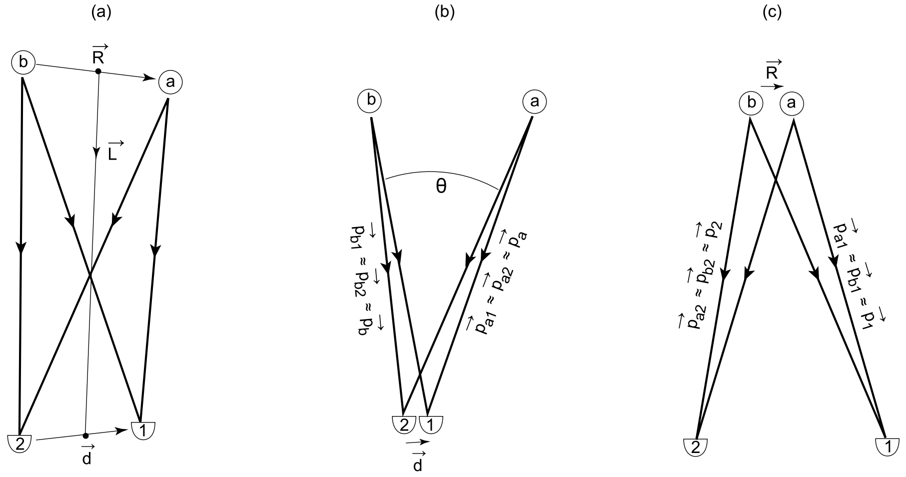

Figure 2.4: Sketch of the geometry of the HBT-experiment. (a) General arrangement of two sources a and b, and two detectors 1 and 2. (b) Setup for astronomical applications where $L \gg R \gg d$. (c) Setup for heavy-ion collisions where $L \gg d \gg R$. From [HJ99].

ultracold atomic lattice systems, I will present it at the end of this chapter.

2.2.3.1 *HBT in Astronomy*

Let us first consider the simplified case where two photons are emitted at two points $\mathbf{r}_a$ and $\mathbf{r}_b$ in a large distance $L \gg R, d$ from the detectors at positions $\mathbf{r}_1$ and $\mathbf{r}_2$ (Figure 2.4). The single particle modes can in the far field be described as plane waves which are emitted by two atoms at the points a and b. For each mode, the field that reaches the detector is $\psi_\alpha(\mathbf{r}_j) \propto e^{i(\mathbf{k}\cdot(\mathbf{r}_\alpha - \mathbf{r}_j)) + \phi_\alpha} \equiv e^{i(kr_{j\alpha} + \phi_\alpha)}$ with an initial phase ϕ_α, wavenumber $k = 2\pi/\lambda$, label α for the modes of the source, and label j for the detector. The argument $kr_{j\alpha}$ simply corresponds to the phase that the photon has gathered after traveling the distance $r_{j\alpha}$. It is also sensible to assume that the photons were not created by the same atom, therefore, the density matrix can be described by the Fock-state $|1,1\rangle$.

We can now calculate the expectation value of the two-point correlation function (2.22) according to eq. (2.12) in the Fock basis. Using our assumptions and applying the commutation relations, we can bring it to the form

$$\begin{aligned} &G^{(2)}(\mathbf{r}_1, \mathbf{r}_2, \mathbf{r}_2, \mathbf{r}_1) = \\ &\sum_{\alpha\beta\gamma\delta} \psi^*_\alpha(\mathbf{r}_1)\psi^*_\beta(\mathbf{r}_2)\psi_\gamma(\mathbf{r}_2)\psi_\delta(\mathbf{r}_1)\Big[\delta_{\alpha\delta}\delta_{\beta\gamma}\left\langle \hat{n}_\alpha \hat{n}_\beta \right\rangle \\ &+ \delta_{\alpha\gamma}\delta_{\beta\delta}\left\langle \hat{n}_\alpha \hat{n}_\beta \right\rangle + \delta_{\alpha\beta}\delta_{\alpha\gamma}\delta_{\alpha\delta}\left\langle \hat{n}_\alpha(1 - \hat{n}_\alpha)\right\rangle\Big]. \end{aligned} \tag{2.28}$$

The explicit calculation for a two-mode system can be found in Appendix A. Upon inserting the fields ψ_α, we can write the correlation function as

$$\begin{aligned} &G^{(2)}(\mathbf{r}_1, \mathbf{r}_2, \mathbf{r}_2, \mathbf{r}_1) = \\ &\sum_{\alpha\beta\gamma\delta=\{a,b\}} e^{-i\{k(r_{1\alpha}+r_{2\beta}-r_{2\gamma}-r_{1\delta})+\phi_\alpha+\phi_\beta-\phi_\gamma-\phi_\delta\}} \\ &\times \Big[\delta_{\alpha\delta}\delta_{\beta\gamma}\left\langle \hat{n}_\alpha \hat{n}_\beta \right\rangle + \delta_{\alpha\gamma}\delta_{\beta\delta}\left\langle \hat{n}_\alpha \hat{n}_\beta \right\rangle + \delta_{\alpha\beta}\delta_{\alpha\gamma}\delta_{\alpha\delta}\left\langle \hat{n}_\alpha(1-\hat{n}_\alpha)\right\rangle \Big]. \end{aligned} \tag{2.29}$$

The terms where $\alpha = \delta$ and $\beta = \gamma$ will have a constant amplitude while the phase factor remains only for the terms with $\alpha \neq \delta$, $\beta \neq \gamma$. The initial phases ϕ_α, etc., cancel out in all terms. After performing the trace over the density matrix, the correlation function can then be expressed as

$$\begin{aligned} G^{(2)}(\mathbf{r}_1, \mathbf{r}_2, \mathbf{r}_2, \mathbf{r}_1) =& 3 + \frac{1}{2} e^{ik(r_{1b}-r_{1a}+r_{2a}-r_{2b})} \\ &+ \frac{1}{2} e^{-ik(r_{1b}-r_{1a}+r_{2a}-r_{2b})} \\ =& 3 + \cos\left(k\left(r_{1b} - r_{1a} + r_{2a} - r_{2b}\right)\right). \end{aligned} \tag{2.30}$$

The argument of the cosine compares the phases $\phi_{i\alpha} = k r_{i\alpha}$ of all combinations of both sources $\alpha = a, b$ and both detectors $i = 1, 2$. Hence, the correlation function compares the phase relation of four fields simultaneously.

Now, we can start evaluating these phases given the geometry of the problem. For $L \gg R \gg d$, which is reasonable when comparing the distance of a star to its size to the size of the detector, the correlation function can be simplified to [HJ99]:

$$\begin{aligned} G^{(2)}(d) &\sim \cos(\mathbf{d} \cdot (\mathbf{k}_a - \mathbf{k}_b)) \\ &\sim \cos\left(2\pi \frac{\theta d}{\lambda}\right) \end{aligned} \tag{2.31}$$

This depends on the separation of the detectors d and the wavelength λ, which are known quantities, and the angular separation of the sources θ. Varying the separation of the detectors would lead to a sinusoidal pattern in the two-point correlation which depends on the angular separation of the sources.

Of course, many astronomical objects cannot be described by just two pointlike emitters, but by an angular distribution $\rho(\Omega)$ of emitters. The correlation function the becomes

$$G^{(2)}(d) \sim \int d\Omega\, \rho(\Omega) \cos\left(2\pi \frac{\Omega d}{\lambda}\right), \tag{2.32}$$

which corresponds to the Fourier transform of the original distribution. This method can been used to accurately measure the diameter of stars and other astronomical objects.

2.2.3.2 *HBT in Particle Physics*

A conceptually similar detection method has been applied in the description of high-energy collisions of particles such as protons or heavy ions. Here, it can also be assumed that the collision products have been created independently. Again, one can correlate the detection position of identical particles with eq. (2.30). However, in contrast to the astronomical application, the separation of the detectors is now much larger than the typical system size, $d \gg R$. Instead of inferring the angular size of the source from the separation of the detectors, one measures the momentum difference $\mathbf{k}_a - \mathbf{k}_b$ (see Figure 2.4) to extract the source density distribution $S_{\mathbf{K}}(\mathbf{R})$ over the relative distance $\mathbf{R}$:

$$g^{(2)}(\mathbf{k}_a - \mathbf{k}_b) \sim \int d^3R \, S_{\mathbf{K}}(\mathbf{R}) \cos(\mathbf{R} \cdot (\mathbf{k}_a - \mathbf{k}_b)), \tag{2.33}$$

Because the source distribution is the result of complex processes that take place earlier in the collision, the pair momentum $\mathbf{K}$ must *a prior* also be taken into account as a parameter.

Furthermore, we have to consider that the particles that are being detected are typically hadrons, and not photons. They can interact among each other or with the source via Coulomb interactions or strong interactions, called final-state interactions. This means that the plane waves of the free-particle description are not the correct basis of the final state. Instead, the particles expand with waves which are distorted by interactions. We will also apply a similar concept for the description of interacting ultracold atoms in our experiments.

2.3 ENTANGLEMENT

While correlations provide a way of describing quantum many-body systems, they are by no means a purely quantum phenomenon. Classical systems can also show strong correlations. However, for quantum systems, there exist states exhibiting correlations which cannot occur for classical systems, as was first shown by Bell [Bel64]. The detection of these correlations in experiments confirms that quantum mechanics is required in some form to describe reality. The states which provide the largest amount correlation on top of classically explainable correlations, i.e., which maximally violate Bell's inequality (or the more general CHSH inequality [Cla+69]), are entangled states called Bell states.

2.3.1 *Definition and Properties of Entanglement*

As it turns out that entangled states are also essential for understanding the correlations that we observe in our experiments, it makes sense to have a closer look at the concept of entanglement and the ways of measuring it. While Bell states are a practical example of entangled states and their contribution to correlations, they are not suitable as a definition of entanglement. Entanglement is a general concept in quantum mechanics and extends for example to systems with more than two identical or non-identical particles (many-body entanglement), more than two observers (multipartite entanglement), mixed states, etc. Defining entanglement in a general manner can be very delicate and is presently still being debated (see, e.g., [WV03]). I will treat entanglement in a manner which is practical for the systems we realize in our experiment, for a more differentiated treatment I refer to reviews such as [AOV08; GT09].

One common concept of defining a non-entangled (separable) state is the possibility of finding subsystems $A, B, C, \ldots$ which can be fully characterized independently. For pure states in a bipartite system, this means that a state $|\psi\rangle$ from a Hilbert space $\mathcal{H}$ is called separable if it can be written as a product of states from the Hilbert spaces of the subsystems, $|\psi_A\rangle \in \mathcal{H}_A, |\psi_B\rangle \in \mathcal{H}_B$,

$$|\psi\rangle = |\psi_A\rangle \otimes |\psi_B\rangle \,. \tag{2.34}$$

If that is not possible, the state is called entangled.

As an example, let us look at a system of two spins on two sites. If we split our system such that A measures the spin on one site and B on the other, then the state

$$|\uparrow\uparrow\rangle + |\uparrow\downarrow\rangle = |\uparrow\rangle_A \otimes (|\uparrow\rangle + |\downarrow\rangle)_B$$

is a separable state, while the state

$$|\downarrow\uparrow\rangle + |\uparrow\downarrow\rangle$$

is entangled.

To define entanglement for mixed states, we have to adapt the previous definition. A product state in this case can be written as $\rho = \rho_A \otimes \rho_B$. These states are separable, however, the complete set of separable states is defined as [GT09]

$$\rho = \sum_i p_i \, \rho_{i,A} \otimes \rho_{i,B}, \tag{2.35}$$

where p_i are convex weights of the product states $\rho_{i,A} \otimes \rho_{i,B}$. The first case of separable states describes an uncorrelated state, while the second case of separable states describes classically correlated states.

An example for an uncorrelated mixed state would be $\rho = \rho_A \otimes \rho_B$ with

$$\rho_A = (|\uparrow\rangle\langle\uparrow|)_A = \begin{pmatrix} 1 & 0 \\ 0 & 0 \end{pmatrix}_A$$

$$\rho_B = \frac{1}{2}(|\uparrow\rangle\langle\uparrow| + |\downarrow\rangle\langle\downarrow|)_B = \begin{pmatrix} 1/2 & 0 \\ 0 & 1/2 \end{pmatrix}_B .$$

Here, the measurement outcome in subsystem A is independent of the measurement outcome in subsystem B. A classically correlated state would, for example, be $\rho = \frac{1}{2}\rho_{1,A} \otimes \rho_{1,B} + \frac{1}{2}\rho_{2,A} \otimes \rho_{2,B}$, with

$$\rho_{1,A} \otimes \rho_{1,B} = \begin{pmatrix} 1 & 0 \\ 0 & 0 \end{pmatrix}_A \otimes \begin{pmatrix} 0 & 0 \\ 0 & 1 \end{pmatrix}_B$$

$$\rho_{2,A} \otimes \rho_{2,B} = \begin{pmatrix} 0 & 0 \\ 0 & 1 \end{pmatrix}_A \otimes \begin{pmatrix} 1 & 0 \\ 0 & 0 \end{pmatrix}_B ,$$

where the outcomes are always anti-aligned. A state with a density matrix

$$\rho = \frac{1}{2}\begin{pmatrix} 0 & 0 & 0 & 0 \\ 0 & 1 & -1 & 0 \\ 0 & -1 & 1 & 0 \\ 0 & 0 & 0 & 0 \end{pmatrix} ,$$

using the basis $|\uparrow\uparrow\rangle, |\uparrow\downarrow\rangle, |\downarrow\uparrow\rangle, |\downarrow\downarrow\rangle$, is an example of an entangled state in the density matrix notation [Ved03].

2.3.2 *Entanglement Witnesses and Entanglement Entropy*

Determining whether or not a state is entangled by analyzing its density matrix can be a hard problem [Gur04; Gha10]. Therefore, it makes sense to look for entanglement witnesses. These are observables which, if evaluated with a separable state, are bounded. If a measurement violates this bound, then the observed state was entangled (Figure 2.5). The exact expression for the witness depends on the system which is being studied. The witnesses specific to our experiments with a double well will be presented in Chapter 7.

While entanglement witnesses can be very convenient, some of the entangled states may not be detected by the witness if they do not

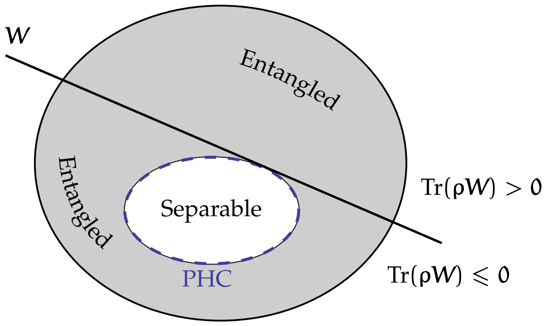

Figure 2.5: Visualization of an entanglement witness W which separates the Hilbert space in a part containing only entangled states and a part containing also separable states. The Peres-Horodecki criterion (dashed, blue curve) exactly separates entangled from separable states for appropriate systems.

violate the bound. For small systems, one can instead look at the partial transpose of the density matrix,

$$\rho = \sum_{ijkl} p_{ij,kl} \left|i\right\rangle \left\langle j\right| \otimes \left|k\right\rangle \left\langle l\right| \tag{2.36}$$

$$\Rightarrow \quad \rho^{T_A} = \sum_{ijkl} p_{ij,kl} \left(\left|i\right\rangle \left\langle j\right|\right)^{T} \otimes \left|k\right\rangle \left\langle l\right| = \sum_{ijkl} p_{ji,kl} \left|i\right\rangle \left\langle j\right| \otimes \left|k\right\rangle \left\langle l\right|, \tag{2.37}$$

where the system has been divided into two parts A and B. The Peres-Horodecki criterion (PHC) [Per96; HHH96] tells us that, for a separable state, the eigenvalues of the density matrix after a partial transpose are positive-semidefinite ($\rho^{T_A} \geqslant 0$). For systems with dimensions 2×2 or 2×3, this is a necessary and sufficient condition for separability, meaning that it will exactly distinguish between entangled and separable states.

Another quantity which is often used in larger systems (for example in [Isl⁺15]) to identify entanglement is the entanglement entropy. As we had noted earlier, the separability of states is related to the ability to fully describe subsystems individually. It turns out that, for a pure, entangled state, its subsystems will be mixed states when treated independently. A peculiar consequence is that the subsystems can actually have more entropy than the combined system [HH96], a behavior that would not occur for classical systems. While we may not have to rely on entanglement entropy for our small experimental systems, where we may use the use the PHC or other entanglement witnesses instead, its usage for large systems makes it an interesting quantity nevertheless.

One way to quantify the entanglement entropy is by determining the purity of a (sub)system. While for any closed system $\mathrm{Tr}\,\rho = 1$ by definition, only pure states will have $\mathrm{Tr}\,\rho^2 = 1$. Hence, we can use

$V \equiv \operatorname{Tr}\rho^2$ as a measure for the purity. It can be used to define the linear entropy

$$S_{\text{lin}}(\rho_A) \equiv 1 - \operatorname{Tr}\rho_A^2, \tag{2.38}$$

as, for example, in [Zan02]. Here, ρ_A stands for the state that remains if subsystem B is traced out of the combined state ψ, also called a partial trace:

$$\rho_A = \sum_i {}_B\langle i|\,\hat{\rho}\,|i\rangle_B\,. \tag{2.39}$$

If the linear entropy of the subsystem is larger than zero, it was entangled to the other subsystem and the combined state is said to be entangled[7]. The purity can also be measured with the Rényi entropy $S_n(\rho_A) = \frac{1}{1-n}\log_2 \operatorname{Tr}\rho_A^n$ in second order ($n = 2$):

$$S_{\text{Ren2}}(\rho_A) = -\log_2 \operatorname{Tr}\rho_A^2. \tag{2.40}$$

The linear entropy and the second-order Rényi entropy can be seen as a lower bound of a more familiar definition of entropy, the von Neumann entropy $S_{\text{vN}}(\rho) = -\operatorname{Tr}(\rho\log_2\rho)$. With it, we can define the *entanglement of formation* [Woo98]

$$E_F(\psi) = S_{\text{vN}}(\rho_A) = S_{\text{vN}}(\rho_B) \tag{2.41a}$$

$$E_F(\rho) = \min\sum_i p_i E_F(\psi_i). \tag{2.41b}$$

In the first line, the entropy of subsystem ρ_A quantifies the entanglement of the combined state ψ. The second line contains the definition for mixed states, where the density matrix is written in a pure-state decomposition $\rho = \sum_i p_i |\psi_i\rangle\langle\psi_i|$. The minimum refers to choice of the basis for the decomposition which provides the least average entanglement.

Yet another definition of entanglement is the *entanglement of particles* [WV03; DDW06]. It is motivated by the fact that the observers know how many particle they measure, i.e., the particle number is conserved for each partition. Therefore entanglement between modes of with different particle numbers n_A, n_B may not contribute to the entanglement of particles. It can be calculated by first evaluating the mode entanglement E_M for fixed particle numbers separately, and then summing over the results, weighted by the probability of finding a state with such particle number P_{n_A,n_B}:

$$E_P(\rho) = \sum_{n_A,n_B} P_{n_A,n_B} E_M(\rho_{n_A,n_B}) \tag{2.42}$$

---

[7] The entanglement measured in this way is the *mode entanglement*.

A measure for the mode entanglement can for example be the entanglement of formation E_F.

The difference between entanglement of particles and mode entanglement can be easily understood by looking at a system containing only one particle: It may contain entanglement between two or more of the modes, but there typically is no simple way to distinguish it from a mixed state, because the particle can be measured only in one mode at a time [DDW06]. Thus, the entanglement of particles would be zero.

2.4 HUBBARD MODEL

The previous sections showed the role of correlations and entanglement for quantum systems in a very general manner. It was shown that the many-body wavefunction of identical particles could be expressed in the Fock basis by the occupation numbers of its single-particle modes. Also, operators could be written in such a way that they acted on this Hilbert space, forgoing the need to calculate integrals explicitly to obtain expectation values of observables.

A particular application of this formalism in the context of condensed matter physics and ultracold atoms is the Hubbard model. It was conceived originally to describe interacting electrons on a crystal lattice [Hub63], however it can also be applied to ultracold atomic gases [Jak+98; JZ05; Ess10], where neutral atoms are confined in optical lattice potentials. The Hubbard model is seen as a promising model to describe many-body problems, because it provides a simplified description, but is still complex enough to give rise to a multitude of interesting phases and behaviors. In this section, I will show the approximations which enter in the most basic version of the Hubbard model and highlight a few of its properties.

2.4.1 *Hubbard Model Hamiltonian*

The single-particle modes of the Hubbard model are Wannier states $w_i(\mathbf{x}) = w(\mathbf{x} - \mathbf{x}_i)$ which describe particles localized on the sites $\mathbf{x}_i$ of a spatial array, for example, a lattice. In the single-band approximation, a Wannier state describes only one of the motional states of its site, typically the ground state. For example, if the potential is harmonic on each site, the Wannier function would be the lowest eigenstate, a Gaussian.

This tight-binding approximation is used to introduce several simplifications to the general many-body Hamiltonian. The kinetic term of the Hubbard Hamiltonian only contains the movement of the particle to neighboring sites (also called hopping or tunneling), and two-body interactions are assumed to be short-range and apply only if multiple particles occupy the same site. Expressed with operators which act on the Fock basis, it reads [Sca16]

$$H = -J \sum_{\sigma,\langle i,j\rangle} \hat{a}^{\dagger}_{i\sigma}\hat{a}_{j\sigma} + U \sum_{j} \hat{n}_{j\downarrow}\hat{n}_{j\uparrow} - \mu \sum_{j} \left(\hat{n}_{j\downarrow} + \hat{n}_{j\uparrow}\right) \tag{2.43}$$

for fermionic atoms with two spin components, where the first sum runs over all neighboring sites $\langle i, j\rangle$. For identical bosonic atoms, the Hamiltonian is slightly different, mainly due to the fact that multiple bosons can occupy the same mode,

$$H_B = -J \sum_{\langle i,j\rangle} \left(\hat{a}^{\dagger}_{i}\hat{a}_{j}\right) + \frac{U}{2} \sum_{j} \hat{n}_{j}\left(\hat{n}_{j} - 1\right) - \mu \sum_{j} \hat{n}_{j}. \tag{2.44}$$

In both cases, the kinetic and interaction terms are characterized by a single parameter each, which furthermore is the same for all lattice sites. For the further discussion, it is sufficient to treat these parameters as values, however, they can also be explicitly calculated:

$$J \equiv J_{ij} = \int d\mathbf{r}\, w_i^*(\mathbf{r})\, \hat{h}\, w_j(\mathbf{r}) \tag{2.45a}$$

$$U \equiv U_{ii} = \int\int d\mathbf{r}_1\, d\mathbf{r}_2\, w_i^*(\mathbf{r}_1) w_i^*(\mathbf{r}_2)\, V_{\text{int}}(\mathbf{r}_1, \mathbf{r}_2)\, w_i(\mathbf{r}_2) w_i(\mathbf{r}_1) \tag{2.45b}$$

The tunnel coupling energy J depends on the wavefunction overlap on neighboring sites i, j and is a single-particle effect (with the single-particle Hamiltonian $\hat{h}$). The interaction energy U is a two-particle effect and depends on the square of the on-site density and the interaction potential V_{int}. The chemical potential term μ corresponds to the energy needed to add a particle to the system. If it depends on the lattice site, it can be used to include external potentials in the Hubbard model.

We can now characterize the energy spectrum and the eigenstates of the Hubbard model, i.e., diagonalize the Hamiltonian. We see that we have two competing terms, the kinetic term, which is off-diagonal in our choice of basis, and the interaction term, which gives contributions along the diagonal. For different tunneling strengths and interaction strengths, the eigenvalue problem will give different results. Additional factors to take into account are the system size (number of sites) and the filling factor (average number of particles per site). Solutions can be found analytically for finite systems by exact diagonalization [Lin+93; Rav+17], however, the increasing size of the Hilbert space makes this approach impractical for large systems. For large systems away from half filling[8] and for different extensions of the Hubbard model, other techniques such as quantum Monte Carlo or

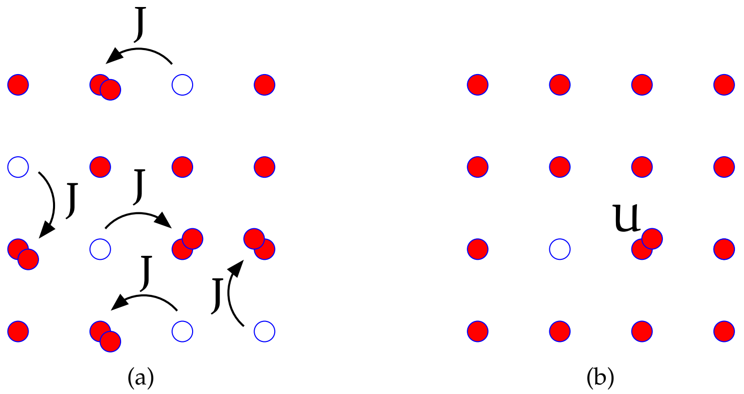

Figure 2.6: (a) Non-interacting state, where hopping and double occupancy are allowed. (b) Strongly repulsive state, where double occupancy is suppressed by the interaction energy U. Adapted from [Sca16]

dynamical mean-field theory have to be used. Due to the complexity of these systems, they are still a subject of ongoing research [LNW06; Dut+15].

2.4.2 *Limiting States of the Fermi-Hubbard Model*

To gain an intuition of the eigenstates of the Hubbard model, it makes sense to look at its limits, namely, strong repulsive interactions $U \gg J$, strong tunneling $J \gg |U|$, and strong attractive interactions $|U| \gg J$, $U < 0$ (Figure 2.6). In this section, we will restrict ourselves to the results for fermionic particles.

In the first case with $U \gg J$ and $J = 0$, we see that the Fock states on each separate lattice site i, $|0\rangle_i$, $|\uparrow\rangle_i = \hat{a}^\dagger_{i,\uparrow}|0\rangle$, $|\downarrow\rangle = \hat{a}^\dagger_{i,\downarrow}|0\rangle$, and $|\uparrow\downarrow\rangle = \hat{a}^\dagger_{i,\uparrow}\hat{a}^\dagger_{i,\downarrow}|0\rangle$, are eigenstates of the Hamiltonian with the eigenenergies 0, $-\mu$, $-\mu$, and $-2\mu + U$. The many-body eigenstates are simply product states over all M sites, $\Psi = \prod_{i=1}^{M} |n_i\rangle = |n_1, \ldots, n_M\rangle$. For chemical potentials $0 < \mu < U$, our system will be half-filled with $N = N_\uparrow + N_\downarrow = M$ particles, and the energy of the system will be $-\mu M$.

At zero temperature and zero tunneling, interactions prevent particles from hopping to already occupied sites. In the ground state, there will be exactly one particle per site, while excitations are gapped by the interaction energy U. This means that the particle number fluctuations on each site are suppressed. This is also clearly visible in the local moment [Sca16],

$$\langle \hat{m}_i \rangle = \left\langle (\hat{n}_{i,\uparrow} - \hat{n}_{i,\downarrow})^2 \right\rangle = \left\langle \hat{n}_{i,\uparrow} + \hat{n}_{i,\downarrow} \right\rangle - 2 \left\langle \hat{n}_{i,\uparrow}\hat{n}_{i,\downarrow} \right\rangle, \tag{2.46}$$

---

[8] $N_\uparrow = N_\downarrow = M/2$, where M is the number of sites.

which is exactly 1 in the extreme case of $J = 0$. The first term counts the particle on site i, while the second term subtracts the doubly occupied sites $D_i = \langle \hat{n}_{i,\uparrow}\hat{n}_{i,\downarrow} \rangle$. Any admixture of non-occupied or doubly-occupied sites, for example from tunneling or finite temperatures, will reduce the local moment below 1, while still maintaining overall half-filling.

In the non-interacting case $U = 0$, the Hamiltonian is not diagonal anymore in the $a_{i,\sigma}$ basis. Instead, one can transform the creation and annihilation operators to the momentum basis,

$$a^\dagger_{\mathbf{k},\sigma} = \frac{1}{\sqrt{M}} \sum_j e^{i\mathbf{k}\cdot\mathbf{r}_j}\, a^\dagger_{j,\sigma}. \tag{2.47}$$

Using these operators, the Hamiltonian becomes

$$H = \sum_{\mathbf{k},\sigma} (\epsilon_{\mathbf{k}} - \mu)\, a^\dagger_{\mathbf{k},\sigma} a_{\mathbf{k},\sigma}. \tag{2.48}$$

$\epsilon_{\mathbf{k}}$ stands for the dispersion relation. For a one-dimensional lattice, $\epsilon_k = -2J\cos kd$ with lattice spacing d. For $\mu = 0$, the lattice will be half-filled and each spin state will occupy half of its band[9]. The energy will be lower than compared to the strongly repulsive case by $-2JM$. Because half of the band is empty for either spin state, this state has no excitation gap and resembles a metallic state.

Still at half-filling, the average occupation in the position basis of a site i will still be $\langle n_{i,\uparrow} + n_{i,\downarrow} \rangle = 1$. However, the local moment will be only $\langle m \rangle = 1/2$ due to empty and doubly occupied sites. This is possible because the individual particles are mobile and uncorrelated to the other particles, meaning that, for each site, the four states of its individual Fock space will be occupied with equal probability.

For strong attractive interactions $U \ll 0$, the system can be treated in the same way as in the strongly repulsive case[10]. While, for $0 < \mu < |U|/2$, the average particle number per site will be 1, the particles will favor double occupancy. The resulting state will have $\langle m \rangle = 0$ and resemble a charge-density wave.

If the system is not in one of these three extreme cases, there is no obvious basis choice anymore to diagonalize the Hamiltonian and it is more difficult to find its ground state. Both the tunneling term and interaction term of the Hamiltonian are now relevant and a new energy scale $\propto -J^2/U$ enters the problem, the superexchange energy. It is caused by a second-order process which can be derived from perturbation theory. This process describes the exchange of two spins ($\propto J^2$) via an intermediate, forbidden doubly occupied state ($\propto U$, see Figure 2.7). The superexchange term can be understood as an

---

[9] The particles cannot all occupy the lowest momenta due to the exclusion principle.

[10] This can be shown rigorously by performing a particle-hole transformation.

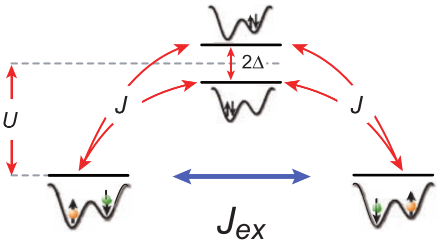

Figure 2.7: Schematic depiction of the superexchange process which swaps two distinguishable spins via an intermediate excited state. This process lowers the energy of the system by $4J^2/U$. Superexchange is suppressed for identical spins which cannot occupy the same lattice site. From [Tro+08].

effective spin-spin coupling and the repulsive Hubbard model can be mapped to the Heisenberg model which describes spins on a lattice. This mechanism can lead to magnetically ordered phases such as the antiferromagnetic state [LM62; Lie89] and other interesting phases, for example, resonating valence bonds [And87].

2.4.3 *Correlations in the Hubbard Model*

There are plenty of approaches to characterize the phases of systems which are described by the Hubbard model. Depending on the experimental realization, one can measure the compressibility, double-occupancy, singlet fraction, etc. In this section, I will describe an experiment with ultracold bosonic atoms where two-point correlations in the density $\langle n(x_1)n(x_2)\rangle$ were studied after a time-of-flight expansion [Föl+05; Föl08; Rom+06; Rom09] (for a review of several similar experiments, see [Föl14]). This type of measurement can be related directly to the HBT correlation measurements introduced earlier in this chapter and can also be applied to some of our experiments. Therefore, I will briefly explain the concepts of the experiment by Fölling *et al.* in this section, and show more detailed derivations specific to our experiment in Chapter 7.

In Fölling's experiment, bosonic ^{87}Rb atoms are cooled to quantum degeneracy and then transferred into an optical lattice, where they can be described by the Bose-Hubbard model. For weak interactions, the gas is in superfluid state [Gre+02], while for strong interactions, it forms a Mott insulator. The density of the system is measured after releasing the atoms, essentially projecting each atom on a set of free plane waves originating from its initial lattice site and letting these free waves propagate.

After a long time-of-flight (TOF) expansion, this corresponds to a measurement of the momentum density $n(x) \approx n\left(\frac{\hbar k}{m}t\right) \propto n(k)$. The density is probed by absorption imaging, where a laser beam passes through the atom cloud and its shadow is recorded with a camera

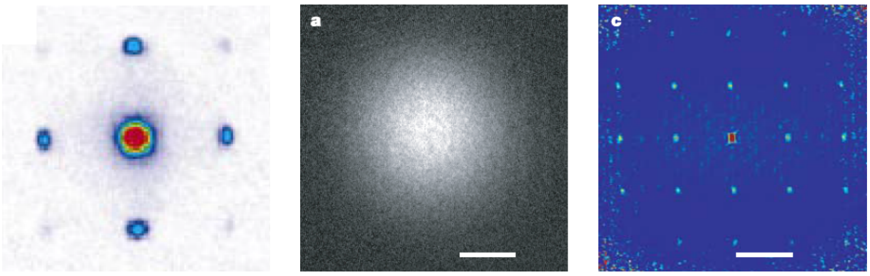

(a) (b) (c)

Figure 2.8: (a) Density distribution of the superfluid phase of the Bose-Hubbard model after time-of-flight expansion. From [Gre+02]. (b) Density distribution of the Mott-insulating phase. (c) Two-point density correlations of the Mott-insulating phase. Panels (b) and (c) are from [Föl+05].

from different direction. From these projections, the actual density distribution of the atoms can be inferred, and this imaging method is equivalent to the array of detectors in Section 2.2.3.

Let us first look at the case where there are no interactions. Before the release, each atom will be delocalized over the entire lattice and will have an equal occupation probability on any site. Because the atoms do not interact with each other, the density distribution of the many-particle system can be seen as a sum of the density distribution of the individual particles. Using eq. (2.20) to evaluate the density (one-point correlation function), we see that the phases of the different sites add up coherently for each single atom. Consequently, the measured density distribution resembles the pattern of a diffraction grating (Figure 2.8a).

The density distribution looks drastically different in the case of strong repulsive interactions[11]. It is described by a Gaussian distribution, seemingly the sum of many independent atoms localized on their individual sites prior to release. Looking at the two-point correlation function, i.e., the fluctuations on this density profile, reveals that the atoms are in fact not independent from each other. The Mott-insulating state $|1, 1, \ldots, 1\rangle$ resembles the states which we discussed in the context of the HBT effect (Section 2.2.3). Therefore, the two-point correlation function shows an oscillatory behavior similar to (2.30). Because in these experiments particles from M periodic lattice sites can interfere, the peaks will be sharper and the correlation function will be $C(d) \propto \sin(\pi M d)^2 / \sin(\pi d)^2$ [Föl08].

---

[11] For now, we will ignore the interactions during the expansion after the lattice has been turned off.

3

ATOMIC PHYSICS

In the previous chapter, we have seen how correlations can be used to probe the properties of a many-body system. They can reveal the inherent (anti)symmetry of many-body states consisting of indistinguishable particles (e.g., via the HBT bump/dip). They can also show the properties of generic quantum many-body states, for example, in systems with interactions between the particles. If we want to study these states systematically, we must be able to create and control them in a deterministic way. This is where systems of ultracold atomic gases excel, with their long coherence times, their high level of control over the spatial and motional degrees of freedom of individual particles and the tunable interaction between particles. Additionally, ultracold gases provide a range of different observables to detect the prepared quantum states (see [BZ08] for a review). Even though the goal of ultracold-atom experiments is to study abstract quantum systems, it is important to understand their actual implementation. Therefore, we will review two concepts of atomic physics and scattering theory which are relevant for our experiments.

First, we will look at the mechanism used to control the external degrees of freedom of individual atoms. A neutral atom can interact with its environment via electromagnetic fields of various characters, for example with light fields, static magnetic fields, radio frequency (RF) fields, etc. [CT03; CTD05] We will focus on off-resonant atom-light interactions, which can give rise to conservative potentials called optical dipole traps (ODTs). These potentials confine our atoms and create the spatial modes of our quantum systems.

Next, we will see how multiple atoms interact among each other. This has to be described in principle by a many-body Hamiltonian $\hat{H}_{\mathrm{IA}}(\mathbf{r}_1, \ldots, \mathbf{r}_N)$, which depends on the states of all N particles. However, in our experiment, the interactions can be effectively described by two-body s-wave scattering and Feshbach resonances, which arise from an interplay of the Van der Waals (VDW) interactions and an external magnetic field.

With both optical confinement and two-body scattering, we will be able to describe our experiments in Chapters 6 and 7, which explore the dynamics of interacting particles in harmonic potentials.

3.1 DIPOLE TRAPPING OF NEUTRAL ATOMS

Dipole trapping of neutral atoms relies on dipole interactions between the oscillating electric field of light and the induced electric dipole moment of the atom. If the oscillation frequency of the electric field resonantly matches a transition frequency between two atomic eigenstates (and all relevant selection rules), the atom can absorb a photon from the light field or scatter a photon into the light field. Because there always is a random contribution to this process (spontaneous emissions), it does not result in a conservative potential and is therefore not suited for making quantum systems with long coherence times[1].

If the light is instead far off-resonant, it will neither drive transitions between internal states of the atom nor will photons be taken out of the light field. Therefore, one can treat its effect as a perturbation on the states of the bare atom. Applying perturbation theory, the energy shift for a generic state $|j\rangle$ becomes

$$\Delta E_j = \sum_{k \neq j} \frac{\left|\langle j| \hat{h}_{AL} |k\rangle\right|^2}{E_k - E_j}. \tag{3.1}$$

We can arrive at an expression for the atom-light Hamiltonian $\hat{h}_{AL}$ by comparing to classical theory. Classically, the energy of a dipole in an electric field is $E_{dip} = -\mathbf{p} \cdot \mathbf{E}$, which becomes $E_{dip} = -\frac{1}{2}\left\langle \alpha E^2 \right\rangle$ for a dipole which has been induced by oscillating field itself, introducing the polarizability α. The goal of the perturbative calculation is to obtain the value of α for the atom, using the operator

$$\hat{h}_{AL} = -e\,\hat{\mathbf{r}} \cdot \mathbf{E}. \tag{3.2}$$

The states $|j\rangle$ in eq. (3.1) contain the eigenstates of the bare atom $|J, m_J\rangle$ (with electronic angular momentum J and the corresponding magnetic quantum number m_J) as well as the state of the light field.

To gain an intuition, it makes sense to look at a two-level atom with states $|g\rangle$ and $|e\rangle$. The sums in eq. (3.1) will now contain only one term, namely $\left|\langle e, \mathcal{L}'| \hat{h}_{AL} |g, \mathcal{L}\rangle\right|^2$, where $\mathcal{L}$, $\mathcal{L}'$ stand for the states of the light field $E(t) \propto |E|\, e^{i\omega t}$ which couples both atomic states. We can take its contribution into account by evaluating in the dressed-state picture. The energy with the dressing light field will be $E_{g,0} = n\hbar\omega$ for the ground state and $E_{e,0} = \hbar\omega_0 + (n-1)\,\hbar\omega$ for the excited state, where $\hbar\omega_0$ is the energy difference for the bare atomic states. In the second expression, one energy quantum of the light field has been absorbed and the atom has been excited. The problem can now be treated as a textbook coupled two-level system with an energy shift (see Figure 3.1, [GWO00]):

$$\Delta E_{e,g} = \pm \frac{|\langle e| \hat{p} |g\rangle|^2}{\Delta} |E|^2 = \pm \frac{3\pi c^2}{2\omega_0^3} \frac{\Gamma}{\Delta} |E|^2, \tag{3.3}$$

---

[1] However, light scattering is essential for preparing and detecting these systems, as will be described in Chapters 4 and 5.

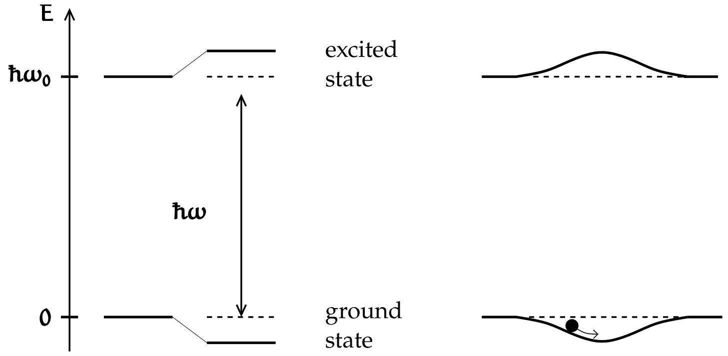

Figure 3.1: Energy diagram of a two-level atom with a light shift. The left panel shows how coupling decreases the ground state energy and increases the excited state energy. The right panel shows how this can lead to a confining potential if the energy shift is spatially dependent. From [GWO00].

where $\hbar\Delta = E_{g,0} - E_{e,0} = \hbar(\omega - \omega_0)$ is the detuning of the light field with respect to the bare transition. In the second step, the coupling matrix element was replaced by the spontaneous decay rate $\Gamma = \frac{\omega_0^3}{3\pi\epsilon_0\hbar c^3} |\langle e|\,\hat{p}\,|g\rangle|^2$. We can see that the coupling decreases the energy of the ground state while it increases the energy of the excited state.

Often, real atoms cannot be described by two-level systems and all allowed transitions between electronic states $|J, m_J\rangle$ and $|K, m_K\rangle$ in eq. (3.1) have to be taken into account for the calculation of the polarizability. For excited states, the negative energy shifts from the coupling to other excited states will compete with the positive energy shift from the coupling to the ground state, and a qualitative prediction of the polarizability like in the two-level case is difficult. The calculation of the polarizabilities is quite lengthy [För15; KLH68; Joh09] and involves transition rules and Clebsch-Gordan coefficients. It results in

$$\alpha = e^2 \left(\alpha_J^{(0)} + \frac{3m_J^2 - J(J+1)}{J(2J-1)} \alpha_J^{(2)} \right), \tag{3.4}$$

which contains the scalar polarizability $\alpha_J^{(0)}$ and the tensor polarizability $\alpha_J^{(2)}$. These quantities can be calculated from the overlap integrals of the dipole operator and the energy eigenvalues of the bare atom. For ^{6}Li, the polarizabilities are shown in Figure 4.3. In general, every state with different quantum numbers J, m_J has a different value for the polarizability for every wavelength[2].

If we are far enough away from the resonance, we can effectively treat the energy shift induced by off-resonant light as an external,

---

[2] Exceptions are the points where two polarizability curves cross, called magic wavelengths. There, atoms in different states may experience the same optical potential.

conservative potential for the bare atoms. It depends on the intensity profile of the laser $I = \frac{1}{2}c\epsilon_0 |E|^2$, which we can use to express the optical dipole potential:

$$V_{\text{dip}}(\mathbf{r}) = -\frac{1}{2\epsilon_0 c}\,\Re(\alpha)\, I(\mathbf{r}). \tag{3.5}$$

We can therefore create attractive potentials using far-red detuned light fields, which yield a positive polarizability. If we choose an appropriate spatial mode of the light field, e.g., a Gaussian beam, we can confine neutral atoms in these potentials.

3.2 SCATTERING THEORY AND FESHBACH RESONANCES

While we treated the interactions of atoms with the external light field in the single-particle picture[3], the description of interactions between atoms in general requires the total wavefunction of multiple particles. For systems with long-range interactions, such as the Coulomb interaction for charged particles, it can be difficult to reduce the description of the interactions to a few-particle problem[4].

In our experiment, the collisions between the neutral atoms are governed by Van der Waals interactions which have a short effective range r_{sc} on the order of the Van der Waals length [Fri13]

$$\beta_6 = (2\mu C_6/\hbar^2)^{1/4}, \tag{3.6}$$

where μ is the reduced mass and C_6 the Van der Waals C_6 coefficient. In a dilute gas, it is therefore a good assumption that collisions between more than two particles are rare, which allows for a simpler, two-particle description of the interactions. However, this argument breaks down for degenerate quantum gases, where the number density per phase space cell can exceed one. This becomes apparent especially for strongly interacting Bose gases, where inelastic three-body collisions lead to significant losses when the atoms are strongly interacting [Ino+98]. In the case of Fermi gases, however, Pauli blocking between the identical fermions suppresses the probability of finding more than two particles close to each other [Tan04; Zwe16] and the interactions can again be described by elastic two-body collisions.

3.2.1 *Scattering at Low Energies*

First, let us look at how short-range scattering can be described generically, without specifying the scattering potential. If we treat only

---

[3] Collective effects like superradiance are not covered by this description.

[4] Phenomena such as shielding may lead to effective short-range interactions even in these cases.

two-body collisions, we may transform to relative coordinate frame $\mathbf{r} = \mathbf{r}_1 - \mathbf{r}_2$ and $\mathbf{R} = (\mathbf{r}_1 + \mathbf{r}_2)/2$ instead of using the coordinates of the individual particles $\mathbf{r}_i$. As the interactions depend only on the relative coordinate $\mathbf{r}$, we can then separate the problem into a center-of-mass (COM) part without interactions and a relative (REL) part containing the scattering potential $V_{sc}(\mathbf{r})$. Henceforth, we will only treat the relative part, which effectively presents a one-body problem:

$$\left(-\frac{\hbar^2}{2\mu}\nabla^2 + V_{sc}(\mathbf{r})\right)\psi_{\mathbf{k}}(\mathbf{r}) = E_k \psi_{\mathbf{k}}(\mathbf{r}) \tag{3.7}$$

Detailed discussions of this scattering problem can be found, for example, in [LL77; Dal99; Fri13].

Next, we restrict ourselves to scattering potentials which have a finite range r_{sc}, for example, as in equation (3.6). As we are observing the scattering process from a large distance, we are interested in the stationary solution of eq. (3.7) far outside this range. For a given wavevector $\mathbf{k}$, a general solution can be expressed as the sum of the incident plane wave and the scattered wavefunction

$$\psi_{\mathbf{k}}(\mathbf{r}) \sim e^{i\mathbf{k}\cdot\mathbf{r}} + f(\mathbf{k}, \mathbf{r})\,\frac{e^{ikr}}{r}, \tag{3.8}$$

where the scattering amplitude $f(\mathbf{k}, \mathbf{r})$ contains the magnitude of the scattered part and the phase shift relative to the incident wave[5]. The scattering amplitude is related to the scattering cross section as

$$\frac{d\sigma}{d\Omega} = |f|^2. \tag{3.9}$$

We are now interested in low-energy scattering ($r_{sc} \ll 1/k$) with an isotropic, central scattering potential $V_{sc}(r)$, which are valid approximations for the scattering process of two ultracold atoms. Under these conditions, the scattered wavefunction will be isotropic and only depend on the depth of the potential, the wavenumber k and the angle between incoming and scattered wave θ:

$$\psi_{\mathbf{k}}(\mathbf{r}) \sim e^{i\mathbf{k}\cdot\mathbf{r}} + f(k, \theta)\,\frac{e^{ikr}}{r} \tag{3.10}$$

To calculate the value of the scattering amplitude, we first look at the series expansion of a general wavefunction in spherical harmonics, which is a sum of radial and angular wavefunctions that depend

---

[5] Note that the scattered part in the far field is described by a spherical wave; its wavenumber is the same as the incident wavenumber, as we are looking at elastic collisions.

on the main quantum number k and the angular momentum quantum numbers l and m:

$$\psi_k(\mathbf{r}) = \sum_{l=0}^{\infty} A_l P_l(\cos\theta) \frac{u_{kl}(r)}{r} \tag{3.11}$$

Here, we already used the fact that our wavefunctions must be azimuthally symmetric (independent of ϕ, i.e., $m = 0$), which reduces the angular part of the wavefunction to Legendre polynomials P_l. The radial wavefunction is given by u_{kl}, and A_l are the expansion coefficients to be determined.

We can now use this wavefunction to evaluate eq. (3.7). If we write our operators in spherical coordinates, we obtain a set of independent radial equations, one for each value of l:

$$\left(-\frac{\hbar^2}{2\mu}\frac{d^2}{dr^2} + \frac{l\,(l+1)\,\hbar^2}{2\mu r^2} + V_{sc}(r)\right) u_{kl}(r) = E_k\, u_{kl}(r) \tag{3.12}$$

From [LL77; Fri13] we know that the asymptotic radial solutions are[6]

$$\begin{aligned} u_{kl} &\approx 2\sin(kr - l\pi/2 + \delta_l) \\ &= \frac{1}{i}\left(-i^l e^{-i(kr+\delta_l)} + (-i)^l e^{i(kr+\delta_l)}\right), \end{aligned} \tag{3.13}$$

with the scattering phase shifts δ_l.

Inserting (3.13) back into (3.11), the full wavefunction can now be written as

$$\psi_k = \frac{1}{ir}\sum_{l=0}^{\infty} A_l P_l(\cos\theta) e^{-i\delta_l}\left(-i^l e^{-ikr} + (-i)^l e^{2i\delta_l} e^{ikr}\right). \tag{3.14}$$

It is a superposition of spherical waves with different phases δ_l, which is similar to the structure of the second term of our *ansatz* (3.10). Also, the first term in our *ansatz* describing the incident particle can be expressed in this form by using spherical coordinates:

$$e^{ikz} = \frac{1}{2ikr}\sum_{l=0}^{\infty}(2l+1)P_l(\cos\theta)\left((-1)^{l+1}e^{-ikr} + e^{ikr}\right), \tag{3.15}$$

where we defined the axis of incidence to be along the z-axis. If we can find out how this equation is contained in (3.14), then we can identify the scattering amplitude f. Or, stating it differently, if we can find A_l such that (3.15) splits off from (3.14) while only outgoing

---

[6] In the far field, where the V_{sc} becomes negligible, the solution must be a linear combination of the free-particle solutions $u_{kl} \propto A\sin(kr - l\pi/2) + B\cos(kr - l\pi/2) \propto \sin(kr - l\pi/2 + \delta_l)$, with $\tan\delta_l = \frac{B}{A}$.

waves with e^{+ikr} remain, then we can identify those as the part of the wavefunction that has been scattered. This is the case for

$$A_l = \frac{1}{2k}(2l+1)i^l e^{i\delta_l}, \tag{3.16}$$

which brings (3.14) into the form of (3.10) with the scattering amplitude

$$f(k,\theta) = \sum_l (2l+1) f_l P_l(\cos\theta). \tag{3.17}$$

Here, we have defined the partial scattering amplitudes[7]

$$f_l = \frac{1}{2ik}\left(e^{2i\delta_l} - 1\right) = \frac{1}{k\cot\delta_l - ik}, \tag{3.18}$$

which express with which magnitude and phase the scattering potential scatters the individual partial waves of the incident particle.

Now we want to see which partial waves contribute most to the scattering at low energies ($kr_{sc} \ll 1$). It turns out that the phase depends on the momentum as [LL77; Fri13]

$$\tan(\delta_l) \propto k^{2l+1}. \tag{3.19}$$

Intuitively, this behavior can be understood from the Wigner threshold law: For small k, the effect of scattering will be suppressed for higher angular momenta l due to the larger centrifugal barrier[8]. Consequently, the partial scattering amplitudes for $l > 0$ vanish[9] for low-energy scattering as $f_l \propto k^{2l} \xrightarrow{k\to 0} 0$.

For $l = 0$, we insert the relation

$$\tan(\delta_0) = -ak \tag{3.20}$$

into eq. (3.18), where the proportionality factor a is called the s-wave scattering length. Now, for $k \to 0$, we obtain the value for the total scattering amplitude:

$$f(k,\theta) \approx f_0 \approx -a \tag{3.21}$$

Let us consider a few important consequences of this relation:

---

[7] Using the identity $\cot\alpha - i = \frac{\cos\alpha - i\sin\alpha}{\sin\alpha} = \frac{e^{-i\alpha}}{\sin\alpha}$

[8] Note that this is a general result without choosing a specific scattering potential.

[9] Depending on the exact shape of V_{sc}, resonant bound states may lead to shape resonances which can enhance the contributions of the partial scattering amplitudes with $l > 0$.

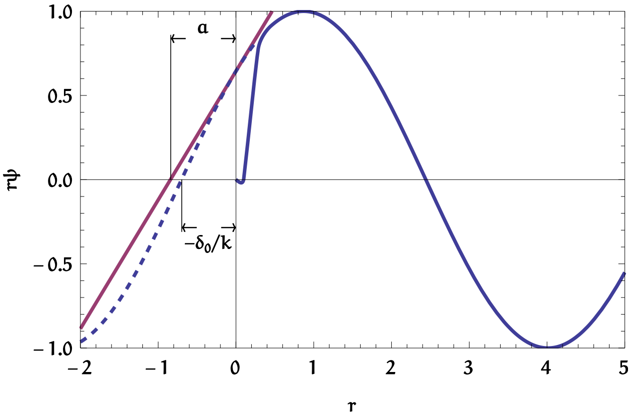

Figure 3.2: Geometrical visualization of the scattering length. The radial wavefunction in shown in blue. For $r < r_{sc}$, its behavior depends strongly on the scattering potential. The asymptotic behavior for $r \to \infty$ can be described with the scattering length a and the phase shift δ_0 (see text).

- At low energies, only the partial wave with $l = 0$ can scatter off the scattering potential. The partial waves with higher angular momentum are reflected by the centrifugal barrier. This type of scattering is called s-wave scattering.

- The effect of the scattering potential depends only on a single parameter a and expresses itself as a shift and scaling of the asymptotic scattered partial wave, called the scattering amplitude f.

- The scattering length a can be understood as the point where the linear expansion around $r = 0$ of the asymptotic wave function $u \sim \sin(kr + \delta_0)$ crosses the abscissa [FM47] (Figure 3.2),

  $$u_{\text{lin}} \propto \left(r + \frac{\tan \delta_0}{k} \right).$$

- The scattering amplitude does not depend on the collision angle or momentum of the scattering particles. The scattering cross section for distinguishable particles becomes

  $$\sigma = \int |f|^2 \, d\Omega = 4\pi a^2. \tag{3.22}$$

- For identical fermions, symmetric spatial wavefunctions with $l = 0, 2, 4, \ldots$ cannot be populated because of the antisymmetry requirement for their total wavefunction. Therefore, they cannot interact for $k \to 0$, as also s-wave scattering is suppressed.

It has become clear that the scattering length a is crucial for describing interactions between ultracold atoms. In the next section, I will show how a depends on the underlying scattering potential.

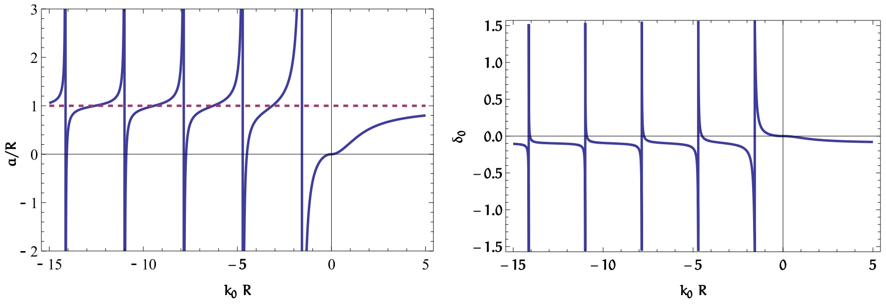

(a) (b)

Figure 3.3: (a) Scattering length a and (b) phase shift δ_0 in a square potential. The scattering length diverges and acquires a sign flip at $k_0R = (2n-1)\pi/2$, with $n \geqslant 1$ and $k_0 = \sqrt{2\mu V_0}/\hbar$. Note that, for deep potentials with multiple bound states ($V_0 \ll 0$), the resonance become narrow and a/R will remain close to one away from the resonance (dashed line). For the phase shift, $((\delta_0 + \pi/2) \bmod \pi) - \pi/2$ is shown for $kR = 0.1$.

3.2.2 *Zero-Energy Scattering Resonances*

The value of the scattering length a depends *a priori* on the exact characteristics of the scattering potential. However, it may show universal resonant behavior if the energy of the incoming particle is resonant with a (nearly) bound state. As a result, the scattering length may become very large and can even switch sign, compared to the non-resonant case. The simplest example for such a scattering length resonance is a zero-energy resonance. I will show an example of this using a generic square well potential following [Dal99], but realistic potentials exhibit similar behavior.

A spherical hard-core potential is described by an infinitely high box potential of size R in the radial Schrödinger equation. This means that the wavefunction will be expelled from the region $r < R$ and all of its nodes will be displaced by $d_0 = R$. This displacement can be related to the phase shift as $d_0 = \delta_0/k$. Clearly, for longer wavelengths it will amount to a smaller phase shift, whereas the scattering length will be independent of k: $a \approx -\delta_0/k = R$.

For a potential with a finite height V_0, the wavefunction will be only partially expelled from the core region. In the far field, a displacement of the nodes will remain, however its value will be $0 < d_0 < R$. Also, the scattering length will take values between 0 and R. One can calculate the exact value by solving the radial Schrödinger equation in and outside the box separately and matching both solutions on the boundary (see Figure 3.3a for $k_0R > 0$).

For attractive potentials, the wavefunction will be pulled inward and the scattering length becomes negative. Unlike the repulsive case, it is not bounded and can become smaller than $-R$. The reason is the first bound state that appears at a depth of $V_0 = -\frac{\pi^2\hbar^2}{2\mu R^2}$ and that

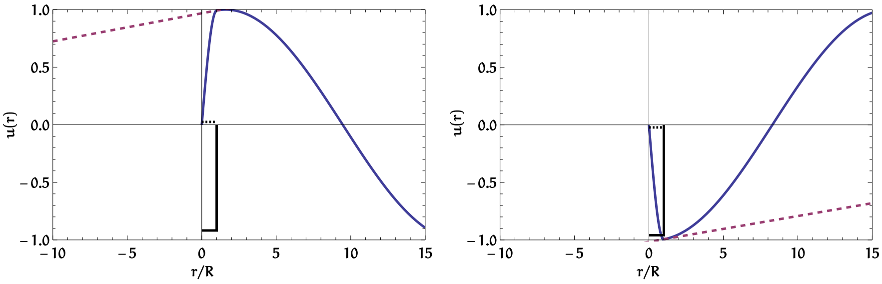

(a)

(b)

Figure 3.4: Wavefunction (blue) above (a) and below (b) a zero-energy resonance of a square well scattering potential (black). The linear expansion of the wavefunction (dashed, magenta) intercepts the abscissa at a (not shown in the graphs). The energy of the bound state is shown as a dotted line.

pulls in a node from the continuum into the range $r < R$. This causes the phase δ_0 to increase to $\pi/2$, which leads to a singularity with a sign flip in a. When increasing the depth of the potential further, the bound state becomes more deeply bound and the phase shift will tend to $\pi - kR$. An illustration of this process close to a resonance is shown in Figure 3.4.

This behavior of δ_0 and a is called a zero-energy resonance and reoccurs as the depth of the potential is increased and additional bound states appear. a and δ_0 are shown for a range of potential depths in Figure 3.3. These resonances are not exclusive to square potential wells, but can be found for any potential that supports bound states. This means that, by changing the depth of the scattering potential around a zero-energy resonance, the scattering behavior can be tuned from "infinitely repulsive" all the way to "infinitely attractive".

3.2.3 *Feshbach Resonances*

Up to this point, we considered two abstract scatterers with a convenient scattering potential. Of course, for actual atomic collisions, we should use the correct molecular potential, which cannot be manipulated so easily to make use of scattering resonances. Among other things, it depends on the symmetry of the scattering wavefunction: A spatially symmetric electronic wavefunction allows much better shielding of the repulsive nuclei from each other than an antisymmetric wavefunction, leading to a much deeper molecular potential. These two cases lead to two separate scattering channels[10], depending on the initial configuration of the scatterers. A channel whose potential energy at $R \to \infty$ which is smaller than the energy of the

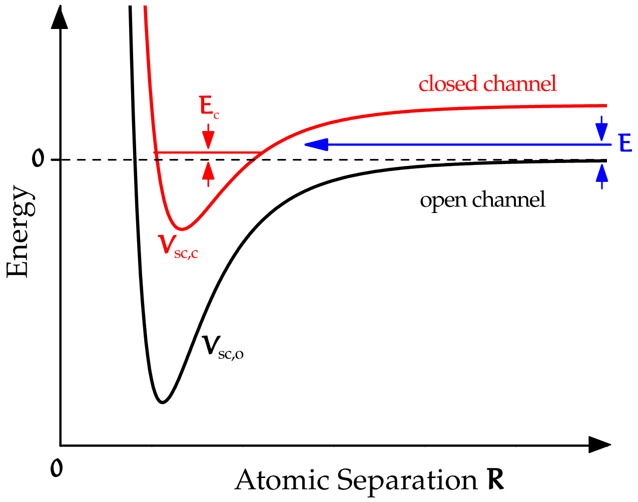

Figure 3.5: Open- and closed-channel scattering potentials of a particle with energy E close to a Feshbach resonance ($E_c \approx E$). Adapted from [Chi+10].

scatterers is called an open channel, while channels above this threshold are called closed channels.

If there is a mechanism which couples these channels, e.g., the spin-spin coupling of the electron spins at short distances, the properties of closed channels can influence the scattering behavior of the open channel. In particular, if a bound state of a coupled closed channel is resonant to the energy of the scatterers, this causes a *Feshbach resonance* (Figure 3.5). On the resonance, the scattering length diverges similar to the case of a zero-energy resonance. A simple model of Feshbach resonances has been described in [Chi05], a more general description was provided in [SMF12].

In the description of the scattering process, we can take the coupling between channels into account by coupling the Schrödinger equations (3.12) of the bare channels. This is done by replacing the scalar scattering potentials $V_{sc,o}$ and $V_{sc,c}$ (o for open channel, c for closed channel) with a matrix containing the off-diagonal coupling terms $V_{o,c}$, $V_{c,o}$. Following the derivation in [Fri13], we arrive at an asymptotic solution for the scattering wavefunction

$$u_{kl}(r) \overset{r\to\infty}{\longrightarrow} \frac{1}{\cos\delta_{res}} \sin(kr + \delta_{bg} + \delta_{res}), \tag{3.23}$$

---

[10] For scatterers which have multiple internal states, the different combinations of internal states form separate channels. For a full calculation, the coupling to these channels also has to be considered [Hou+98], but this will be ignored here for simplicity.

where δ_{bg} is the background phase shift of the uncoupled open channel (cf. eq. (3.13)) and δ_{res} is the additional phase shift due to the Feshbach resonance. It is described by

$$\tan \delta_{res} = -\frac{\Gamma/2}{E - E_R}, \tag{3.24}$$

where its width is proportional to the coupling strength between the channels $\Gamma = 2\pi |\langle u_c| V_{c,o} |u_o\rangle|^2$. The position of the resonance E_R is shifted with respect to the energy of the bound state in the uncoupled closed channel E_c to $E_R = E_c + \langle u_c |V_{c,o}\hat{G}V_{o,c}| u_c\rangle$. The shift contains the open-channel propagator $\hat{G}$ and is reminiscent of self-energy corrections in the T-matrix approach of scattering. It is clear that the scattering length is strongly influenced by this phase shift and it may diverge for $E \approx E_R$.

In experiments with ultracold gases, the energy of the scattering particles is typically $E \sim k_B \times 100\,\mathrm{nK} \sim h \times 2\,\mathrm{kHz}$, which is small compared to molecular bound state energies corresponding to GHz or even THz. Instead of tuning the energy E of the scatterers to match a bound state in order to control δ_{res}, it is more practical to tune E_R into resonance by manipulating the scattering potential of the channels. This can be done by changing the coupling between two channels with an optical field (*optical Feshbach resonance*, see for example [Fed+96; Nic+15]) or by shifting the energy offset of the potentials relative to each other with a magnetic field B (*magnetic Feshbach resonance*). The latter case applies only when the magnetic moment μ differs between the channels, where the energy difference will be $E \propto (\mu_o - \mu_c)\, B$. For the magnetic Feshbach resonance, the scattering length can be expressed as [Chi05]

$$a(B) \approx a_{bg}\left(1 - \frac{\Delta B}{B - B_0}\right), \tag{3.25}$$

where a_{bg} is the background scattering length of the uncoupled open channel and approximately independent of B, and ΔB is the width of the resonance, i.e., the difference between the resonance position B_0 and the zero-crossing $B|_{a=0}$. In our experiment, we rely on the magnetic Feshbach resonance of ^{6}Li to tune the interactions. This Feshbach resonance has some particular properties which I will lay out in detail in Section 4.1.3.

3.2.4 *Feshbach Molecules*

Since the open and closed channel are coupled, the adiabatic theorem tells us that we can transfer population from free scattering states in the open channel to bound molecular states in the closed channel by slowly ramping the magnetic field accross the resonance [Hod+05].

With this procedure, we can associate diatomic molecules in the highest vibrational state without releasing energy or introducing entropy [GFK09]. Close to the resonance, the two-particle system will consist of a superposition of free particles and bound particles. It turns out that, for a wide resonance, the contribution of the free particles is larger (open-channel dominated), while the bound particle state contributes more for narrow resonances (closed-channel dominated) [Chi05].

Close to the Feshbach resonance, the energy of a Feshbach molecule relative to the energy of the bare open channel $E_{o,b}$ scales as

$$E - E_{o,b} = -\frac{\hbar^2}{2\mu a^2}. \tag{3.26}$$

This means that there is a bound state only for positive scattering length. In this regime, where $a \gg r_{sc}$, the wavefunction in the far field becomes universal and does not depend on the exact shape of the scattering potential. It behaves as

$$\psi(r) \propto e^{-r/a}, \tag{3.27}$$

and the particles form a halo dimer: On average, the particles are separated by $a/2$, which means that they are much further apart than the range of the scattering potential r_{sc}. When approaching the resonance, a diverges and the molecule becomes unbound.

Farther away from the resonance, for small positive a, the state is described well by the bare closed channel. The energy then scales proportionally to the difference in magnetic moments of the bare channels, $E - E_{o,b} \approx (\mu_o - \mu_b)\,|B|$.

3.2.5 *Contact Interaction*

In the previous sections, we have seen that the long-range scattering behavior for ultracold atoms only depends on the scattering length a and that a Feshbach resonance can be used to tune its value. Now, we can incorporate this into the Hamiltonian (3.7) by using a simpler, effective interaction term V_{int} instead of the detailed scattering potential V_{sc} that would require a precise description of the wavefunction for short ranges.

We accomplish this by shrinking the range of the scattering potential $r_{sc} \to 0$, while maintaining the correct phase shift δ of the scattering waves in the far field. If we want to extend the long-range solution of our wavefunction from eq. (3.13) to $r = 0$, the boundary condition to the Schrödinger equation changes from $u(0) = 0$ to

$$\tan\delta = \frac{\sin\delta}{\cos\delta} = -ka \Leftrightarrow \left.\frac{u'}{u}\right|_{r=0} = -\frac{1}{a}. \tag{3.28}$$

As a consequence, we also have to include unphysical terms in the radial Schrödinger equation (3.12) that we had implicitly omitted earlier. Using the fact that we can write our radial wavefunction as $\psi(r) = \frac{u(r)}{r} = \frac{u(0)}{r} + \frac{u(r)-u(0)}{r}$ and that $\nabla^2 \frac{1}{r} = -4\pi\,\delta(r)$, we instead obtain

$$-\frac{\hbar^2}{2\mu}\left(-4\pi\,u(0)\,\delta(r) + \frac{u''(r)}{r}\right) + V(\psi(r)) = E\,\frac{u(r)}{r}. \qquad (3.29)$$

Here, higher angular momenta $l > 0$ have been excluded, because their boundary condition remains $u_l(0) = 0$ due to the centrifugal potential. For the s-wave contribution, we can insert the asymptotic solution from eq. (3.13) and evaluate the second derivative:

$$\left(\frac{\hbar^2 k^2}{2\mu} - E + V\right)\psi(r) = -\frac{2\pi\hbar^2}{\mu}\,u(0)\delta(r). \qquad (3.30)$$

The first two terms in the sum cancel, and, after substituting the boundary condition (3.28) on the right hand side, we obtain an effective pseudo-potential for contact interactions

$$V_{\text{int}}(\psi(r)) = \frac{2\pi\hbar^2}{\mu}\,a\,\delta(r)\,u'(0) = g\,\delta(r)\frac{d}{dr}\left(r\psi(r)\right). \qquad (3.31)$$

The strength of the interaction potential is defined as $g = \frac{4\pi\hbar^2}{m}a$ and is proportional to the scattering length.

4

EXPERIMENTAL SETUP AND PREPARATION

In this chapter, we will lay out the steps necessary to prepare a few-fermion system in a deterministic manner. First, we will examine the properties of Lithium which are relevant for the methods and results of our experiments. With these properties, we will then describe the cooling procedure of a ^{6}Li gas. This is the basis our final preparation step, with which we create deterministic few-fermion systems [Ser11; Ser$^+$11]. Finally, we will examine how to prepare low-entropy systems in multiple microtraps by adiabatically coupling the microtraps.

4.1 PROPERTIES OF LITHIUM

Our experiments use the fermionic isotope of Lithium, ^{6}Li. Due to the simple structure of its optical transitions and its broad Feshbach resonance, it is widely used in cold-atoms experiments. This section will present its optical and collisional properties, which can be found in more detail in the comprehensive overview written by M. Gehm [Geh03a].

4.1.1 *Internal States and External Magnetic Fields*

^{6}Li is made up of three protons, three neutrons and three electrons, and is therefore, in total, fermionic. Its nucleus has a nuclear spin of $I = 1$. Two of its electrons occupy the 1S orbital with the remaining one being in the 2S orbital. This unpaired electron determines the chemical and optical properties of Lithium and has a total electronic angular momentum of $J = 1/2$. From the ground states, the excited states $2P_{1/2}$ and $2P_{3/2}$ can be reached via electric dipole transitions called the D_1 and D_2 lines, respectively. In our experiment, we only use the D_2-line for optical transitions.

In absence of strong magnetic offset fields, the magnetic moments of the electron and the nucleus couple to each other leading to the hyperfine splitting of the energy levels (Figure 4.1) and to new eigenstates with the total-angular-momentum quantum number F. Due to the coupling of J and I, the optical transitions are typically not closed and can for example couple the $F = 1/2$ and $F = 3/2$ ground states manifolds.

When applying an external magnetic field, the magnetic moments of the electron and nucleus will start to couple to it. This means that the quantum states described with the total angular momentum F

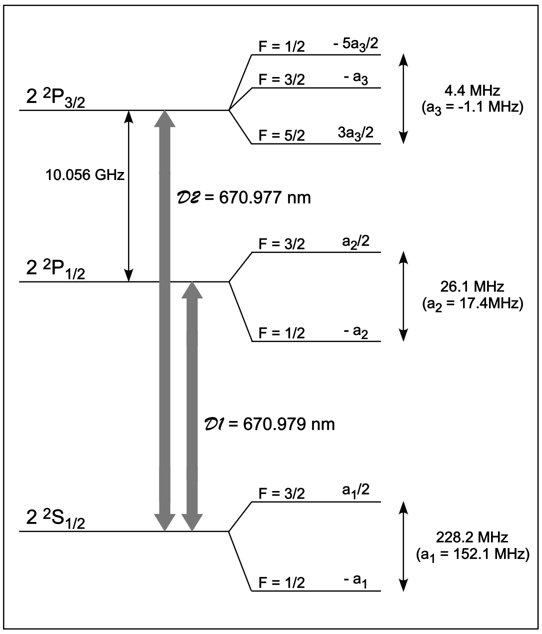

Figure 4.1: Hyperfine splitting of three lowest-energy states of ^{6}Li for vanishing magnetic field. In our experiment, we currently only use the D_2-line for optical transitions. From [Geh03a].

are no longer eigenstates. The new eigenstates of the ground state manifold can be expressed in the $|m_J, m_I\rangle$-basis as

$$\begin{aligned}
|1\rangle &= |F = 1/2, m_F = 1/2\rangle = \sin\theta_+ \,|1/2, 0\rangle - \cos\theta_+ \,|-1/2, 1\rangle \\
|2\rangle &= |F = 1/2, m_F = -1/2\rangle = \sin\theta_- \,|1/2, -1\rangle - \cos\theta_- \,|-1/2, 0\rangle \\
|3\rangle &= |F = 3/2, m_F = -3/2\rangle = |-1/2, -1\rangle \\
|4\rangle &= |F = 3/2, m_F = -1/2\rangle = \cos\theta_- \,|1/2, -1\rangle + \sin\theta_- \,|-1/2, 0\rangle \\
|5\rangle &= |F = 3/2, m_F = 1/2\rangle = \cos\theta_+ \,|1/2, 0\rangle + \sin\theta_+ \,|-1/2, 1\rangle \\
|6\rangle &= |F = 3/2, m_F = 3/2\rangle = |1/2, 1\rangle \,.
\end{aligned} \tag{4.1}$$

We can see that four of the hyperfine states consist of a superposition of two states in the $|J, m_J\rangle$-basis. Their coefficients can be understood as mixing angles, which depend on the strength of the external magnetic field and the magnetic moment of the 2S orbital. We will forgo a detailed discussion of the properties of $\theta_\pm$, which can be found in [Geh03a]. For our experiment, the most important property is that the coefficients $\sin\theta_\pm$ tend to zero for large magnetic fields and the uncoupled m_J and m_I states form a good basis again (hyperfine Paschen-Back effect).

The two remaining states only consist of one basis state each, with an extremal value for m_F. As their angular-momentum components align, these states are called stretched states and can be identified from the energy level diagram Figure 4.2 as the states with a constant slope.

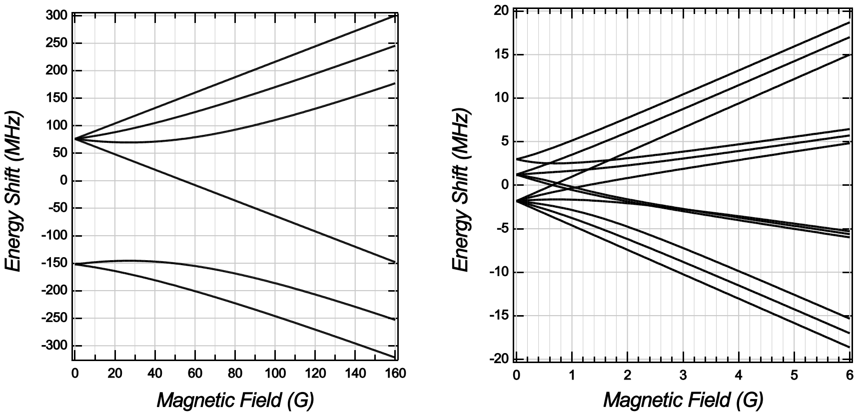

(a) (b)

Figure 4.2: (a) Zeeman splitting of the 2S ground state. (b) Zeeman splitting of the $2P_{3/2}$ excited state. From [Geh03a].

The eigenstates of the $2P_{3/2}$ excited state look similar to the ground state manifold, however, they have more m_J and m_I states available. Also, they enter the hyperfine Paschen-Back regime at much lower magnetic fields, since the coupling between the electron and nuclear magnetic moments is smaller (Figure 4.2b). Unfortunately, they cannot be diagonalized analytically and the eigenvalue-problem has to be solved numerically [Geh03b].

4.1.2 *Optical Properties*

Both during the preparation phase and the detection phase of our experiment, we utilize light resonant with the D_2-line to excite the atoms. To understand how the atoms scatter the light, we have to know the resonance frequency of the atomic transition depending on the magnetic field (Figure 4.2). In the Paschen-Back limit, the frequency shift is approximately proportional to

$$\Delta E_{m_J}(B) \approx -g_J m_J \mu_B B, \tag{4.2}$$

where g_J is the Landé factor and $\mu_B = h \times 1.40\,\text{MHz/G}$ is the Bohr magneton.

The scattering behavior of the atoms also depends on the polarization, intensity I and detuning Δ relative to the atomic transition of the external light field. For example, at $900\,\text{G}$, the transition between $|3\rangle = |-1/2, -1\rangle$ and $|3'\rangle = |-3/2, -1\rangle$ can be addressed with σ^--light, in accordance to the angular-momentum selection rules. Compared to the D_2-line at $0\,\text{G}$ (eq. 4.2, Figure 4.1), the resonance frequency of this transition is lowered by $-1.34\,\text{GHz}$.

The excited atom can return to the ground state via spontaneous emission or via stimulated emission. In the spontaneous emission pro-

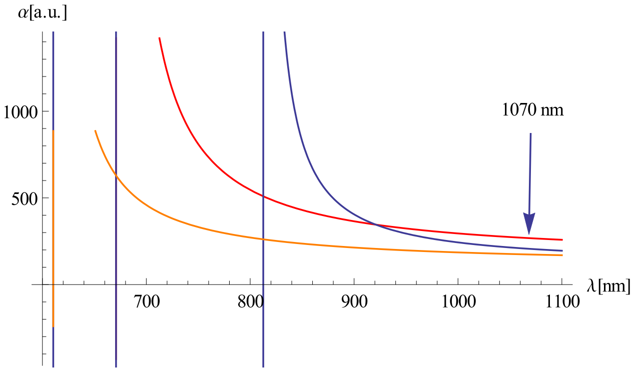

Figure 4.3: Polarizability of ^{6}Li for the $2P_{3/2}$, $m_j = 1/2$ ground state (red) and the $2P_{3/2}$, $m_j = 1/2$ and $m_j = 3/2$ excited states (blue and orange, respectively). From [För15].

cess, the atom will emit into a random direction following the dipole emission pattern. The spontaneous emission rate can be calculated as

$$\Gamma_{sc} = \frac{\Gamma}{2} \frac{I/I_{sat}}{1 + I/I_{sat} + (2\Delta/\Gamma)^2} \tag{4.3}$$

and depends on the spontaneous decay rate Γ and the saturation intensity I_{sat}, which are given in Table 4.1.

Stimulated emission leads to a coherent transfer of the excited-state atom back to the ground state, as the photon is re-emitted into the original mode of the external light field. This happens at a rate called the Rabi frequency,

$$\frac{\Omega}{\Gamma} = \sqrt{\frac{I}{2I_{sat}}}. \tag{4.4}$$

In both cases, because the light mainly couples to the electrons electric dipole moment (see eq. 3.2), the atom will decay to a state with a certain electronic quantum number m_J. As we can see from eq. (4.1), this is not necessarily an eigenstate of the atom, therefore the atom may end up in a different hyperfine state after having scattered a photon (open transition). Only the stretched states consist of a single basis state and can be used for closed optical transitions.

If the light is far off-resonant, the scattering rate will decrease as Δ^{-2} (eq. (4.3)), until it barely excites the atoms anymore. In this case, the effect of the light field on the atoms can be described by a shift of the bare atomic energy levels (AC-Stark shift, see Section 3.1). The energy shift is proportional to the polarizability α, which can be calculated for Lithium with perturbation theory [SSC13; För15]. For wavelengths above approximately 820 nm, both the 2S-state and the $2P_{3/2}$-state have a positive polarizability (Table 4.1, Figure 4.3). This means

Optical Properties	Value
Wavelength D_2-line	670.977 nm
Frequency D_2-line	446.780 GHz
Lifetime D_2-line	27.1 ns
Natural linewidth D_2-line	$36.9 \times 10^6\,s^{-1}$
Atomic recoil velocity D_2-line	$9.89\,cm\,s^{-1}$
Recoil temperature D_2-line	3.54 μK
Saturation intensity I_{sat} D_2-line	$2.54\,mW\,cm^{-2}$
Polarizability of 2S at 1064 nm	270 a.u.
Polarizability of 2P3/2, $m_J = 1/2$ at 1064 nm	208 a.u.
Polarizability of 2P3/2, $m_J = 1/2$ at 1064 nm	175 a.u.
Scattering Properties	**Value**
Singlet background scattering length	$38.75\,a_0$
Triplet background scattering length	$-2240\,a_0$
1-2 resonance position B_0	832 G
1-2 resonance width ΔB	527 G
1-3 resonance position B_0	690 G
1-3 resonance width ΔB	568 G
2-3 resonance position B_0	810 G
2-3 resonance width ΔB	589 G

Table 4.1: Properties of ^{6}Li, adapted from [Geh03a]. The abbreviation a.u. stands for atomic unit.

that both the ground state and the first excited states of ^{6}Li are attracted to the high-intensity regions of the light field. According to eq. (3.5), the energy shift is

$$\Delta E(\mathbf{r}) = -\frac{1}{2\epsilon_0 c}\,\Re(\alpha)\,I(\mathbf{r})$$

and scales with the laser detuning as approximately Δ^{-1} (c.f. eq. (3.3)). We exploit this behavior to trap atoms in the intensity maximum of far-red detuned (1064 nm and 1070 nm) high-power laser beams, where off-resonant scattering is strongly suppressed.

4.1.3 *Collisional Properties*

The scattering between two neutral atoms at low energies can be described by the s-wave scattering length a (Section 3.2). The exact value of a is determined by the scattering potential, which depends on the combination of the hyperfine states of the atoms involved in the scattering process. For example, the scattering potential between a particle in state $|1\rangle$ and a particle in state $|2\rangle$ will be different from the potential between state $|1\rangle$ and $|3\rangle$.

However, the potential is influenced most by the configuration of the electronic spin pair, namely if the particles form a $S = 0$ singlet or a $S = 1$ triplet. In the case of Lithium, a low lying virtual bound state in the triplet potential and the strong coupling to one of the singlet states gives rise to a broad Feshbach resonance. For the description of its most important features, we will only discuss the mixture of the hyperfine states $|1\rangle$ and $|2\rangle$. However, the other combinations of the three lowest hyperfine states behave similarly. Measurements of the ^{6}Li-Feshbach s- and p-wave resonances can be found in [Sch$^+$05; MVA95; Bar$^+$05], detailed review on Feshbach resonances in general and the ^{6}Li-resonance in particular can be found in [Chi$^+$10].

At zero magnetic field, the scattering particles can be in a superposition of the singlet and triplet state, since these are degenerate at large distances. The singlet potential supports 38 vibrational levels, the highest one lying 1.38 GHz below the continuum and consisting of two states with $I = 0; 2$. Because also the next-higher lying (virtual) state does not lie very close to the continuum, the singlet background scattering length $a_{S,bg} = 45.2\, a_0$ is not influenced by zero-energy resonances and is similar to the effective range[1] r_{sc}, as expected (see Section 3.2 and [Dal99]). The triplet potential features a remarkably large scattering length $a_{T,bg} = -2140\, a_0$. This is caused by a zero-energy resonance: the highest bound state is relatively deeply bound, with the next possible bound state slightly above the continuum. This explains the large and negative scattering length (see Section 3.2.2).

As the magnetic field is increased from 0, the atoms will enter the Paschen-Back regime and $S = 1$ triplet configuration will become energetically favorable and thus the only open channel. At the same time, the coupling between the channels will lead to a triplet potential that is slightly deeper than the bare triplet potential. However, this is already enough to support the additional, previously virtual bound state. As the magnetic field is increased, this state becomes more and more similar to the bare triplet state, causing the bound state to move closer to the continuum and a to be positive. At $B_0 = 832\,\text{G}$, the potential can no longer support this bound state and the scattering length shows a zero-energy resonance and diverges. For even higher fields, the scattering length approaches $a_{T,bg}$.

We can describe the tuning of the scattering length with the magnetic field approximately with the heuristic formula (3.25),

---

[1] It is of the same order of magnitude as the van-der-Waals length for ^{6}Li, $\beta_6 = 62.5\, a_0$ [Yan$^+$96]

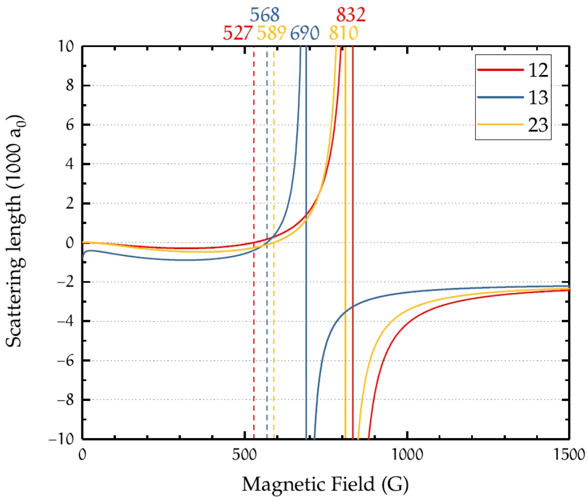

Figure 4.4: Feshbach resonances of the three lowest hyperfine states. The positions of the zero crossings and resonances are marked (see also Table 4.1).

$$a(B) = a_{T,bg}\left(1 - \frac{\Delta B}{B - B_0}\right).$$

The values of the parameters are listed in Table 4.1, and a graph of scattering lengths of the $|1\rangle$-$|2\rangle$, $|1\rangle$-$|3\rangle$, and $|2\rangle$-$|3\rangle$ mixtures is shown in Figure 4.4.

Because this Feshbach resonance is open-channel dominated, the scattering is universal[2] over a wide range. This kind of Feshbach resonance typically has a large width ΔB, which makes it particularly easy to control experimentally. Therefore, we can use the ^{6}Li Feshbach resonance to study systems with contact interactions of almost arbitrary interaction strength, as explained in Section 3.2.5.

4.2 COOLING A FERMI GAS

The experiments which are presented in this thesis all have a small, deterministic sample of fermions as their starting point. To get to this point, we first create a degenerate, ultracold Fermi gas. The experimental procedure has been established on our experiment already several years ago [Ser11] and has been used ever since. However, for the experiments shown in chapter 6, we had to modify our cooling scheme. Therefore, I will briefly describe the cooling steps following one cycle of the experiment (Figure 4.5). More detailed information about how to cool atomic gases can for example be found in [DCT89; GWO00; KZ08; MS99].

---

[2] I.e., it can be described with only the scattering range as a parameter, see [Chi$^+$10].

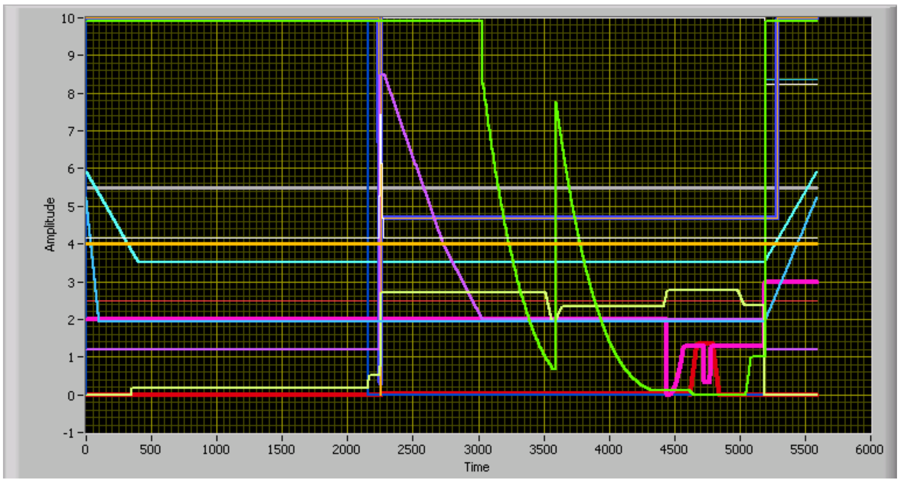

Figure 4.5: Experimental sequence for high-field evaporation. The evaporation starts at 2250 ms after the MOT has been loaded by transferring the MOT to the ODT. The intensity of the laser is first reduced by linearly decreasing the laser output (purple curve). When the minimum output power of our laser is reached, we attenuate the laser beam using two AOMs (green curve) following a polynomial curve $\propto (1 - t/\tau)^{3.24}$, with $\tau = 1000$ ms. At the kink in the green curve, the intensity stabilization is switched to a photodiode with a higher gain. The Landau-Zener RF passage from state $|2\rangle$ to $|3\rangle$ is performed at 3550 ms for 5 ms. Before the atoms are transferred to the microtrap at 4450 ms, the field is increased to above the resonance (900 G, yellow curve) in order to dissociate Feshbach molecules that have formed during the evaporation. Finally, the microtrap is spilled at 4650 ms by lowering its depth (pink curve) and applying a magnetic field gradient (red curve).

The first step towards an ultracold Lithium gas is the evaporation in our oven chamber. The hot gas leaves the oven chamber as an atomic beam and is first slowed down by a Zeeman slower. The atoms which are sufficiently slow are then captured in a magneto-optical trap (MOT). During this first stage of the experiment, the MOT is loaded for 2 s with approximately 1×10^8 atoms mainly in the $|1\rangle$ and $|2\rangle$ hyperfine states.

Next, the atomic beam is turned off with a shutter and the atoms in the MOT are transferred into the crossed optical dipole trap (ODT). To increase the overlap between the MOT and the ODT, we compress the MOT by applying a stronger gradient and by reducing the detuning of our light. Still, because the beams of the ODT only have a waist of 45 µm, we transfer less than 1 % of the atoms.

Then, we start cooling our sample by evaporative cooling, i.e., reducing the depth of the ODT. Initially, we reduce the output power of the laser directly, while at later stages we attenuate the power of the laser beam using two acousto-optic modulators (AOMs). The cooling during this phase depends on the thermalization rate of the sample, and thereby also on the scattering cross section and the scattering length, which we tune to large values by using the Feshbach resonance. For the initial stages of the evaporation, we therefore evaporate at a field of 795 G which corresponds to $a_s \approx 9600\, a_0$. Also, we apply an RF field to mix the lowest two hyperfine states and keep their numbers balanced.

As we prefer[3] to perform our experiment with the states $|1\rangle$ and $|3\rangle$, we transfer the atoms in state $|2\rangle$ to state $|3\rangle$ with an RF Landau-Zener passage after about 1.35 s of evaporation.

After this step, we can continue to evaporate either left or right of the zero-crossing (see Table 4.1). In the first case (low-field evaporation), we evaporate at around 300 G to ensure efficient thermalization due to the reasonably large, negative scattering lengths. As there is no bound state at these scattering length, the gas remains a Fermi gas during the entire evaporation. Because the thermalization relies on momentum redistribution which happens only near the Fermi surface, this evaporation slows down the colder the gas gets. However, it is a useful method to access few-fermion systems on the repulsive branch (see Figure 4.6), because we can tune to positive scattering lengths by passing the zero crossing again[4]. We have been predominantly using this method of evaporation during the last few years, for example for the experiments described in Chapter 7.

The second method (high-field evaporation) is performed at a magnetic field near the resonance (685 G) and results in a gas of weakly

---

[3] Firstly, its Feshbach resonance allows us to work with smaller fields, which spares our Feshbach coils. Secondly, state $|3\rangle$ provides a closed transition for imaging and we have less off-resonant scattering due to the 160 MHz separation in energy between the states at high magnetic fields (Figure 4.2a).

[4] For positive scattering lengths, the repulsive branch is not the ground state.

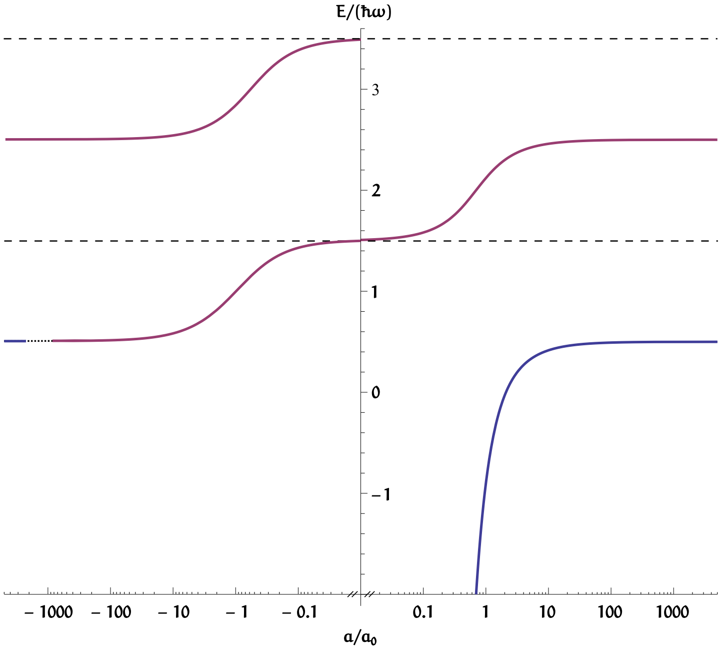

Figure 4.6: Range of experimentally accessible energy states in an isotropic trap, depending on the scattering length a (more details in Chapter 6). The states which have less energy than the non-interacting ground state (marked by the lower dashed line) are called the attractive branch, while the states with higher energy are called the repulsive branch. Blue (magenta) lines show the scattering lengths which are accessible with high-field (low-field) preparation of atoms in a $|1\rangle$-$|3\rangle$ mixture. Note that a is shown on a double logarithmic scale, its values around the Feshbach resonance are outside the graph to the left and right and can also be accessed. The dotted segment on the left shows the scattering lengths we cannot access (see also Figure 4.4). Effects of the confinement-induced resonance [Ols98; BMO03] are not shown in this graph.

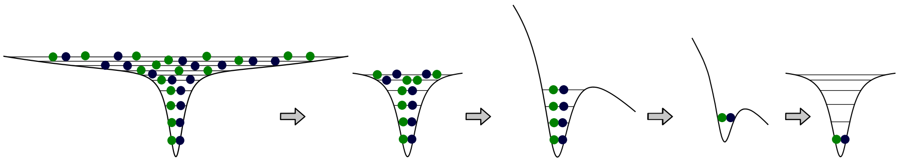

Figure 4.7: Spilling technique (description in the text), adapted from [Zür12a]. The different hyperfine states of the atoms are represented by dots of different color.

bound Feshbach molecules. Due to their bosonic statistics, they thermalize faster and we can accelerate our evaporation. After finishing the evaporation, this evaporation method allows us to access large negative scattering lengths while still remaining in the ground state of the system by crossing the Feshbach resonance (see also [Zür12a], chapter 5). At the end of either evaporation process, we typically have a sample containing 6×10^4 atoms at a temperature of $250\,\mathrm{nK}$.

4.3 PREPARING FEW-FERMION SYSTEMS

To perform our experiments, we need systems with a small, well-known atom number in the ground state of an optical potential. We achieve this by loading an optical microtrap from the previously prepared dipole trap reservoir. We have used this technique already prior to this thesis [Ser11; Ser+11], however, in the meantime, we have installed a new objective which can make smaller foci and thereby deeper microtraps [Ber13; Kli12]. After having installed the new objective, we had to revisit our preparation scheme (Figure 4.7) and optimize its parameters.

4.3.1 *Spilling Technique*

After completing the evaporation phase in the optical dipole trap, we superimpose a small focus of $1064\,\mathrm{nm}$ light (waist of $1.65\,\mu\mathrm{m}$). We slowly ramp up the intensity to ca. $390\,\mu W$, which corresponds to a depth of $5\,\mu\mathrm{K}$. Because the microtrap is small compared to the reservoir, only a fraction of the atoms will fit in the potential and the absolute temperature of our system will not be increased by turning it on. However, because the Fermi temperature of the combined system is much higher ($7\,\mu\mathrm{K}$) that that of the dipole trap alone, we achieve a much better degeneracy of $T/T_F \approx 0.05$. This corresponds to an occupation probability of ideally over $99.99\,\%$ in the lowest levels of the microtrap.

Next, we want to perform experiments using only the lowest levels of the microtrap, since those contain the least amount of entropy. First, we reduce the interaction strength (e.g., by going to the zero-crossing of the scattering length for the low-field preparation). Then, we turn off the ODT and apply a magnetic field gradient. The higher trap levels of the microtrap are now not bound anymore, and only the (quasi-)bound states with the lowest energy remain. We fine-tune the number of bound states by adjusting the depth of the microtrap.

However, due to the tunneling effect, even particles in bound states can still escape from the microtrap as long as the gradient is on and the barrier is low and narrow enough. Therefore, we must keep the tunneling time sufficiently short. The tunneling time constant for each of the energy levels of the microtrap can be calculated and optimized with the Wentzel-Kramers-Brillouin (WKB) method (see [Ser11]). Finally, we increase the depth of the microtrap to its original value and turn off the gradient. This suppresses the tunneling and concludes the preparation method for deterministic few-fermion systems.

4.3.2 *Optimization of the Preparation Fidelity*

The fidelity of the preparation method described in the previous section depends, among other things, on the choice of the tunneling time. We want to choose it long enough so the atoms in the higher levels can tunnel out of the potentials, and short enough to retain the atoms in the lower levels (the ones we want to keep for the experiments). With accurate knowledge of the optical potential and the strength of the gradient, it is possible calculate these probabilities using the WKB method.

However, we cannot monitor the intensity distribution of the microtraps directly inside the vacuum chamber with a camera. Therefore, we do not know the exact shape of our optical potential for the WKB calculations. This means that it is still necessary to optimize various spilling parameters experimentally. Typically, the parameters we can tune are the depth of the optical potential P_{spill} (given as the total optical power of the microtrap), the strength of the magnetic field gradient B'_{spill} and the duration of the spill t_{spill}. Because this spans a large parameter space, we usually optimize only one or two of the parameters simultaneously.

We optimize the preparation parameters by measuring atom number statistics and preparation fidelities for different combinations of spilling parameters by re-transferring the prepared sample into an imaging MOT after the preparation has been completed. Taking account the losses from this final transfer ($< 1\,\%$, [Zür12b]), we can then infer the atom number in each realization from the fluorescence intensity of the MOT (for more details, see Section 5.1), which allows us to extract the average atom number and the probability for having a certain number of atoms.

For the first optimization method called "stufenplot", we keep B'_{spill} fixed to typically $60\,\mathrm{G/cm}$ and t_{spill} to typically between $10\,\mathrm{ms}$ and $50\,\mathrm{ms}$, while tuning the depth of the optical potential. One can see

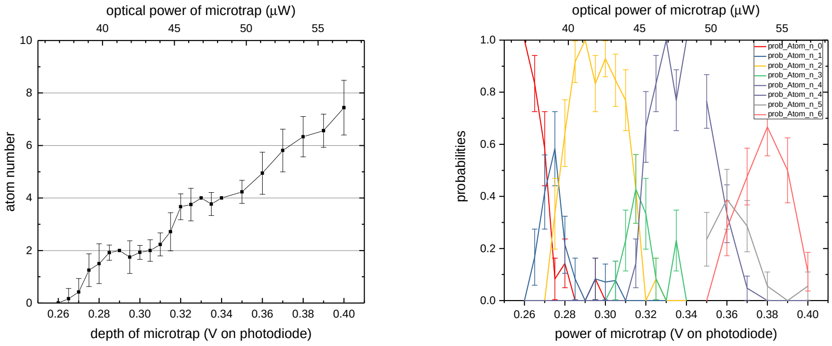

(a)

(b)

Figure 4.8: Atom number after spill when varying P_{spill}. (a) Mean atom number vs. P_{spill}. (b) Probability of finding a certain atom number vs. P_{spill}. Only the values for up to 6 atoms are shown, higher numbers have been omitted for clarity. The errorbars represent the standard deviation after 12-21 repeats per setting. At 0.3 V, for example, the probability for finding two atoms is 93(7) %, and 7(7) % for finding one atom. This leads to a mean atom number of 1.93(27) at 0.3 V, as shown in the left panel.

that, for certain depths of the optical potential, the atom number stays relatively constant at an even number (Figure 4.8a). This is the case when one trap level has long tunneling times whereas the atoms in the next higher trap level tunnel quickly or even become unbound. This makes it possible to prepare $2n$ atoms with a high fidelity $f_2(n)$ of over 95 % (Figure 4.8b).

Still, even when testing a wide range of parameters, a perfect, 100 % preparation fidelity is never reached. While the actual preparation fidelity may be influenced by multiple settings, parameters and uncontrolled drifts thereof, the fundamental limitation to the fidelity are the tunneling times of the highest bound energy level τ_2 and the next lowest energy level τ_1. The probability of the atom in the higher state tunneling while retaining the atom in the lower state then becomes

$$p_1(t) = e^{-t/\tau_1}\left(1 - e^{-t/\tau_2}\right). \tag{4.5}$$

This function has a global maximum value which only depends on the quotient of the tunneling times $q = \tau_1/\tau_2$:

$$p_{1,\text{opt}} = q\,(1+q)^{-\frac{1+q}{q}} \tag{4.6}$$

at the time

$$t_{\text{opt}} = \tau_2\,\ln(1+q). \tag{4.7}$$

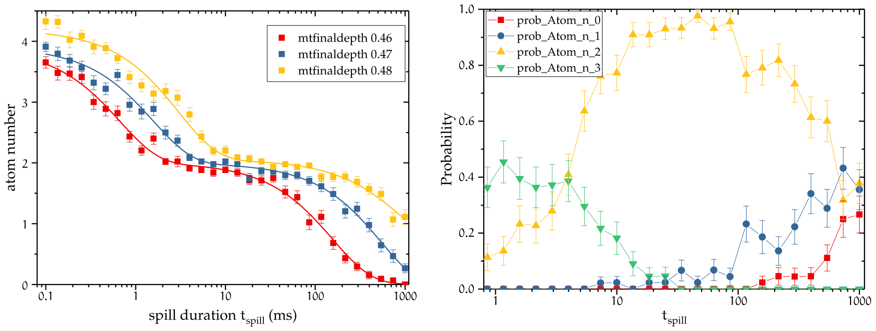

(a) (b)

Figure 4.9: Atom number after spill when varying t_{spill} with $B'_{spill} = 75\,G/cm$ for different P_{spill}. (a) Mean atom number. The lines represent double-exponential fits. (b) Probability of finding n atoms for $P_{spill} = 0.48\,V$ (voltage on the photodiode). If "good" values are chosen for P_{spill} and B'_{spill}, there is a range of t_{spill} where the fidelity stays high, in this example between $20\,ms$ and $90\,ms$.

Thus, by determining the tunneling times for different experimental parameters, we can find the values with the best possible quotient and the best corresponding spilling duration, leading to an optimal preparation fidelity.

The tunneling times can be determined by measuring the mean atom number depending on the spilling duration (Figure 4.9a). The values for τ_1 and τ_2 and the derived quantities for a few typical settings are listed in Table 4.2. With the correct settings, fidelities of 97 % have been reached experimentally.

4.4 TRANSFER TO MULTIPLE MICROTRAPS

Once we have prepared a well-defined state in a single well, we can start manipulating the optical potential and the interaction strength. We can create multiple microtraps by diffracting the initial microtrap beam in an acousto-optic deflector (AOD), which was characterized in [Kli12]. It is integrated into our optical setup as described in [Ber17] (Figure 4.10). We use the AOD to shape the optical potential by controlling the intensity and position of each individual microtrap. Effectively, this allows us manipulate the tilt Δ and tunnel coupling J in the Hubbard Hamiltonian from eq. (7.1).

If we want to maintain a pure state while we change our potential, we must ensure all our manipulations happen adiabatically, i.e., slowly compared to the energy gap to other states. Depending on the system in question, the gap may be of the size of Δ or J, but also, for example, $\hbar\omega_{trap}$, U or J^2/U (see Section 7.1). In this section, I will explain how we prepare a double well adiabatically and how we plan to make larger arrays of microtraps.

Field & Gradient	P_{spill}	τ_1 (ms)	τ_2 (ms)	q	$p_{1,\mathrm{opt}}$ (%)	t_{opt}/τ_2
$B = 300\,\mathrm{G}$, $B'_{\mathrm{spill}} = 60\,\mathrm{G/cm}$	0.38	147(19)	0.868(112)	169(31)	96.4(5)	5.14(18)
	0.39	641(72)	1.52(21)	442(75)	98.3(3)	6.05(18)
	0.40	$2.31(66) \times 10^3$	3.73(59)	618(203)	98.8(3)	6.43(33)
$B = 300\,\mathrm{G}$, $B'_{\mathrm{spill}} = 75\,\mathrm{G/cm}$	0.45	179(10)	0.821(83)	218(25)	97.1(3)	5.39(12)
	0.46	539(39)	2.07(18)	261(30)	97.5(2)	5.57(11)
	0.47	$2.09(37) \times 10^3$	4.00(40)	522(105)	98.6(2)	6.26(20)
$B = 568\,\mathrm{G}$, $B'_{\mathrm{spill}} = 60\,\mathrm{G/cm}$	0.38	78.6(75)	0.530(79)	148(26)	96.0(6)	5.01(18)
	0.39	176(18)	0.841(87)	209(30)	97.0(4)	5.35(14)
	0.40	822(430)	1.82(19)	451(241)	98.4(7)	6.11(53)
$B = 568\,\mathrm{G}$, $B'_{\mathrm{spill}} = 75\,\mathrm{G/cm}$	0.46	157(14)	0.661(68)	237(32)	97.3(3)	5.47(14)
	0.47	547(113)	1.56(14)	351(79)	98.1(4)	5.86(22)
	0.48	906(634)	3.01(28)	301(212)	97.8(13)	5.71(70)

Table 4.2: Spilling times for different spilling parameters.

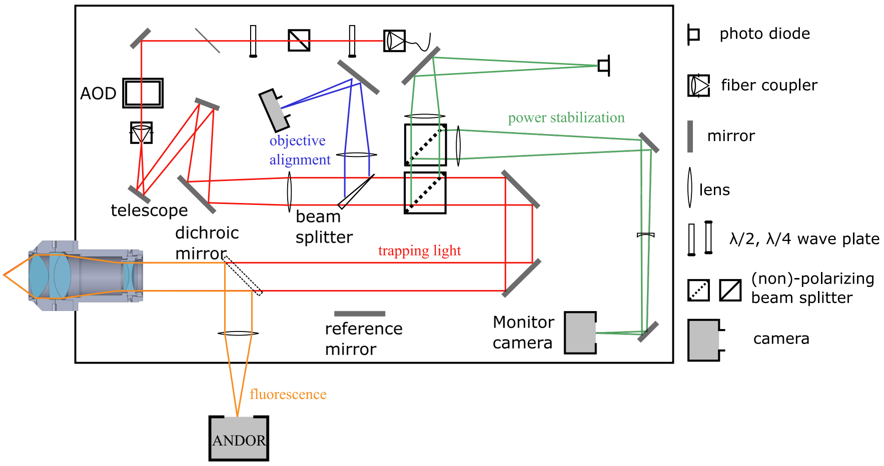

Figure 4.10: Current optical setup for generating multiple microtraps, adapted from [Ber17]. The stabilization path is shown in green.

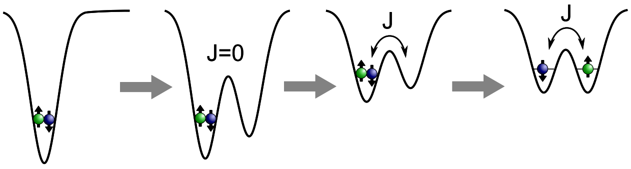

Figure 4.11: Double-well preparation scheme, adapted from [Ber17].

4.4.1 *Double Well*

For the double-well experiments, we want to transfer the state which we have prepared in a single microtrap to two microtraps. We do this with a scheme shown in Figure 4.11, where the atoms are non-interacting ($U = 0$). First, we turn on a second well which is slightly less deep than the first well which contains the atoms. In the beginning, the coupling between the wells is kept to $J \approx 0$. Consequently, the atoms remain in the ground state of the system, $|LL\rangle$, which is gapped by $\Delta \sim -\hbar\omega_{\text{trap}}/2$. Then, we couple the wells with typically $J/\hbar \approx 70\,\text{Hz}$ by reducing the overall depth of the potential. Now, we we can reduce $|\Delta|$ to zero by balancing both wells. If we do this slowly compared to $\hbar/J$, we end up with the ground state of the double-well system, $|a\rangle = \frac{1}{2}\left(|LL\rangle + |RL\rangle + |LR\rangle + |RR\rangle\right)$ (see eq. (7.6) and Figure 4.12).

We can apply a similar preparation procedure to prepare an excited state of the double well, namely state $|c\rangle$. Instead of the ground state, we initialize the system in the highest excited state (of the lowest band) by making the tilt Δ positive. As in the previous case, we then balance both wells. This state is interesting to study because its behavior is just the opposite of the ground state (see Section 7.2).

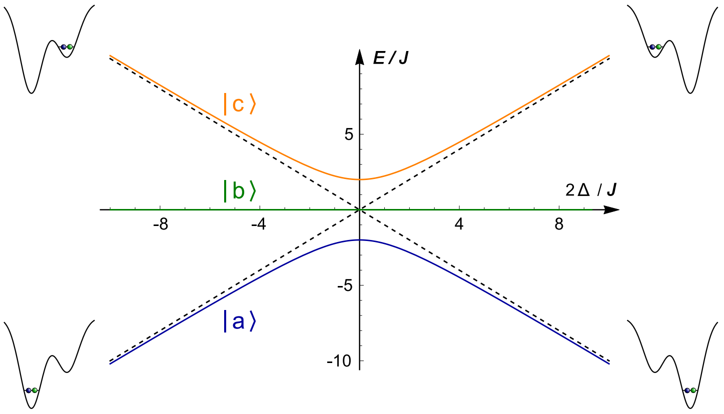

	$\Delta \to -\infty$	$\Delta = 0$	$\Delta \to +\infty$
$\lvert a\rangle$	$\lvert\uparrow\downarrow,\cdot\rangle$	$\frac{1}{2}\left(\lvert\uparrow\downarrow,\cdot\rangle + \lvert\uparrow,\downarrow\rangle + \lvert\downarrow,\uparrow\rangle + \lvert\cdot,\uparrow\downarrow\rangle\right)$	$\lvert\cdot,\uparrow\downarrow\rangle$
$\lvert b\rangle$	$\frac{1}{\sqrt{2}}\left(\lvert\uparrow,\downarrow\rangle + \lvert\downarrow,\uparrow\rangle\right)$	$\frac{1}{\sqrt{2}}\left(\lvert\uparrow\downarrow,\cdot\rangle + \lvert\cdot,\uparrow\downarrow\rangle\right)$	$\frac{1}{\sqrt{2}}\left(\lvert\uparrow,\downarrow\rangle + \lvert\downarrow,\uparrow\rangle\right)$
$\lvert c\rangle$	$\lvert\cdot,\uparrow\downarrow\rangle$	$\frac{1}{2}\left(\lvert\uparrow\downarrow,\cdot\rangle - \lvert\uparrow,\downarrow\rangle - \lvert\downarrow,\uparrow\rangle + \lvert\cdot,\uparrow\downarrow\rangle\right)$	$\lvert\uparrow\downarrow,\cdot\rangle$

Figure 4.12: Energy levels during the preparation of the double well, according to Hamiltonian (7.1). The table shows the eigenstates for different tilts Δ without interactions. The ground state of the balanced double well (see Section 7.1) is connected to the single-well state $\lvert\uparrow\downarrow,\cdot\rangle$ and gapped by at least $2J$. Adapted from [Mur⁺15b].

4.4.2 *Multiple Wells*

The double well introduced in the previous section may be seen as the fundamental building block of the Hubbard model. It has been proposed that larger Hubbard systems may be assembled out of such building blocks with very low entropy [Lub⁺11; Mat⁺01; Oje⁺16]. However, this is only possible if the energy gap during the preparation of such a system remains large enough and if one can control the individual sites sufficiently well. Therefore, we have theoretically examined the energy gap of a four-well system in [Mül16], which will briefly be presented here.

In all of the three studied cases, we starts from a configuration where two atoms each sit in each of the two energetically lower wells (Figure 4.13). The final state is the balanced four-well system, where $\delta = 0$. In all of the initial configurations, the lowest energy state is has an energy of -2Δ and is unique. The energy gap to the next-higher state is on the order of Δ, which may be arbitrarily large initially.

In the final state of the system, the energy gap is on the order of J. If the system is non-interacting, the energy gap is approximately $1.4\,J$, which is similar to the gap of $2\,J$ in the double-well system. When tuning Δ to zero, the energy gap in the system will monotonously evolve from initially Δ towards this minimal, final value. Since the initial and final states are very similar for all three configurations, this

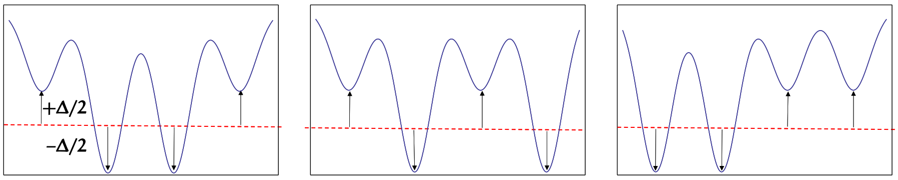

Figure 4.13: Three different four-well preparation schemes, where the wells are all tilted by the same amount $\pm\Delta/2$. From [Mül16].

behavior will appear in all three studied cases and the exact choice of configurations is not important. As the final energy gap is $\sim J$, the size of the energy gap should not be an obstacle for preparing a four-well system[5].

A prerequisite for these experiments is that the tilt can actually be controlled on these energy scales. Detrimental effects of an uncontrolled tilt can be seen in two ways. Firstly, tunneling experiments will have different effective tunneling rates $J_{\text{eff}} = \sqrt{J^2 + \Delta^2}$ depending on the tilt. For a typical trap depth of $40\,\text{kHz}$ and tunneling rate $J = 70\,\text{Hz}$, a relative drift of 10^{-3} in the tilt would already cause the effective tunneling rate to change by $15\,\%$. Secondly, also stationary states may be influenced by a tilt, especially when using attractive interactions $U/J \ll -1$. Here, the tilt would change the balanced, coherent state $|a\rangle \approx |\uparrow\downarrow, \cdot\rangle + |\cdot, \uparrow\downarrow\rangle$ to either $|\uparrow\downarrow, \cdot\rangle$ or $|\cdot, \uparrow\downarrow\rangle$ once $|\Delta| \gtrsim 4J^2/|U|$. These states are localized to a site and potentially obscure interesting non-local effects present in the balanced system.

There are two ways to address these issues: Increase the other energy scales of the system[6] J and U or reduce the undesired tilt.

4.5 INTENSITY STABILIZATION OF MULTIPLE MICROTRAPS

In the previous section we have demonstrated need to control the tilts Δ of our individual wells. Already for a intensity drift of 10^{-3} relative to the total intensity in a microtrap, the effects would be significant. In our double-well experiments, we relied on the passive stability of the balancing between our microtraps and observed two kinds of unwanted imbalance mechanisms.

One is a relatively fast ($\sim 400\,\text{ms}$) drift when we change the RF powers on the AOD. This drift is relatively deterministic and we compensated it with a feedforward in the double-well system. However, as we want to prepare systems with more microtraps and hence need more RF frequencies, this feedforward would become unpractical.

The other imbalance we observed as a gradual drift of the relative depth of our microtraps over the course of several days. The source

---

[5] It is worth noting that the gap in the balanced four-well system is largest for repulsive $U \approx 2J$.

[6] For attractive interactions, this means that one has to work at fields above the resonance (larger than B_0) to be able to reach sufficiently large scattering lengths.

of this drift has not yet been identified and we had to regularly recalibrate our double well to complete our experiments.

To be able to efficiently deal with both kinds of drifts, we wanted to find a way to actively control the intensities of the individual microtraps to a level of 10^{-4}. We identified two different approaches: One uses a downconverted optical signal of each microtrap to a different RF frequency. The challenge is then to precisely measure these RF intensities. The development of this method has just recently started and is still in progress.

The other method is based on direct imaging of the microtraps with a camera and will be presented in this section.

4.5.1 *Optical Setup and Camera*

To stabilize our microtraps in real-time, we have to detect them synchronized to the experiment cycle. We do this by splitting the trapping light into two branches, one which produces the actual microtraps and the other which we use for the stabilization of the microtraps (Figure 4.10). This light we split once more, which allows us to have an overall power stabilization with a photodiode and the stabilization with the camera in parallel[7]. In the camera branch, we then produce an image of the microtraps on with an $f = 250\,\mathrm{mm}$ and an $f = -50\,\mathrm{mm}$ lens.

The key requirement for this method is that the intensity measured on the sensor is proportional to the intensity in the actual microtraps. This means that the optical device splitting the beam paths must be chosen with great care, since the relative intensity fluctuations it introduces on the beams will, via the stabilization, lead to enhanced fluctuations of the intensity of the actual microtraps. For example, if the beamsplitter shows a dependence on the polarization for the splitting ratio, then noise on the polarization of the light will directly translate to intensity noise on the microtraps. From these considerations, together with the constraints on the clear aperture (at least $50\,\mathrm{mm}$) and space constraints on the breadboard[8], we decided to use two Edmund Optics non-polarizing beamsplitters (#49-006) for our stabilization optics.

Now we have to choose the optics for creating the microtrap pattern on the camera and the camera itself. As already mentioned we want to measure the intensities of the microtraps, i.e., a photon number. If, on average, N photons are generated by a coherent (uncorrelated)

---

[7] Even though, in the final setup, only one of the branches will be used for stabilization, it is very convenient to have an additional diagnostics setup.

[8] If it had been possible to have a beamsplitter under a small angle of incidence instead of 45° as proposed in [Hol17], then the polarization dependence would generically have been weak.

laser source, the shot-to-shot photon number n will follow a Poisson distribution $\frac{N^n e^{-N}}{n!}$ with a relative number fluctuation of

$$\frac{\sigma}{N} = \frac{1}{\sqrt{N}}. \tag{4.8}$$

This fundamental uncertainty on the photon number is called shot noise. It sets a lower threshold for how many photons we have to collect per microtrap per image for our desired $\sigma = 10^{-4}$, namely $N = \sigma^2 \approx 10^8$.

With a power of $P \approx 0.144\,\mathrm{mW/V} \cdot 0.4\,\mathrm{V} \approx 58\,\mu\mathrm{W}$, we have a flux of 3.1×10^{14} photons s^{-1} on the camera. However, we have to account for the finite quantum efficiency of the camera. For our wavelength of $\lambda = 1064\,\mathrm{nm}$, the quantum efficiency strongly depends on the semiconductor material used for the sensor. For InGaAs, quantum efficiencies of $QE_{\mathrm{InGaAs}}(1064\,\mathrm{nm}) \gtrsim 80\,\%$ can be reached. However, these sensors tend to have more thermal (dark) noise, so the camera must be actively cooled [And]. With on the order of 3×10^{14} photons at our disposal, we decided that we could also work with a Si-based camera that can be operated at room temperature, despite its quantum efficiency of only $QE_{\mathrm{Si}}(1064\,\mathrm{nm}) \approx 1\,\%$ [Fli].

Another aspect for choosing the correct camera is its frame rate. If we want to have a fast intensity feedback, we have to measure faster than the typical timescale in our system, which is in our case $J/\hbar \sim 100\,\mathrm{Hz}$. For photodiodes, where the entire sensor measures only a single value, bandwidths of $> 100\,\mathrm{MHz}$ are common. However, for cameras, every pixel has to be read out individually and the data has to be transferred to a computer, which often limits the frame rate. Still, especially when restricting the readout region on the sensor, frame rates up to 1 kHz are possible with commercially available cameras.

The fact that the readout region scales inversely with the readout rate means that we have to restrict the size of the focus on the sensor by choosing the correct magnification. Also, we still have to make sure that we are able to collect enough photons to avoid shot noise. Therefore, a large full-well depth per pixel is important. It specifies how many photo-electrons a pixel can hold and is different for every sensor[9]. It typically ranges from 5000 e⁻/pix to 100 000 e⁻/pix.

Keeping all these requirements in mind, we chose the compact CMOS camera Grasshopper3 (model GS3-U3-23S6M-C) from Point Grey (specifications in [Pg2]) for our stabilization setup. It has a full-well depth of 32 000 e⁻, which means that an area of $50 \times 50\,\mathrm{pix}^2$ can contain required number of $\sim 1 \times 10^8$ photoelectrons.

Combining this with the size of each pixel (5.86 µm), we can calculate the size of the focus. We need a magnification that is approximately 100 times larger than that of the objective, therefore, we would

---

[9] Roughly speaking, it depends on the volume of each pixel. Therefore, sensors with large pixels areas tend to have larger full-well depths.

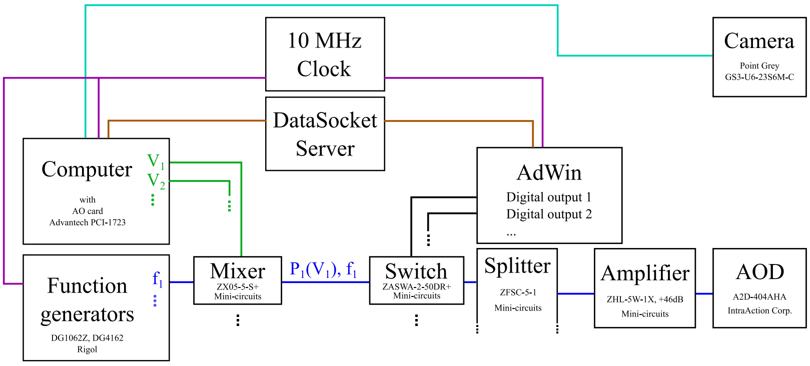

Figure 4.14: RF setup for generating multiple microtraps. The frequencies are generated by different output ports of a frequency generator. A DAC sets the mixers which control the signal power. The computer calculates the setpoint with data from the camera and from the real-time processor ADwin. The signals are combined with a splitter, amplified and sent to the AOD. All devices are synchronized with a clock.

have to use a lens with $f = 2000\,\mathrm{mm}$. As this is impractical, we shorten the length of the optical path by using a combination of an $f = 250\,\mathrm{mm}$ focusing and an $f = -50\,\mathrm{mm}$ defocusing lens, which gives us a Gaussian focus with $4\sigma \approx 15$ pixels.

4.5.2 *RF Setup*

To create multiple microtraps, we use an AOD (model A2D-404AH4 from IntraAction Corp.) to split our initial microtrap beam. The AOD is driven by an RF source between $25\,\mathrm{MHz}$ and $55\,\mathrm{MHz}$, where the frequency determines the position of the microtrap and the intensity determines the depth of the microtrap. We can modify the intensity directly at the RF source, however, with the current setup it is easier to control the intensity of each single frequency by applying a DC voltage to a mixer (Figure 4.14). These voltages we can generate with a 16-bit analog output card (Advantech PCI-1723). The card is installed in the computer which reads out the camera and generates the control values calculated by the feedback loop. After having set the intensities, the signals are then passed through a switch and combined using a 4-way splitter. The combined signal[10] is then amplified to $4\,W$ and sent to the AOD.

For the generation of up to four RF frequencies, we currently use two Rigol frequency generators. In the future, we may switch to an arbitrary waveform generator or to software-defined radio. We would then directly generate the superimposed RF signal with the correct frequencies, phases and amplitudes.

---

[10] One has to keep in mind that the splitter adds the amplitudes of every signal. If this happens in-phase, doubling the number of signals may quadruple the power.

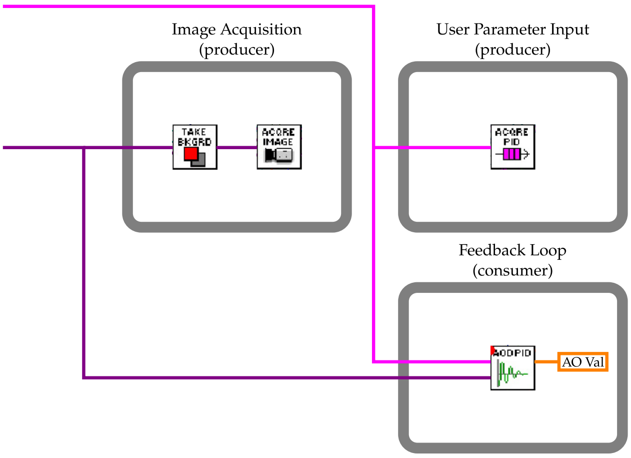

Figure 4.15: Simplified structure of the LabVIEW program for the intensity feedback. The gray boxes represent continuously running while-loops. In the upper row, an image stream of the intensity pattern and the PID parameters are acquired and queued (violet and magenta lines). The feedback sub-VI runs independently and evaluates these queued values with low latency (typically $< 100\,\mu s$) to calculate the control voltages for the mixers (orange).

4.5.3 *Feedback Software*

The feedback software runs on a computer which contains an analog-output (AO) card and is connected to the camera. It has to perform following tasks:

- Acquire images from camera and extract intensities.
- Read timing table from main experiment computer.
- Synchronize with the experiment.
- Acquire PID parameters.
- Run feedback loop.
- Switch between feedback and feedforward.
- Output the voltages for the mixers on the AO card.

The program has been implemented in LabVIEW in a producer-consumer structure (Figure 4.15). It acquires the images with regular IMAQ modules at the maximum frame rate of the camera and queues them. From the user interface, it acquires the PID parameters. Meanwhile, it listens to the datasocket server and downloads the timing table which has been uploaded from the experiment computer. When a trigger signal is received from the ADWin, it starts extracting the intensities from the images and passes those to a PID loop. The setpoints for the microtrap intensities are extracted from the timing table and continuously updated. The results from the PID loop are then output with the AO card.

4.5.4 *First Results*

Two major obstacles were encountered when we tested the intensity stabilization: First, the program currently runs on a computer with a Windows-OS. The operating system will schedule when tasks are executed, which means that the execution time may jitter by tens of µs. This problem was alleviated by declaring the VIs as subroutines and thus increasing their priority. Also, three cores were assigned exclusively to LabVIEW, leaving fewer tasks to disrupt the feedback program. In this way, the execution time was reduced to a median of 4 µs/cycle (160 µs/cycle at most). However, running the program in a real-time environment would be more reliable. Still, the execution of the feedback loop is fast enough compared with the frame rate of the camera (up to 1 kHz).

The other major problem was that the relative intensity noise that was observed was $\sim 10^{-3}$, which is much higher than the design goal of 10^{-4}. A possible reason is pointing noise on the microtrap beams, which leads to a position fluctuation of the microtraps on the camera. If the active region on the sensor is stationary, these position fluctuations will be converted into intensity noise of up to 10^{-2}. Because this problem has not yet been completely resolved, a reduction of the noise to the design goal has so far not been achieved.

In spite of these problems, we tested the stabilization in the experiment. First, we calibrated the heating rates with the feedback turned off (only feedforward for intensity jumps) by measuring the loss rate of two atoms in the microtrap. The observed losses were on a timescale of 12 s. Also, we performed tunneling experiments between two wells, first without active feedback from the camera. We observed coherent oscillations with a contrast up to 90 %, however, they decayed by more then 10 % after only 3 periods[11]. With the feedback active, the contrast of the coherent oscillations was limited to approximately only 50 %.

To summarize, the feedforward feature of the stabilization setup works well and is able to compensate the intensity jumps caused by a change in RF power. However, we will require an optimized version of the feedback with less intensity noise to be able to fully use it for multiple-well experiments. For the remainder of this thesis, only the total intensity of the microtraps was stabilized with a photodiode, while relying on passive stability for the relative depths of the microtraps.

---

[11] This may be due to the intensity noise of the stabilization setup, however, at a later point, we observed a similar decoherence using only passive relative stabilization. This suggests that part of the decoherence has a different source.

5

SINGLE-ATOM DETECTION

As we have seen in Chapter 2, many-body quantum states can be described with the occupation numbers of single-particle modes. What kind of modes are suited to describe the system depends on the specific implementation. Often, the modes are described by their spatial or momentum coordinates state, by their energy state, or by an internal state.

In our experiment, we prepare small systems of ^{6}Li atoms, typically up to 10 in total, in a spatial array of microtraps. The atoms are in two of the lowest three ^{6}Li hyperfine states which we can identify as (pseudo-)spin modes. Because we are considering systems where the potential has a spatial structure, we can extract information about its state by measuring the occupation and coherence of the spatial modes. As the spin configuration of the system may also matter, we must be able to distinguish the internal states of the atoms.

The imaging technique which we used in our original experiments was developed to reliably detect the total atom number in the system in a MOT. By manipulating our system prior to detecting the atoms in the MOT, it was also possible to use this imaging technique to measure mode occupation. For example, for a double-well system, we could release the atoms from one site (spatial mode) to measure the occupation of the other site (see Chapter 7).

However, this imaging method has a severe limitation: To describe a many-body system in many modes, we had to measure many repetitions of the experiment to gather statistics for every mode individually. To extract this information more efficiently, we needed an imaging technique which was able to detect the occupation of all modes at the same time for both spin states in each single image. Keeping the double well as an example, it should hence be able to measure the number of both spins states in both wells simultaneously.

With our new imaging scheme [Bec16; Ber17], we can spatially- and spin-resolve atom distributions with single-atom sensitivity. Briefly explained, it works as follows; in an optional first step, we can release the atoms from their initial potential and let them expand in time-of-flight. We illuminate the resulting atom distribution with short, resonant light pulses, and focus the scattered light with a high-NA objective on an electron-multiplying CCD (EMCCD) camera, recording the spatial information of the atoms in one hyperfine state. We then quickly repeat this procedure on the same sample for the other hyperfine state.

In this chapter, we will first briefly summarize how our MOT imaging works, as it is still important for calibrating the experiment. Then, we will describe how the different requirements (detection efficiency, spatial resolution, etc.) have influenced the implementation of our new imaging technique. We will also present several ways of how to use the new imaging to obtain different, complementary information about our systems.

5.1 DETECTION IN A MAGNETO-OPTICAL TRAP

Our original imaging method works by recapturing the atoms from the microtrap in a MOT and counting the number of scattered photons on a camera [Ott10; Ser11; Ser⁺11]. For dilute samples, the recorded intensity of the MOT is proportional to the number of atoms it contains. For sufficiently long exposures (typically 1 s), the strength of the fluorescence signal varies very little[1], allowing us to resolve the atom number up to 10 with a certainty exceeding 98 % [Ser11]. Combining this with the losses during transfer and in the MOT, we can count atoms with approximately 97 % fidelity.

This method provided us with a reliable way for counting the total number of atoms and has also been adapted to extract information about the mode occupation from the studied systems. This is typically done by manipulating the system of microtraps in different ways prior to transferring into the MOT: The number of atoms per energetic mode can be inferred from performing spills to different trap levels prior to detection. The number of atoms per spatial mode can be measured by turning off all but one microtrap before transfer into the MOT [Mur⁺15b; Mur15]. The number of particles in hyperfine state $|2\rangle$ can be obtained by performing an additional spill at 27 G, where it has zero magnetic moment and thus remains unaffected by the magnetic field gradient (see Figure 4.2a). The symmetry of the state can be inferred from the ground state occupation: The spatially symmetric two-particle state will occupy only the single-particle ground state of the microtrap, while the spatially antisymmetric state also occupies the first excited single-particle level (see Chapter 7 for more details).

As one can see from these examples, imaging with the MOT makes it possible to measure a diverse set of quantities. However, once one has decided which quantity one wants to measure, the occupation of each of the modes has to be measured one at a time. This means that the number of measurements required to characterize a system scales with the number of modes. Also, it is difficult to directly detect correlations between modes with this imaging method. For these reasons, we developed a new imaging scheme, which focuses on an improved spatial detection of the atoms.

---

[1] The relative fluctuation σ_N of the detected number of photons N is $\sigma_N/N = N^{-\frac{1}{2}}$ for random scattering through spontaneous emission.

5.2 SPATIAL RESOLUTION

Improved spatial resolution is one of the key features of our new imaging scheme. However, several limitations apply to it: There is an optical resolution limit, which depends on the optical setup of the imaging system. But in our experiment, mainly the back-action of our imaging light on our sample limits our spatial resolution. The fundamental problem is that the recoil momentum that an atom receives from a photon will lead to a random motion, or to heating if the atom is trapped during imaging. As this process happens hundreds or thousands of times during the acquisition of a single image, the path of the atom will be integrated on each image and can lead to significantly degraded position information. I will present two recent approaches how to overcome this problem, the *quantum gas microscope* (see [Bak⁺09] for bosonic atoms, and [Par⁺15; Che⁺15; Hal⁺15] for fermionic atoms), and our approach, the *matterwave microscope* (see [Büc⁺09] for a similar method).

5.2.1 *Optical Resolution Limit*

The most intuitive limitation of the resolving power of an optical setup is the diffraction limit: it is not possible to directly resolve structures which are smaller than the wavelength λ of the light that one uses for imaging. Furthermore, the resolution also depends on the numerical aperture (NA) of the imaging optics, which leads to the Abbe limit for the smallest resolvable structure size:

$$d = \frac{\lambda}{2\mathrm{NA}} = \frac{\lambda/n}{2\sin\theta}, \tag{5.1}$$

where n is the refractive index of the medium and θ the half opening angle of the objective[2]. For our system (Figures 4.10 and 5.1), the theoretical Abbe limit (in absence of imaging aberrations) is $\frac{671\,\mathrm{nm}}{2\times 0.6} = 0.68\,\mu\mathrm{m}$.

Another way of understanding Abbe's limit is through the point spread function (PSF) of an imaging system. The PSF describes how an optical system images a perfect, pointlike source: different spatial frequencies will be transmitted with different efficiencies through the system, leading to a smeared out spot instead of a perfect point in the imaging plane. This can be understood as a convolution of the PSF characteristic to the optical system with the object being imaged. The Abbe limit marks the highest spatial frequency which is transmitted, i.e., the frequency where the Fourier transform of the PSF (optical transfer function) vanishes.

---

[2] There are ways to overcome Abbe's limit, often referred to as super-resolution imaging [SHL10; YSF14].

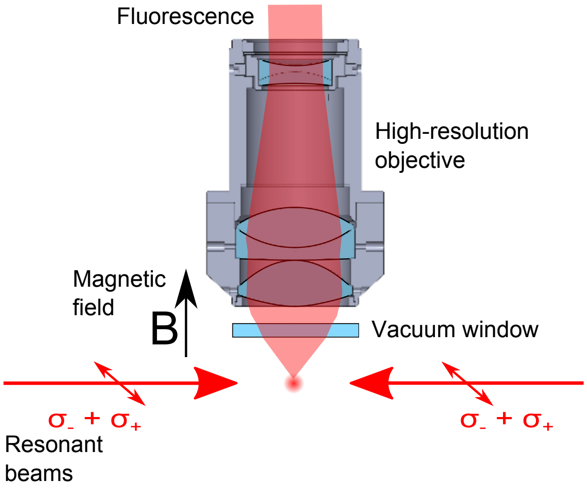

Figure 5.1: Schematic of the detection of fluorescence with the imaging setup. The atoms are illuminated with alternating, counter-propagating light pulses. The emitted fluorescence which is collected by the objective is shaded in red. From [Ber17]

In practice, imperfections and aberrations in the optics will prevent the imaging system from reaching the theoretical diffraction limit. Phase shifts in the wavefront corresponding to less than a wavelength will already deteriorate the quality of the PSF. A detailed simulation has been performed in [Ser11] to take these possible aberrations into account when we designed our objective. The resolution of the real objective we use in our experiment amounts to $0.9\,\mu\mathrm{m}$ at a wavelength of $671\,\mathrm{nm}$.

5.2.2 *Quantum Gas Microscopes*

Apart from the resolution limits of the optical setup, random motion of the atom while it scatters photons also limits the ability to determine its position precisely. One of the most straight-forward ways to reduce this motion is to use atoms with a larger mass, as the recoil velocity $v_{\mathrm{rec}} = \hbar k_{\mathrm{photon}}/m_{\mathrm{atom}}$ of the atoms depends inversely on its mass. However, this quantity is fixed by the element that is used in the experiment, and cannot be easily changed.

Alternatively, we can restrict the motion of the atom by pinning it in an optical standing-wave lattice. As the lattice site spacing is typically similar to the resolution limit of the imaging system, the position of the atoms has to be determined very precisely to be able to distinguish the individual lattice sites. Therefore, a large number of photons has to be collected per atom (typically 750 to 1000 [Bak+09]) in order to reconstruct the PSF with sufficiently low noise. For this, the atom typically scatters between 5000 and 20 000 photons, because only a fraction of the scattered photons is collected by the imaging system.

If the atom is confined to a lattice site during imaging, the recoil of the scattered photons will not lead to random motion, but rather to heating of the atom to on average higher motionally excited states of its lattice site. Eventually, it will have obtained enough much energy to start tunneling and move between lattice sites. This can be suppressed by cooling the atom back to the ground state of its lattice site during imaging. Over the past two years, the combined trapping, cooling, and imaging technique in a lattice, called *quantum gas microscope*, has been implemented for fermionic atoms, for example by [Par+15; Che+15; Hal+15], allowing for the first direct observations of antiferromagnetic order [Par+16] and more detailed studies of the 2D Hubbard model.

While this approach has been very successful, it also poses some restrictions to what information can be gathered from a system. For example, it is difficult to combine this method with having spin resolution at the same time. Also, the high density on the lattice sites lead to photo-association losses when multiple atoms occupy the same lattice site. The method is also challenging to implement, as one needs very powerful trapping lasers as well as multiple lasers for cooling the atoms, which greatly increases the complexity of the experiment. Therefore, we developed a different approach for spatially- and spin-resolved imaging.

5.2.3 *Matterwave Microscope*

Let us first consider one key difference of our system to quantum gas microscopes: we perform our experiments with a variable array of microtraps which are separated by typically 1.5 µm. This spacing is much larger than the lattice spacing of the quantum gas microscope experiments. The larger separation of the atoms gives us less strict bounds on the size and accuracy of the PSF. Therefore, we need to collect fewer photons per atom and image to reconstruct the PSF with sufficient accuracy. In turn, this leads to less heating or random motion. Still, we need to collect a minimum number of photons per atoms to discern it from the noise floor of our camera. With our EMCCD camera (Andor iXon DV887) and imaging scheme (explained in more detail in Section 5.6), we only have to detect only approximately 10 photons per atom to be able to detect it. This number should be understood as an estimate for a lower threshold: For fewer photons than this number, we will not be able to identify the atom reliably.

As our imaging setup combined with our camera effectively detects about 9 % of all the scattered photons [Ber17], the atom should scatter at least ~ 100 photons to produce a sufficiently clear signal on the camera. However, because the scattering of light is a random process, the photon number distribution is Poissonian, and the atom may scatter more or fewer photons than the average value. To ensure that we (almost) always detect more photons than our threshold, each atom typically has to scatter 300 photons on average. Nevertheless, this number of photons is an order of magnitude lower compared to the quantum gas microscopes. In the experiment, the atoms are exposed for $20\,\mu s$ at an intensity of $I/I_{sat} \approx 8$ (16.5 photons μs^{-1}) to scatter the required number of photons.

The relatively small number of scattered photons allows us to image the atoms without cooling them or pinning them in the microtraps. Still, the position that we measure strongly depends on the random motion of the atom induced by the photon recoil[3] $v_{rec} = 10\,cm/s$ (see Table 4.1).

The process of scattering a photon can be divided in two contributions: the momentum the atom gains when absorbing a photon and the recoil momentum it receives when emitting a photon. If the atom always absorbs photons from the same imaging beam, it will accumulate a net momentum, similar to the process in a Zeeman slower. Therefore, we use two counter-propagating beams for imaging (Figure 5.1). In order to avoid a standing-wave intensity pattern on the imaging light, we use alternating $200\,ns$ pulses generated by switching the imaging light with two AOMs (Figure 5.2). The duration of the pulses is chosen to be comparable to the lifetime of the excited state $\tau = 27\,ns$ and short compared to the total imaging time of $20\,\mu s$, which ensures that, in the duration of one single pulse, the net momentum transfer remains negligible.

In contrast to the absorption process, the spontaneous emission process will emit photons in random directions, following the dipole radiation pattern of the optical transition. These random recoils result in a random walk[4]. It leads to a diffusion of the atom in all spatial directions, which increases the apparent width of its position distribution during the imaging process.

This diffusion process is the main contributor to uncertainty in determining the position of an atom. With an illumination time of $20\,\mu s$, we measured a standard deviation of $\sigma_{img} = 5.7\,\mu m$ for the average atom distribution. Even though the width of every individual event is smaller and also its center position can be determined more accurately, we can only infer the initial position of the atom up to $\sigma_{img} \approx 4\,\mu m$. Hence, we cannot use this imaging method to directly resolve the different sites of our system separated by just $1.5\,\mu m$.

---

[3] If we image the atom immediatly after releasing it from the microtrap, its initial momentum is negligible. However, we will exploit this momentum in the next section for our time-of-flight measurements.

[4] The effect of the photon recoil can be mitigated by molasses cooling, but cannot be completely avoided.

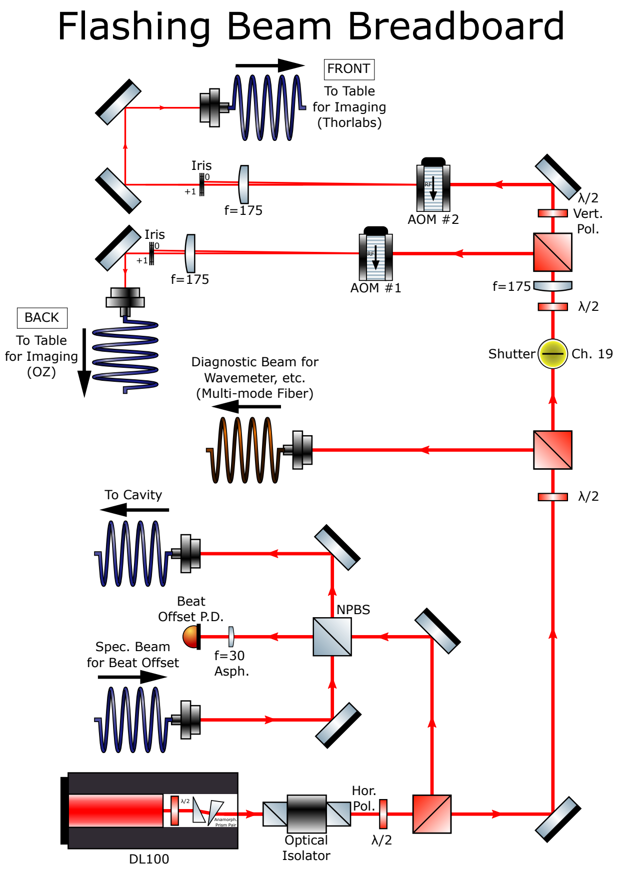

Figure 5.2: Flashing beam setup for imaging. The top two branches are focused through AOMs for fast switching. The middle two branches are for diagnostics, and the lower two branches are for the beat offset lock. From [Nie17].

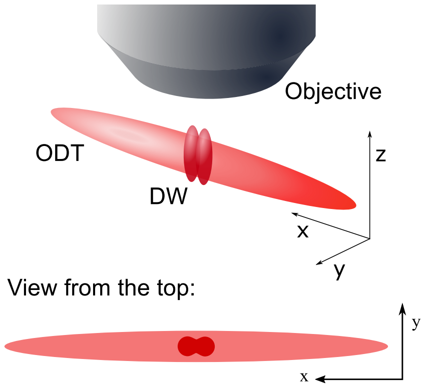

Figure 5.3: Imaging with an ODT, adapted from [Ber17]. The orientation of the double well system is labeled as DW.

5.3 MOMENTUM IMAGING

A way to circumvent the resolution limitation described in the last section is to not image the system we wish to study directly, but to map it to a system with a larger spatial extent in a well-defined manner, first. We do this by letting the atoms expand in time-of-flight, not unlike the procedure described in [Büc+09]. Combined with our highly sensitive fluorescence imaging, the positions determined with this method can give us momentum or position information of each atom in our initial system, depending on the exact mapping that we choose.

The crucial advantage is that, due to the expansion, we image an atom distribution which has a size of $\sim 100\,\mu\mathrm{m}$. This is large enough that even our free-space imaging with its limited resolution can still give us useful position information. However, we have to ensure that the atoms expand only within the focal plane: Even though the objective has a field of view of $200\,\mu\mathrm{m}$ where its imaging performance is diffraction-limited, it will only produce sharp images within its depth of field [IO94]

$$d_{\mathrm{DoF}} = \frac{\lambda n}{\mathrm{NA}^2} + \frac{n}{\mathrm{NA}}\frac{e}{M} \tag{5.2}$$

along the optical axis. The first term comes from the behavior of the electric field around the focus, and corresponds to half the distance to the first intensity minimum along the optical axis. The second term is of geometric nature, and is related to the largest circle of confusion which will still be detected as a point on the camera. Using the camera resolution $e = 16\,\mu\mathrm{m}$ and the magnification $M \approx 6$, we obtain $d_{\mathrm{DoF}} \approx 7\,\mu\mathrm{m}$. The expansion of the atoms along the optical axis has to remain smaller than this value for optimal spatial resolution.

One method is to release the atoms into a potential which confines them along the optical axis instead of releasing them into free space.

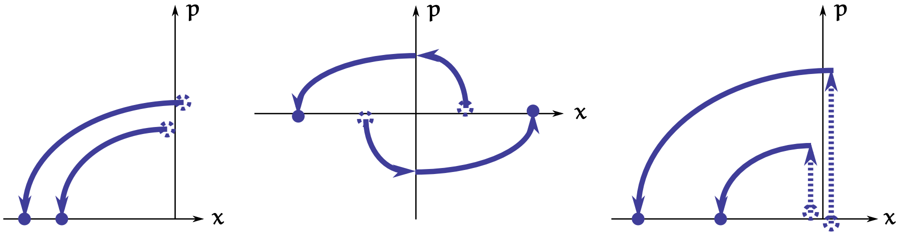

Figure 5.4: Phase space diagrams for momentum and in-situ imaging. The empty circles show the initial positions, the filled circles the final positions of two atoms. The solid arrows represent the expansion in the ODT potential, the dotted arrows represent other matter-wave operations. The left panel shows the momentum mapping of two particles after T/4. The middle panel shows the position mapping if the trapping frequency is changed at T/4 during the expansion, leading to a magnification of the initial system. The right panel shows position mapping after T/4, if the positions have been mapped to momenta prior to the expansion in the ODT.

For example, we can use our optical dipole trap for this purpose (Figure 5.3), or, after a future upgrade of the experiment, a pancake trap similar to [Rie$^+$15].

If we release an atom into the ODT, in the classical picture, it starts oscillating along the three axes of the ODT:

$$x_i(t) = x_{0,i}\cos(\omega_{i,\mathrm{ODT}}t) + \frac{p_{0,i}}{m\omega_{i,\mathrm{ODT}}}\sin(\omega_{i,\mathrm{ODT}}t), \tag{5.3}$$

where $i = x, y, z$ stands for the axis of the ODT, $\omega_{i,\mathrm{ODT}}$ for the according trap frequencies[5] and p_0, x_0 for the initial momentum and position, respectively. If we assume that the initial position is near the center of the ODT ($x_{0,i} \approx 0$) where the potential is approximately harmonic, we see that $x(t)$ becomes largest at the turning point for $\tau_i = T_i/4 = \pi/(2\omega_i)$. Incidentally, the position at this time is an exact map of the momentum the particle had had initially, $p_{0,i} = m\omega_i x_i(T/4)$, and is independent of its starting position (Figure 5.4). This understanding can be applied in the framework of quantum mechanics, replacing the position and momentum coordinates with the respective field operators [Mur$^+$14].

We can now estimate whether the ODT can confine the atom to the focal plane during expansion. For typical parameters, we see that the ground state momentum wavefunction in the microtrap along the imaging axis has a standard deviation of $\sigma_{p_z}(t=0) = \frac{\hbar}{l_{z,\mathrm{MT}}}$ with the

---

[5] Typical values are $T_x = 2\pi/\omega_{x,\mathrm{ODT}} \approx 16\,\mathrm{ms}$ and $\omega_{y,\mathrm{ODT}} \approx \omega_{z,\mathrm{ODT}} \approx 8\omega_{x,\mathrm{ODT}}$.

harmonic oscillator length $l_{z,\mathrm{MT}} = 0.53\,\mu\mathrm{m}$. The maximum position width of the wavefunction during expansion in the ODT is then

$$\sigma_z(T/4) = \frac{\sigma_{p_z}(0)}{m\omega_{z,\mathrm{ODT}}} = \frac{l_{z,\mathrm{ODT}}}{l_{z,\mathrm{MT}}}\, l_{z,\mathrm{ODT}} \approx 5.8\,\mu\mathrm{m}, \tag{5.4}$$

using $l_{z,\mathrm{ODT}} \approx 1.8\,\mu\mathrm{m}$. This value is smaller than the depth of field of our objective (5.2) and can be adjusted by changing the depth of the ODT or of the microtrap.

We have can use the expansion of atoms prior to imaging in two different ways. For the first method, we leave the ODT on during the entire time of the expansion ($T/4$-*method*). When the atoms reach the turning along the x-axis, they will have performed many oscillations along the other two axes. If the interactions during expansion are negligible and the ODT is described by a three-dimensional harmonic oscillator, the three coordinates are decoupled and the dynamics along the y and z-direction do not influence the outcome along the x-axis. By integrating out the z-axis due to the imaging procedure and the y-axis during the data evaluation, we can use this method to determine the initial x-momentum distribution of the atoms:

$$p_x(0) = m\omega_{x,\mathrm{ODT}}\, x(T/4) \tag{5.5}$$

We have to be careful, however, when using this imaging technique for strongly interacting systems. If we want to avoid the refocusing of the atoms along the y and z-axes during the expansion, we turn on the ODT only for the first $T_z/4 \approx 445\,\mu\mathrm{s}$ at the beginning of the expansion and turn it off for the rest of the expansion (similar to [Rie+15]). This means that we maximize the spread of the atoms along the z-axis, and, in our case, also along the y-axis (since $\omega_{z,\mathrm{ODT}} \approx \omega_{y,\mathrm{ODT}}$), minimizing their density and the effects of interactions. Also, their momentum spread (i.e., dispersion) along these axes will be minimal, namely

$$\sigma_{p_z}(T_z/4) = -m\omega_{z,\mathrm{ODT}}\sigma_z(0) = -\sigma_{p_z}(0)\,\frac{\omega_{z,\mathrm{ODT}}}{\omega_{z,\mathrm{MT}}}. \tag{5.6}$$

In our experiment, this means that the wavefunction spreads along the z-axis at only one tenth of its initial velocity, which is why we call this procedure the *brake pulse method*. We can ensure that this spread remains smaller than the depth of field,

$$\frac{\sigma_{p_z}(T_z/4)}{m}\, t_{\mathrm{exp}} = 2\pi\, l_{z,\mathrm{MT}} \frac{t_{\mathrm{exp}}}{T_z} < d_{\mathrm{DoF}}, \tag{5.7}$$

if we choose the expansion time t_{exp} sufficiently short. For typical values, this amounts to $t_{\mathrm{exp}} < 3.7\,\mathrm{ms}$. We compensate center-of-mass momenta caused by initial displacements $z_0 \neq 0$ by applying a weak gradient of ca. $2\,\mathrm{G\,cm^{-1}}$ during the entire expansion.

The position along the x-axis will be an approximate mapping of the initial momentum,

$$p_x(0) = \frac{m\,x(t_{\mathrm{exp}})}{t_{\mathrm{exp}}}, \tag{5.8}$$

as long as the system after expansion is large compared to the initial system,

$$t_{\mathrm{exp}} \gg \frac{x_{\mathrm{init}}}{\hbar\omega_{x,\mathrm{MT}}/m} \approx \frac{x_{\mathrm{init}}}{45\,\mathrm{\mu m\,ms^{-1}}}. \tag{5.9}$$

x_{init} denotes the typical length scale of the initial system, for example, the harmonic oscillator length along x of the microtrap, the separation of the microtraps, or the displacement of the microtrap from the center of the ODT.

With these two methods, we can determine the initial momentum in the system with a resolution of

$$\frac{\Delta p_x}{p_x} = \frac{\sigma_{\mathrm{img}}}{x(t_{\mathrm{exp}})}, \tag{5.10}$$

which is typically smaller than 0.04.

5.4 IN-SITU IMAGING

The momentum imaging technique can also be adapted to perform position imaging, enabling us to take in-situ data of our systems. The most straight-forward way is with a two-step expansion. First, the atoms expand for $T_1/4$ in a deep trap with a trap frequency ω_1, which maps their initial positions to momenta. Next, the depth of the trap is reduced to ω_2. Due to the large momenta of the atoms, their displacement after $T_2/4$ is proportional to their initial positions,

$$x((T_1 + T_2)/4) = -\frac{\omega_1}{\omega_2} x_0, \tag{5.11}$$

where ω_1/ω_2 acts as a magnification (Figure 5.4). The problem with this method is that we do not use harmonic potentials, but Gaussian potentials with a finite depth. This means that, if we make the first trap too deep, the atoms will gain too much momentum to be bound by the second trap.

However, we can achieve similar behavior with a different method. The mechanism that is essential to our magnification scheme is the unambiguous mapping of initial position to momentum in the first step. Instead of implementing this using the dipole trap potential, we displace the microtraps non-adiabatically by different amounts, which gives the atoms in each well an individual momentum kick. We then image these momentum kicks with our established momentum imaging technique as displacements, mapping the final spatial distribution back to the in-situ distribution.

5.5 SPIN RESOLUTION AND PHOTON NUMBER

An important feature of our imaging technique is its ability to distinguish the different hyperfine states $|1\rangle$, $|2\rangle$, and $|3\rangle$ in a single image. To address the hyperfine states individually, we use σ^--light to excite the atoms while applying a large magnetic field $B > 500\,\mathrm{G}$. Due to the Zeeman effect, the hyperfine states are separated by $\delta \approx 80\,\mathrm{MHz}$ (see Section 4.1), hence the light can be tuned to resonance for one of the hyperfine states while being off-resonant for the others. From equation (4.3), we see that off-resonant scattering is suppressed quadratically when the linewidth of the laser is narrow enough and its intensity is low enough. For typical intensities of $I/I_{\mathrm{sat}} \approx 8.5$, we reach $\Gamma_{\text{off-res}} \approx 1.1 \times 10^{-2}\,\Gamma/2$ for $\delta = 80\,\mathrm{MHz}$ (between states $|1\rangle$ and $|2\rangle$, and $|2\rangle$ and $|3\rangle$) and $\Gamma_{\text{off-res}} \approx 2.8\,10^{-3}\,\Gamma/2$ for $\delta = 160\,\mathrm{MHz}$ (between states $|1\rangle$ and $|3\rangle$).

5.5.1 *Photon Scattering Process*

To ensure that the hyperfine states do not mix during imaging, we have to look at their decomposition in the $|m_J, m_I\rangle$-basis as in eq. (4.1). The resonant σ^--photons alter the electronic quantum number by $\Delta m_J = -1$, but leave the nuclear spin quantum numbers I, m_I unchanged. During the emission process, the atom is transferred back to a $m_J = -1/2$ ground state, but we see that different hyperfine states can have an admixture of the same m_I, m_J-state. This leads to a branching ratio during emission, i.e., the excited state may decay with a certain probability to one of two ground hyperfine states. Atoms that decay to a hyperfine state which is different from their initial state will not be resonant anymore with the imaging light and become dark. It is therefore crucial that the branching ratio remains small during imaging.

This is the case for large magnetic fields, where the coupling between electronic and nuclear magnetic moments becomes small and the eigenstates consist mostly of one basis state. The admixture of the other basis state can be calculated with the mixing angles from eq. (4.1) [Geh03a]. For 527 G, the resulting branching ratios after one scattering event are

$$\begin{aligned} p_{BR}(|1\rangle \rightarrow |5\rangle\,, 527\,\mathrm{G}) &= 0.47\,\% \\ p_{BR}(|2\rangle \rightarrow |4\rangle\,, 527\,\mathrm{G}) &= 0.58\,\%. \end{aligned} \tag{5.12}$$

This may sound like a small number, but we have to keep in mind that each atom has to scatter $N_{ph} \sim 300$ photons[6]. The number of photons that an atom scatters N_{sc} before it becomes dark is described by the geometric distribution. The case that the atom has not entered the dark state after N_{ph} scattering events is described by a delta distribution at $N_{sc} = N_{ph}$. The combined distribution looks as follows:

$$p(N_{sc}) = \begin{cases} p_{BR}(1-p_{BR})^{N_{sc}} & \text{for } 0 \leqslant N_{sc} < N_{ph} \\ (1-p_{BR})^{N_{sc}} & \text{for } N_{sc} = N_{ph} \\ 0 & \text{for } N_{sc} > N_{ph} \end{cases} \tag{5.13}$$

The photon number that is actually detected N_{det} is sampled from this distribution with a probability of $p_{det} = 8.7\,\%$. This process is described by the binomial distribution $\mathcal{B}(N_{det}; N_{sc}, p_{det})$, which yields the probability of detecting N_{det} out of N_{sc} photons. The total number distribution for detected photons can be obtained by convolving distribution (5.13) with $\mathcal{B}(N_{det}; N_{sc}, p_{det})$, which results in

$$\begin{aligned} \mathcal{P}(N_{det}) = &\sum_{k=0}^{N_{sc}-1} p_{BR}\,(1-p_{BR})^{k}\,\mathcal{B}(N_{det}; k, p_{det}) \\ &+ (1-p_{BR})^{N_{ph}}\,\mathcal{B}(N_{det}; N_{ph}, p_{det}). \end{aligned} \tag{5.14}$$

For a closed transition, e.g., $|3\rangle \rightarrow |3'\rangle \rightarrow |3\rangle$ with a branching ratio $p_{BR}(|3\rangle \rightarrow |i\rangle\,, 527\,\mathrm{G}) = \delta_{3,i}$, only the second term of the sum remains, resulting in a binomial distribution with a mean value of $N_{sc}\,p_{det}$. The first term, which is important in the case of an open transition with $p_{BR} > 0$, results in a tail towards lower photon numbers as can be seen in Figure 5.5.

In order to optimize our imaging procedure, we must understand how we can influence the parameters of the photon number distribution. We can change the branching ratio by changing the magnetic field and the photon number N_{ph} by changing the duration or intensity of the imaging light pulse, while the detection efficiency is fixed by our optical setup. Also, we must identify a figure of merit $\mathcal{D}$ which relates our imaging performance to the detection fidelity of an atom. We choose the probability for detecting at least a threshold number of

---

[6] This is an average number, however, it is a good approximation to use for the following calculation.

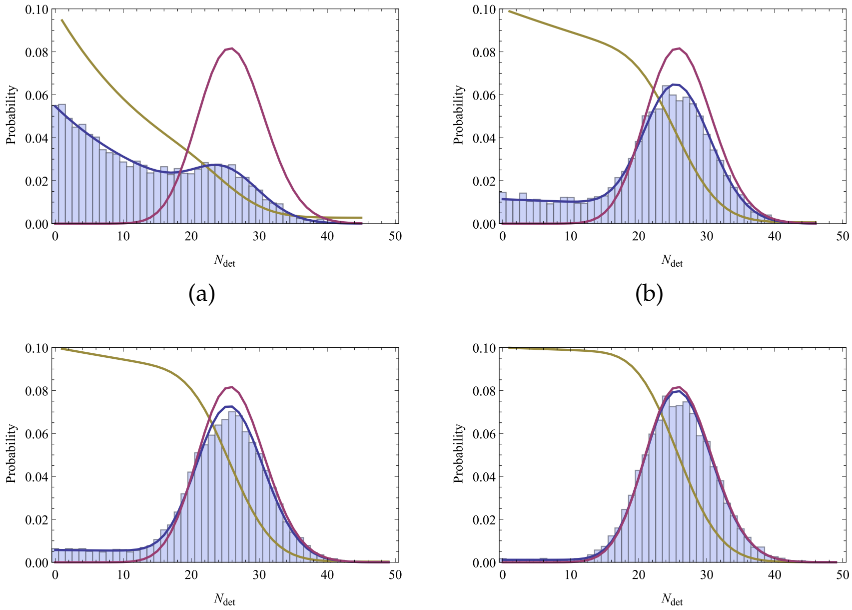

(a) (b)

(c) (d)

Figure 5.5: Numerical simulation of the detected photon numbers from an open transition for (bars), for $N_{\text{ph}} = 300$, $p_{\text{det}} = 8.7\,\%$, and $p_{\text{BR}} = 0.5\,\%, 0.1\,\%, 0.05\,\%$, and $0.01\,\%$ (a, b, c, and d, respectively). The histogram is normalized and contains 10000 trials. The blue lines show the distribution according to eq. (5.14), the red lines show the distribution $\mathcal{B}(N_{\text{det}}; N_{\text{ph}}, p_{\text{det}})$ for a closed transition, and the yellow line shows $1 - \text{CDF}(N_{\text{det}})$ for the cumulative distribution function of eq. (5.14), which corresponds to the fraction of events above a threshold of N_{det} (scaled by 0.1 for display purpose).

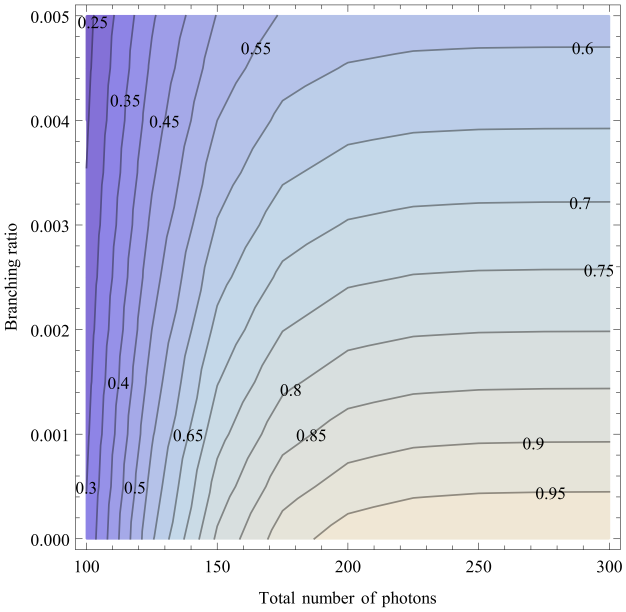

Figure 5.6: Probability of detecting 10 or more photons for different branching ratios and total photon numbers.

photons $N_{th} = 10$ scattered per atom. The exact choice of this number strongly depends on the performance of the camera and the image post-processing (see Sections 5.6 and 5.7).

We can calculate our figure of merit by integrating the probability distribution, $\mathcal{D} = \sum_{k \geqslant N_{th}} \mathcal{P}(k)$. For finite branching ratios, it saturates well below one even for large N_{ph} (Figure 5.6). Therefore, the only way of improving $\mathcal{D}$ is to reduce the branching ratio, that means, image at as high magnetic fields as possible. In our experiment, we typically choose a magnetic field of 900 G whenever possible, leading to branching ratios of less than 0.2 % for the $|1\rangle$ and $|2\rangle$ states, and $\mathcal{D} \approx 80\,\%$.

Currently, we are also working on a different scheme for increasing the number of detected photons. By using a second laser which is resonant to the ground states in the upper m_F-manifold, we can image the atoms in states $|1\rangle$ and $|5\rangle$ or $|2\rangle$ and $|4\rangle$ simultaneously, eliminating the dark states. To avoid mixing the states and reduce off-resonant scattering, we use the transitions to the $m_F = -3/2$ and $m_F = 3/2$ excited-state manifolds, respectively, for this imaging scheme.

5.5.2 *Rapid Spin-Resolved Imaging*

Now that we have established that we can image the hyperfine states individually, we also want image them in a single image. We do this by imaging each of the hyperfine states on a different region of the camera sensor. As this is a sequential process, and we must ensure

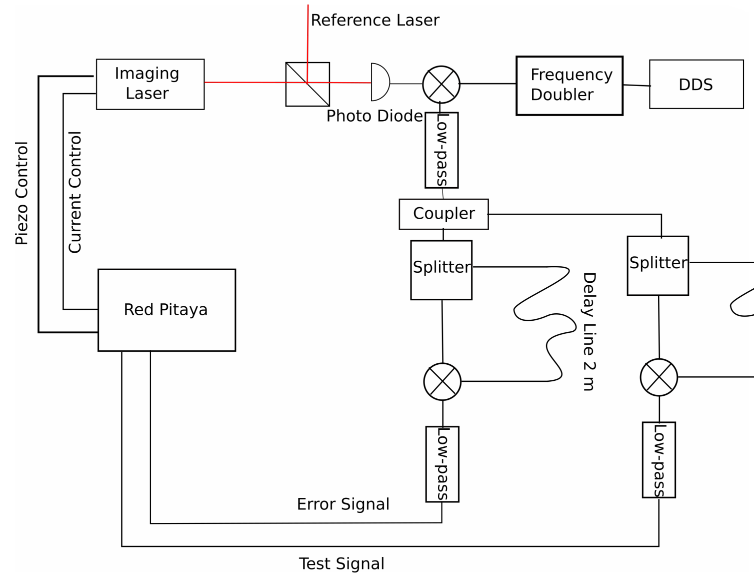

Figure 5.7: Schematic of the laser lock of the imaging laser. The RF setup of the beat lock is shown on the right. The Red Pitaya microprocessor runs a feedback loop on the piezo voltage and diode current of the laser. From [Tho16]

that the time elapsed between imaging the different hyperfine states is short compared to the timescales of the system that we image.

We decided to image the different hyperfine states with one single[7] external-cavity diode laser (ECDL) (Toptica DL-100). Therefore, we have to quickly change the frequency of the laser between imaging two hyperfine states, while still providing long-term frequency stability during imaging. To achieve this, we use a beat offset lock [Sch⁺99] to feedback on both the grating of the laser via the piezo voltage, as well as the current of the laser diode (Figure 5.7). The latter has a high bandwidth and we use it to stabilize the laser while we jump its frequency by up to 160 MHz to match the resonance frequency of the different hyperfine states. The jump can be performed reliably in approximately 10 µs, which is much faster than the typical expansion times $T/4 \sim 4\,\mathrm{ms}$. (In fact, the acquisition of the different hyperfine state images is currently limited by the frame rate of the EMCCD.) For more details on the imaging of two hyperfine states, see [Ste16; Tho16].

5.6 SINGLE PHOTON DETECTION

As we have seen in the previous section, the signal-to-noise ratio on the camera plays an important role for the detection efficiency. There-

---

[7] This is more cost-effective and requires less maintenance than running two separate lasers. More details on the working principles of ECDLs can be found in standard literature, e.g., [Zor95].

fore, it is necessary to take a look at the camera that we use for imaging and its noise and detection characteristics.

CCD cameras are arrays of photo-sensitive detectors (pixels) which measure the intensity of a source. With a certain quantum efficiency (QE), the photons from the light source excite electrons in the semiconductor to the conduction band. These photoelectrons are collected at every pixel of the array. At the end of the exposure, the number of photoelectrons in each pixel is read out sequentially via a common readout amplifier and an analog-to-digital converter (ADC). How well the value extracted by the ADC matches the real intensity at the corresponding pixel depends on different noise sources of the imaging process.

5.6.1 *Noise Sources of CCDs*

The first fundamental noise source of an optical signal is the photon shot noise, which is independent of the detection device. It has its origin in the fact that the light field consists of independent photons, and, for an average photon number N (i.e., a fixed average intensity), the photon number will be given by a Poisson distribution with a width $\sqrt{N}$. This means that the relative fluctuations of the intensity will decrease as $\frac{1}{\sqrt{N}}$ as one increases the intensity. This behavior was also exploited for the stabilization setup in Section 4.5.1.

The next noise source comes from the limited quantum efficiency of the detector. From the photons that arrive at a pixel, only a fraction is converted into photoelectrons. One can model this as a random process, therefore, the relative number fluctuations of the photo-electrons can be described as $\frac{1}{\sqrt{QE \times N}}$.

Apart from the noise related to the generation process of the photoelectrons, there are additional noise sources which stem from the processing of the signal in the camera's electronics. One of these noise sources is the dark noise, which expresses the rate at which photoelectrons are spontaneously excited, even in absence of light. As this happens continuously, the amount of dark noise increases with the exposure time of the image. Because this process is caused by thermal excitations, the dark current can be effectively suppressed by cooling the sensor or using a semiconductor with a larger band gap.

The remaining noise sources are often referred to as read noise or readout noise, as they occur only once during readout and are independent of the exposure time of the sensor. However, when trying to understand the noise of an EMCCD, it makes sense to differentiate between different sources of read noise.

The first type of read noise originates from the shifting of the charges across the sensor. When the gate voltages are applied, excitations and holes can be created for example by impact ionization

[Tul10]. These charges are called clock-induced charges (CICs) or spurious charges, and they occur at a rate typically less than 0.01 e⁻/pix.

For conventional CCDs, CICs are negligible compared to the other source of readout noise, the (pre-)amplifier noise. It is caused by thermal fluctuations (Johnson noise) in the resistors of the readout amplifiers. The best scientific cameras currently have a readout noise of 6 e⁻/pix [Li⁺16]. This means, however, that conventional CCDs cannot be used to detect a single photoelectron coming from a single photon.

5.6.2 *Electron-Multiplying CCDs*

To detect single photons, one has to amplify the signal of the photoelectron before it reaches the noisy readout electronics. In an electron-multiplying CCD, this is done by creating an avalanche of secondary electrons by impact ionization [Hyn01; Jer⁺01]. The primary electrons of each pixel are amplified by shifting them through an electron multiplication register before they reach the conventional amplifier and readout electronics.

The electron-multiplying (EM) amplification works similar as in an avalanche photomultiplier. For every shifting process, there is a probability (typically 1 % to 1.5 %) that a secondary electron is created. This is a stochastic process which, after around 500 shifting processes, can produce up to ~ 2000 secondary electrons for each primary electron. The distribution of the number of secondary electrons follows a Erlang distribution[8] [BHM03]

$$p_{\text{sec}}(x;n) = \frac{x^{n-1} e^{-x/g}}{g^n (n-1)!}, \tag{5.15}$$

where n is the number of primary electrons, x is the number of secondary electrons, and g is the average gain of the electron multiplication register. When using the EMCCD in photon counting mode, where there is one photon per pixel at most, this becomes an exponential distribution.

As we can see from Figure 5.8, this distribution leads to a finite probability that a photoelectron generates very few secondary electrons. For events which fall within the range of the read noise, we cannot reliably identify these events as real events or as noise, therefore we must discard them by only considering events above a certain threshold. Also, we see in the right panel that there is a shoulder present in the distribution which is explained neither by the read noise nor by the avalanche process. We attribute it to secondary CICs, which are created similar to (primary) CICs, but in the multiplication

---

[8] Since the amplification process is stochastic in the same way as the photon shot noise, the noise of both processes is often combined, leading to an effective decrease in quantum efficiency. Note that this does not apply when operating the EMCCD in photon counting mode.

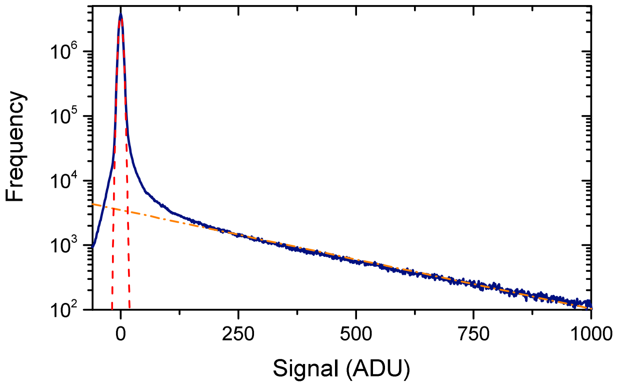

Figure 5.8: Histogram of the pixel values of our EMCCD in photon-counting mode (blue). The Gaussian contribution of the read noise is shown in red (dashed), the contribution of the EM gain is shown in orange (dash-dotted). Below 200 ADU, the shoulder in the signal is caused by secondary CICs. From [Ber17].

register. To avoid counting these false events, we choose a relatively high threshold, typically $8\,\sigma_{\text{read}}$. With this threshold and a gain of $g \approx 90\,\sigma_{\text{read}}$, we detect 88 % of the photoelectrons [Ber17]. Because the exact number of secondary electrons carries only little information about the original number of primary electrons, we assign pixels which are above threshold the value 1 and all other pixels the value 0, which results in a binarized image (Figure 5.9).

Although the electron multiplication makes it possible to detect single photons with a high fidelity, it also means that the CICs cannot be neglected anymore as a noise source. Just as the photoelectrons, they are amplified in the EM register and their signals follow the same distribution. From dark measurements, we concluded that 3 % of the pixels contain a CIC, for typical camera settings. Because, individually, a CIC event looks exactly like a real event, finding the best way to distinguish the real signal from CICs is the main challenge for image processing.

5.7 IMAGE PROCESSING

Once we have collected the signal of an atom, which may consist only of a handful of photons, we have to identify it against the noise on the image. First, we separate the pixels into bright pixels and dark pixels using the threshold from the previous section (binarization). Then, we use the fact that the photons emitted by an atom originate from approximately the same location and will appear as a bunched pattern of bright pixels, even though we do not *a priori* know the number of bright pixels or the shape of the pattern.

The CICs, in contrast, are created in an almost[9] uncorrelated manner, which results in white noise with a uniform spatial frequency

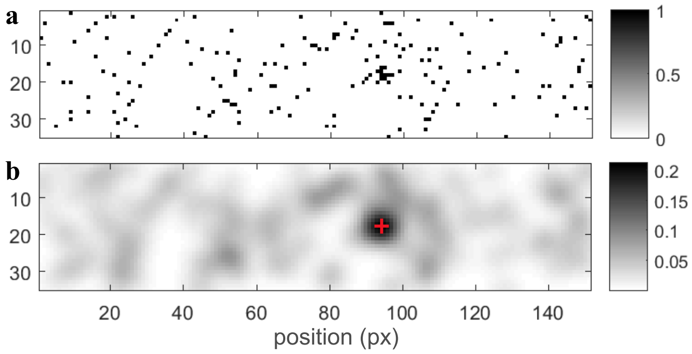

Figure 5.9: Image of a single atom (a) after binarization (b) after low-pass filtering. Darker shades represent higher photon numbers. The red cross shows the intensity peak which we identify as an atom. From [Ber17].

spectrum. This means that a large part of the noise spectrum has high spatial frequencies, unlike our signal. Therefore, we can reduce the contribution of the CICs by applying a low-pass filter with a width of 3 pixels to the binarized images (Figure 5.9). The signal from the atoms has a low spatial frequency and will be damped less than the CICs.

We can see this by analyzing the amplitudes of the local maxima in the images: If atoms are present, the histogram shows a clear bimodal distribution (Figure 5.10). We identify the atoms as the peaks with an amplitude higher than a certain threshold. The threshold value lies close to the minimum between the two peaks in the histogram, however, its exact position can be chosen according to the requirements of the specific experiment: higher values if one wants to definitely exclude CIC events (no false positives) or lower values if one wants to definitely detect all real events (no false negatives). The overlap between the two distributions depends on, for example, the CIC density and the number of photons scattered per atom. We optimize our imaging parameters such that the overlap between real and false events becomes as small as possible.

A different approach for identifying events is estimating the likelihood that a certain pattern has been generated by an atom, or by random CICs [Bom16]. Here, we first estimate the distributions that the events are sampled from. As mentioned before, the CICs are distributed almost uniformly. For the atoms, we use an averaged image to determine the typical photon distribution. We then divide each image into sectors and estimate the probability $p(k|H_i)$ that the photon pattern k in each sector was generated by either distribution (hypothe-

---

[9] The distribution of CICs is not completely uniform: the regions farthest away from the readout register are more likely to contain a CIC because they undergo more line shifts.

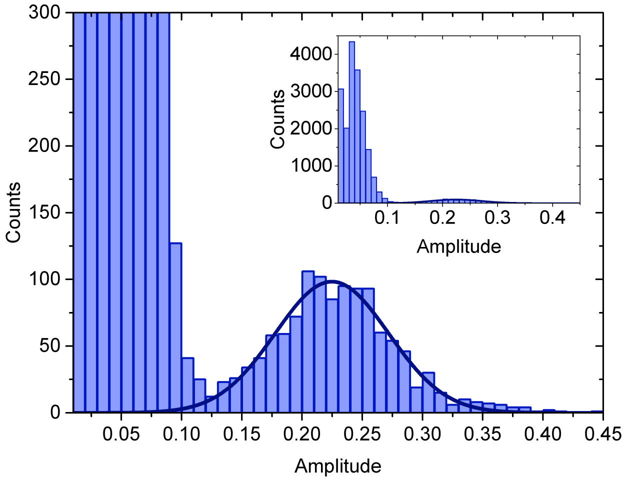

Figure 5.10: Histogram of the amplitudes of local maxima of approximately 1000 low-pass filtered images. The inset shows the complete histogram. From [Ber17].

ses H_i). We can then compare the likelihood of the hypotheses by looking at the logarithmic likelihood ratio (LR), $\ln R = \ln\left(\frac{p(k|H_1)}{p(k|H_0)}\right)$.

If we make a histogram of the LR values of the pixels in an image, we obtain a bimodal distribution, similar to Figure 5.10 of the low-pass method. Unfortunately, the LR method does not produce histograms where the contributions of atoms and noise are separated more than with the low-pass method. This is probably because the LR method still uses a hypothesis that has an average atom distribution at its base, and therefore we do not extract more information out of each image compared to the low-pass method. In the future, we will try to improve the performance of the LR method by, e.g., incorporating correlations between the photons of each image into the hypothesis. This hypothesis should describe the actual imaging process more accurately, as the photons are emitted sequentially while the atom follows a certain trajectory, and therefore the photons should show some amount of correlation.

5.8 SUMMARY

Our new imaging scheme consists of four major components which have been developed and implemented in our experiment over the past years: The imaging optics, in particular the high-NA objective [Ser11], which enables high photon detection efficiency and is essential for the spatial resolution. The laser setup [Ste16; Tho16], which provides the light pulses and the fast frequency jumps for the spin-resolution. The EMCCD camera which detects single photons [Bec16]. And our image processing [Bom16; Ber17], which allows us to identify atoms from the photon patterns.

We have combined these components to implement our matterwave microscope, which allows us to gather both in-situ and momentum information about our system. Because it can detect and identify individual atoms, this novel imaging method will be an essential tool for future experiments with tens or even hundreds atoms. But it can also provide new insight in the small systems with one or two microtraps which we currently realize in our experiments. In the next two chapters, we will study the results that we have obtained with our matterwave microscope.

6

STRONGLY INTERACTING FERMIONS IN A SINGLE WELL

In our first set of experiments, we study the expansion of a strongly-interacting Fermi gas containing only a few attractively-interacting particles. These experiments are motivated by the heavy-ion collision experiments from particle physics that I described in Section 2.2.3. The two-ion system rapidly undergoes several different stages during the collision (see [Hei04] for a review). First, the system thermalizes and forms a quark-gluon plasma (QGP). This plasma evolves hydrodynamically and eventually freezes out. The hadrons resulting from the freeze-out are measured with detectors outside the collision area.

One of the main interests of these studies is how the quark-gluon plasma, a strongly-correlated quantum fluid which also existed in the early universe, behaves. As many other quantum fluids, the QGP can be described hydrodynamically [Ada+12]. In heavy-ion collisions, its properties are studied by looking at the hadrons (mostly pions) which are produced after the QGP freezes out. For example, momentum correlations in the far field can be used to perform an HBT analysis and infer the size of the initial collision product.

We realized that we could perform similar experiments with our newly developed matterwave microscope imaging technique, which we can use to study how an ultracold quantum gas expands. In contrast to the heavy-ion collisions which produce a thermal plasma, we start with ultracold atomic systems in well-known, low-entropy states. In our experiment, we can prepare two-particle states with fidelities up to 97 %. Furthermore, the nature of the interactions is different in our system: we only have short-range interactions which can be described by contact interactions. Still, we can reach strongly-interacting regimes by use of a Feshbach resonance (see Chapter 3).

Previously, we have studied few-fermion systems in a microtrap for strong repulsive interactions [Mur+15a] with our MOT imaging technique. With our new matterwave microscope imaging (Chapter 5), we can measure correlations directly between individual particles. In this chapter, we will present correlation measurements of strongly-attractive few-fermion systems. We will also describe a theoretical model for our measurements and how we currently interpret the observed correlations. However, these are to be seen as preliminary results, as we are still improving our models in collaboration with theorists. While the experiments in this thesis were performed on two-particle systems, we plan to extend this type of measurements to systems containing more particles, which may eventually be described as a hydrodynamic system.

6.1 DESCRIPTION OF THE EXPERIMENTS

In our experiments, we prepare a sample of two atoms in a single microtrap. We use a balanced mixture of the hyperfine states $|1\rangle$ and $|3\rangle$, which we obtain after evaporating at high magnetic fields (see Section 4.2). Before loading the microtrap, we cross the resonance to break up the Feshbach molecules. After having loaded two atoms in our microtrap (see Section 4.3), we set the intensity of the microtrap typically to $185\,\mu W$. This microtrap has an axial trap frequency of $\omega_z \approx 2\pi \times 6\,\mathrm{kHz}$ and radial trap frequencies of $\omega_r \approx 2\pi \times 30\,\mathrm{kHz}$. Then, we slowly ramp our field in $\sim 100\,\mathrm{ms}$ to the scattering length that we want to study. For fields between 660 G and 750 G, we obtain strongly interacting systems with scattering lengths $|a| > 5000\,a_0$ (see Appendix C for a list of values).

In a final step, we release the atoms from the microtrap. We can then ramp to a high magnetic field to improve the performance of the imaging (see Section 5.5). However, we noticed that this ramp influences the expansion dynamics of the atoms, since it corresponds to a ramp in scattering length. Therefore, for the following experiments, we decided to remain at the field where we had prepared our sample, at the cost of decreasing our detection fidelity[1]. Instead, we calibrated the atom number at high fields and then post-selected the images taken at lower fields displaying the correct atom number.

After releasing the atoms from the microtrap, we let them expand in an external potential. Even though an expansion in free space would be easier to understand theoretically, it is experimentally not feasible. Without external confinement, the atoms would exit the focal plane of the objective and we would not be able to detect them. Therefore, we guide the atoms with the ODT potential. This potential typically has an axial trap frequency of $f_{\mathrm{ODT}} = 1/T = 62\,\mathrm{Hz}$ and an aspect ratio of $\eta \approx 8$ (see Chapter 5 for more details). Of course, this elongated potential influences the motion of the atoms and has to be taken into account for the exact interpretation of the measurements.

After the expansion has been completed, we image the atoms optically with spin and position resolution along the elongated axis of the ODT. For each individual image, we measure the position of the atoms along this axis (Figure 6.1a). After repeating the experiment ca. 5000 times for the same settings, we can display the result as a correlated position density map (Figure 6.1b).

6.2 EXPERIMENTAL RESULTS FOR TWO PARTICLES

Before we look at systems containing multiple particles, we first have to understand how two particles expand and which influence the

---

[1] We will overcome this limitation with a new imaging scheme which addresses both the $|1\rangle$ and $|5\rangle$ hyperfine states, eliminating dark states.

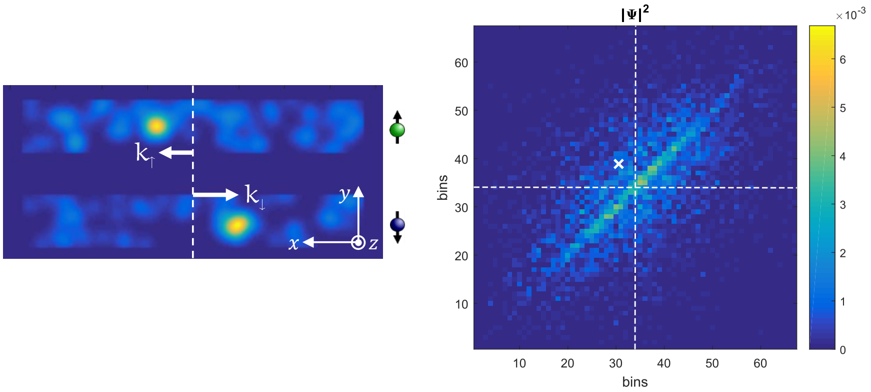

(a) (b)

Figure 6.1: (a) Typical image of two atoms used for correlated density measurements. The two hyperfine states are imaged individually and their distance from the origin after $T/4$ can be interpreted as their initial momentum. (b) Density map of the correlated positions of two atoms for ca. 5000 measurements at 690 G. Each position bin contains two pixels. The cross marks the approximate position of the image in the left panel.

confinement and the interactions have on them. Figure 6.2 shows a collection of correlated density measurements after an expansion time $T/4$ with different settings, in which we can identify several different features.

From looking at the correlated density (diagrams as in, e.g., Figure 6.1b), we observe that structures mainly appear along the diagonal $x_1 = x_2$ and antidiagonal $x_1 = -x_2$ axes. The reason is that, for two particles, the coordinates of the individual particles x_1 and x_2 can be transformed to center-of-mass (COM) and relative (REL) coordinates, $X = (x_1 + x_2)/2$ and $x = x_1 - x_2$ (see Section 3.2). These coordinates are parallel to the diagonal and antidiagonal axes, respectively, of the correlated density images. In the case of harmonically confined particles[2] with interactions that only depend on the particle separation, the equations of motion separate in this coordinate frame, resulting in two decoupled single-particle problems.

Therefore, we can look at the correlated data along the REL coordinate x regardless of the COM coordinate (effectively integrating the X-axis), or vice versa. In Figure 6.2, the densities along these two axes are shown for a range of different scattering lengths and expansion parameters (the complete data set is available in Appendix D). For each setting, two graphs are shown. In the upper (lower) graph, one sees the correlations along the REL (COM) coordinate, where the density along the COM (REL) coordinate has been integrated:

---

[2] Our optical potential is created by Gaussian beams and can, at least for sufficiently low energies of the particles, be approximated by a harmonic potential.

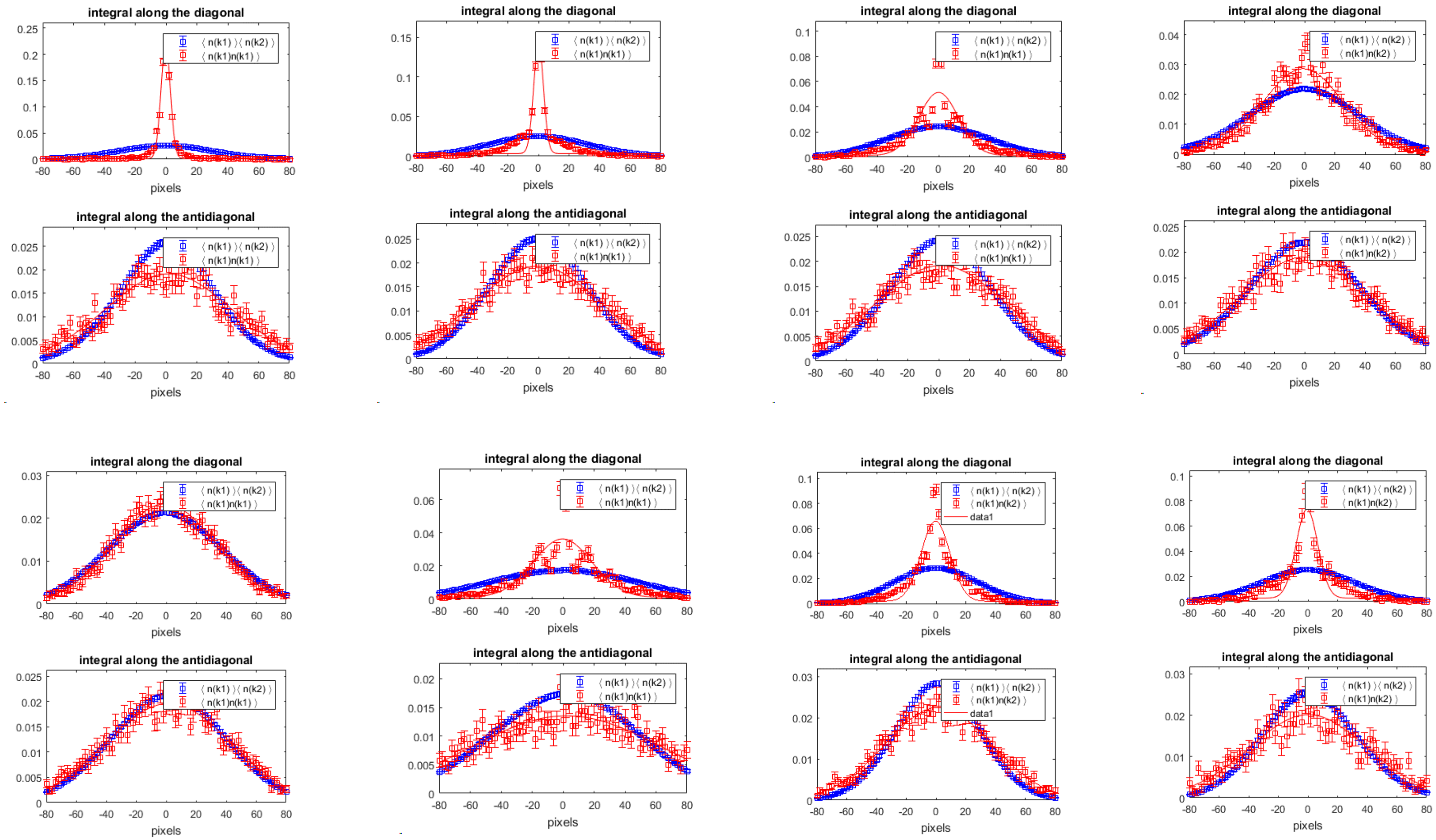

Figure 6.2: Density profiles along the REL and COM coordinates (upper and lower panels of the sub-figures, respectively). The (un)correlated densities n (ñ) are shown as red (blue) data points, with error bars representing the standard error of the mean (see Appendix B). The sub-figures show different preparation and expansion parameters, from left to right, top to bottom: 665 G, 685 G, 690 G, 710 G, 900 G, expansion in ODT of half depth, expansion in single-beam ODT, expansion with brake pulse.

$$\tilde{n}(x) = \int dX \, \langle \hat{n}(x_1)\hat{n}(x_2)\rangle \tag{6.1a}$$

$$\tilde{n}(X) = \int dx \, \langle \hat{n}(x_1)\hat{n}(x_2)\rangle \tag{6.1b}$$

For comparison, we also show the densities profiles which one obtains when integrating over the uncorrelated densities,

$$\tilde{n}_u(x) = \int dX \, \langle \hat{n}(x_1)\rangle \, \langle \hat{n}(x_2)\rangle \tag{6.2a}$$

$$\tilde{n}_u(X) = \int dx \, \langle \hat{n}(x_1)\rangle \, \langle \hat{n}(x_2)\rangle \, . \tag{6.2b}$$

From these quantities, we can define the correlator

$$C(x) = \frac{\tilde{n}(x)}{\tilde{n}_u(x)} - 1, \tag{6.3}$$

which has also been used in [Föl+05; Rom+06]. It corresponds to the correlation function $g^{(2)}(x_1, x_2)$ (eq. (2.26)) and has been normalized by dividing the correlated two-particle density by the uncorrelated single-particle densities.

To reduce the effect of noise in the less dense regions of our measurements, we instead prefer to use different correlators,

$$\Gamma(x) = \tilde{n}(x) - \tilde{n}_u(x) \quad \text{and} \tag{6.4a}$$

$$\Gamma(X) = \tilde{n}(X) - \tilde{n}_u(X). \tag{6.4b}$$

As these correlators do not have measurement data in the denominator, their values should be less susceptible to noise. The correlators that we obtained from our measurements can also be found in Appendix D.

Already by looking at the integrated densities $\tilde{n}(X)$ and $\tilde{n}(x)$ in Figure 6.2, we can see several interesting features in our data. Starting at relatively small negative scattering lengths at 900 G (see Appendix C for the values of the scattering length), the width of the distributions $\tilde{n}(x), \tilde{n}(X)$ is similar to that of the individual, uncorrelated particles $\tilde{n}_u(x), \tilde{n}_u(X)$. This shows that the particles are approximately independent from each other, as in the case of non-interacting particles.

For larger interactions toward the resonance, the width of $\tilde{n}(x)$ decreases as, while the width of $\tilde{n}(X)$ stays approximately the same. Near the resonance, the shape of the density profile changes and resembles a bimodal distribution with wide wings and a sharp central peak. Further below the resonance, the wings disappear and only the central peak remains. This sharp correlation peak is expected as the

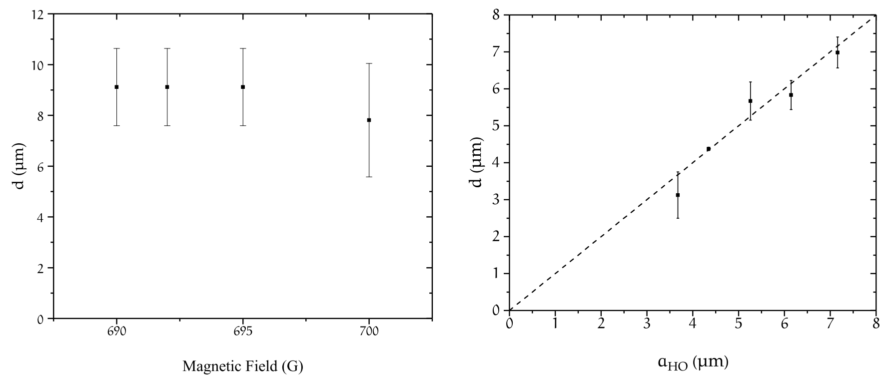

(a)

(b)

Figure 6.3: Length scale d corresponding to the fringe spacing after $T/4$ for different interaction strenghts (a) and for different ODT depths (b). The dashed line, $d = a_{HO}$, is a guide to the eye.

atoms are bound as Feshbach molecules at these values of the scattering length.

For strong interactions just above and on the Feshbach resonance, additional fringes appear next to a central peak. Interestingly, their spacing does not strongly depend on the initial parameters of the microtrap or the scattering length (Figure 6.3a), but mostly on the parameters of the ODT which we use during the expansion. Using the relation

$$1/d \equiv p(T = 0) = m\omega x(T/4), \tag{6.5}$$

where we introduced the length scale d corresponding to the initial momentum[3], we can see that the fringe spacing matches the harmonic oscillator length $a_{HO} = \sqrt{\frac{\hbar}{m\omega}}$ closely for different depths of the ODT (Figure 6.3b). Note that the fringes would scale differently if they depended on the ODT only in a trivial manner: In this case, they would scale with the magnification as $M \propto \omega \propto a_{HO}^2$. Surprisingly, the fringes are present only for some configurations of the dipole trap, and absent for others, the reason for which has as of yet not been identified.

In the next sections, we will provide a theoretical model for understanding several of these features observed in the correlated density profiles.

6.3 THEORETICAL INTERPRETATION

As mentioned in the previous section, the initial state of our experiment consists of two interacting particles in a harmonic trap. This

---

[3] For this evaluation we assumed that the momentum mapping expained in Section 5.3 also works for interacting systems.

problem can be separated in center-of-mass and relative coordinates. As the interactions only depend on the REL coordinate, the wavefunction in the COM coordinate remains that of an ordinary harmonic oscillator, with the modified mass $M = 2m$. The equations of motion in the rel coordinate describe a single particle with reduced mass $\mu = m/2$ in a potential consisting of a central harmonic potential and a central interaction potential (eq. (3.31)). This problem has been has been treated analytically and numerically for different confinement geometries [Bus+98; BTJ02; IC06; LZ08].

In this section, we will first focus on the isotropic and axially symmetric solutions by [Bus+98; IC06] to describe our initial states. Then, we will deduce how these states evolve using our knowledge about low-energy scattering from Section 3.2. Combined, these approaches will result in predictions for correlated density profiles, which we can compare to our measurements.

6.3.1 *Interacting Atoms in an Axially-Symmetric Microtrap*

For the initial system, we have to treat the one-particle harmonic oscillator problem combined with contact interactions, which can be described in relative coordinates by the Schrödinger equation

$$\left(-\frac{1}{2}l^2\nabla^2+\frac{1}{2}\left(\eta^2\frac{\rho^2}{l^2}+\frac{z^2}{l^2}\right)+2\pi\frac{a}{l}\delta(\mathbf{r})\frac{\partial}{\partial r}\frac{r}{l}\right)\Psi(\mathbf{r})=\frac{E}{\hbar\omega_z}\Psi(\mathbf{r}). \tag{6.6}$$

Here, we have explicitly normalized all energy scales with respect to the axial trap frequency $\hbar\omega_z$ and all length scales with respect to the reduced harmonic oscillator length $l = \sqrt{\frac{\hbar}{\mu\omega_z}}$. Energies and lengths will be expressed in these units for the following discussion, including the scattering length a. The radial harmonic oscillator is related to the axial harmonic oscillator by the aspect ratio $\eta = \omega_\perp/\omega_z$.

Instead of using plane waves to find a solution to this problem, it is more suitable to use a basis set consisting of the two-dimensional harmonic oscillator basis $\Phi_{n,m}(\rho,\phi)$ and the one-dimensional harmonic oscillator basis $\Theta_k(z)$. In the case of a prolate (cigar-shaped) trap, we obtain the following relation between the energy $\mathcal{E} = E - E_0 = E - \eta - 1/2$ and the scattering length [IC06]:

$$-\frac{1}{a}=-\frac{2\Gamma(-\mathcal{E}/2)}{\Gamma\left(-\frac{\mathcal{E}+1}{2}\right)}+\frac{\Gamma(-\mathcal{E}/2)}{\Gamma\left(-\frac{\mathcal{E}-1}{2}\right)}\sum_{m=1}^{n-1}{}_2F_1\left(1,-\mathcal{E}/2;-\frac{\mathcal{E}-1}{2};e^{2\pi i m/n}\right), \tag{6.7}$$

where $\Gamma(x)$ is the Euler gamma function and ${}_2F_1(a,b;c;x)$ is the hypergeometric function. This relation is visualized in Figure 6.4. We can see that, compared to the non-interacting system at $\left|a^{-1}\right| \gg 1$, positive scattering lengths increase the energy (called repulsive branch),

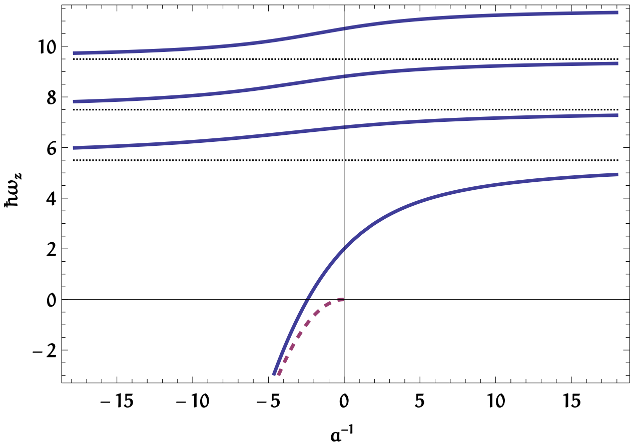

Figure 6.4: Energy of two particles in a harmonic trap for $\eta = 5$ (equation (6.7), blue line) and in free space (magenta dashed line), versus the inverse scattering length a^{-1}. The eigenenergies without interactions are shown as dotted black lines. The zero-point energy of the harmonic trap has not been subtracted.

while negative scattering lengths decrease the energy (called attractive branch). The ground state is connected to the free-space Feshbach molecule for positive scattering lengths. The energy of the Feshbach molecule is barely influenced by the external confinement once its length scale (eq. (3.27)) is small enough compared to l and its binding energy is much larger than the trap depth.

We can learn more about this system if we use the energy eigenvalues to calculate its (unnormalized) eigenstates as a series expansion in the harmonic oscillator basis:

$$\Psi_{\mathcal{E}}(\mathbf{r}) = \sum_{n,k} \frac{\Phi^*_{n,0}(0,\phi)\Theta^*_k(0)}{2\eta n + k - \mathcal{E}} \Phi_{n,0}(\rho,\phi)\Theta_k(z) \tag{6.8}$$

The terms with $m \neq 0$ do not contribute to the solution since they vanish for $\mathbf{r} = 0$ ($\Phi^*_{n,m>0}(0,\phi) = 0$) and cannot be influenced by the contact interaction.

A few observations can already be made from this very general expression, without calculating the wavefunction explicitly. The contribution of each basis wavefunction in the expansion is determined by its prefactor. This coefficient contains the energy difference between the state's energy $\mathcal{E}$ and the energy of the non-interacting harmonic oscillator in the denominator. For weak interactions, where $2\eta n + k \approx \mathcal{E}$, the contribution[4] from the non-interacting harmonic-oscillator wavefunction with matching energy will be resonantly enhanced, while the other terms will contribute small corrections.

For stronger interactions there is no single, resonant coefficient anymore. While the wings of the wavefunction at distances ∼ l still match

---

[4] For $\eta \in \mathbb{Q}$, there may be several resonant terms from degenerate states.

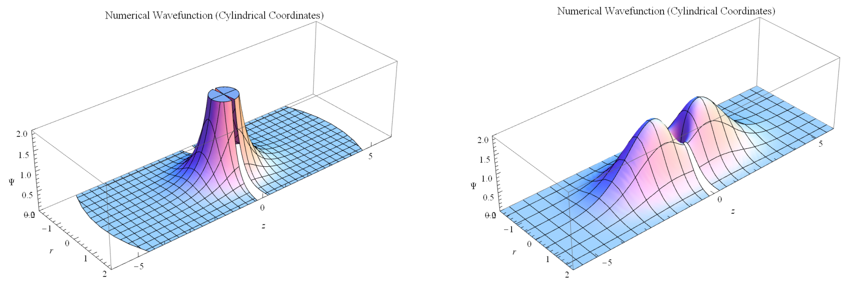

(a) (b)

Figure 6.5: Absolute value of the relative wavefunction of two particles in a harmonic trap with $\eta = 5$. (a) Ground state for $a^{-1} = -2$. (b) Excited state for $a^{-1} = 5.6$. Rendered using data from [Blu17].

the basis functions well, the wavefunction in the center is mainly determined by the boundary condition of the scattering problem, eq. (3.28). Because the non-interacting basis does not follow the same boundary conditions, many high-frequency terms in the expansion are required to describe the wavefunction well at small distances. A similar argument applies for the ground state when it has large overlap with the Feshbach molecular state. In these two cases, it is advantageous to expand the wavefunction in a more suitable basis, or to calculate it numerically. A few examples of numerically calculated wavefunctions [Blu17] for strong interactions are shown in Figure 6.5.

6.3.2 *Interacting Atoms in an Isotropic Microtrap*

For the remaining discussion, it is useful to have a concise, analytic expression for the wavefunction. In the special case of isotropic confinement, such a solution exists [Bus+98]. Just as the confinement, the eigenstates of this problem are also isotropic. They are characterized by the radial wavefunction

$$r\Psi_\nu(r) \propto r\, e^{-r^2/4}\, U(-\nu, 3/2, r^2/2), \tag{6.9}$$

where $U(a, b, z)$ is the confluent hypergeometric function and $\nu = (\mathcal{E} - 3/2)/2$ corresponds to a main quantum number.

It is interesting to observe that this wavefunction is related to a generalized solution of the non-interacting, one-dimensional harmonic oscillator wavefunction $e^{-r^2/2} H_n(r)$, where the main quantum number n in the Hermite polynomial determines the wavelength of the wavefunction inside the trap. If n is allowed to take non-integer values $-\nu$, the Hermite polynomial has to be replaced by the hypergeometric function U, just as in equation (6.9). It becomes clear that ν determines not just the wavelength of the wavefunction, but also its phase shift at $r = 0$ (which, for non-interacting particles and integer

n, always is a multiple of π). This insight will come in handy when treating the dynamical expansion of the wavefunction, as it shows the direct relation between the trapped, interacting particles and the free particles described by scattering waves.

6.3.3 *Free Expansion with Contact Interactions*

As a next step, we have to understand the dynamics of the atoms after they have been released from the microtrap. While, in the experiment, we use an optical potential to guide the released particles, it makes sense to first look at the behavior of freely expanding particles, which is simpler to describe.

From scattering theory (Section 3.2), we know that the eigenstates of free particles with contact interactions are plane waves with a phase shift. In general, they can be written as

$$\psi_{s,k}(r,a) = \frac{\sin(kr+\delta(a))}{2\pi r} = \frac{\sin(kr) - ka\,\cos(kr)}{2\pi r\,\sqrt{(ka)^2+1}}, \tag{6.10}$$

where the scattering phase was replaced by the scattering length in the second step according to $\tan\delta = -ka$. For positive scattering lengths, we also have to consider the bound state

$$\psi_{b,k}(r,a) = \frac{e^{-r/a}}{\sqrt{2\pi a}\,r}. \tag{6.11}$$

These states are all orthogonal to each other and the scattering states have been normalized such that their volume integral is independent of their wavelength.

If we want to know the occupation of a certain momentum mode k, we must calculate the overlap of the scattering waves with the initial wavefunction ψ_0. In position space, this becomes

$$c_k(t=0) = \langle \psi_k \mid \psi_0 \rangle = \int d^3r\,\frac{\sin(kr+\delta)}{r}\,\psi_0(\mathbf{r}) \tag{6.12}$$

at $t=0$ directly after releasing the atoms. Decomposed in these momentum modes, the full wavefunction at time t reads

$$\psi(r,t) = \int d^3k\,e^{-iE_k t/\hbar}\,c_k(0)\psi_k(r), \tag{6.13}$$

where the energies of the modes are $E_k = \frac{\hbar^2 k^2}{2m}$. After long expansion times t_{exp}, the different momentum components will have spatially dispersed and we are able to read off the momentum components from the spatial density distribution, $n(k, t=0) \approx n(r, t_{\text{exp}})$.

While calculating the density distribution in this manner mimics the experimental procedure, it is relatively impractical. A more convenient way of extracting the initial momentum distribution can be found by reformulating equation (6.12) using Bessel functions,

$$\sqrt{\pi/2}\sqrt{kr}\,J_{1/2}(kr) = \sin(kr). \tag{6.14}$$

We obtain the following relationship for the overlap coefficients c_k:

$$\begin{aligned} c_k(t=0) &= \sqrt{\frac{\pi}{2}}\sqrt{k}\int_0^\infty dr\, r\psi_0(r)\,\sqrt{r}\,J_{1/2}(kr) = \frac{1}{2\pi^2}\,k\mathcal{F}(\psi_0(r)) \\ \Leftrightarrow \psi_0(k) &\propto \frac{c_k}{k}, \end{aligned} \tag{6.15}$$

In the second step, the integral was identified as a Hankel transform, which can be in special cases related to the Fourier transform $\mathcal{F}$ [Bra00]. Even though the interaction-induced phase shift has been neglected in this derivation, it shows the connection between the projection coefficients of the initial state on the scattering waves and the momentum representation of the initial state.

6.3.4 *Free Expansion of Isotropic Trapped States*

We will now see how strong interactions influence the expansion dynamics of an isotropically-trapped initial state, which will henceforth be called the Busch state [Bus+98] (see eq. (6.9)). When this state is released from its confinement, it is projected on the scattering states $\psi_{s,k}(r,a)$ and the molecular bound state $\psi_{b,k}(r,a)$ (eq. (6.10) and (6.11), respectively).

In Figure 6.6, we can compare the Busch state with these states, and also with free spherical waves $\psi_{f,k}(r) = \frac{\sin(kr)}{2\pi r}$ with momentum $k = \sqrt{2mE}$. For small and intermediate positive scattering lengths, the Busch wavefunction closely resembles the molecular wavefunction, while at large positive scattering lengths, the molecular wavefunction extends far outside the trap and is no good description of the Busch state. Instead, the scattering spherical wave $\psi_{s,k}(r,a)$ matches it better for $r \lesssim l$ (neglecting the phase shift of π). For larger distances, however, the scattering waves do not match well because the Busch wavefunction vanishes outside the trap. Also for large and intermediate negative scattering lengths, where there is no bound state $\psi_{b,k}(r,a)$, the scattering states match the Busch state for small distances.

For comparison, the overlap with a free wavefunction $\psi_{f,k}(r)$ with the same momentum is worse, because the it does not describe the Busch wavefunction well around $r = 0$, i.e., the phase does not match. For weak interactions, the initial wavefunction is approximately a Gaussian, $r\psi_{\text{Busch}}(r, a \approx 0) \propto r\,e^{-r^2/2}$, and the scattering and free waves provide almost identical overlap.

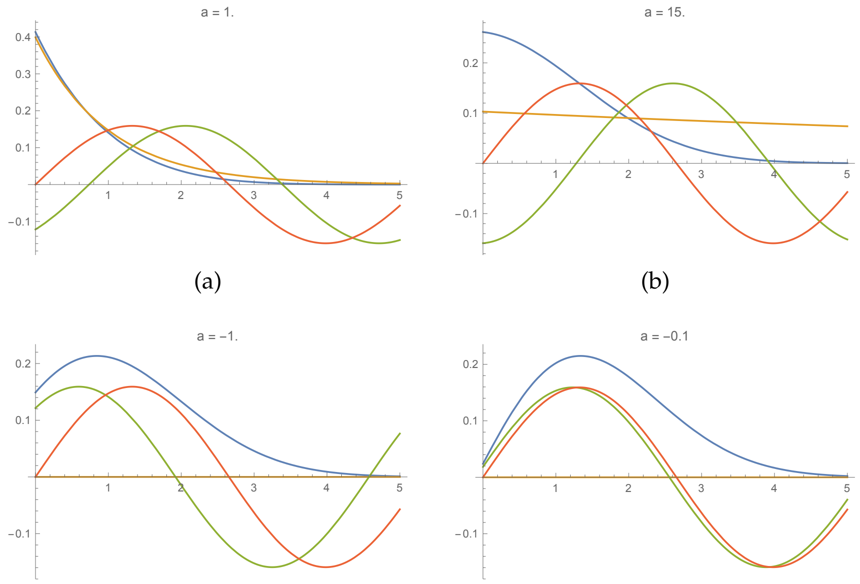

(a) (b)

(c) (d)

Figure 6.6: Overlap of Busch's wavefunction (blue) with the bound state (yellow), scattering spherical waves (green) and non-interacting spherical waves (red). For the spherical waves, only the waves with momentum $k = \sqrt{2mE(a)}/\hbar$ are shown. The horizontal axis gives the radial coordinate r. All wavefunctions are radial wavefunctions $r\psi$. The values of the scattering lengths are given in each panel and are typical for intermediate repulsive, strongly repulsive, intermediate attractive and weakly attractive interactions.

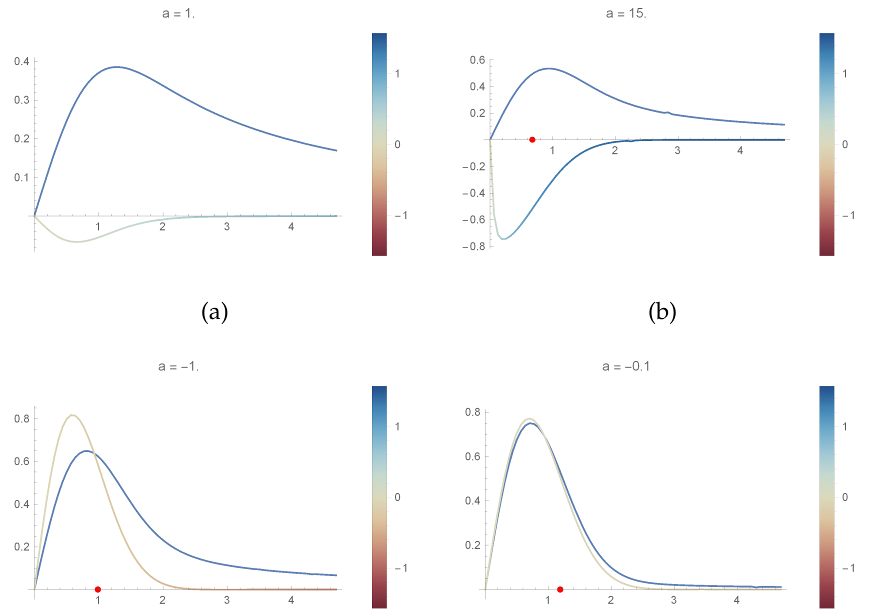

(a) (b)

(c) (d)

Figure 6.7: Overlap of the scattering waves (color gradient) and free waves (blue) with Busch's wavefunction vs. momentum. The different panels show the overlap for different interaction lengths, as in Figure 6.6. The color of the curve specifies the phase of that momentum component. For free waves, that phase is always zero. The red dot marks $k = \sqrt{2mE}$.

It is clear that the initial Busch state will not project only on a single scattering wave, since it is a trapped state with a finite extent and the scattering states are infinitely extended states. Instead, we have to calculate the overlap with a whole spectrum of scattering waves with different momenta. This spectrum has to be such that the scattering waves interfere constructively inside the trap and destructively outside the trap, for $t = 0$.

Depending on the scattering length and the momentum, the scattering waves may have different phase shifts and contribute differently the overlap. This may be seen in Figure 6.7, where the overlap c_k with different momenta k is shown together with the phase shift $\delta = \arctan(-ka)$. While the phase shift is zero for all momenta at weak interactions, large momenta obtain a phase shift at larger scattering lengths, until all momenta display a phase shift of $\pi/2$ on the Feshbach resonance.

At large scattering lengths, also the distribution of overlap coefficients c_k starts to differ, depending on if we project on scattering waves or on free waves. This can be understood from the boundary condition (3.28) which is determined by the scattering length: It is the same for the initial Busch state and the scattering waves, while it is different for the free waves ($u|_{r=0} = 0$). Therefore, the initial wavefunction can be decomposed into scattering waves with relatively low momenta. In contrast, decomposing a strongly-interacting trapped state in the free-waves basis requires large momenta to emulate the boundary condition correctly. This additional momentum comes from the released interaction energy, which remains contained if we project on scattering waves instead.

With these results, we can try to reproduce our experimental results theoretically. The wavefunction expressed in scattering waves, which are eigenfunctions of the Hamiltonian during expansion, can be propagated by unitary time evolution (eq. (6.13)). It is clear that the part which has been projected onto the molecular state remains stationary, while the scattering waves expand outwards. If we wait for sufficiently long times and rescale the position axis $r \approx \frac{\hbar k}{\mu} t$ and the amplitude of the wavefunction, the part which has been projected onto the scattering waves converges to $c(k)/k$. This behavior was also expected from eq. (6.15). The wavefunction of bound state will in this case remain narrow and not contribute to the expansion. In the experiment, however, it will have a finite width which is given by the resolution of the imaging system.

To mimic the imaging procedure in our experiment, we project this radially symmetric wavefunction onto one axis of the Cartesian coordinate system using an Abel transform [Pou10]. The numerical results are shown in Figure 6.8. While there is a clear bound state for small and intermediate positive scattering lengths, a base appears when approaching the resonance, until the molecular peak and the base

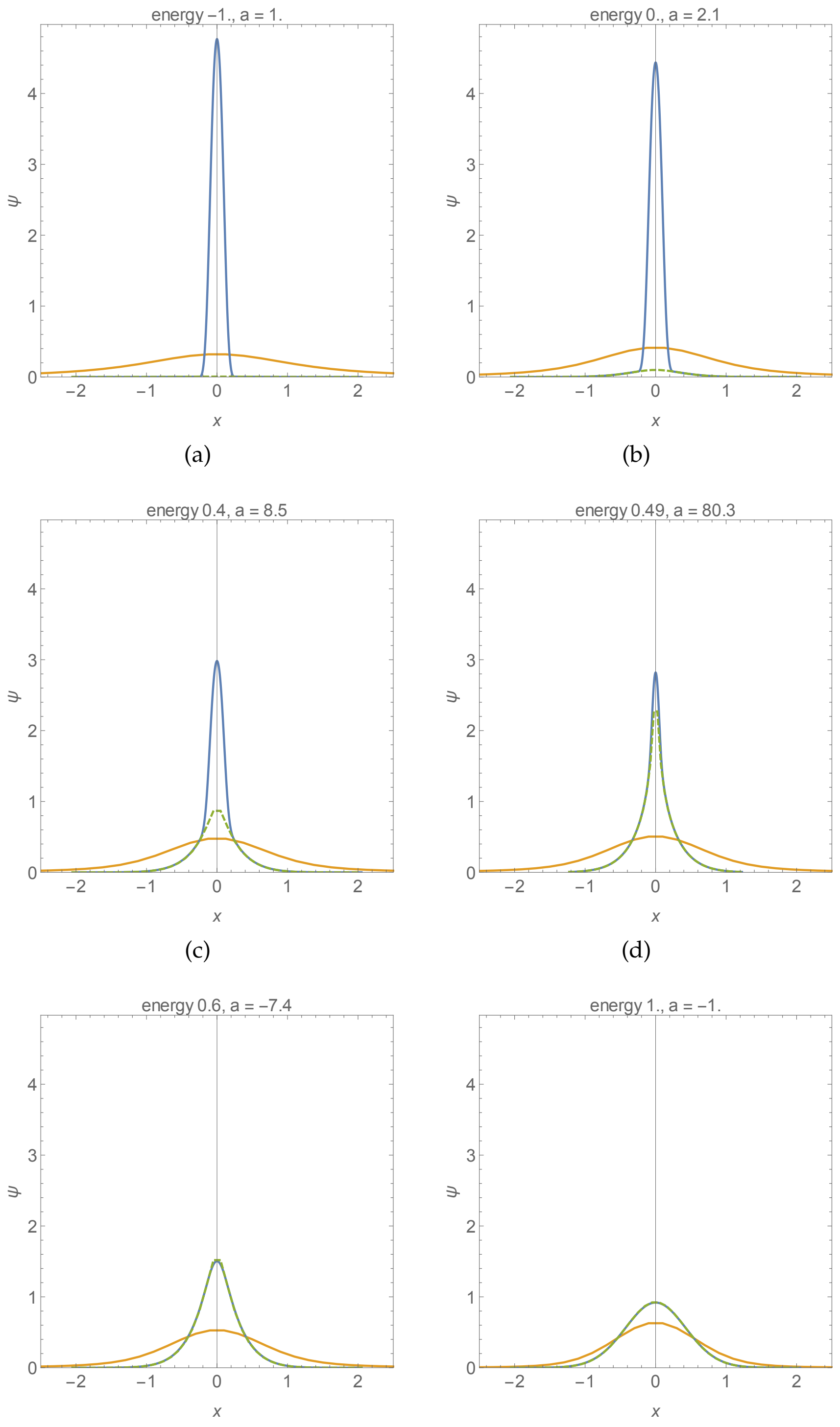

(a) (b) (c) (d) (e) (f)

Figure 6.8: Busch wavefunction after projection on scattering waves and bound state, after long expansion times and integrated over two axes (blue curve). The contribution from the scattering waves is shown in green and corresponds to the momentum components of the initial wavefunction. For comparison, also the projection on free waves without interaction ($a = 0$) is shown (yellow curve). The panels show the results for different scattering lengths comparable to the experimental values (see Appendix C).

merge on resonance. For negative scattering lengths, the narrow distribution becomes wider and more similar to a Gaussian the farther away one goes from the resonance. The fringes which are a striking feature in the experimental data do not appear in the calculations for any scattering length. This may be due to the approximations and assumptions made during the calculation, for example, that the initial state and the expansion is isotropic. Currently, we suspect that the anisotropy may indeed give rise to the fringes, however, this still has to be investigated.

6.4 SUMMARY

We have used a simple system of two strongly-interacting fermions in a single microtrap to study their expansion dynamics. Due to the attractive interactions between the particles, correlations appear in the relative coordinate, which we have detected with our matterwave microscope. Two distinctive features in the correlated densities close to the Feshbach resonance are the bimodal distribution at negative scattering lengths and the fringe pattern at positive scattering lengths.

Due to the different spatial symmetries of the microtrap and the ODT, it is difficult to exactly describe our system theoretically. However, a preliminary calculation based on isotropic, interacting initial states and an isotropic, interacting expansion has already been able to explain the bimodal structure at negative scattering lengths. We are still working on an explanation for the fringe pattern, which we suspect is caused by the anisotropy of our system.

The measurements in these chapter show the importance of interactions during the expansion of strongly-coupled systems. By performing these measurements with increasing numbers of particles, we want to study transition between microscopic dynamics and hydrodynamic behavior in strongly-coupled quantum fluids.

7

EXPERIMENTS WITH A DOUBLE WELL

We can also study interacting few-fermion systems which occupy not a single microtrap, but two coupled microtraps. This system can be seen as the fundamental building block of the Hubbard model. While the Hubbard model was originally developed to describe the behavior of interacting electrons in a metal, it can also be applied to ultracold atoms in a lattice [Jak+98]. It provides a greatly simplified way of treating the many-body problem, because it typically contains only two characteristic parameters, the tunnel coupling J and the on-site interaction U (see Chapter 2). The interplay of these parameters gives rise to interesting phases which have been studied in many different variations over the years [Tas98; JZ05; Ess+05; Ess10; Dut+15].

Even though some unexpected properties may only arise in very large systems (as was advocated early on by P.W. Anderson [And72]), they are caused by the microscopic behavior of the constituent particles. This behavior can be studied conveniently in very small systems, with only two sites and up to four particles. These double-well systems or Hubbard dimers have attracted considerable interest from theorists (for example [Zan02; DDW06; Car+15]) and experimentalists (for example [Föl+07; Tro+08; Gre+13; Kau+14]) alike.

In this chapter, we will look at our realization of the two-site Hubbard model, starting with a brief theoretical description. From the measurements performed in our experiment (including those published in [Mur+15b]), we will be able to identify the states that we prepared and match them to the theoretical predictions. Also, we will use our matterwave microscope to extract information about the coherence and entanglement of our system.

7.1 DOUBLE-WELL HUBBARD HAMILTONIAN

For the double-well system, the description of the Hubbard model and the Hamiltonian (2.43) is greatly simplified:

$$H = -J\sum_{\sigma}\left(\hat{a}^{\dagger}_{L\sigma}\hat{a}_{R\sigma} + \hat{a}^{\dagger}_{R\sigma}\hat{a}_{L\sigma}\right) + U\sum_{j=L,R}\hat{n}_{j\downarrow}\hat{n}_{j\uparrow} + \Delta\sum_{\sigma}\left(\hat{n}_{L\sigma} - \hat{n}_{R\sigma}\right) \tag{7.1}$$

Here, there are only the sites left and right (L and R) and the chemical potential has been replaced with a tilt 2Δ between the sites. We can now define a basis which counts the occupation of the sites for each spin separately. Since the Hamiltonian conserves the number of parti-

Dim.	States	Hamiltonian
1	$\lvert\cdot,\cdot\rangle$	0
1	$\lvert\uparrow,\uparrow\rangle$; $\lvert\downarrow,\downarrow\rangle$	0
1	$\lvert\uparrow\downarrow,\uparrow\downarrow\rangle$	2U
2	$\lvert\uparrow,\cdot\rangle$, $\lvert\cdot,\uparrow\rangle$; $\lvert\downarrow,\cdot\rangle$, $\lvert\cdot,\downarrow\rangle$	$\begin{pmatrix} \Delta & -J \\ -J & -\Delta \end{pmatrix}$
2	$\lvert\uparrow\downarrow,\uparrow\rangle$, $\lvert\uparrow,\uparrow\downarrow\rangle$; $\lvert\uparrow\downarrow,\downarrow\rangle$, $\lvert\downarrow,\uparrow\downarrow\rangle$	$\begin{pmatrix} U+\Delta & -J \\ -J & U-\Delta \end{pmatrix}$
4	$\lvert\uparrow\downarrow,\cdot\rangle$, $\lvert\uparrow,\downarrow\rangle$, $\lvert\downarrow,\uparrow\rangle$, $\lvert\cdot,\uparrow\downarrow\rangle$	$\begin{pmatrix} U+2\Delta & -J & -J & 0 \\ -J & 0 & 0 & -J \\ -J & 0 & 0 & -J \\ 0 & -J & -J & U-2\Delta \end{pmatrix}$

Table 7.1: Dimensionality, states, and Hamiltonians of the subspaces of the 2-site Hubbard model. Adapted from [Kli12].

cles per spin state, it will in this basis consist of eight block-diagonal entries (Table 7.1), which may be diagonalized separately.

7.1.1 *One Particle in a Double Well*

The simplest non-trivial case that we can study is one particle with spin $\sigma = \{\uparrow,\downarrow\}$ in the double well. Even though there will obviously be no interactions, it can show us the influence of the tunnel coupling between the wells. In our experiment, we did not directly realize this system. However, if we prepare two distinguishable, non-interacting particles, we can treat each of these particles independently in a similar manner (see Section 7.4.1).

For a double well without coupling, the localized basis states given in the fourth line of Table 7.1 are also its eigenstates. If there is coupling, this system forms a textbook coupled two-level system. The eigenstates will be a superposition of the basis states, $|\sigma,\cdot\rangle \pm |\cdot,\sigma\rangle$, and have the eigenenergies $\Delta \mp J$.

In our experiment, we also have to consider that we may have prepared a mixed state instead of a pure state. Therefore, it is necessary to describe the state with the general density matrix

$$\begin{aligned} \rho_1 &= \rho_{LL}\, |\sigma,\cdot\rangle\langle\sigma,\cdot| + \rho_{LR}\, |\sigma,\cdot\rangle\langle\cdot,\sigma| + \rho_{LR}^*\, |\cdot,\sigma\rangle\langle\sigma,\cdot| + \rho_{RR}\, |\cdot,\sigma\rangle\langle\cdot,\sigma| \\ &= \begin{pmatrix} \rho_{LL} & \rho_{LR} \\ \rho_{LR}^* & \rho_{RR} \end{pmatrix}. \end{aligned} \tag{7.2}$$

For the eigenstates, the corresponding density operators are

$$\rho_- = \frac{1}{2}\begin{pmatrix} 1 & -1 \\ -1 & 1 \end{pmatrix} \tag{7.3a}$$

$$\rho_+ = \frac{1}{2}\begin{pmatrix} 1 & 1 \\ 1 & 1 \end{pmatrix}. \tag{7.3b}$$

If we want to fully characterize a state in the experiment, we have to measure all independent elements of the density matrix. While there are different ways of doing this, one method is to measure the different correlation functions of the system. In the simple case of a single particle, the only relevant correlation function is the one-point correlation function, i.e., the spatial density distribution $n(x)$. We can express it in a general form according to eq. (2.18) as

$$\begin{aligned} \langle n(x)\rangle = & \rho_{LL}\, |\psi_L(x)|^2 + \rho_{LR}\, \psi_L^*(x)\psi_R(x) \\ & + \rho_{LR}^*\, \psi_R^*(x)\psi_L(x) + \rho_{RR}\, |\psi_R(x)|^2 \, . \end{aligned} \tag{7.4}$$

The precise shape of $\langle n(x)\rangle$ still depends on the type of measurement which we perform, as this determines the shape of the modes $\psi_i(x)$.

Notwithstanding the above, we can already assess in which cases we are able to determine the off-diagonal terms ρ_{LR}. If the state is completely mixed ($\rho_{LR} = 0$) or if there is no overlap between the modes ψ_L and ψ_R, we can see that the cross-terms vanish. Therefore, we will not be able to detect coherences between the modes from in-situ measurements: mixed and pure states with the same populations ρ_{ii} will look alike. They can instead be detected if the modes overlap and interfere during the measurement, analogous to the coherences that are observed in a double-slit experiment (see Section 2.2.2). This property also extends to higher order correlation functions for larger systems and will be used in the momentum measurements in Section 7.4.

7.1.2 *Two Particles in a Double Well*

7.1.2.1 *Eigenstates and Eigenenergies*

Now, we will look at systems containing two particles with different spins. They can be described in the four-dimensional subspace shown in the last line of Table 7.1. This type of system is the fundamental building block of the half-filled Hubbard model, since it contains both nearest-neighbor tunneling and on-site interactions.

If the tilt is negligible ($\Delta = 0$), we can write the eigenenergies as

$$\begin{aligned} E_a &= 2J\,\alpha_-(U/4J) \\ E_b &= U \\ E_c &= 2J\,\alpha_+(U/4J) \\ E_d &= 0 \end{aligned} \tag{7.5}$$

and the (unnormalized) eigenstates as

$$\begin{aligned} |a\rangle &= |{\uparrow\downarrow},\cdot\rangle + \alpha_+(U/4J)\,(|{\uparrow},{\downarrow}\rangle + |{\downarrow},{\uparrow}\rangle) + |\cdot,{\uparrow\downarrow}\rangle \\ |b\rangle &= |{\uparrow\downarrow},\cdot\rangle - |\cdot,{\uparrow\downarrow}\rangle \\ |c\rangle &= |{\uparrow\downarrow},\cdot\rangle + \alpha_-(U/4J)\,(|{\uparrow},{\downarrow}\rangle + |{\downarrow},{\uparrow}\rangle) + |\cdot,{\uparrow\downarrow}\rangle \\ |d\rangle &= |{\uparrow},{\downarrow}\rangle - |{\downarrow},{\uparrow}\rangle\,, \end{aligned} \tag{7.6}$$

where we have used $\alpha_\pm(x) \equiv x \pm \sqrt{1+x^2}$ as a shorthand. Note that we have chosen the sites as the modes which we occupy with particles of either spin in this notation. Because we have an equal number of spin and spatial modes in this particular system, it is equivalently possible to instead choose the spin as the modes to construct a basis (c.f. the notation in [Mur⁺15b]).

First, let us look at the symmetry of the eigenstates. While we are treating systems of identical particles (both are ^{6}Li atoms), they can be distinguished by their spatial mode and their spin mode. As these two quantum numbers are not coupled by the Hamiltonian, the total state of each atom can be expressed as a product of the state in position space and in spin space, $\psi(x) \otimes \chi(m_F)$.

Also for two-particle states, the wavefunction can still be separated into position and spin Hilbert spaces. However, it must be totally antisymmetric under particle exchange due to Fermi statistics. For the expressions given in (7.6), we can determine the symmetry of the spatial wavefunction by swapping the position of the two particles (L ↔ R): The first three states are spatially symmetric, and the fourth state is spatially antisymmetric. Conversely, if we swap the spins ($\uparrow \leftrightarrow \downarrow$), the first three states are all spin singlets and antisymmetric under exchange, while the fourth state is in a symmetric spin triplet state (with a spin projection value of zero). Under exchange of both quantum numbers, i.e., particle exchange, all states are antisymmetric.

7.1.2.2 *Occupation Numbers*

We can characterize the eigenstates (7.6) by measuring the occupation of the basis states of our system. While this kind of measurement does not give us explicit information about the coherence between the basis states, it does allow us to discern between the different eigenstates. For all values of the interaction, except at $U = 0$, each eigenstate has a unique distribution of the occupation of the basis states. Therefore, if we assume that our states are pure, this measurement allows us to precisely determine the eigenstate that we have prepared.

In fact, we can already identify the eigenstates by measuring just the fraction of single and double occupancy of the spatial modes without spin-resolution. The expectation values for the different eigenstates are

$$\langle D\rangle = \frac{1}{N}\sum_i 2\langle D_i\rangle = \begin{cases} \left(1+(\alpha_+(U/4J))^2\right)^{-1} & \text{for state } |a\rangle \\ 1 & \text{for state } |b\rangle \\ \left(1+(\alpha_-(U/4J))^2\right)^{-1} & \text{for state } |c\rangle \\ 0 & \text{for state } |d\rangle \end{cases} \tag{7.7}$$

for the double occupancy and $\langle m\rangle = \frac{1}{N}\sum_i\langle m_i\rangle = 1-\langle D\rangle$ for the single occupancy (lines in Figure 7.1), using the local moments $(n_{i,\uparrow}-n_{i,\downarrow})^2$ and local double occupancy $n_{i,\uparrow}n_{i,\downarrow}$ from eq. (2.46).

7.2 IN-SITU MEASUREMENTS

Our first measurements of the double well system have the goal to show that we could prepare states with a high fidelity and purity (published in [Mur⁺15b]). We prepare the system by adiabatically connecting a decoupled, tilted double well to a coupled, balanced double well as described in Section 4.4. This means that we can easily access the ground state if we start with a state with two particles in the deeper well ($E=-2\Delta$) or the highest-energy state if we start with two particles in the shallower well ($E=+2\Delta$). After introducing a coupling on the order of $J\approx 70\,\text{Hz}$ and balancing the wells to $\Delta=0$, we ramp the interaction to $-1.3<U/J<10.1$ with the magnetic Feshbach resonance[1]. More details on the preparation and calibration of this coupled, interacting double-well system can be found in [Mur15; Ber17].

Before performing our measurements, we also test the adiabaticity of our preparation scheme by reversing the ramps and measuring the final ground-state fraction in a single well. We conclude that the preparation scheme for the double well has the same fidelity as the preparation of the ground state of a single well, i.e., up to 97 %. We therefore expect our system to be in an almost completely pure state.

7.2.1 *Occupation Number Measurements*

To demonstrate which states we could prepare, we measure the occupation number for each site. Experimentally, we first freeze the oc-

---

[1] Because we use low-field preparation for this measurement, our access to large negative scattering lengths is limited.

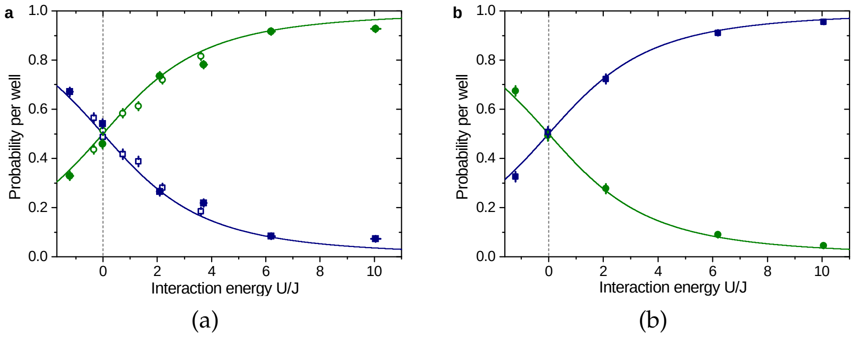

(a) (b)

Figure 7.1: Double occupancy (blue) and single occupancy (green) for state $|a\rangle$ (a) and state $|c\rangle$ (b). The open (filled) symbols were measured for $J/h \approx 142\,\mathrm{Hz}$ ($J/h \approx 67\,\mathrm{Hz}$). The lines show the curves obtained from eq. (7.7). From [Mur+15b].

cupation number of our system by quenching the tunnel coupling to $J = 0$. Then, we reduce the magnetic field to zero and release the atoms from the site which we do not want to detect. Finally, we transfer the atoms from the remaining site into a MOT and measure the atom number in the MOT (see Section 5.1 for details on the detection method).

The resulting occupation numbers (Figure 7.1) convincingly[2] match the theoretical predictions from eq. (7.7) for the ground state $|a\rangle$ and the highest excited state $|c\rangle$ over the entire range of accessible interactions. At zero interactions, where the two particles are uncorrelated, single occupancy is as likely as double occupancy. At strong repulsive interactions, particles in the ground state avoid double occupancy, while particles in the highest excited state in fact prefer double occupancy.

7.2.2 *Spectroscopic Measurements*

As the occupation number measurements suggest that we can prepare eigenstates of the double-well system, we can now study the eigenenergies of the system (7.5) (see curves in Figure 7.3). Without interactions ($U = 0$), there is one state with an energy $-2J$, two with zero energy and one with $2J$. This is consistent with the four ways of combining the uncorrelated single-particle energies from Section 7.1.1. For strong interactions $|U| \gg J$, there are two doublets of states, one with an energy approximately proportional to U and one with an energy approximately independent of U. The states $|b\rangle$ and $|d\rangle$, whose composition does not change with U, show an exact linear behavior with U, while the other states asymptotically approach them

---

[2] We did take the finite preparation fidelity into account in the model shown in the figure [Mur+15b; Mur15].

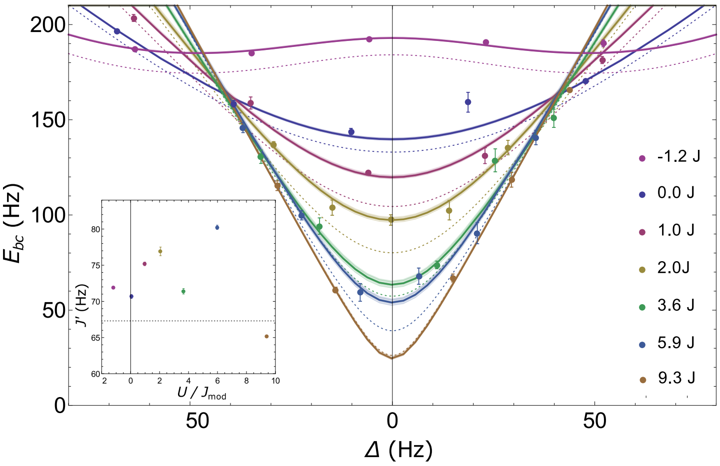

Figure 7.2: Resonance energy E_{bc} vs. tilt Δ. Different values of the interaction strength are shown in different colors. The dotted line shows the prediction from the Hubbard model without free parameters ($J/h = 67\,\text{Hz}$). The fits (shown as solid lines with error bands) are compatible with a larger, effective tunnel coupling J' (see inset). From [Mur⁺15b].

as $4J^2/U$. As we had seen in Section 2.4.2, this is the energy scale related to the superexchange process.

For the measurement of the energy spectrum, we use trap modulation spectroscopy. First, we initialize state $|c\rangle$ at different interaction strengths. Then, we modulate the total intensity of the microtraps sinusoidally between 30 Hz and 300 Hz. The intensity modulation results in a modulation of the tunnel coupling with an amplitude of $0.11J$. We choose this small modulation amplitude to minimize the perturbation of our system.

For the frequency matching $E_{bc} = E_c - E_b$, a fraction of the atoms is transferred to state $|b\rangle$. We measure the resonance position from the occupation of the eigenstates $|c\rangle$ and $|b\rangle$. We do this by reversing the preparation procedure after the modulation and measuring the occupation of the original microtrap. If the system has remained in state $|c\rangle$, both atoms return to the original microtrap, while it will be singly occupied if the system has been transferred to state $|b\rangle$ (see also Figure 4.12).

This measurement also shows that the energy depends on the tilt of the system. Because we could not guarantee that our system was perfectly balanced, we decided to perform the spectroscopy for different values of Δ and to extract the value for $\Delta = 0$ from these measurements by fitting a numerical model to it. We noticed that the model without free parameters did not fit our data and suspected that the tunnel coupling J may have been modified due to the modulation. Therefore, we decided to leave J as a free parameter and to fit E_{bc}. As we can see in Figure 7.2, the value of E_{bc} at $\Delta = 0$ can then be read of as the ordinate.

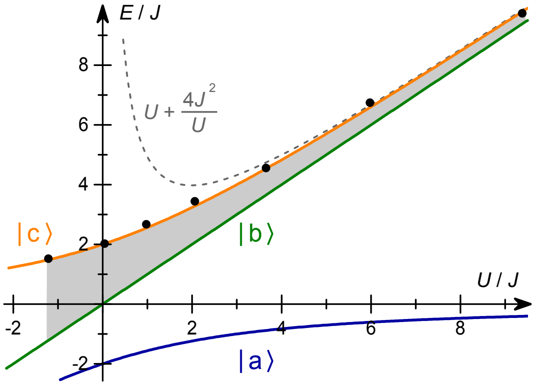

Figure 7.3: Energy of the double well extracted from Figure 7.2 at $\Delta = 0$, versus the interaction energy. An energy offset of U has been added to show the measurements together with the complete spectrum of the double-well Hubbard model. The dotted line shows the asymptotic value for $U/J \gg 1$. From [Mur+15b].

If we look at the energy against the interaction strength (Figure 7.3), we see that the values match the theoretical prediction, both for the regime where $E_{bc} \approx 2J$ as well as for the superexchange regime where $E_{bc} \propto 4J^2/U$. This suggests that we should be able to see effects caused by the superexchange in our system, e.g., spin ordering.

7.3 SINGLET-TRIPLET OSCILLATIONS

While the occupation number measurements indicates that we had prepared an eigenstate, they are not able to directly distinguish between pure and mixed states with the same mode populations. If we want to show that we have prepared a pure state, we must measure the coherence between the modes of our system. These coherences appear as the off-diagonal terms of the density matrix (see Section 2.1.2). For our system consisting of two distinguishable spins in a double well, the general density matrix

$$\rho = \begin{pmatrix} \rho_{11} & \rho_{12} & \rho_{13} & \rho_{14} \\ & \rho_{22} & \rho_{23} & \rho_{24} \\ & & \rho_{33} & \rho_{34} \\ \text{h.c.} & & & \rho_{44} \end{pmatrix} \tag{7.8}$$

contains six entries describing coherences between different modes, each of which consists of a magnitude and a phase. The indices of the entries refer to the basis states from Table 7.1.

There are multiple ways of determining the off-diagonal elements of this matrix experimentally. A direct method is to measure the correlation functions, e.g., $\langle \hat{n}_\uparrow(x) \rangle$, $\langle \hat{n}_\downarrow(x) \rangle$, or $\langle \hat{n}_\uparrow(x_1)\hat{n}_\downarrow(x_2) \rangle$, after time-of-flight expansion. However, we have only been able to mea-

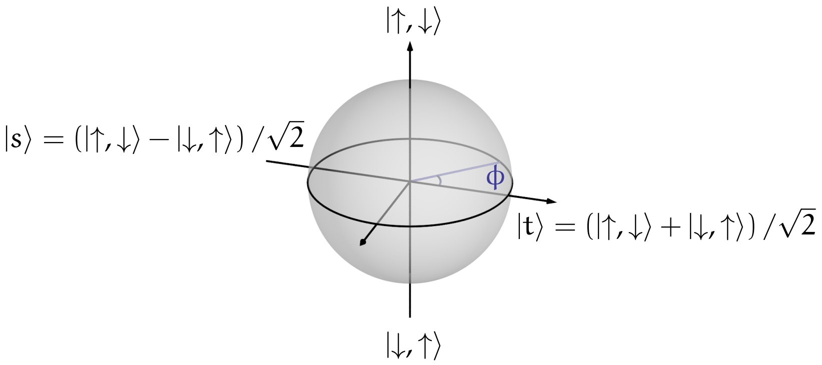

Figure 7.4: Bloch sphere of states spanned by the basis $|\uparrow,\downarrow\rangle$, $|\downarrow,\uparrow\rangle$ in the singly-occupied sub-space. Pure states lie on its surface, while mixed states lie in the interior. The states will time-evolve along lines of constant latitude around the axis connecting the eigenstates of the system.

sure these quantities after we having implemented the matterwave microscope (Chapter 5). Still, with our MOT imaging, we were able to detect one of the off-diagonal density matrix elements by measuring the fraction of singlets and triplets via singlet-triplet oscillations.

In our double-well system, it is convenient to perform the measurement of singlet and triplets with strong repulsive interactions ($U \gg J$). In this limit, the states $|a\rangle$ and $|d\rangle$ can be expressed entirely in the subspace of singly-occupied states $\{|\uparrow,\downarrow\rangle, |\downarrow,\uparrow\rangle\}$. This subspace can be represented by the states on and in the Bloch sphere (Figure 7.4). Within this subspace, we can transform our basis to the singlet-triplet basis

$$|s\rangle = (|\uparrow,\downarrow\rangle - |\downarrow,\uparrow\rangle)/\sqrt{2} \tag{7.9a}$$

$$|t\rangle = (|\uparrow,\downarrow\rangle + |\downarrow,\uparrow\rangle)/\sqrt{2}. \tag{7.9b}$$

In this basis, the eigenstates can be identified as $|a\rangle \approx |t\rangle$ and $|d\rangle \approx |s\rangle$ for $U \gg J$.

We can now substitute these new singlet-triplet states in the expression of our partial density matrix

$$\rho_{so} = \rho_{22} |\uparrow,\downarrow\rangle\langle\uparrow,\downarrow| + \rho_{23} |\uparrow,\downarrow\rangle\langle\downarrow,\uparrow| + \rho_{23}^* |\downarrow,\uparrow\rangle\langle\uparrow,\downarrow| + \rho_{33} |\downarrow,\uparrow\rangle\langle\downarrow,\uparrow|.$$

In the $\{|s\rangle, |t\rangle\}$ basis, the partial density matrix becomes

$$\rho_{so} = \begin{pmatrix} \frac{1}{2} - |\rho_{23}| \cos\phi & \frac{1}{2}(\rho_{22} - \rho_{33}) + i|\rho_{23}| \sin\phi \\ \frac{1}{2}(\rho_{22} - \rho_{33}) - i|\rho_{23}| \sin\phi & \frac{1}{2} + |\rho_{23}| \cos\phi \end{pmatrix}, \tag{7.10}$$

where we have expressed the complex density matrix element ρ_{23} in its polar form, $\rho_{23} = |\rho_{23}|\, e^{i\phi}$. By projecting our initial state on the singlet or triplet state,

$$\langle P_s \rangle = \rho_{ss} = \frac{1}{2} - |\rho_{23}| \cos\phi \tag{7.11a}$$

$$\langle P_t \rangle = \rho_{tt} = \frac{1}{2} + |\rho_{23}| \cos\phi, \tag{7.11b}$$

we can measure the coherences between the $|\uparrow,\downarrow\rangle$ state and the $|\downarrow,\uparrow\rangle$ state from a population measurement in the singlet-triplet basis. As projection operators, we used $\hat{P}_j = |j\rangle\,\langle j|$.

However, the singlet-triplet populations only contain a term which depends on both the magnitude and the phase of ρ_{23}. We can separate the two contributions by making the phase time-dependent. The initial state will rotate on the Bloch sphere, which introduces an oscillation of $\langle P_s \rangle$ and $\langle P_t \rangle$. We can then identify $|\rho_{23}|$ as the contrast of these oscillations.

To introduce this time dependence, we have to make sure that the singlet and triplet states are not eigenstates anymore. We can do this by lifting the energy degeneracy of the position basis states $|\uparrow,\downarrow\rangle$ and $|\downarrow,\uparrow\rangle$. Experimentally, we use the difference in magnetic moment of the hyperfine states $|1\rangle \equiv |\uparrow\rangle$ and $|2\rangle \equiv |\downarrow\rangle$, combined with a magnetic field gradient along the axis connecting the wells. The magnetic field gradient induces a position-dependent Zeeman shift

$$E_{\sigma,i} = -\mu_\sigma B^z(x_i), \tag{7.12}$$

where B^z is the magnetic field component along the quantization axis. The term added to the Hubbard Hamiltonian (7.1) is

$$\begin{pmatrix} 0 & 0 & 0 & 0 \\ 0 & \Delta_B & 0 & 0 \\ 0 & 0 & -\Delta_B & 0 \\ 0 & 0 & 0 & 0 \end{pmatrix}, \tag{7.13}$$

with $2\Delta_B = (\mu_\uparrow - \mu_\downarrow)(B^z(x_L) - B^z(x_R))$. For vanishing tunnel coupling and tilt, the position basis states become the eigenstates with eigenenergies $U, -\Delta_B, \Delta_B, U$. If our initial state was a coherent superposition of the basis states $|\uparrow,\downarrow\rangle$ and $|\downarrow,\uparrow\rangle$, for example, $|s\rangle$ or $|t\rangle$, it will start rotating along the latitudes of the Bloch sphere at a rate $\omega_{st} = \phi/t = 2\Delta_B/\hbar$.

To perform singlet-triplet oscillations in our experiment [Mur15], we first prepare our system as described in Section 4.3 with strong repulsive interactions ($U \approx 10\,J$). Then, we quench the tunnel coupling to zero to freeze tunneling dynamics and pin the on-site populations.

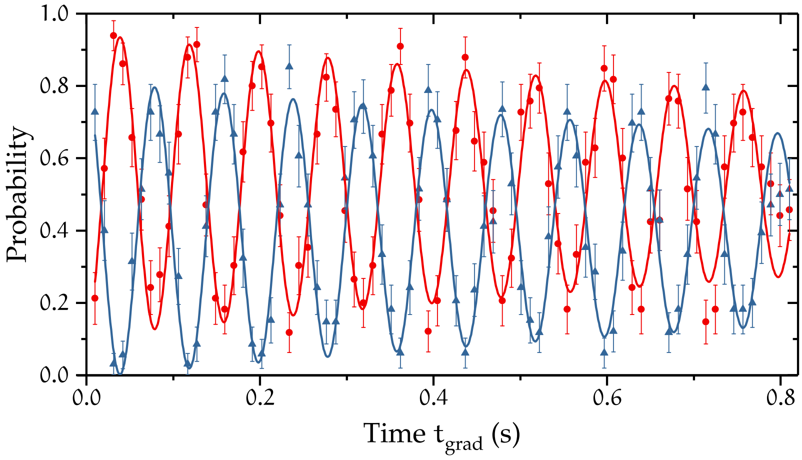

Figure 7.5: Singlet-triplet oscillations in a double well. The blue (red) points show the measured single (double) occupancy of the ground state, corresponding to a fraction of spatial singlets (triplets) as described in the text. From damped sinusoidal fits (lines), damping timescales of 1.85(39) s (1.60(39) s) were extracted. Adapted from [Mur15].

We reduce the magnetic field to below 100 G to increase the differential magnetic moment and apply a magnetic field gradient between the wells. After a time t_{grad}, we turn off the gradient again and return to high magnetic fields.

To detect the singlet and triplet fraction of our state, we merge the wells and measure the occupation in the ground state. The atoms which are in the spatial triplet state will both be in the ground state, while atoms in a spatially antisymmetric singlet state will end up in a superposition of ground and first excited state. If we release all atoms in motionally excited states and measure the atom number remaining in the ground state, we will measure two atoms if the state was projected on a spatial triplet, and one atom if the state was projected on a spatial singlet[3].

The time dynamics show the oscillations of our initial state between the singlet and the triplet state (Figure 7.5). The contrast corresponds to a value of $|\rho_{23}| = 0.414(15)$. Compared to the maximum possible value of 0.5, this shows that a large fraction of our state can be described as a pure state. Unfortunately, we cannot extract a reliable value for the initial phase ϕ, since the state will already start to evolve while the magnetic field gradient is being turned on.

A remarkable property of the singlet-triplet oscillations is the long decoherence timescale of approximately 2 s. As both the singlet and the triplet states have the same local occupation numbers and total

---

[3] Alternatively, we can measure the occupation of the spin states after performing a $\pi/2$-rotation on the hyperfine states, similar to [Kau+15]. This maps the spin triplet state on a state with spin projection 1, while the spin projection of the spin singlet state remains 0.

spin projection, they are insensitive to local fluctuations of the optical potential and global fluctuations of the offset magnetic field. Therefore, this system is part of a decoherence-free subspace.

7.4 MOMENTUM-SPACE MEASUREMENTS

With our new matterwave microscope imaging method, we can measure the position and spin of each atom in every realization of the experiment. This allows us to measure the correlation functions of our system. Compared to the singlet-triplet oscillation measurements in the previous section, the correlation functions can be used to extract different off-diagonal elements of the density matrix, including their magnitude and phase. Which specific density matrix elements can be measured depends on the order of the correlation function and the shape of the mode wavefunction $\psi_i(x)$.

7.4.1 *Two Non-Interacting Particles*

If we measure the lowest-order correlation function, this is equivalent to measuring the density distribution of one of the particles $\langle \hat{n}_\sigma(x) \rangle$. Effectively, we trace out the other particle during this measurement, resulting in the partial density matrices

$$\rho_\uparrow = \begin{pmatrix} \rho_{11} + \rho_{22} & \rho_{13} + \rho_{24} \\ \text{h.c.} & \rho_{33} + \rho_{44} \end{pmatrix} \quad \text{and} \tag{7.14a}$$

$$\rho_\downarrow = \begin{pmatrix} \rho_{11} + \rho_{33} & \rho_{12} + \rho_{34} \\ \text{h.c.} & \rho_{22} + \rho_{44} \end{pmatrix}. \tag{7.14b}$$

With these density matrices, we can treat each particle as a single-particle system (Section 7.1.1). The entries of the matrix describe the populations left and right, and the coherence between the left and right spatial mode. However, we have to keep in mind that the entries of the density matrices may look different from the (non-interacting) single-particle case if there are interactions between the particles.

Now, we can evaluate the spatial single-particle density distribution after the time-of-flight expansion. When the atoms are released from the microtraps, each spatial mode at x_i is projected on spherical waves $\propto e^{ikx_i}$. In the far field, this results in a Fourier transform of the in-situ wavefunction,

$$\psi_i(k) = \mathcal{F}(\psi_i(x)) = \mathcal{F}(w * \delta(x - x_i)) = \tilde{w}(k)\, e^{ikx_i}, \tag{7.15}$$

where the transform variable k is the momentum and the $\tilde{w}$ is the Fourier transform of the Wannier function, which we assume to be

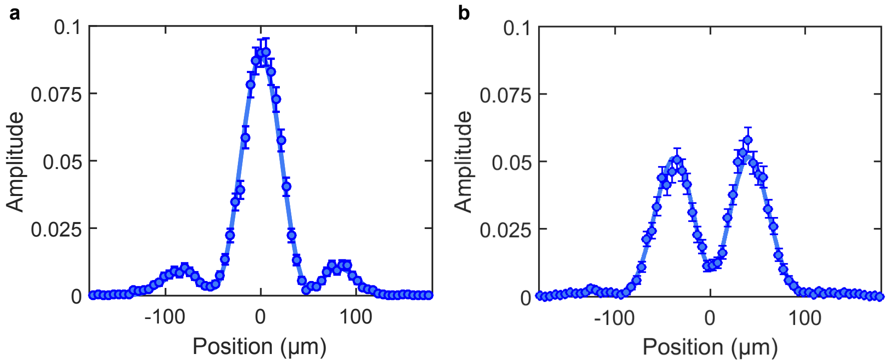

Figure 7.6: Single-particle density of non-interacting particles prepared in state $|a\rangle$ (a) or $|c\rangle$ (b). From [Ber17].

identical for each site. Inserting this expression in the density distribution (7.4), we obtain the single-particle density distribution

$$\begin{aligned}\langle n_\sigma(k)\rangle &= |\tilde{w}(k)|^2 \Big(\rho_{LL} + \rho_{RR} \\ &\qquad + |\rho_{LR}| \left(e^{i\phi}\, e^{ik(x_L - x_R)} + e^{-i\phi}\, e^{-ik(x_L - x_R)}\right)\Big) \\ &= |\tilde{w}(k)|^2 \; (1 + 2\,|\rho_{LR}| \cos(kd + \phi))\,, \end{aligned} \tag{7.16}$$

where d is the separation of the wells, and the matrix elements ρ_{ij} have to be taken from eq. (7.14). This density distribution can be related to the spatial density distribution that we measure with the matterwave microscope by transforming $\hbar k \to m\omega_{ODT}x$.

This single-particle density distribution is sufficient to describe our experiments if the two particles in the coupled double well are non-interacting. Since the wavefunction factorizes, it is reasonable that both spins can be treated as independent particles. If we prepare our system in the non-interacting ground state or the highest excited state, its state should ideally be described by

$$|a\rangle \longrightarrow (|\uparrow,\cdot\rangle + |\cdot,\uparrow\rangle) \otimes (|\downarrow,\cdot\rangle + |\cdot,\downarrow\rangle) \quad \text{and} \tag{7.17a}$$

$$|c\rangle \longrightarrow (|\uparrow,\cdot\rangle - |\cdot,\uparrow\rangle) \otimes (|\downarrow,\cdot\rangle - |\cdot,\downarrow\rangle), \tag{7.17b}$$

respectively. The corresponding density matrices would be

$$\rho_a = \frac{1}{2}\begin{pmatrix} 1 & 1 \\ 1 & 1 \end{pmatrix} \quad \text{and} \tag{7.18a}$$

$$\rho_c = \frac{1}{2}\begin{pmatrix} 1 & -1 \\ -1 & 1 \end{pmatrix} = \frac{1}{2}\begin{pmatrix} 1 & e^{i\pi} \\ e^{-i\pi} & 1 \end{pmatrix}. \tag{7.18b}$$

With these density matrices, we expect spatial density distributions

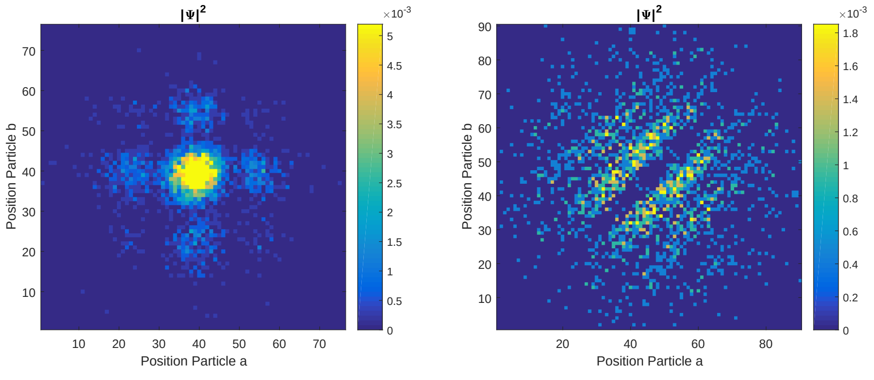

(a)

(b)

Figure 7.7: Correlated density of two non-interacting particles in a double well. (a) Two particles in different hyperfine states. (b) Two particles in the same hyperfine state.

$$n_{\sigma,a}(k) = |\tilde{w}(k)|^2 \ (1+\cos(kd)) \quad \text{and} \tag{7.19a}$$

$$n_{\sigma,c}(k) = |\tilde{w}(k)|^2 \ (1-\cos(kd)) \,. \tag{7.19b}$$

The density distributions that we measure in our experiment qualitatively match the expected oscillatory patterns (Figures 7.6 and 7.7a). We can fit the data with eq. (7.16), where we approximate the envelope function $\tilde{w}(k)$ with a Gaussian. From the fits, we extract the parameters[4] $\phi_a = -0.007(24)\,\pi$, $|\rho_{LR,a}| = 0.449(7)$, and $\phi_c = 0.957(23)\,\pi$, $|\rho_{LR,c}| = 0.387(7)$. We see that the magnitude of the coherence is slightly reduced from its maximum possible value, $\rho_{LR} \leqslant \sqrt{\rho_{LL}\rho_{RR}} \leqslant 1/2$. Due to the lack of in-situ data from these measurements, we cannot determine the values for ρ_{LL} and ρ_{RR} in order to distinguish whether this due to an imbalance $\rho_{LL} \neq \rho_{RR}$, or due to impurity of the state, which would show as $\operatorname{Tr}\rho^2 = \rho_{LL}^2 + \rho_{RR}^2 + 2\,|\rho_{LR}|^2 < 1$.

For the width of the envelope, which is determined by the local wavefunctions in the individual microtraps, we find $\sigma_a = 43.4(5)\,\mu m$ and $\sigma_a = 47.8(5)\,\mu m$, while we find $d_a = 102(1)\,\mu m$ and $d_c = 96.1(7)\,\mu m$ for the separation of the wells. Both the larger width and smaller separation of the energetically higher state suggest that we may have excited to higher bands during the preparation of this state, which would also explain the reduced purity of this state.

7.4.2 *Two Indistinguishable Particles*

For two particles in the same hyperfine state (same spin), we might expect similar results as in the previous section, since identical particles cannot interact via contact interactions. However, due to their

---

[4] We did not extract the parameters $\rho_{13} + \rho_{24}$, etc., from eq. (7.14) from these fits, as the spatial density distribution of both spins was combined in this data set.

indistinguishability, these particles are in fact not independent from each other. When looking at the initial state of the Hubbard model, the Pauli principle forbids the particles to occupy the same site. Effectively, they block each other in position space and only the band-insulating state $|\sigma,\sigma\rangle$ is available (see Table 7.1). Our initial state therefore resembles the states studied in [Föl⁺05; Rom⁺06] on a smaller scale (see Section 2.4.3 for a summary) and we may apply the same evaluation as was used in those experiments.

We can begin to describe our system by evaluating the expectation value for the single-particle density distribution as in eq. (2.18),

$$\langle \hat{n}(k) \rangle = |\tilde{w}(k)|^2 \sum_{i,j=L,R} e^{ik(x_i - x_j)} \langle \hat{n}_i \rangle \delta_{ij} = |\tilde{w}(k)|^2 . \tag{7.20}$$

We have already taken into account that the cross-terms vanish for fermions, e.g., $\hat{a}_L^\dagger \hat{a}_R |1,1\rangle = 0$. Consequently, we do not observe density oscillations, but only the transformed envelope function $|\tilde{w}(k)|^2$ as the single-particle density (Figure 7.8a).

For the correlated density distribution, we can relate our observable to the two-point correlation function:

$$\langle \hat{n}(k_1)\hat{n}(k_2) \rangle = \langle \hat{n}(k_1) \rangle \delta(k_1 - k_2) + \left\langle \hat{\Psi}^\dagger(k_1)\hat{\Psi}^\dagger(k_2)\hat{\Psi}(k_2)\hat{\Psi}(k_1) \right\rangle \tag{7.21}$$

By inserting the wavefunctions of the modes into the fermionic equivalent of eq. (2.28) (see Appendix A), we obtain

$$G^{(2)}(k_1, k_2) = |\tilde{w}(k_1)|^2 \, |\tilde{w}(k_2)|^2 \big(1 - \cos((k_1 - k_2)d)\big). \tag{7.22}$$

The correlation pattern of two indistinguishable particles along the relative coordinate is a result of the Hanbury Brown and Twiss effect. This behavior is caused not by specifically preparing an antisymmetric initial state, e.g., through interactions, but by the required antisymmetry of two indistinguishable fermions.

In the experiment, both the single-particle density and the correlated density qualitatively look as we expect from eq. (7.20) and (7.22) (Figures 7.8a and 7.7b). By integrating along the diagonal CoM-axis, we can display a density profile along the relative coordinate $k_1 - k_2$ as in Figure 7.8b. Both fits to the data of Figure 7.8 show a similar envelope with a width of approximately 82 µm and, in the correlated density, fringes are visible with the expected phase. For the correlated density, there is no peak visible in the center at $k_1 = k_2$ as predicted by the first term of eq. (7.21). This is an artifact from our imaging scheme which cannot resolve two atoms if they are too close to each other.

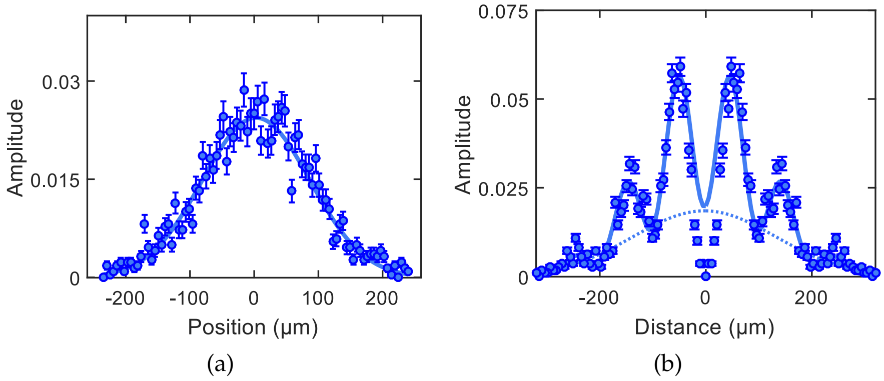

(a) (b)

Figure 7.8: Two indistinguishable fermions in a double well. (a) Single-particle density distribution $\langle \hat{n}(k) \rangle$. (b) Correlated density left $\langle \hat{n}(k_1)\hat{n}(k_2) \rangle$. The solid lines are fits to the data, the dotted line shows a Gaussian offset which effectively accounts for the reduced contrast. Adapted from [Ber17].

For the same reason, we seem to have perfect contrast for the central fringe. However, the actual contrast can be seen from the neighboring fringes and is smaller than unity. This is now more difficult to explain than for a system containing two distinguishable particles, because a system with a Hilbert space dimension of 1 does not support mixed states. We suspect that the reduced contrast is caused by unintentionally including systems with more than two atoms per spin state or systems with motionally excited atoms in our data set.

7.4.3 *Two Repulsively-Interacting Particles*

In our final set of measurements, we revisit the systems with repulsive interactions studied in Sections 7.2 and 7.3. Due to the interactions, we cannot describe the particles as individual particles in independent subspaces. Therefore, measuring the single-particle density distribution is not sufficient to characterize the two-particle system, similar to the case of two indistinguishable fermions.

Instead, we measure the correlated densities $\langle n_\uparrow(x_1) n_\downarrow(x_2) \rangle$, which is equivalent to measuring the two-point correlation function (see Chapter 2):

$$\langle \hat{n}_\uparrow(x_1)\hat{n}_\downarrow(x_2) \rangle = \left\langle \hat{\Psi}^\dagger_\uparrow(x_1)\hat{\Psi}^\dagger_\downarrow(x_2)\hat{\Psi}_\downarrow(x_2)\hat{\Psi}_\uparrow(x_1) \right\rangle \equiv G^{(2)}_{\uparrow\downarrow}(x_1, x_2). \tag{7.23}$$

By inserting the Fock-space expansion of the field operators from eq. (2.15) and the density matrix (7.8), we obtain

$$\begin{aligned} G^{(2)}_{\uparrow\downarrow}(x_1, x_2) = \sum_{ijklmn} & \psi^*_i(x_1)\psi^*_j(x_2)\psi_k(x_2)\psi_l(x_1)\, \rho_{mn} \\ & \times \langle n|\, \hat{a}^\dagger_{\uparrow,i}\hat{a}^\dagger_{\downarrow,j}\hat{a}_{\downarrow,k}\hat{a}_{\uparrow,l}\, |m\rangle\,. \end{aligned} \tag{7.24}$$

This expression contains all entries of the density matrix ρ_{mn}, because the different combinations of annihilation and creation operators let all possible states $|m\rangle, |n\rangle$ contribute to the sum. By performing measurements of the correlated density, we can therefore obtain full information about the density matrix of the two-particle system, both of its populations and coherences.

Which of the elements ρ_{mn} can be extracted from a particular measurement again depends on the character of the mode wavefunctions $\psi_i(x)$ for this measurement. For our momentum-space measurements with the matterwave microscope, we insert the mode wavefunction (7.15), and the correlated density distribution (7.24) evaluates to

$$\begin{aligned} \frac{\langle \hat{n}_\uparrow(k_1)\hat{n}_\downarrow(k_2)\rangle}{|\tilde{w}(k_1)|^2\,|\tilde{w}(k_2)|^2} &= \rho_{11} + \rho_{22} + \rho_{33} + \rho_{44} \\ &+ 2\,|\rho_{13} + \rho_{24}|\, \cos(k_1 d + \phi_1) \\ &+ 2\,|\rho_{12} + \rho_{34}|\, \cos(k_2 d + \phi_2) \\ &+ 2\,|\rho_{23}|\, \cos(kd + \phi_{23}) + 2\,|\rho_{14}|\, \cos(Kd + \phi_{14}). \end{aligned} \tag{7.25}$$

Here, the sum and difference of the momenta have been defined as $K \equiv k_1 + k_2$ and $k \equiv k_1 - k_2$, respectively, and the phases ϕ_1 and ϕ_2 are associated to the combined density matrix elements $(\rho_{13} + \rho_{24})$ and $(\rho_{12} + \rho_{34})$.

From the amplitudes and phases of the different momentum oscillations in (7.25), we can determine the complex-valued density matrix elements $(\rho_{13} + \rho_{24})$, $(\rho_{12} + \rho_{34})$, ρ_{14}, and ρ_{23}. For this, we define a basis of fitting functions consisting of horizontal, vertical, diagonal, and anti-diagonal sines and cosines (Figure 7.9). Additionally, we fit an offset term to account for the sum of the populations, $\rho_{11} + \rho_{22} + \rho_{33} + \rho_{44}$.

With these functions, we fit our measurements for different repulsive interactions (Figure 7.10). We see that, for increasing interactions, the interference pattern in the single-particle coordinates k_i becomes suppressed, while an interference pattern along the relative coordinate k emerges. The relative-momentum interference pattern entirely depends on ρ_{23}, a quantity which is absent, e.g., in the single-particle density matrices (7.14). This suggests that the two particles are strongly correlated. In contrast to the indistinguishable particles, where the correlations are a consequence of the fermionic antisymmetrization requirement, the correlations in this system originate from the strong repulsive interactions.

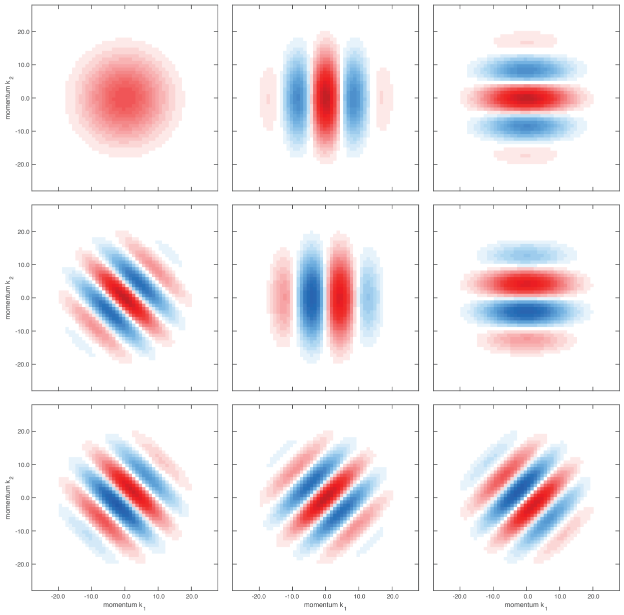

Figure 7.9: Basis functions used for fitting the measured correlated densities $\langle \hat{n}_\uparrow(k_1)\hat{n}_\downarrow(k_2)\rangle$ (eq. (7.25)). The envelope $\tilde{w}$ has been fit with a Gaussian.

7.5 ENTANGLEMENT IN THE DOUBLE WELL

Our double well containing two particles can also serve as a minimal system to study entanglement. As the system is described by two Hilbert spaces (position and spin) with two modes each (L,R and $\uparrow, \downarrow$), it is possible to share entanglement between two partitions of the system [DDW06]. With the density matrix elements from Sections 7.3 and 7.4, we can evaluate different entanglement measures introduced in Section 2.3 to detect the entanglement in our systems.

7.5.1 *Entanglement Witnesses*

First, we can construct an entanglement witness following a procedure similar to [Kau+15]. Starting with a separable state $\rho = \rho_\uparrow \otimes \rho_\downarrow$, we can determine bounds for $\rho_{23} = \rho_{\uparrow,LR}\rho_{\downarrow,RL}$. For its magnitude, we find

$$\begin{aligned} |\rho_{23}| &= \left|\rho_{\uparrow,LR}\right| \left|\rho_{\downarrow,RL}\right| \\ &\leqslant \sqrt{\rho_{\uparrow,LL}\rho_{\uparrow,RR}}\sqrt{\rho_{\downarrow,LL}\rho_{\downarrow,RR}} = \sqrt{\rho_{11}\rho_{44}} = \sqrt{\rho_{22}\rho_{33}} \\ &\leqslant \frac{1}{4}. \end{aligned} \tag{7.26}$$

Note that the labels L and R stand for the modes of the single-particle Hilbert space, as in eq. (7.2), and the numeric indices for the modes of the two-particle Hilbert space, as in eq. (7.8). In the inequality in the

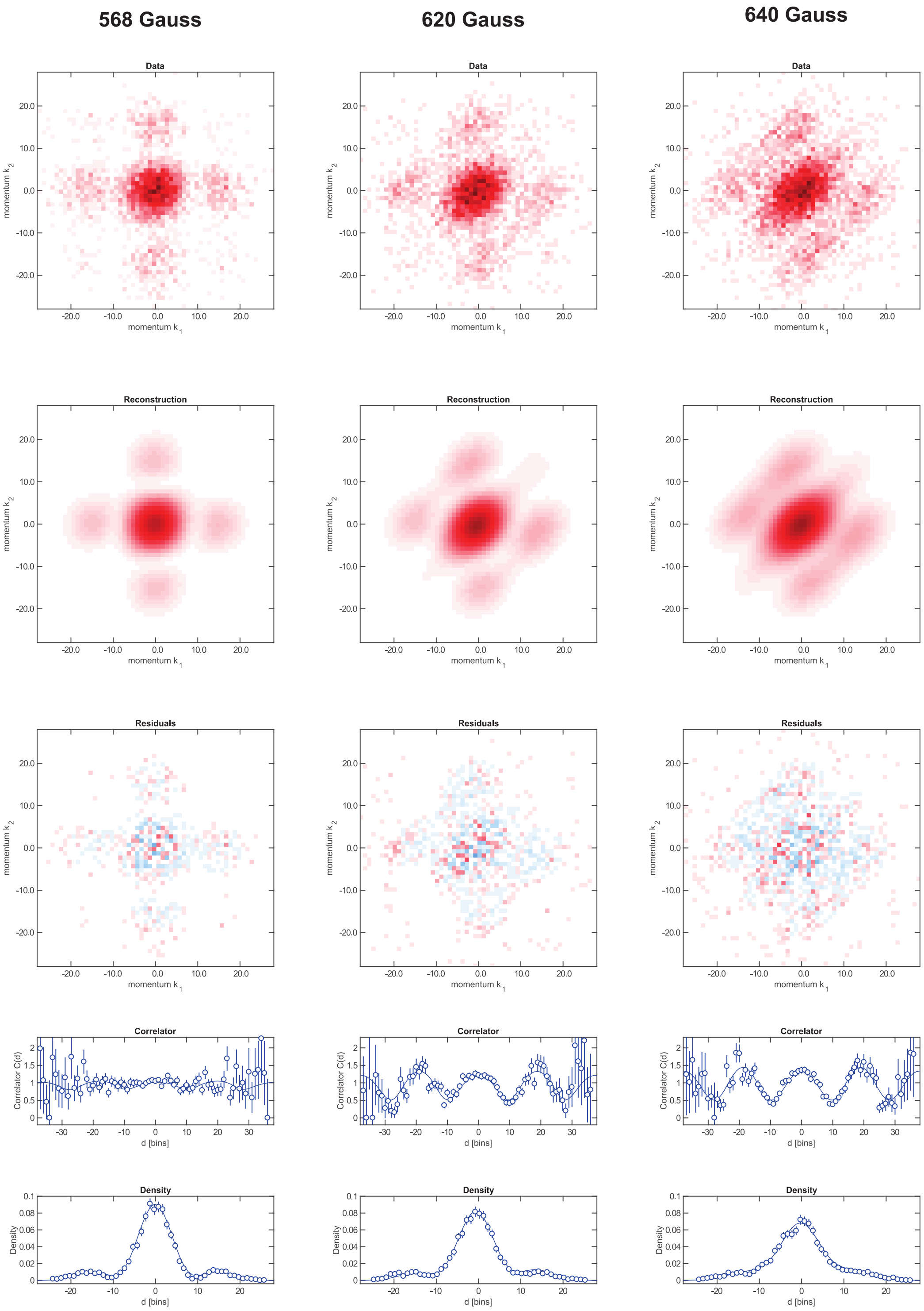

Figure 7.10: Fitted correlated densities for three different interaction strengths. The magnetic fields are equivalent to $U/J = 0$, 4.3, and 7.7, respectively. The rows show, from top to bottom, the measured data, the fitted function, the residuals, the profile along the relative coordinate k, and the profile along the single-particle coordinate k_1.

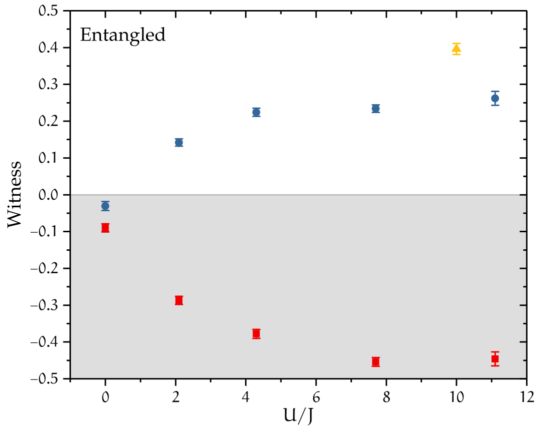

Figure 7.11: Entanglement witnesses measured in the double well. The blue circles (red squares) show the witness W (Y) from the correlated density measurements, the yellow triangle shows W obtained from the singlet-triplet oscillations. The white area above zero certifies entanglement.

second line, we used from eq. (2.5) that the magnitude of coherences is limited by the corresponding populations. We then expressed the product of the single-particle populations as two different combinations of the two-particle populations, using $\rho_{11} = \rho_{\uparrow,LL}\rho_{\downarrow,LL}$, etc. As the particles must be in either one of the sites, $\rho_{\sigma,LL} + \rho_{\sigma,RR} = 1$, we obtain the upper bound of $1/4$ if both sites have equal populations $\rho_{\sigma,LL} = \rho_{\sigma,RR} = 1/2$.

We can then define an entanglement witness using the first inequality from (7.26),

$$W = |\rho_{23}| - \sqrt{\rho_{11}\rho_{44}}. \tag{7.27}$$

If it evaluates to a positive value for a state, this state cannot be explained by any separable states, therefore it must be entangled. As the products of the populations $\rho_{11}\rho_{44}$ and $\rho_{22}\rho_{33}$ are not necessarily equal for non-separable states, we have chosen the combination which provides the strictest bound for separability in our system. A similar entanglement witness can be constructed from the density matrix element ρ_{14} as

$$Y = |\rho_{14}| - \sqrt{\rho_{22}\rho_{33}}. \tag{7.28}$$

Which of these witnesses is more suitable to detect entanglement depends on the specific state in question. The results using the density matrix elements obtained from the correlated density measurements (Section 7.4) and the singlet-triplet oscillations (Section 7.3) are displayed in Figure 7.11 and listed in Table E.2. Note that we used theoretical values derived from the eigenstates (7.6) to estimate the

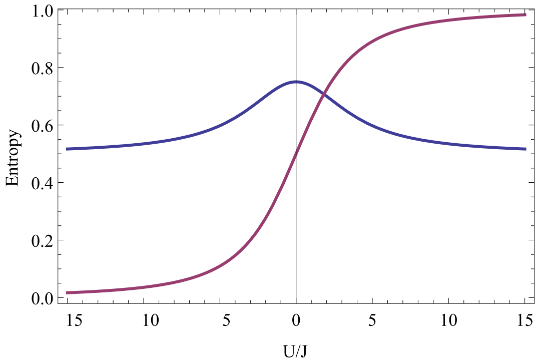

Figure 7.12: Mode entanglement in the double well calculated with the linear entropy (blue line) and entanglement of particles (magenta line).

values for the populations, as we could not extract in-situ information from our measurements[5]. We can see that, for repulsive interactions (see [Ber17] for a derivation of the values), the witness W shows that our states are entangled, while we cannot make any statement for zero interactions.

7.5.2 *Entanglement Entropy*

Next, let us look at the entanglement entropies that we can determine from the measured density matrix elements. We can calculate the mode entanglement shared between the two spatial modes by tracing out one of the sites. This leaves us with a Hilbert space spanned by the basis states $|\uparrow\downarrow\rangle$, $|\uparrow\rangle$, $|\downarrow\rangle$, and $|0\rangle$, and a density matrix

$$\rho_L = \begin{pmatrix} \rho_{11} & & & \\ & \rho_{22} & & \\ & & \rho_{33} & \\ & & & \rho_{44} \end{pmatrix}. \tag{7.29}$$

It contains no coherences because of particle number conservation on the site, and because we have no mechanism that flips the spin. The linear entropy (2.38) becomes $S_{\text{lin}} = 1 - \sum_i \rho_{ii}^2$.

When evaluated for the pure ground state $|a\rangle$ [Zan02], we find that $S_{\text{lin}} = 1 - \frac{1}{2}\frac{\alpha_+^4+1}{(\alpha_+^2+1)^2}$ is maximal without interactions and decreases for repulsive and attractive interactions (blue line in Figure 7.12). Without interactions, all modes are equally occupied, and therefore the subsystems also maximize their entropy (and mode entanglement). For

---

[5] Even though we did determine $\rho_{11} + \rho_{44}$ and $\rho_{22} + \rho_{33}$ as the single and double occupancies in Section 7.2, these measurements were performed roughly two years prior to the measurements with the matterwave microscope. Therefore, we cannot assume that those measurements were performed with comparable settings and preparation fidelities.

strong repulsive interactions, only the spin entropy remains while the density entropy vanishes, which reduces the mode entanglement. Also the Rényi entropy or the von Neumann entropy show a similar behavior for the mode entanglement.

This result is somewhat counter-intuitive as, for strong repulsion, the ground state resembles a Bell state, which we know to be a maximally-entangled state. To recover this result, we have to look at the entanglement of particles (eq. (2.42)) instead of the mode entanglement. The density matrix (7.29) can be separated in three parts with total particle numbers $n = 2, 1, 0$:

$$\rho_L^{(2)} = 1, \quad \rho_L^{(1)} = \frac{1}{\rho_{22} + \rho_{33}} \begin{pmatrix} \rho_{22} & \\ & \rho_{33} \end{pmatrix}, \quad \rho_L^{(0)} = 1, \tag{7.30}$$

which have been normalized separately. These three cases occur with probabilities ρ_{11}, $\rho_{22} + \rho_{33}$ and ρ_{44}. The entanglement of particles then becomes

$$E_{P,\mathrm{lin}} = \frac{2\rho_{22}\rho_{33}}{\rho_{22} + \rho_{33}} \tag{7.31a}$$

$$E_{P,\mathrm{Ren2}} = -\left(\rho_{22} + \rho_{33}\right) \log_2 \frac{\rho_{22}^2 + \rho_{33}^2}{(\rho_{22} + \rho_{33})^2} \tag{7.31b}$$

$$\begin{aligned} E_{P,\mathrm{vN}} = &- \rho_{22} \log_2 \rho_{22} - \rho_{33} \log_2 \rho_{33} \\ &+ \left(\rho_{22} + \rho_{33}\right) \log_2(\rho_{22} + \rho_{33}), \end{aligned} \tag{7.31c}$$

where the first line has been calculated using the linear entropy, the second using the second-order Rényi entropy and the third using the von Neumann entropy (or entanglement of formation). For the ground state, they all evaluate to

$$E_{P,\mathrm{GS}} = \frac{(\alpha_+(U/4J))^2}{1 + (\alpha_+(U/4J))^2}. \tag{7.32}$$

For strong repulsive interactions (magenta line in Figure 7.12), the entanglement of particles becomes unity and we recover the maximally-entangled Bell state. For strong attractive interactions, we would detect no entanglement of particles, as both particles would always be detected in the same spatial mode.

From eq. (7.31) we can see that the spatial mode entanglement only depends on the populations which we cannot currently measure. Instead, we can determine the mode entanglement in the spin subspaces (see eq. (7.14)). With these density matrices, we can determine the purities

$$V_\uparrow = (\rho_{11} + \rho_{22})^2 + (\rho_{33} + \rho_{44})^2 + 2|\rho_{13} + \rho_{24}|^2 \tag{7.33a}$$

$$V_\downarrow = (\rho_{11} + \rho_{33})^2 + (\rho_{22} + \rho_{44})^2 + 2|\rho_{12} + \rho_{34}|^2. \tag{7.33b}$$

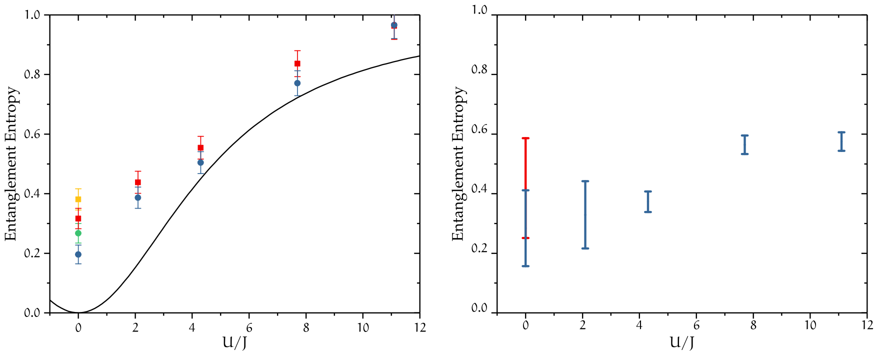

(a) (b)

Figure 7.13: (a) Spin entanglement entropies $S_{\sigma,\text{Ren2}} = -\log_2 V_\sigma$. The squares show $S_\uparrow$, the circles $S_\downarrow$. Red and blue points are from ground state measurements, the yellow and green points from the excited state measurements. The line shows the prediction for a pure ground state $|a\rangle$. (b) Entanglement entropies of the entire system, given as an interval of $S_{\text{tot,Ren2}} = -\log_2 V$. The blue bars show the values from ground state measurements, the red bar from the excited state.

For comparison, we also determine the purity of the entire system

$$V = \operatorname{Tr} \rho^2 = \sum_{ij} |\rho_{ij}|^2. \tag{7.34}$$

From these purities, we calculate the corresponding entanglement entropies as $S = -\log_2 V$ (Figure 7.13).

We can see that, while the entropy follows the predicted value qualitatively, there is no quantitative agreement. There may be several reasons for this. For example, we have observed that the coherence time of our system has been worse when performing the measurements with the matterwave microscope than when the singlet-triplet oscillations had been performed. We are currently investigating this and hope to restore the reliability of our experiment soon.

Additionally, we plan to perform in-situ measurements, which will make it possible to measure the populations ρ_{ii}. This will certainly reduce the uncertainties of the entanglement witnesses and entropies, and also will allow us to measure other entanglement measures, such as the entanglement of the spatial modes. With these improvements, we ultimately hope to study entanglement in systems containing more particles.

8

CONCLUSION

8.1 SUMMARY

In the experiments presented in this thesis, correlations in two different interacting few-fermion systems have been measured. Two crucial ingredients made it possible to study these delicate quantum systems: First, the reliable preparation and manipulation of quantum states and, second, their efficient detection. The former had already been developed in large parts prior to this thesis. It includes deterministically preparing small numbers of ^{6}Li atoms in a microtrap and controlling their scattering behavior with a magnetic Feshbach resonance. The measurements presented in this thesis have been made possible by a newly developed imaging scheme, which combines spin-resolved single-atom detection with spatial resolution (Chapter 5).

In brief, the imaging method works as follows: In a first step, we release our system in a large optical potential with which we can manipulate the matterwaves. We use this to map the small initial state, which we cannot directly resolve, to a large spatial distribution. Then, we image this distribution optically.

One of the key features of our imaging scheme is the manipulation of the matterwave prior to imaging. For the measurements presented in this thesis, we evolve our system coherently for a quarter trap period in an optical potential to measure its initial momentum distribution (see Figure 5.4). The expansion of the initial system also leads to interference of atoms originating from different spatial modes. From this interference, we can probe coherences of the initial state as correlations in the momenta of the atoms. By choosing different potentials for manipulating the matterwave, we are also able to magnify and detect the position distribution instead of the momentum distribution, which we are currently implementing for the double-well system.

The atom distribution is then imaged with a relatively straightforward optical imaging scheme (Sections 5.5–5.7). By exposing the atoms to resonant imaging light for a short time up to 20 µs, we are able to extract a sufficiently strong photon signal to identify single atoms, while limiting the heating and diffusion due to the photon recoil. This allows us to determine the spatial distribution of each atom individually, at the same time, its hyperfine state (pseudo-spin) by exploiting the Zeeman splitting at high magnetic fields.

Combining the matterwave manipulations with the optical detection scheme gives us access to a *matterwave microscope*, with which we can extract full spatial and spin information from our atom distribu-

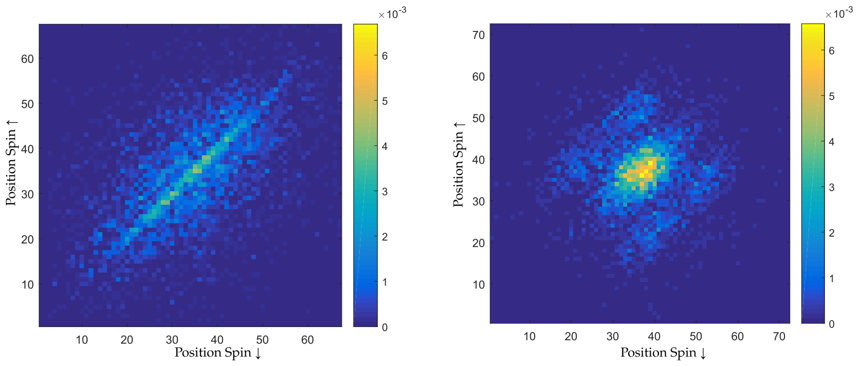

(a)

(b)

Figure 8.1: Correlated densities of systems with one spin-up and one spin-down particle at 690 G in a single microtrap (a) and at 640 G in a coupled double well (b). Brighter colors show higher densities. The horizontal and vertical axes give the coordinates of the individual particles. The relative coordinate is along the anti-diagonal, the center-of-mass coordinate is along the diagonal.

tions in every single image. This helps significantly reduce the number of repetitions of the experiment needed to determine the state of a system, and it also makes it possible to directly measure coherences of the states. Moreover, this new imaging technique should also work for larger systems containing more particles.

One of the systems that we have studied with this powerful new imaging technique are attractively interacting atoms in a single microtrap (Chapter 6). This system serves as a very simple basis for understanding how contact interactions influence the expansion dynamics. These experiments are motivated by the prediction of universal hydrodynamic properties of strongly-interacting quantum fluids, which may appear in vastly different systems ranging between ultracold atomic gases similar to our system [Cao+11] and quark-gluon plasmas in heavy-ion collisions [Ada+12; Cre11]. Our two-particle system provides a first step for exploring the connection between microscopic and macroscopic strongly-interacting quantum systems.

For two atoms contained in a single microtrap, we performed correlation measurements with our matterwave microscope at different attractive interaction strengths. From the correlated densities (Figure 8.1a), we can see that interactions can introduce several kinds of correlations between the atoms. In the relative coordinate of the two particles (see Figure 6.2), we have observed a central peak, a bimodal distribution, and interference fringes depending on the interaction strength. Some of the features we were able to explained by calculating the approximate initial state of our system and its expansion dynamics (see Section 6.3). To explain the fringes, we are currently working on a theoretical model in collaboration with theorists.

From these results, we have learned that the expansion process of two particles strongly depends both on the inter-particle interactions and the expansion potential. Even though we model the interactions as very short-ranged contact interactions (of the order of a nanometer), their influence cannot be neglected even if the particles are separated by hundreds of micrometers. As a next step, we can use these insights to study systems containing more particles and try to make a connection to the hydrodynamic description of strongly-coupled quantum fluids.

The other system that we studied with our new imaging technique were interacting particles in a double well (Chapter 7). We had studied this system previously with a MOT-imaging method [Mur^{+}15b] and the obtained mode populations had been consistent with the eigenstates predicted by the two-site Hubbard model. However, we it had been difficult to measure off-diagonal density matrix elements of our state and to directly show that we had prepared the state coherently.

The matterwave microscope has made it possible to directly observe the coherences between spatial modes. Depending on the initial state and the interactions, we have observed interference patterns in the coordinates of the individual particles, as well as in the center-of-mass and relative coordinates (Figure 8.1b). From the amplitude and phase of these oscillations, we have been able to extract several of the off-diagonal density matrix elements of our state and show the coherence of our systems.

We have studied three different kinds of systems in the ground state of a double well (Section 7.4): particles with identical spins and particles with different spins, with and without interactions. In the case of non-interacting distinguishable particles, the atoms independently delocalize over the double-well system. The occupation of either site is coherent for each particle individually, resulting in an interference pattern in the single-particle momentum resembling the pattern from a double-slit experiment.

For two non-interacting particles with identical spins, this pattern disappears, because the atoms are not independent from each other due to Pauli blocking, which prevents fermionic modes from being occupied twice. Even though there were no interactions between the particles, we have observed correlations in their relative momentum. They are a manifestation of the antisymmetrization requirement analogous to the Hanbury Brown and Twiss effect: Because the two atoms were indistinguishable, there were two equivalent paths for the two-particle state leading to the same measurement outcome. The interference between those two paths caused an interference pattern in relative momentum coordinate. The antisymmetry also shows up in the phase of the interference pattern, where it results in a central minimum for vanishing spatial separation of the particles.

For two repulsively interacting particles, we have observed similar interference patterns (Figures 7.10 and 8.1b). Because they had distinguishable spins, these correlations are not formed by the antisymmetrization requirement as in the previous case. Instead, they are a consequence of the interactions and depend on the interaction strength. With the measured off-diagonal density matrix elements, we are able to calculate entanglement witnesses and show that the states we have prepared with strong repulsive interactions are entangled (Figure 7.11). In forthcoming in-situ measurements, we will be able to measure additional entries of the density matrix and to improve the bounds on the detected entanglement.

8.2 OUTLOOK

By studying two systems containing few fermions, we have shown that our matterwave microscope has the capability of detecting particle densities, correlations, and entanglement in quantum systems with single-particle resolution. In the future, we will apply this imaging method to a variety of larger systems, containing more particles or consisting of different potential geometries. In the regime of strong interactions, we can presume that correlations will play a prominent role for a range of different many-body systems.

In strongly interacting bulk systems, increasing the number of particles could link two-particle system, which can be treated with a microscopic description, to the many-body regime, which can be treated hydrodynamically [Cao+11]. Measuring relatively small, but deterministically prepared systems can serve as a benchmark for studies of the quark-gluon plasma. It would however be helpful to first overcome some limitations of our imaging scheme, for example the *ad-hoc* implementation of our matterwave optics with the optical dipole trap. We are already planning an optical setup which can create light sheets [Rie+15], in order to look at two-dimensional expansion dynamics.

Also, we could study bulk systems for different kinds of interactions, for example repulsive interactions or p-wave interactions. In particular, interaction quenches have been predicted to lead to interesting correlation effects, for example, the change in the scattering boundary condition may generate correlation waves [CC06; CB15; CB16]. From the response of the entanglement after a quench of the Hamiltonian [CC05; LK08], it may be possible to study the ground state [NS06; Has07] and non-equilibrium states of the system [BHV06; ECP10]. The spreading of correlations and entanglement can be used to study transport and thermalization behavior of isolated quantum systems [RDO08; Che+12; Kau+16].

If we want to study systems beyond bulk physics, we have to upgrade our experiment. We will have to match the advances from our new imaging method with improved control over our optical potentials. For example, we may use the AOD to create different trap geometries by using time-dependent potentials. This is also one of the reasons to implement a light sheet, which gives us independent control over the potential in the z-axis.

With rotating microtraps, we would be able to simulate strong gauge fields. We could then, for example, deterministically prepare Laughlin states [Lau83] and analyze their correlations. These states had been proposed originally to explain the fractional quantum Hall effect, which occurs naturally in certain alloys exposed to strong magnetic fields [TSG82]. This effect is a famous example of a topological phase transition, which, in contrast to most other phase transitions, cannot be explained by symmetry breaking. These systems possess highly correlated ground states and anyonic quasi-particle excitations with fractional charges and statistics which are not described by bosons or fermions. Due to their non-local nature, these excitations are robust against perturbations and are seen as a candidate for fault-tolerant quantum computing [Kit03; Nay+08].

We also consider implementing a spatial light modulator, which will allow us to create larger arrays of microtraps. By creating chains of microtraps, we could study a particular phase called the Luttinger liquid. Due to the dimensionality, it is highly susceptible to interactions and the role of fluctuations and correlations is enhanced (see [Rec+03] for a summary in the context of ultracold atoms). These systems can be used to describe electrons in edge states, nanotubes or quantum wires in condensed matter.

If, instead, we want to study two-dimensional physics, we could start by looking at a single plaquette, which forms the fundamental building block of the two-dimensional Hubbard model [PB08]. While the double well studied in this thesis does support a bond between two particles on different sites, it lacks the dimensionality and size to study exchange phenomena between multiple bonds. The plaquette supports multiple bonds which can resonate [And87; KRS87] and the atoms in the plaquette may form d-wave pairs if the system is doped [Tre+06]. This type of pairing is suspected to be responsible for high-T_c superconductivity and could be detected from its correlation signature [ADL04]. Several plaquettes can be combined to a ladder, where several different correlated states are expected [UG15]. With these larger systems, we could study interesting ground state entanglement properties [KP06; LW06] and scaling laws [ECP10], with the ultimate goal of building a link to strongly-correlated phases in actual materials.

A

DERIVATION OF THE TWO-POINT CORRELATION FUNCTION

This appendix shows how the field correlation function (2.22) can be expressed in the Fock basis. First, we expand the correlation function using the definition for the field operators from eq. (2.15):

$$G^{(2)}_{\sigma\vartheta}(x_1,x_2,x_2,x_1) = \sum_{ijkl} \psi_i^*(x_1)\psi_j^*(x_2)\psi_k(x_2)\psi_l(x_1) \left\langle \hat{a}^\dagger_{\sigma,i}\hat{a}^\dagger_{\vartheta,j}\hat{a}_{\vartheta,k}\hat{a}_{\sigma,l}\right\rangle \tag{A.1}$$

The labels σ and ϑ allow us to treat two cases, distinguishable particles ($\sigma \neq \vartheta$) and indistinguishable particles ($\sigma = \vartheta$).

Next, we can simplify this sum by identifying the terms that vanish. We will do this explicitly for a system with two modes $\{i,j,k,l\} = \{1,2\}$ per particle for a singly occupied state containing two particles, but the final result can be extended to any number of modes and different states. For distinguishable particles σ, ϑ, the two-point correlator then becomes

$$\begin{aligned}
&\hat{\Psi}^\dagger_\sigma(x_1)\hat{\Psi}^\dagger_\vartheta(x_2)\hat{\Psi}_\vartheta(x_2)\hat{\Psi}_\sigma(x_1) = \\
&\psi_1^*(x_1)\psi_1^*(x_2)\psi_1(x_2)\psi_1(x_1)\, \hat{a}^\dagger_{\sigma,1}\hat{a}^\dagger_{\vartheta,1}\hat{a}_{\vartheta,1}\hat{a}_{\sigma,1} \\
&+\psi_1^*(x_1)\psi_2^*(x_2)\psi_1(x_2)\psi_2(x_1)\, \hat{a}^\dagger_{\sigma,1}\hat{a}^\dagger_{\vartheta,2}\hat{a}_{\vartheta,1}\hat{a}_{\sigma,2} \\
&+\psi_1^*(x_1)\psi_2^*(x_2)\psi_2(x_2)\psi_1(x_1)\, \hat{a}^\dagger_{\sigma,1}\hat{a}^\dagger_{\vartheta,2}\hat{a}_{\vartheta,2}\hat{a}_{\sigma,1} \\
&+\psi_2^*(x_1)\psi_1^*(x_2)\psi_1(x_2)\psi_2(x_1)\, \hat{a}^\dagger_{\sigma,2}\hat{a}^\dagger_{\vartheta,1}\hat{a}_{\vartheta,1}\hat{a}_{\sigma,2} \\
&+\psi_2^*(x_1)\psi_1^*(x_2)\psi_2(x_2)\psi_1(x_1)\, \hat{a}^\dagger_{\sigma,2}\hat{a}^\dagger_{\vartheta,1}\hat{a}_{\vartheta,2}\hat{a}_{\sigma,1} \\
&+\psi_2^*(x_1)\psi_2^*(x_2)\psi_2(x_2)\psi_2(x_1)\, \hat{a}^\dagger_{\sigma,2}\hat{a}^\dagger_{\vartheta,2}\hat{a}_{\vartheta,2}\hat{a}_{\sigma,2} \\
&=\psi_1^*(x_1)\psi_1^*(x_2)\psi_1(x_2)\psi_1(x_1)\, \hat{a}^\dagger_{\sigma,1}\hat{a}_{\sigma,1}\hat{a}^\dagger_{\vartheta,1}\hat{a}_{\vartheta,1} \\
&+\psi_1^*(x_1)\psi_2^*(x_2)\psi_2(x_2)\psi_1(x_1)\, \hat{a}^\dagger_{\sigma,1}\hat{a}_{\sigma,1}\hat{a}^\dagger_{\vartheta,2}\hat{a}_{\vartheta,2} \\
&+\psi_2^*(x_1)\psi_1^*(x_2)\psi_1(x_2)\psi_2(x_1)\, \hat{a}^\dagger_{\sigma,2}\hat{a}_{\sigma,2}\hat{a}^\dagger_{\vartheta,1}\hat{a}_{\vartheta,1} \\
&+\psi_2^*(x_1)\psi_2^*(x_2)\psi_2(x_2)\psi_2(x_1)\, \hat{a}^\dagger_{\sigma,2}\hat{a}_{\sigma,2}\hat{a}^\dagger_{\vartheta,2}\hat{a}_{\vartheta,2} \\
&=\sum_{ijkl}\psi_i^*(x_1)\psi_j^*(x_2)\psi_k(x_2)\psi_l(x_1)\delta_{il}\delta_{jk}\,\hat{n}_{\sigma,i}\hat{n}_{\vartheta,j}.
\end{aligned} \tag{A.2}$$

In the first step, we made use of the fact that all terms vanish where the number of creation operators per mode does not match the number of annihilation operators per mode, because this would create doubly occupied states. In the second step, we removed the second and fifth term where the labels σ, ϑ were mismatched, because, for distinguishable particles, these would also alter the state of the system. Finally, we sorted the operators using the (anti-)commutation relations in order to express the sum with number operators.

For indistinguishable particles (where the labels σ, ϑ can be omitted), we have to keep all terms in the first equality of (A.2). When bringing their operators into the right order, the correlation operator becomes:

$$
\begin{aligned}
&\hat{\Psi}^\dagger(x_1)\hat{\Psi}^\dagger(x_2)\hat{\Psi}(x_2)\hat{\Psi}(x_1) = \\
&\psi_1^*(x_1)\psi_1^*(x_2)\psi_1(x_2)\psi_1(x_1)\, \hat{a}_1^\dagger \left(1 \pm \hat{a}_1 \hat{a}_1^\dagger\right) \hat{a}_1 \\
&\pm \psi_1^*(x_1)\psi_2^*(x_2)\psi_1(x_2)\psi_2(x_1)\, \hat{a}_1^\dagger \hat{a}_1 \hat{a}_2^\dagger \hat{a}_2 \\
&+ \psi_1^*(x_1)\psi_2^*(x_2)\psi_2(x_2)\psi_1(x_1)\, \hat{a}_1^\dagger \hat{a}_1 \hat{a}_2^\dagger \hat{a}_2 \\
&+ \psi_2^*(x_1)\psi_1^*(x_2)\psi_1(x_2)\psi_2(x_1)\, \hat{a}_2^\dagger \hat{a}_2 \hat{a}_1^\dagger \hat{a}_1 \\
&\pm \psi_2^*(x_1)\psi_1^*(x_2)\psi_2(x_2)\psi_1(x_1)\, \hat{a}_2^\dagger \hat{a}_2 \hat{a}_1^\dagger \hat{a}_1 \\
&+ \psi_2^*(x_1)\psi_2^*(x_2)\psi_2(x_2)\psi_2(x_1)\, \hat{a}_2^\dagger \left(1 \pm \hat{a}_2 \hat{a}_2^\dagger\right) \hat{a}_2 \\
&= \sum_{ijkl} \psi_i^*(x_1)\psi_j^*(x_2)\psi_k(x_2)\psi_l(x_1) \\
&\times \left[\delta_{il}\delta_{jk}\, \hat{n}_i \hat{n}_j \pm \delta_{ik}\delta_{jl}\, \hat{n}_i \hat{n}_j + \delta_{ij}\delta_{ik}\delta_{il} \hat{n}_i (1 - \hat{n}_i)\right], \qquad \text{(A.3)}
\end{aligned}
$$

where the plus sign is for bosons, the minus sign for fermions.

B

ERROR ESTIMATES FOR SINGLE-WELL MEASUREMENTS

For the density profiles in Figure 6.2 and Appendix D, we specify the errors as standard error of the mean. The data points represent probabilities of finding atoms with a certain separation d in the REL coordinate,

$$\tilde{n}(d) = \frac{1}{N_{tot}} \int_{x=d} dX \, N(x_1, x_2) = \frac{N(d)}{N_{tot}}, \tag{B.1}$$

where $N(x_1, x_2)$ is the number of events with coordinates x_1 and x_2 and N_{tot} the total number of events, i.e., measurements.

The error bars represent the standard error of the mean for each data point,

$$\Delta\tilde{n}(d) = \frac{\Delta N(d)}{N_{tot}} \approx \frac{\sqrt{N(d)}}{N_{tot}} = \sqrt{\frac{\tilde{n}(d)}{N_{tot}}}. \tag{B.2}$$

In the second step, we have assumed that the individual realizations of the experiment are independent of each other and that their number statistics are described by a Poisson distribution with a standard deviation $\Delta N(d) = \sqrt{N(d)}$. Cases where $N(d) = 0$ occur with a probability of $\frac{1}{N_{tot}+2} \approx \frac{1}{N_{tot}}$, according to the rule of succession. We substitute this probability in the last line of eq. (B.2) to estimate the error bar for these cases.

For the density profiles in the COM coordinates, we calculate the error bars analogously.

C

SCATTERING LENGTHS FOR THE SINGLE-WELL EXPERIMENTS

The following table contains all magnetic fields and the corresponding scattering lengths which were used for the experiments with a single microtrap described in Chapter 6 and Appendix D. The values are given in Bohr radii a_0 and in harmonic oscillator lengths $\bar{l} = \sqrt{\frac{\hbar}{\mu\bar{\omega}}} \approx 390\,\mathrm{nm} \approx 7400\,a_0$, with the reduced mass μ and the averaged trap frequency $\bar{\omega} \approx 2\pi \times 22\,\mathrm{kHz}$.

Field (G)	a (a_0)	a^{-1} (${a_0}^{-1}$)	a ($\bar{l}$)	a^{-1} ($\bar{l}^{-1}$)
660	5203	1.92×10^{-4}	0.703	1.42
665	6609	1.51×10^{-4}	0.893	1.12
685	4.23×10^{4}	2.36×10^{-5}	5.72	0.175
690	-6.48×10^{5}	-1.54×10^{-6}	-87.5	-1.14×10^{-2}
692	-9.07×10^{4}	1.10×10^{-5}	-12.3	-8.16×10^{-2}
695	-4.06×10^{4}	-2.47×10^{-5}	-5.48	-0.182
700	-2.18×10^{4}	-4.59×10^{-5}	-2.94	-0.340
710	-1.19×10^{4}	-8.38×10^{-5}	-1.61	-0.620
750	-5213	-1.92×10^{-4}	-0.704	-1.42
900	-2825	-3.54×10^{-4}	-0.382	-2.62

Table C.1: Magnetic fields and corresponding scattering lengths for the $|1\rangle$-$|3\rangle$-mixture used in the single-well experiments in Chapter 6.

D

CORRELATION MEASUREMENTS WITH A SINGLE WELL

The following graphs show all measurements performed on two attractive atoms in a single microtrap with our matterwave microscope, as described in Chapter 6. The first four pages show the densities in the REL and COM coordinates, the latter four pages show the correlator Γ from eq. (6.4).

Prep.: 900G IPGval: 1V
Expans.: 900G MT: 1.3V
Ipghold: 3.5ms

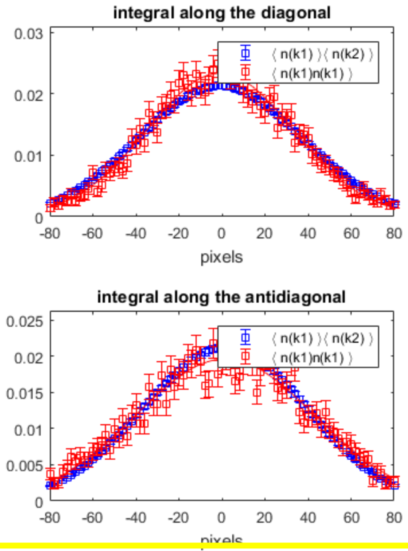

Prep.: 750G Jmptm.: 1ms
Expans.: 900G IPGval: 1V
Ipghold: 3.5ms MT: 1.3V

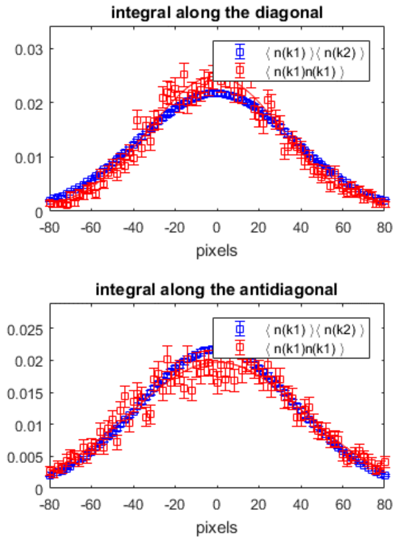

Prep.: 665G Jmptm.: 1ms
Expans.: 900G IPGval: 1V
Ipghold: 3.5ms MT: 1.3V

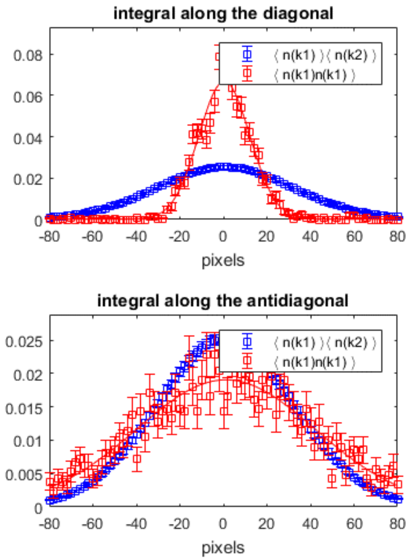

Prep.: 660G Jmptm.: 1ms
Expans.: 900G IPGval: 1V
Ipghold: 3.5ms MT: 1.3V

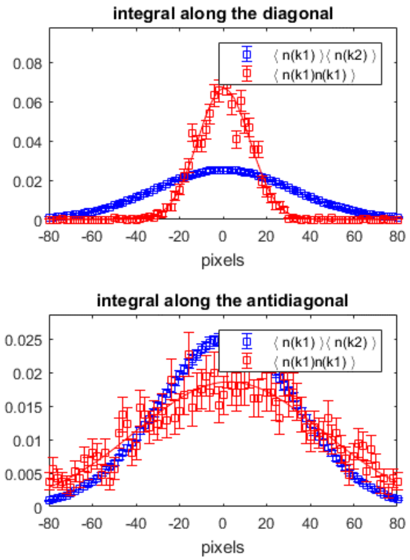

Prep.: 690G Jmptm.: 0ms
Expans.: 900G IPGval: 1V
Ipghold: 3.5ms MT: 1.3V

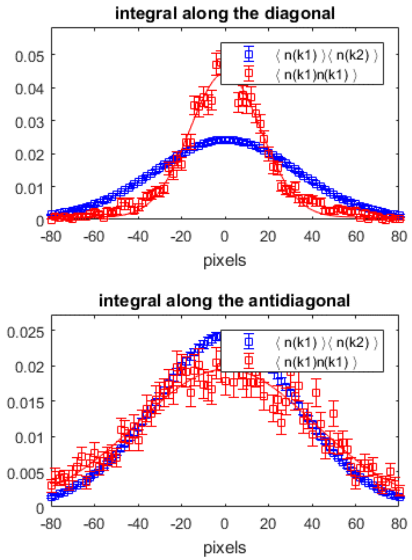

Prep.: 690G Jmptm.: 1ms
Expans.: 900G IPGval: 1V
Ipghold: 3.5ms MT: 1.3V

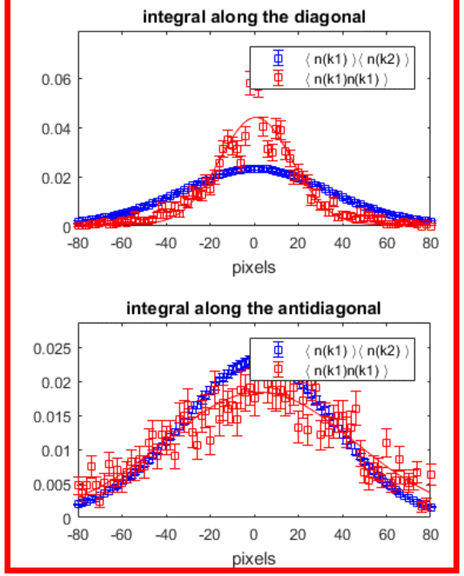

Prep.: 690G Jmptm.: 2ms
Expans.: 900G IPGval: 1V
Ipghold: 3.5ms MT: 1.3V

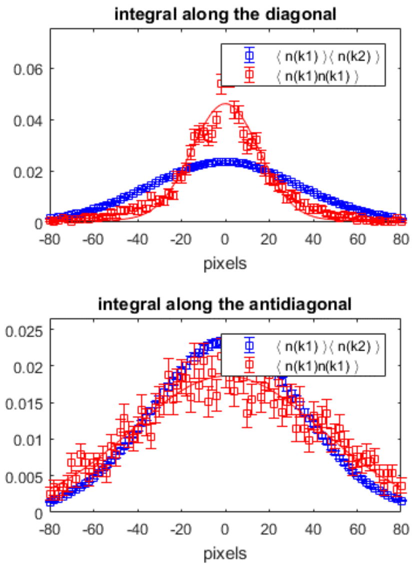

Prep.: 690G IPGval: 1V
Expans.: 690G MT: 1.3V
Ipghold: 3.5ms

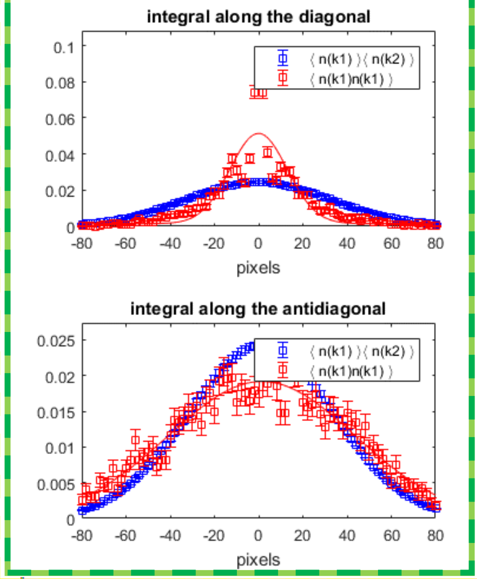

Prep.: 665G IPGval: 1V
Expans.: 665G MT: 1.3V
Ipghold: 3.5ms

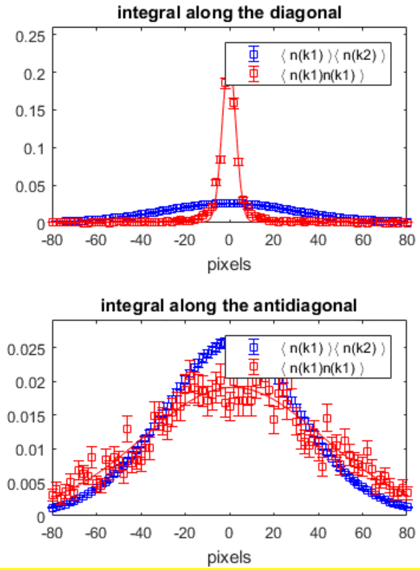

Prep.: 685G IPGval: 1V
Expans.: 685G MT: 1.3V
Ipghold: 3.5ms

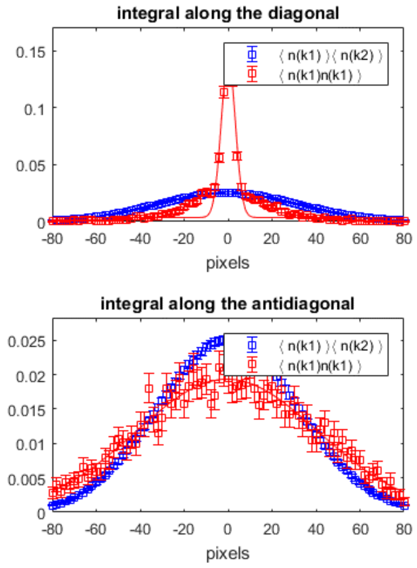

Prep.: 692G IPGval: 1V
Expans.: 692G MT: 1.3V
Ipghold: 3.5ms

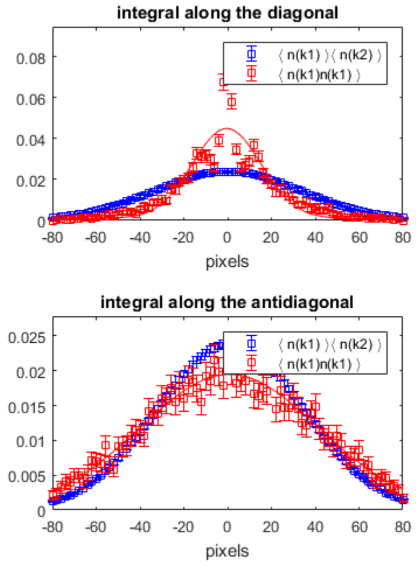

Prep.: 695G IPGval: 1V
Expans.: 695G MT: 1.3V
Ipghold: 3.5ms

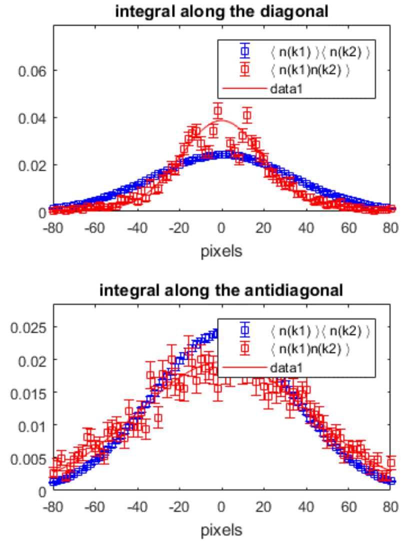

Prep.: 700G IPGval: 1V
Expans.: 700G MT: 1.3V
Ipghold: 3.5ms

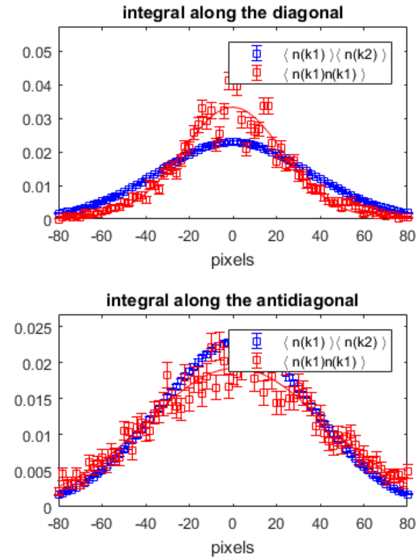

Prep.: 710G IPGval: 1V
Expans.: 710G MT: 1.3V
Ipghold: 3.5ms

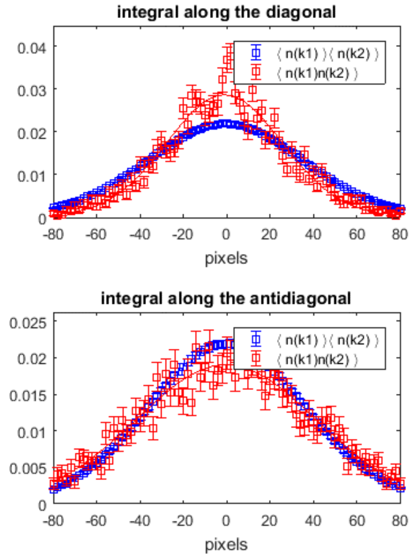

Prep.: 690G IPGval: 1V
Expans.: 690G MT: 5V
Ipghold: 3.5ms

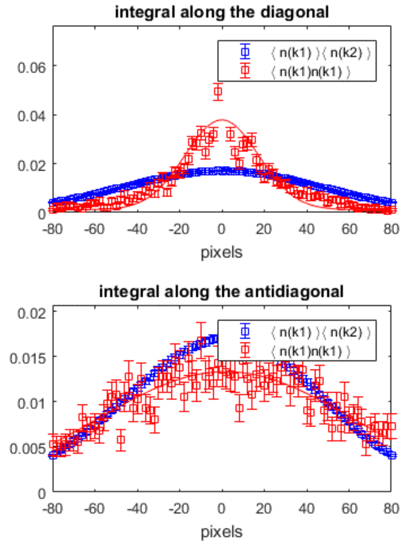

Prep.: 690G IPGval: 1V
Expans.: 690G MT: 1.3V
Ipghold: 0.5ms

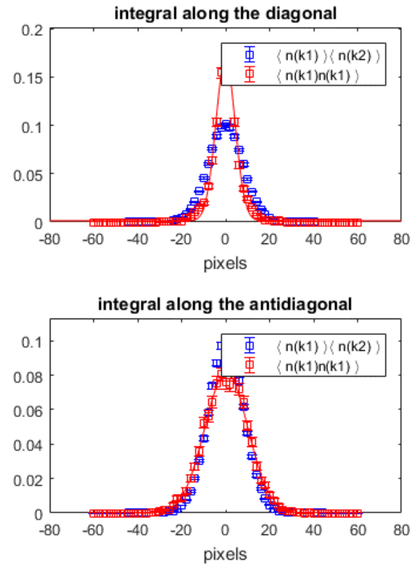

Prep.: 690G IPGval: 1V
Expans.: 690G MT: 1.3V
Ipghold: 1ms

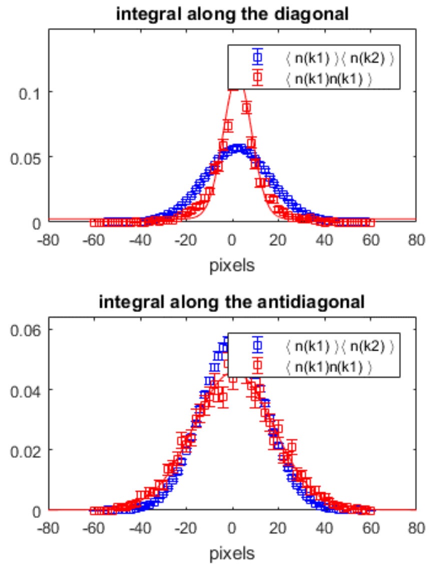

Prep.: 690G IPGval: 1V
Expans.: 690G MT: 1.3V
Ipghold: 2ms

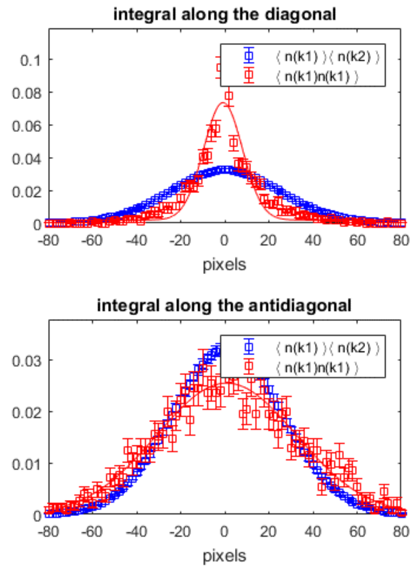

Prep.: 690G IPGval: 1V
Expans.: 690G MT: 1.3V
Ipghold: 2.5ms

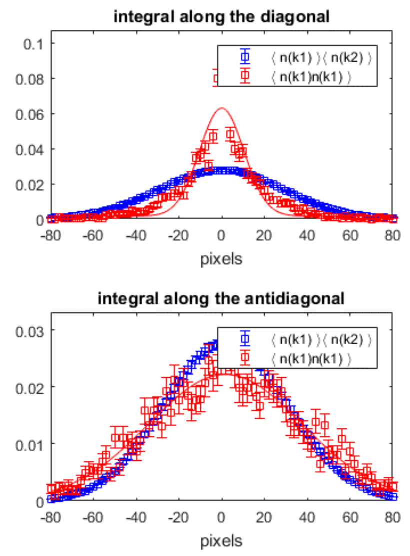

Prep.: 690G IPGval: 1V
Expans.: 690G MT: 1.3V
Ipghold: 7ms

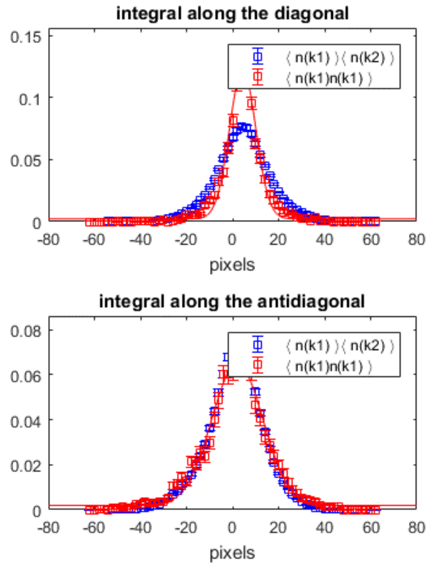

Legend

- 🟥 Prepare at X G, jump to 900 G after 1 ms of expansion
- 🟧 Prepare at 690 G, jump to 900 G after X ms of expansion
- 🟨 Prepare and stay at X G
- 🟩 Prepare and stay at 690 G, expand for X ms
- 🟩 Prepare and stay at 690 G, expand with IPG power X V
- 🟦 Prepare and stay at 690 G, prepare with MT depth X V
- 🟦 Prepare and stay at 690 G, free exp. after brake pulse
- 🟦 Expansion in one-armed ODT

Prep.: 690G IPGval: 0V
Expans.: 690G MT: 1.3V
Ipghold: 0.5ms

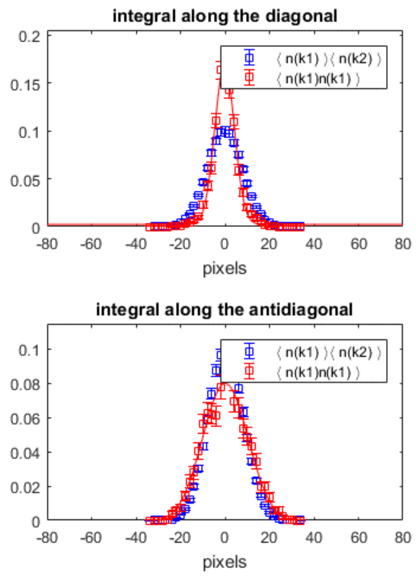

Prep.: 690G IPGval: 0.25V
Expans.: 690G MT: 1.3V
Ipghold: 7.6ms

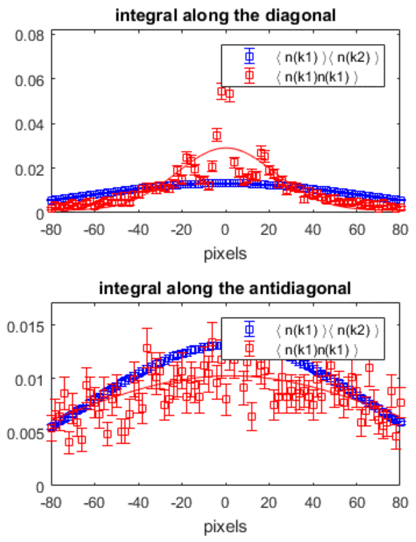

Prep.: 690G IPGval: 0.5V
Expans.: 690G MT: 1.3V
Ipghold: 5.6ms

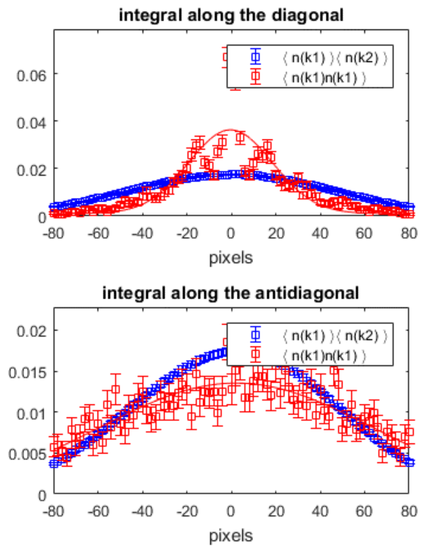

Prep.: 690G IPGval: 2V
Expans.: 690G MT: 1.3V
Ipghold: 2.8ms

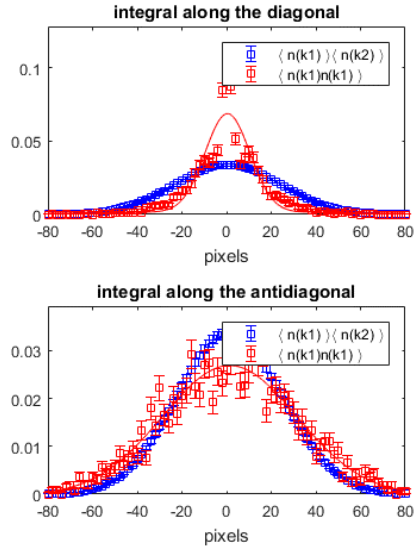

Prep.: 690G IPGval: 4V
Expans.: 690G MT: 1.3V
Ipghold: 2ms

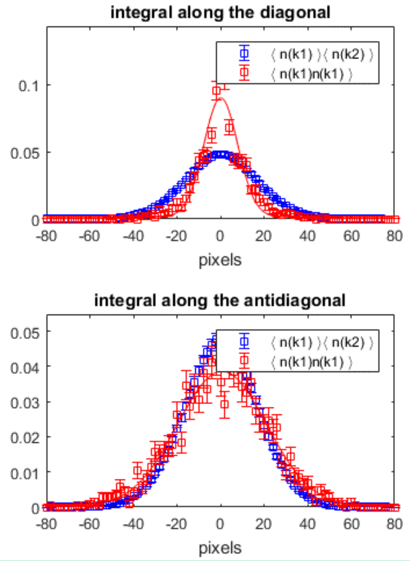

Prep.: 690G With brake pulse
Expans.: 690G
MT: 1.3V

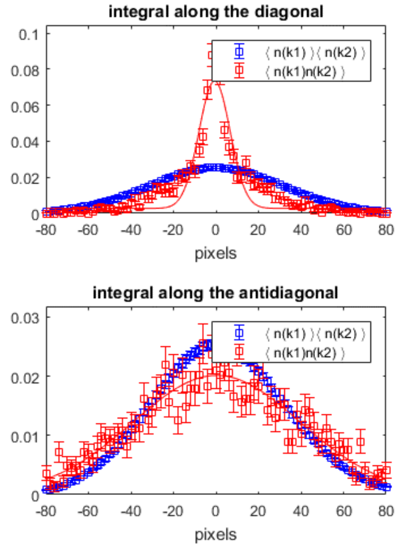

Prep.: 690G IPGval: 2V
Expans.: 690G Ipghold: 2ms
MT: 1.3V

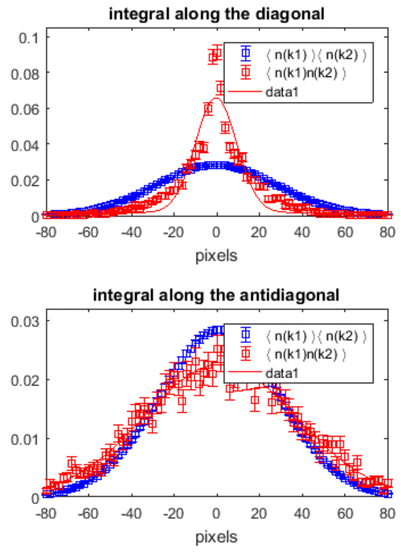

Prep.: 700G IPGval: 2V?
Expans.: 700G Ipghold: 2ms
MT: 1.3V

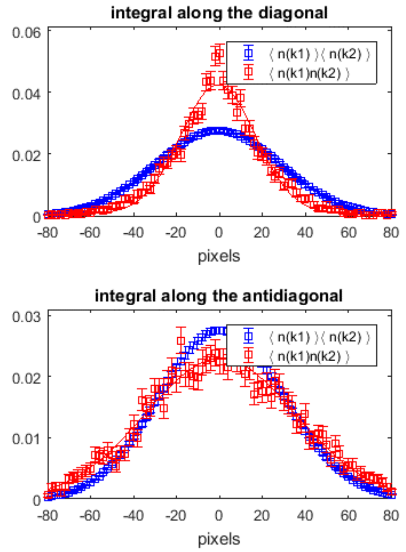

Prep.: 900G IPGval: 1V
Expans.: 900G MT: 1.3V
Ipghold: 3.5ms

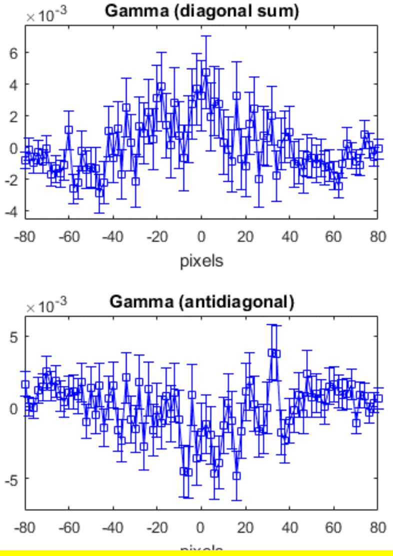

Prep.: 750G Jmptm.: 1ms
Expans.: 900G IPGval: 1V
Ipghold: 3.5ms MT: 1.3V

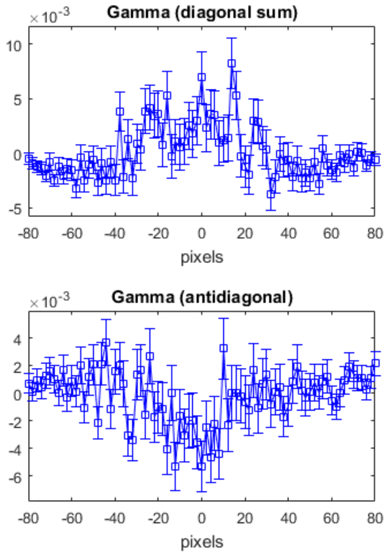

Prep.: 665G Jmptm.: 1ms
Expans.: 900G IPGval: 1V
Ipghold: 3.5ms MT: 1.3V

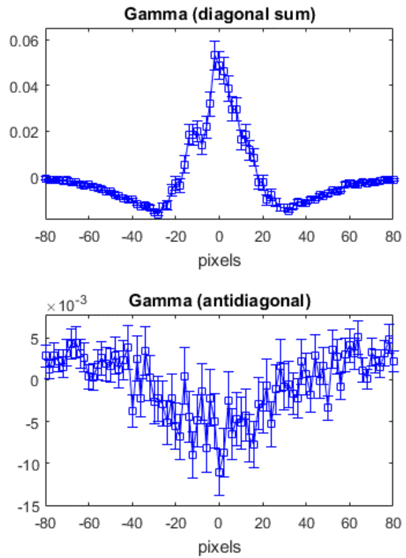

Prep.: 660G Jmptm.: 1ms
Expans.: 900G IPGval: 1V
Ipghold: 3.5ms MT: 1.3V

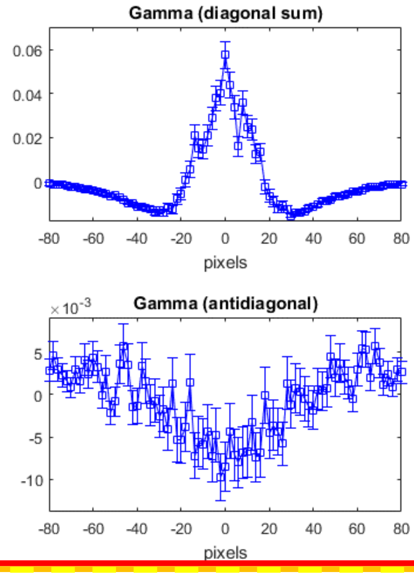

Prep.: 690G Jmptm.: 0ms
Expans.: 900G IPGval: 1V
Ipghold: 3.5ms MT: 1.3V

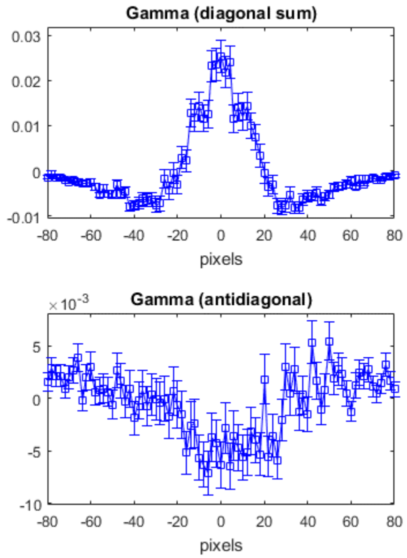

Prep.: 690G Jmptm.: 1ms
Expans.: 900G IPGval: 1V
Ipghold: 3.5ms MT: 1.3V

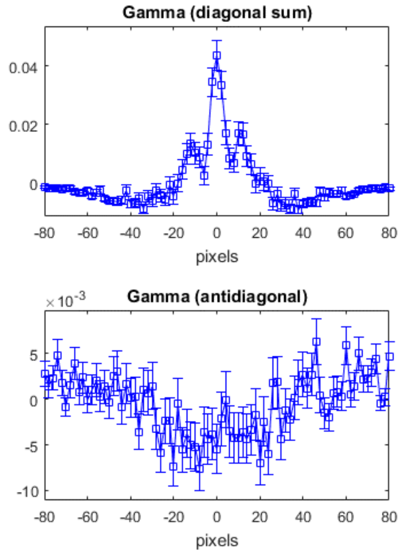

Prep.: 690G Jmptm.: 2ms
Expans.: 900G IPGval: 1V
Ipghold: 3.5ms MT: 1.3V

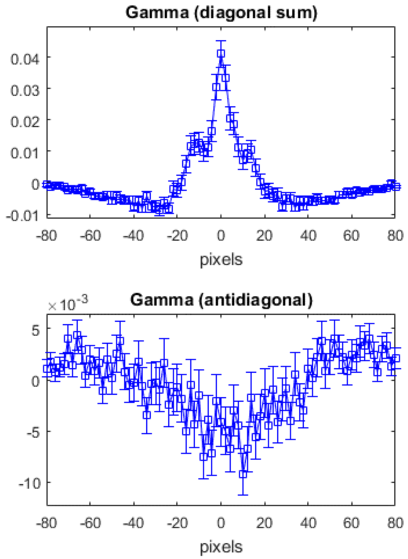

Prep.: 690G IPGval: 1V
Expans.: 690G MT: 1.3V
Ipghold: 3.5ms

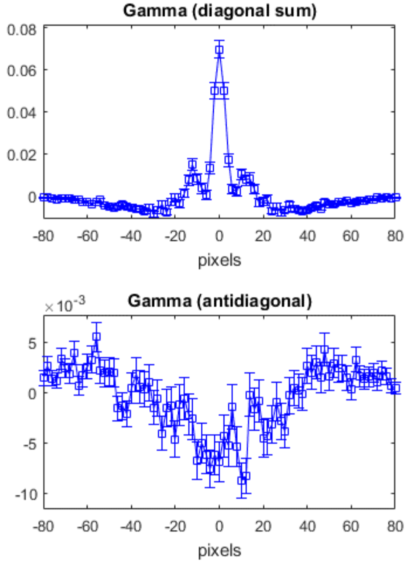

Prep.: 665G IPGval: 1V
Expans.: 665G MT: 1.3V
Ipghold: 3.5ms

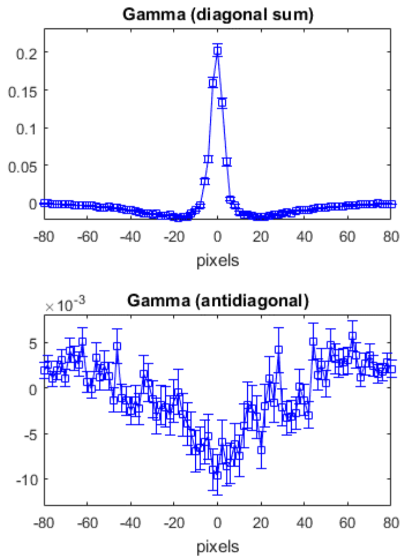

Prep.: 685G IPGval: 1V
Expans.: 685G MT: 1.3V
Ipghold: 3.5ms

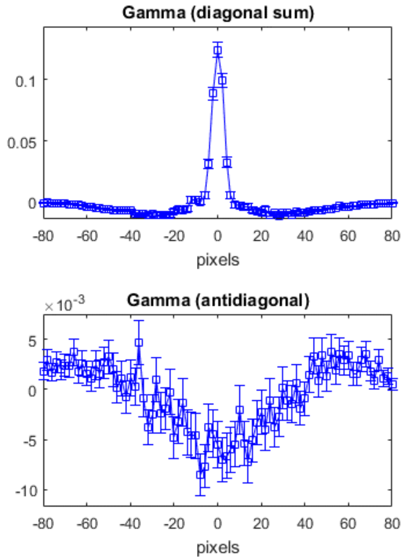

Prep.: 692G IPGval: 1V
Expans.: 692G MT: 1.3V
Ipghold: 3.5ms

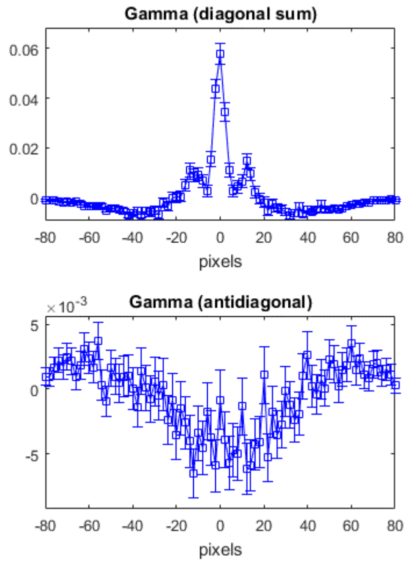

Prep.: 695G IPGval: 1V
Expans.: 695G MT: 1.3V
Ipghold: 3.5ms

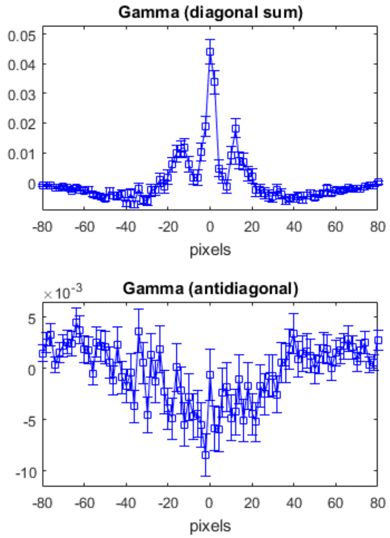

Prep.: 700G IPGval: 1V
Expans.: 700G MT: 1.3V
Ipghold: 3.5ms

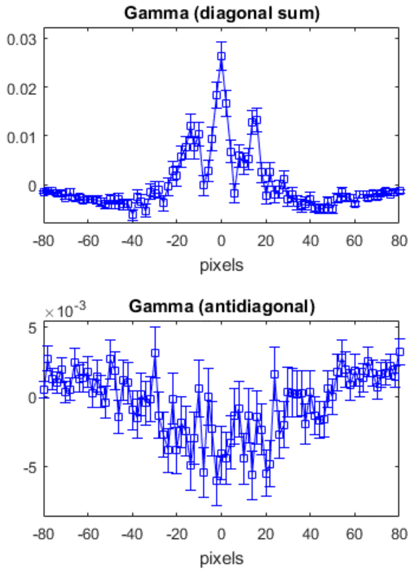

Prep.: 710G IPGval: 1V
Expans.: 710G MT: 1.3V
Ipghold: 3.5ms

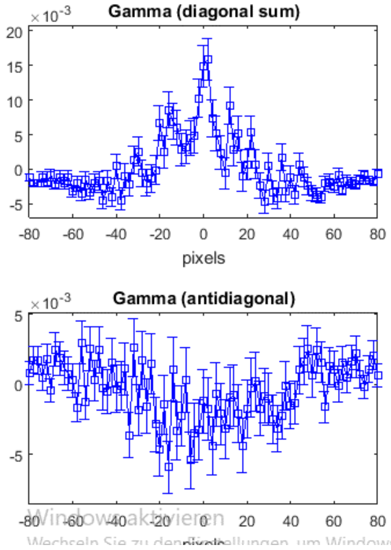

Prep.: 690G IPGval: 1V
Expans.: 690G MT: 5V
Ipghold: 3.5ms

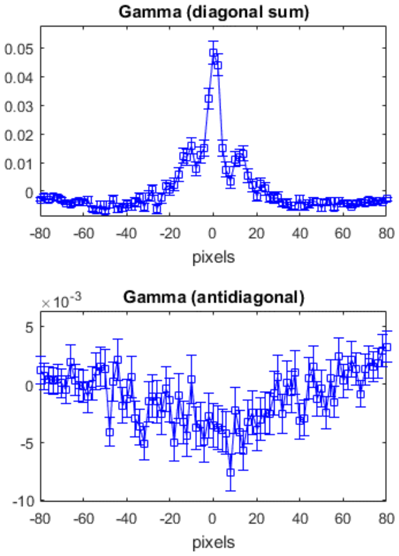

Prep.: 690G IPGval: 1V
Expans.: 690G MT: 1.3V
Ipghold: 0.5ms

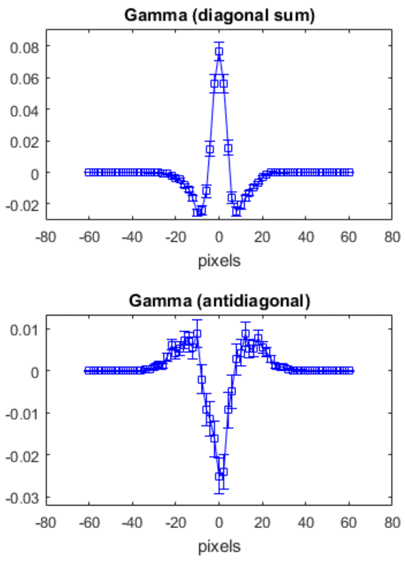

Prep.: 690G IPGval: 1V
Expans.: 690G MT: 1.3V
Ipghold: 1ms

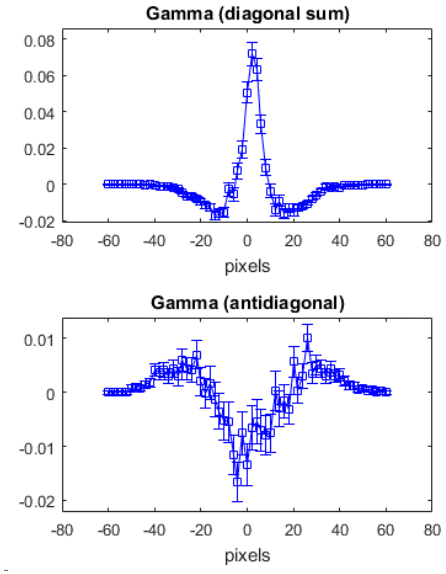

Prep.: 690G IPGval: 1V
Expans.: 690G MT: 1.3V
Ipghold: 2ms

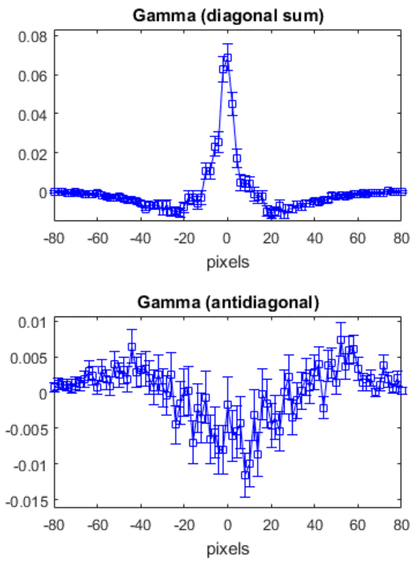

Prep.: 690G IPGval: 1V
Expans.: 690G MT: 1.3V
Ipghold: 2.5ms

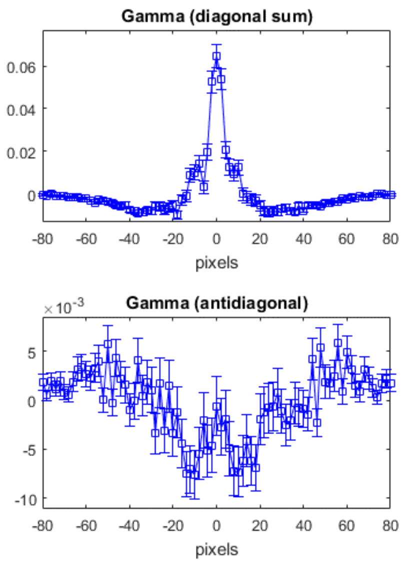

Prep.: 690G IPGval: 1V
Expans.: 690G MT: 1.3V
Ipghold: 7ms

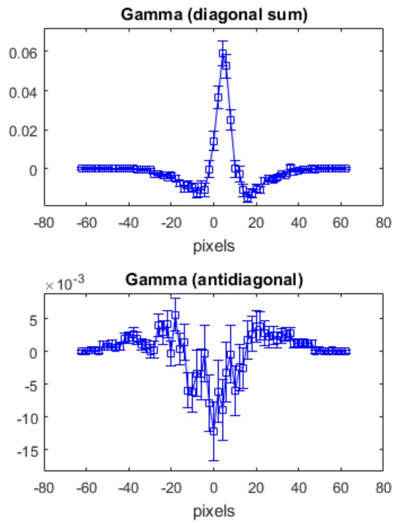

Legend

🟥 Prepare at X G, jump to 900 G after 1 ms of expansion
🟧 Prepare at 690 G, jump to 900 G after X ms of expansion
🟨 Prepare and stay at X G
🟩 Prepare and stay at 690 G, expand for X ms
🟩 Prepare and stay at 690 G, expand with IPG power X V
🟦 Prepare and stay at 690 G, prepare with MT depth X V
🟦 Prepare and stay at 690 G, free exp. after brake pulse
🟦 Expansion in one-armed ODT

Prep.: 690G IPGval: 0V
Expans.: 690G MT: 1.3V
Ipghold: 0.5ms

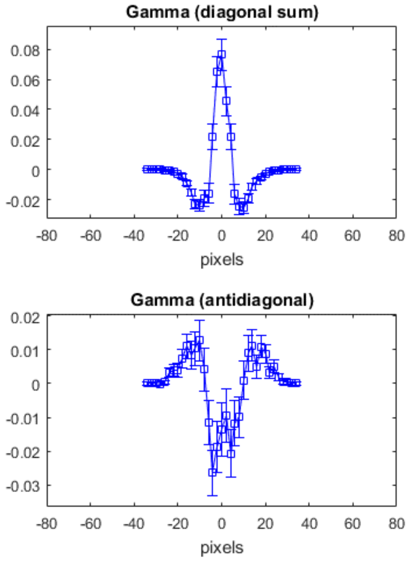

Prep.: 690G IPGval: 0.25V
Expans.: 690G MT: 1.3V
Ipghold: 7.6ms

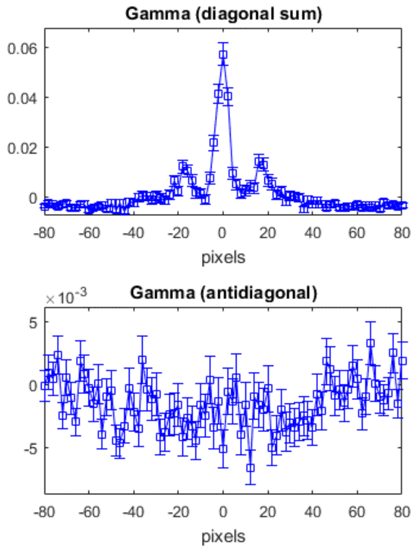

Prep.: 690G IPGval: 0.5V
Expans.: 690G MT: 1.3V
Ipghold: 5.6ms

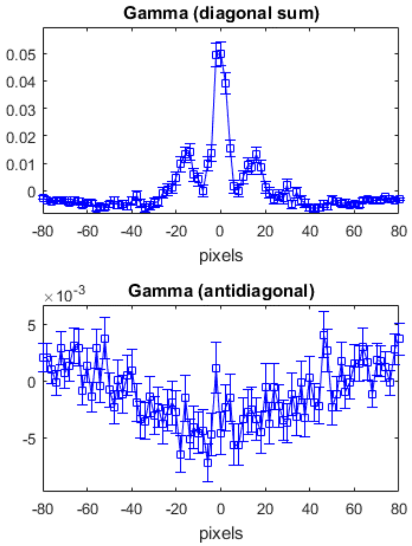

Prep.: 690G IPGval: 2V
Expans.: 690G MT: 1.3V
Ipghold: 2.8ms

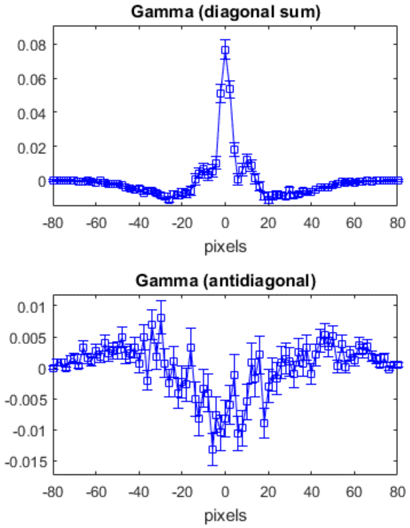

Prep.: 690G IPGval: 4V
Expans.: 690G MT: 1.3V
Ipghold: 2ms

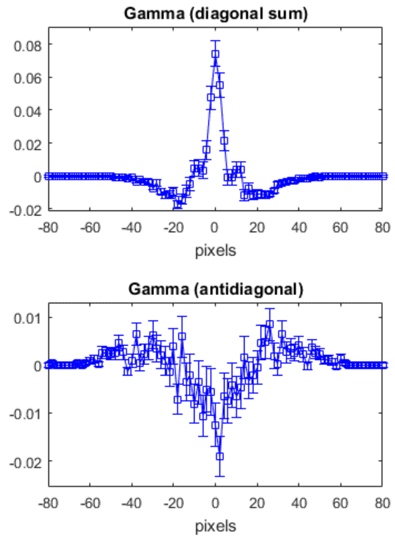

Prep.: 690G With brake pulse
Expans.: 690G
MT: 1.3V

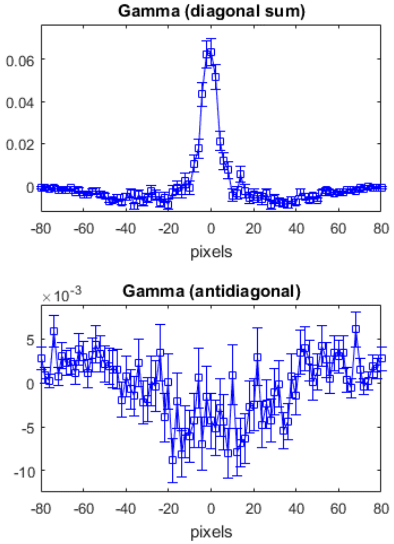

Prep.: 690G IPGval: 2V
Expans.: 690G Ipghold: 2ms
MT: 1.3V

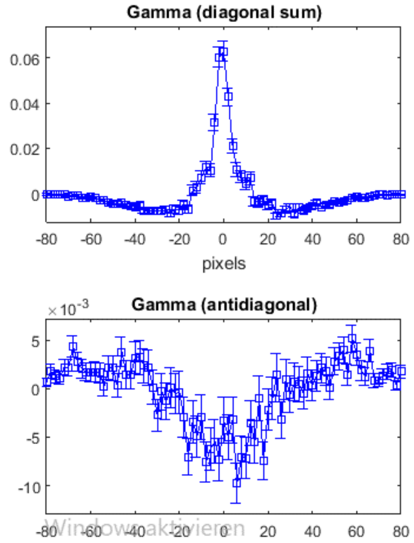

Prep.: 700G IPGval: 2V?
Expans.: 700G Ipghold: 2ms
MT: 1.3V

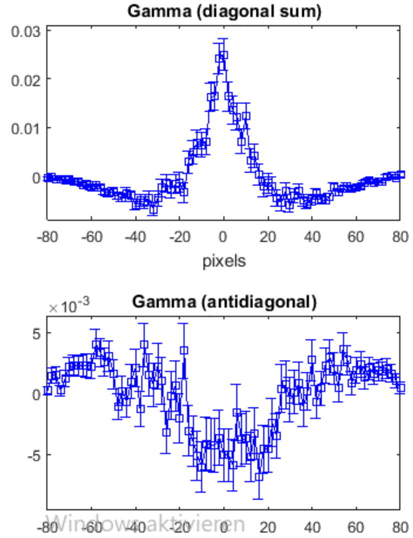

E

ENTANGLEMENT ENTROPIES AND WITNESSES

The following tables contain the values measured for the purities, entanglement entropies, and entanglement witnesses in the double well, as described in Section 7.5. The quantities in Table E.1 are defined in eq. (7.34) and (7.33). The Renyi entropies have been calculated from the purities as $S = -\log_2 V$.

The maximum values for the coherences ρ_{23} and ρ_{14} in Table E.2

$$\rho_{23}^{\max} = \sqrt{\rho_{22}\rho_{33}} \tag{E.1a}$$

$$\rho_{14}^{\max} = \sqrt{\rho_{11}\rho_{44}} \tag{E.1b}$$

are theoretical predictions for state $|a\rangle$.

U/J	V_{min}	V_{max}	$V_{\uparrow}$	$V_{\downarrow}$
0.0	0.752(6)	0.897(6)	0.80(2)	0.87(2)
2.1	0.736(7)	0.861(7)	0.74(2)	0.77(2)
4.3	0.754(8)	0.791(8)	0.68(2)	0.71(2)
7.7	0.662(8)	0.691(8)	0.56(2)	0.59(2)
2.1	0.736(7)	0.861(7)	0.74(2)	0.77(2)
11.1	0.657(9)	0.686(9)	0.51(2)	0.51(2)
0.0	0.666(6)	0.840(6)	0.77(2)	0.83(2)

U/J	S_{min}	S_{max}	$S_{\uparrow}$	$S_{\downarrow}$
0.0	0.41(1)	0.16(1)	0.32(3)	0.20(3)
2.1	0.44(1)	0.22(1)	0.44(4)	0.39(4)
4.3	0.41(1)	0.34(1)	0.55(4)	0.50(4)
7.7	0.60(2)	0.53(2)	0.84(4)	0.77(4)
11.1	0.61(2)	0.54(2)	0.96(4)	0.97(5)
0.0	0.59(1)	0.25(1)	0.38(4)	0.27(3)

Table E.1: Summary of all purities and entanglement entropies obtained from the measurements. The five topmost rows were obtained from ground state measurements, the bottom row from excited state measurements.

U/J	ρ_{14}	ρ_{14}^{max}	ρ_{23}	ρ_{23}^{max}	Y	W
0.0	0.16(1)	0.25	0.22(1)	0.25	−0.09(1)	−0.03(1)
2.1	0.08(1)	0.13	0.28(1)	0.37	−0.29(1)	0.14(1)
4.3	0.06(1)	0.07	0.29(1)	0.43	−0.38(1)	0.22(1)
7.7	0.02(1)	0.03	0.26(1)	0.47	−0.45(1)	0.23(1)
11.1	0.04(2)	0.01	0.28(2)	0.49	−0.45(2)	0.26(2)
10			0.41(2)	0.48		0.40(2)

Table E.2: Summary of all entanglement witnesses obtained from the measurements. The five topmost rows were obtained from ground state measurements, the bottom row from the singlet-triplet oscillations.

[Ada+12] A. Adams et al. “Strongly correlated quantum fluids: ultracold quantum gases, quantum chromodynamic plasmas and holographic duality.” In: *New Journal of Physics* 14.11 (2012), p. 115009. DOI: `10.1088/1367-2630/14/11/115009`.

[ADL04] E. Altman, E. Demler, and M. D. Lukin. “Probing many-body states of ultracold atoms via noise correlations.” In: *Physical Review A - Atomic, Molecular, and Optical Physics* 70.1 (2004), pp. 6–9. DOI: `10.1103/PhysRevA.70.013603`.

[AOV08] L. Amico, A. Osterloh, and V. Vedral. “Entanglement in many-body systems.” In: *Reviews of Modern Physics* 80.2 (2008), pp. 517–576. DOI: `10.1103/RevModPhys.80.517`.

[And72] P. W. Anderson. “More is different.” In: *Science (New York, N.Y.)* 177.4047 (1972), pp. 393–396. DOI: `10.1126/science.177.4047.393`.

[And87] P. W. Anderson. “The Resonating Valence Bond State in La2CuO4 and Superconductivity.” In: *Science* 235.4793 (1987), pp. 1196–1198. DOI: `10.1126/science.235.4793.1196`.

[Bak+09] W. S. Bakr et al. “A quantum gas microscope for detecting single atoms in a Hubbard-regime optical lattice.” In: *Nature* 462.7269 (2009), pp. 74–77. DOI: `10.1038/nature08482`.

[Bar+05] M. Bartenstein et al. “Precise Determination of Li6 Cold Collision Parameters by Radio-Frequency Spectroscopy on Weakly Bound Molecules.” In: *Physical Review Letters* 94.10 (2005), p. 103201. DOI: `10.1103/PhysRevLett.94.103201`.

[BHM03] A. G. Basden, C. A. Haniff, and C. D. Mackay. “Photon counting strategies with low-light-level CCDs.” In: *Monthly Notices of the Royal Astronom. Society* 345.3 (2003), pp. 985–991. DOI: `10.1046/j.1365-8711.2003.07020.x`.

[Bec14] F. Becattini. “The Quark Gluon Plasma and relativistic heavy ion collisions in the LHC era.” In: *Journal of Physics* 527 (2014), p. 012012. DOI: `10.1088/1742-6596/527/1/012012`.

[Bec16] J. H. W. Becher. “Towards Spin and Site-Resolved, Single-Atom Imaging of 6Li Atoms in a Multiwell Potential T.” Master’s Thesis. 2016.

[Bel64] J. S. Bell. "On the Einstein Podolsky Rosen Paradox." In: *Physics* 1.3 (1964), pp. 195–290.

[BMO03] T. Bergeman, M. Moore, and M. Olshanii. "Atom-Atom Scattering under Cylindrical Harmonic Confinement." In: *Physical Review Letters* 91.16 (2003), p. 163201. DOI: `10.1103/PhysRevLett.91.163201`.

[Ber13] A. Bergschneider. "Ultracold few-fermi systems in multiwell potentials." Master's Thesis. Ruperto-Carola University of Heidelberg, 2013.

[Ber17] A. Bergschneider. "Strong correlations in few-fermion systems." PhD thesis. Ruperto-Carola University of Heidelberg, 2017.

[BZ08] I. Bloch and W. Zwerger. "Many-body physics with ultracold gases." In: *Reviews of Modern Physics* 80.3 (2008), pp. 885–964. DOI: `10.1103/RevModPhys.80.885`.

[Blu17] D. Blume. *private communications*. 2017.

[BTJ02] E. L. Bolda, E. Tiesinga, and P. S. Julienne. "Effective scattering length model of ultracold atomic collisions and Feshbach resonances in tight harmonic traps." In: *Physical Review A* 66.1 (2002), p. 013403. DOI: `10.1103/PhysRevA.66.013403`.

[Bom16] P. L. Bommer. "Identification and Localization of Single Atoms in Fluorescence Images based on Image Processing." Bachelor's Thesis. Ruperto-Carola University of Heidelberg, 2016.

[Bra00] R. N. Bracewell. *The Fourier Transform and Its Applications*. McGraw-Hill, 2000.

[BHV06] S. Bravyi, M. Hastings, and F. Verstraete. "Lieb-Robinson bounds and the generation of correlations and topological quantum order." In: *Physical Review Letters* 97.5 (2006), pp. 1–4. DOI: `10.1103/PhysRevLett.97.050401`.

[Büc+09] R Bücker et al. "Single particle sensitive imaging of freely propagating ultracold atoms." In: *New Journal of Physics* 11.10 (2009), p. 103039. DOI: `10.1088/1367-2630/11/10/103039`.

[Bus+98] T. Busch et al. "Two Cold Atoms in a Harmonic Trap." In: *Foundations of Physics* 28.4 (1998), pp. 549–559. DOI: `10.1023/A:1018705520999`.

[CC05] P. Calabrese and J. Cardy. "Evolution of Entanglement Entropy in One-Dimensional Systems." In: (2005). DOI: `10.1088/1742-5468/2005/04/P04010`.

[CC06] P. Calabrese and J. Cardy. "Time dependence of correlation functions following a quantum quench." In: *Physical Review Letters* 96.13 (2006), pp. 1–4. DOI: `10.1103/PhysRevLett.96.136801`.

[Cao+11] C. Cao et al. "Universal Quantum Viscosity in a Unitary Fermi Gas." In: *Science* 331.6013 (2011), pp. 58–61. DOI: `10.1126/science.1195219`.

[Car+15] D. J. Carrascal et al. "The Hubbard dimer: a density functional case study of a many-body problem." In: *Journal of Physics: Condensed Matter* 27.39 (2015), p. 393001. DOI: `10.1088/0953-8984/27/39/393001`.

[Che+12] M. Cheneau et al. "Light-cone-like spreading of correlations in a quantum m.-b. system." In: *Nature* 481.7382 (2012), pp. 484–487. DOI: `10.1038/nature10748`.

[Che+15] L. W. Cheuk et al. "Quantum-Gas Microscope for Fermionic Atoms." In: *Physical Review Letters* 114.19 (2015), p. 193001. DOI: `10.1103/PhysRevLett.114.193001`.

[Chi05] C. Chin. "A simple model of Feshbach molecules." In: (2005).

[Chi+10] C. Chin et al. "Feshbach resonances in ultracold gases." In: *Reviews of Modern Physics* 82.2 (2010), pp. 1225–1286. DOI: `10.1103/RevModPhys.82.1225`.

[Cla+69] J. F. Clauser et al. "Proposed Experiment to Test Local Hidden-Variable Theories." In: *Physical Review Letters* 23.15 (1969), pp. 880–884. DOI: `10.1103/PhysRevLett.23.880`.

[CT03] C. Cohen-Tannoudji. "Manipulating Atoms with Photons." In: *Nobel Lectures in Physics 1996 - 2000*. 2003, p. 166.

[CTD05] C. Cohen-Tannoudji and J. Dalibard. "Manipulating Atoms with Photons." In: *The New Physics for the Twenty-First Century*. 2005, pp. 145–170.

[CB15] J. P. Corson and J. L. Bohn. "Bound-state signatures in quenched Bose-Einstein condensates." In: *Physical Review A - Atomic, Molecular, and Optical Physics* 91.1 (2015), p. 1. DOI: `10.1103/PhysRevA.91.013616`.

[CB16] J. P. Corson and J. L. Bohn. "Ballistic quench-induced correlation waves in ultracold gases." In: *Physical Review A* 94.2 (2016), pp. 1–10. DOI: `10.1103/PhysRevA.94.023604`.

[Cra+10] M. Cramer et al. "Efficient quantum state tomography." In: *Nature Communications* 1.9 (2010), pp. 147–149. DOI: `10.1038/ncomms1147`.

[Cre11] S. Cremonini. "The shear viscosity to entropy ratio: a status report." In: *Modern Physics Letters B* 25.23 (2011), pp. 1867–1888. DOI: `10.1142/S0217984911027315`.

[DCT89] J. Dalibard and C. Cohen-Tannoudji. "Laser cooling below the Doppler limit by polarization gradients: simple theoretical models." In: *Journal of the Optical Society of America B* 6.11 (1989), p. 2023. DOI: `10.1364/JOSAB.6.002023`.

[Dal99] J. Dalibard. "Collisional dynamics of ultra-cold atomic gases." In: *Proceedings of the International School of Physics "Enrico Fermi", Volume 140: Bose-Einstein Condensation in Atomic Gases*. 1999, pp. 321–349. DOI: `10.3254/978-1-61499-225-7-321`.

[DDW06] M. R. Dowling, A. C. Doherty, and H. M. Wiseman. "Entanglement of indistinguishable particles in condensed-matter physics." In: *Physical Review A - Atomic, Molecular, and Optical Physics* 73.5 (2006), pp. 1–12. DOI: `10.1103/PhysRevA.73.052323`.

[Dut+15] O. Dutta et al. "Non-standard Hubbard models in optical lattices: a review." In: *Reports on Progress in Physics* 78.6 (2015), p. 066001. DOI: `10.1088/0034-4885/78/6/066001`.

[ECP10] J. Eisert, M. Cramer, and M. B. Plenio. "Colloquium: Area laws for the entanglement entropy." In: *Reviews of Modern Physics* 82.1 (2010), pp. 277–306. DOI: `10.1103/RevModPhys.82.277`.

[Ess+05] F. H. L. Essler et al. *The One-Dimensional Hubbard Model*. Cambridge University Press, 2005. DOI: `10.1017/CBO9780511534843`.

[Ess10] T. Esslinger. "Fermi-Hubbard Physics with Atoms in an Optical Lattice." In: *Annual Reviews of Condensed Matter Physics* 1 (2010), pp. 129–152. DOI: `10.1146/annurev-conmatphys-070909-104059`.

[Fed+96] P. O. Fedichev et al. "Influence of nearly resonant light on the scat. length in low-temperature atomic gases." In: *Physical Review Letters* 77.14 (1996), p. 12. DOI: `10.1103/PhysRevLett.77.2913`.

[FM47] E. Fermi and L. Marshall. "Interference phenomena of slow neutrons." In: *Physical Review* 71.10 (1947), pp. 666–677. DOI: `10.1103/PhysRev.71.666`.

[FW71] A. L. Fetter and J. D. Walecka. *Quantum Theory of Many-Particle Systems*. McGraw-Hill, 1971.

[Föl14] S. Fölling. "Qu. noise correlation experiments with ultracold atoms." In: *arXiv preprint arXiv:1403.6842v1* (2014), p. 26.

[Föl+07] S Fölling et al. "Direct observation of second-order atom tunnelling." In: *Nature* 448.7157 (2007), pp. 1029–32. doi: `10.1038/nature06112`.

[Föl08] S. Fölling. "Probing Strongly Correlated States of Ultracold Atoms in Optical Lattices." In: (2008).

[Föl+05] S. Fölling et al. "Spatial quantum noise interferometry in expanding ultracold atom clouds." In: *Nature* 434.7032 (2005), pp. 481–484. doi: `10.1038/nature03500`.

[För15] J. Förste. "The AC-Stark Shift of Lithium-6 in a Dipole Trap." Bachelor's Thesis. Ruperto-Carola University of Heidelberg, 2015.

[Fri13] H. Friedrich. *Scattering Theory*. Springer Berlin Heidelberg, 2013. doi: `10.1007/978-3-642-38282-6`.

[Geh03a] M. E. Gehm. *Properties of 6Li*. 2003. url: `https://www.physics.ncsu.edu/jet/techdocs/pdf/PropertiesOfLi.pdf`.

[Geh03b] M. E. Gehm. "Preparation of an Optically Trapped Degenerate Fermi Gas of 6 Li." PhD thesis. 2003.

[Gha10] S. Gharibian. "Strong NP-Hardness of the Quantum Separability Problem." In: *Quantum Information & Computation* 10.3 & 4 (2010), pp. 343–360.

[Gla63a] R. J. Glauber. "Coherent and incoherent states of the radiation field." In: *Physical Review* 131.6 (1963), pp. 2766–2788. doi: `10.1103/PhysRev.131.2766`.

[Gla63b] R. J. Glauber. "The Quantum Theory of Optical Coherence." In: *Physical Review* 130.6 (1963), pp. 2529–2539. doi: `10.1103/PhysRev.130.2529`.

[Gla06] R. J. Glauber. *Quantum Theory of Optical Coherence*. Wiley-VCH Verlag GmbH & Co. KGaA, 2006. doi: `10.1002/9783527610075`.

[Gla07] R. J. Glauber. "Einstein Lecture – One hundred years of light quanta." In: *Annalen der Physik* 16.1 (2007), pp. 6–23. doi: `10.1002/andp.200610222`.

[Gol+60] G. Goldhaber et al. "Influence of Bose-Einstein statistics on the antiproton-proton annihilation process." In: *Physical Review* 120.1 (1960), pp. 300–312. doi: `10.1103/PhysRev.120.300`.

[Gre+13] D. Greif et al. "Short-Range Qu. Magnetism of Ultracold Fermions in an Optical Lattice." In: *Science* 340.6138 (2013), pp. 1307–1310. doi: `10.1126/science.1236362`.

[Gre⁺02] M. Greiner et al. “Quantum phase transition from a superfluid to a Mott insulator in a gas of ultracold atoms.” In: *Nature* 415.6867 (2002), pp. 39–44. DOI: `10.1038/415039a`.

[GFK09] R. Grimm, F. Ferlaino, and S. Knoop. “Ultracold Feshbach Molecules.” In: *Cold Molecules*. Vol. cond-mat.o. 1. 2009, pp. 584–585. DOI: `10.1201/9781420059045.pt3`.

[GWO00] R. Grimm, M. Weidemüller, and Y. B. Ovchinnikov. “Optical Dipole Traps for Neutral Atoms.” In: 2000, pp. 95–170. DOI: `10.1016/S1049-250X(08)60186-X`.

[GT09] O. Gühne and G. Tóth. “Entanglement detection.” In: *Physics Reports* 474.1-6 (2009), pp. 1–75. DOI: `10.1016/j.physrep.2009.02.004`.

[Gur04] L. Gurvits. “Classical complexity and quantum entanglement.” In: *Journal of Computer and System Sciences* 69.3 SPEC. ISS. (2004), pp. 448–484. DOI: `10.1016/j.jcss.2004.06.003`.

[Hal⁺15] E. Haller et al. “Single-atom imaging of fermions in a quantum-gas microscope.” In: *Nature Physics* 11.9 (2015), pp. 738–742. DOI: `10.1038/nphys3403`.

[HT56a] R. Hanbury Brown and R. Q. Twiss. “A Test of a New Type of Stellar Interfer. on Sirius.” In: *Nature* 178.4541 (1956), pp. 1046–1048. DOI: `10.1038/1781046a0`.

[HT56b] R. Hanbury Brown and R. Q. Twiss. “Correlation between Photons in two Coherent Beams of Light.” In: *Nature* 177.4497 (1956), pp. 27–29. DOI: `10.1038/177027a0`.

[HT54] R. Hanbury Brown and R. Twiss. “LXXIV. A new type of interferometer for use in radio astronomy.” In: *The London, Edinburgh, and Dublin Philosophical Magazine and Journal of Science* 45.366 (1954), pp. 663–682. DOI: `10.1080/14786440708520475`.

[Har⁺15] R. A. Hart et al. “Observation of antiferromagnetic correlations in the Hubbard model with ultracold atoms.” In: *Nature* 519.7542 (2015), pp. 211–214. DOI: `10.1038/nature14223`.

[Has07] M. B. Hastings. “An area law for one dimensional quantum systems.” In: (2007). DOI: `10.1088/1742-5468/2007/08/P08024`.

[Hei04] U. W. Heinz. *Concepts of Heavy-Ion Physics*. 2004. URL: `http://arxiv.org/abs/hep-ph/0407360`.

[HJ99] U. Heinz and B. V. Jacak. “Two-Particle Correlations in Relativistic Heavy-Ion Collisions.” In: *Annual Review of Nuclear and Particle Science* 49.1 (1999), pp. 529–579. DOI: `10.1146/annurev.nucl.49.1.529`.

[Hod+05] E. Hodby et al. “Production efficiency of ultracold feshbach molecules in bosonic and fermionic systems.” In: *Physical Review Letters* 94.12 (2005), pp. 2–5. DOI: `10.1103/PhysRevLett.94.120402`.

[Hod+17] S. S. Hodgman et al. “Solving the qu. many-body problem via correlations measured with a mom. microscope.” In: *Physical Review Letters* 118.24 (2017), p. 240402. DOI: `10.1103/PhysRevLett.118.240402`.

[Hol17] M. Holten. “Collective Modes and Turbulence in Two-Dimensional Fermi Gases.” Master’s Thesis. 2017.

[HHH96] M. Horodecki, P. Horodecki, and R. Horodecki. “Separability of mixed states: necessary and sufficient conditions.” In: *Physics Letters A* 223.1-2 (1996), pp. 1–8. DOI: `10.1016/S0375-9601(96)00706-2`.

[HH96] R. Horodecki and M. Horodecki. “Information-theoretic aspects of inseparability of mixed states.” In: *Physical Review A* 54.3 (1996), pp. 1838–1843. DOI: `10.1103/PhysRevA.54.1838`.

[Hou+98] M. Houbiers et al. “Elastic and inelastic collisions of 6Li atoms in magnetic and optical traps.” In: *Physical Review A* 57.3 (1998), R1497–R1500. DOI: `10.1103/PhysRevA.57.R1497`.

[Hub63] J. Hubbard. “Electron Correlations in Narrow Energy Bands.” In: *Proceedings of the Royal Society A* 276.1365 (1963), pp. 238–257. DOI: `10.1098/rspa.1963.0204`.

[Hyn01] J. Hynecek. “Impactron — A new solid state image intensifier.” In: *IEEE Transactions on Electron Devices* 48.10 (2001), pp. 2238–2241. DOI: `10.1109/16.954460`.

[IC06] Z. Idziaszek and T. Calarco. “Analytical solutions for the dynamics of two trapped interacting ultracold atoms.” In: *Physical Review A* 74.2 (2006), p. 022712. DOI: `10.1103/PhysRevA.74.022712`.

[Fli] *Imaging Performance Specification FLIR Grasshopper3*. 2017. URL: `https://www.ptgrey.com/support/downloads/10304`.

[IO94] S. Inoue and R. Oldenbourg. “Microscopes.” In: *Handbook of Optics, Vol. 2: Devices, Measurements, and Properties*. 2nd ed. 1994. Chap. 17.

[Ino⁺98] S Inouye et al. "Observation of Feshbach resonances in a Bose-Einstein condensate." In: *Nature* 392 (1998), pp. 151–154. DOI: `10.1038/32354`.

[Isl⁺15] R. Islam et al. "Measuring entanglement entropy in a quantum many-body system." In: *Nature* 528.7580 (2015), pp. 77–83. DOI: `10.1038/nature15750`.

[Jak⁺98] D. Jaksch et al. "Cold Bosonic Atoms in Optical Lattices." In: *Physical Review Letters* 81.15 (1998), pp. 3108–3111. DOI: `10.1103/PhysRevLett.81.3108`.

[JZ05] D. Jaksch and P. Zoller. "The cold atom Hubbard toolbox." In: *Annals of Physics* 315.1 (2005), pp. 52–79. DOI: `10.1016/j.aop.2004.09.010`.

[Jer⁺01] P. Jerram et al. "The LLCCD: low-light imaging without the need for an intensifier." In: 2001, p. 178. DOI: `10.1117/12.426953`.

[Joh09] W. R. Johnson. "Scalar and Tensor Polariz. of Atoms." In: *Lecture Notes* (2009), pp. 1–7.

[Kau⁺16] A. M. Kaufman et al. "Quantum thermalization through entanglement in an isolated many-body system." In: *Science* 353.6301 (2016), pp. 794–800. DOI: `10.1126/science.aaf6725`.

[Kau⁺14] a. M. Kaufman et al. "Two-particle quantum interference in tunnel-coupled optical tweezers." In: *Science* 345.6194 (2014), pp. 306–309. DOI: `10.1126/science.1250057`.

[Kau⁺15] a. M. Kaufman et al. "Entangling two transportable neutral atoms via local spin exchange." In: *Nature* 527.7577 (2015), pp. 1–9. DOI: `10.1038/nature16073`.

[KZ08] W. Ketterle and M. W. Zwierlein. "Making, probing and understanding ultrac. Fermi gases." In: June 2006 (2008), pp. 20–30. DOI: `10.1393/ncr/i2008-10033-1`.

[KLH68] A. Khadjavi, A. Lurio, and W. Happer. "Stark effect in the excited states of Rb, Cs, Cd, and Hg." In: *Physical Review* 167.1 (1968), pp. 128–135. DOI: `10.1103/PhysRev.167.128`.

[Kit03] A. Y. Kitaev. "Fault-tolerant quantum computation by anyons." In: *Annals of Physics* 303.1 (2003), pp. 2–30. DOI: `10.1016/S0003-4916(02)00018-0`.

[KP06] A. Kitaev and J. Preskill. "Topological entanglement entropy." In: *Physical Review Letters* 96.11 (2006), pp. 2–5. DOI: `10.1103/PhysRevLett.96.110404`.

[KRS87] S. A. Kivelson, D. S. Rokhsar, and J. P. Sethna. “Topology of the resonating valence-bond state: Solitons and high-Tc superconductivity.” In: *Physical Review B* 35.16 (1987), pp. 8865–8868. DOI: `10.1103/PhysRevB.35.8865`.

[Kli12] V. M. Klinkhamer. “An apparatus for few-fermion systems in multiple well potentials.” Master's Thesis. Ruperto-Carola University of Heidelberg, 2012.

[Koo77] S. E. Koonin. “Proton pictures of high-energy nuclear collisions.” In: *Physics Letters B* 70.1 (1977), pp. 43–47. DOI: `10.1016/0370-2693(77)90340-9`.

[KSS05] P. K. Kovtun, D. T. Son, and A. O. Starinets. “Viscosity in Strongly Interacting Quantum Field Theories from Black Hole Physics.” In: *Physical Review Letters* 94.11 (2005), p. 111601. DOI: `10.1103/PhysRevLett.94.111601`.

[And] *LN2 versus TE cooling*. 2017. URL: `http://www.andor.com/learning-academy/ln2-versus-te-cooling-for-brdd-and-ingaas-sensors`.

[LL77] L. Landau and E. Lifshitz. “Elastic Collisions.” In: *Quantum Mechanics*. 1977, pp. 502–590. DOI: `10.1016/B978-0-08-020940-1.50024-4`.

[LK08] A. M. Läuchli and C. Kollath. “Spreading of correlations and entanglement after a quench in the one-dimensional Bose–Hubbard model.” In: *Journal of Statistical Mechanics: Theory and Experiment* 2008.05 (2008), P05018. DOI: `10.1088/1742-5468/2008/05/P05018`.

[Lau83] R. B. Laughlin. “Anomalous quantum Hall effect: An incompressible quantum fluid with fractionally charged excitations.” In: *Physical Review Lett.* 50.18 (1983), p. 1395. DOI: `10.1103/PhysRevLett.50.1395`.

[LNW06] P. A. Lee, N. Nagaosa, and X.-G. Wen. “Doping a Mott insulator: Physics of high-temperature superconductivity.” In: *Reviews of Modern Physics* 78.1 (2006), pp. 17–85. DOI: `10.1103/RevModPhys.78.17`.

[LW06] M. Levin and X. G. Wen. “Detecting topological order in a ground state wave function.” In: *Physical Review Letters* 96.11 (2006), pp. 3–6. DOI: `10.1103/PhysRevLett.96.110405`.

[Li+16] L. Li et al. “Assessing low-light cameras with photon transfer curve method.” In: *Journal of Innovative Optical Health Sciences* 09.03 (2016), p. 1630008. DOI: `10.1142/S1793545816300081`.

[LZ08] J.-J. Liang and C. Zhang. “Two ultracold atoms in a completely anisotropic trap.” In: *Physica Scripta* 77.2 (2008), p. 025302. DOI: `10.1088/0031-8949/77/02/025302`.

[Lie89] E. H. Lieb. “Two theorems on the Hubbard model.” In: *Physical Review Letters* 62.10 (1989), pp. 1201–1204. DOI: `10.1103/PhysRevLett.62.1201`.

[LM62] E. Lieb and D. Mattis. “Ordering Energy Levels of Interacting Spin Systems.” In: *Journal of Mathematical Physics* 3.4 (1962), pp. 749–751. DOI: `doi:10.1063/1.1724276`.

[Lin+93] H. Lin et al. “Exact Diagonalization Methods for Quantum Systems.” In: *Computers in Physics* 7.4 (1993), p. 400. DOI: `10.1063/1.4823192`.

[Lub+11] M. Lubasch et al. “Adiabatic preparation of a Heisenberg antiferromagnet using an optical superlattice.” In: *Physical Review Letters* 107.16 (2011), pp. 1–10. DOI: `10.1103/PhysRevLett.107.165301`.

[Mar11] G. Martinez. “Advances in Quark Gluon Plasma.” In: *Proceedings of the École Joliot Curie: Physics at the Femtometer Scale*. 2011.

[Mat+01] M. Matsumoto et al. “Ground-State Phase Diagram of Quantum Heisenberg Antiferromagnets on the Anisotropic Dimerized Square Lattice.” In: *Physical Review B* 65 (2001), p. 014407. DOI: `10.1103/PhysRevB.65.014407`.

[Maz+17] A. Mazurenko et al. “A cold-atom Fermi–Hubbard antiferromagnet.” In: *Nature* 545.7655 (2017), pp. 462–466. DOI: `10.1038/nature22362`.

[MS99] H. J. Metcalf and P. van der Straten. *Laser Cooling and Trapping*. Springer New York, 1999. DOI: `10.1007/978-1-4612-1470-0`.

[MVA95] A. Moerdijk, B. Verhaar, and A. Axelsson. “Resonances in ultracold collisions of 6Li, 7Li, and 23Na.” In: *Physical Review A* 51.6 (1995), pp. 4852–4861. DOI: `10.1103/PhysRevA.51.4852`.

[Pg2] *Mono Camera Sensor review*. 2015.

[MAH76] C. A. Moyer, S. Arajs, and L. Hedman. “Magnetic susceptibility of antiferromagnetic chromium.” In: *Physical Review B* 14.3 (1976), pp. 1233–1238. DOI: `10.1103/PhysRevB.14.1233`.

[Mül16] A. Müller. “Characterizing the Eigenstates of the Four-Well Hubbard Model.” Bachelor’s Thesis. Ruperto-Carola University of Heidelberg, 2016.

[Mur+15a] S. Murmann et al. “Antiferromagnetic Heisenberg Spin Chain of a Few Cold Atoms in a One-Dimensional Trap.” In: *Physical Review Letters* 115.21 (2015), p. 215301. DOI: `10.1103/PhysRevLett.115.215301`.

[Mur15] S. Murmann. "Few-particle quantum magnetism with ultracold atoms." PhD thesis. Ruperto-Carola University of Heidelberg, 2015.

[Mur+15b] S. Murmann et al. "Two Fermions in a Double Well: Exploring a Fundamental Building Block of the Hubbard Model." In: *Physical Review Letters* 114.8 (2015), p. 080402. DOI: `10.1103/PhysRevLett.114.080402`.

[Mur+14] P. A. Murthy et al. "Matter-wave Fourier optics with a strongly interacting two-dimensional Fermi gas." In: *Physical Review A* 90.4 (2014), p. 043611. DOI: `10.1103/PhysRevA.90.043611`.

[NS06] B. Nachtergaele and R. Sims. "Lieb-Robinson bounds and the exponential clustering theorem." In: *Communications in Mathematical Physics* 265.1 (2006), pp. 119–130. DOI: `10.1007/s00220-006-1556-1`.

[Nay+08] C. Nayak et al. "Non-Abelian anyons and topological quantum computation." In: *Rev. of Modern Physics* 80.3 (2008), pp. 1083–1159. DOI: `10.1103/RevModPhys.80.1083`.

[Nic+15] T. L. Nicholson et al. "Optical Feshbach resonances: field-dressed theory and comparison with experiments." In: *Physical Review A - Atomic, Molecular, and Optical Physics* 92.2 (2015), pp. 1–15. DOI: `10.1103/PhysRevA.92.022709`.

[Nie17] J. F. Niedermeyer. *Personal Communication*. 2017.

[Oje+16] M. Ojekhile et al. "Sudden and Slow Quenches into the Antiferromagnetic Phase of Ultracold Fermions." In: *Zeitschrift für Naturforschung A* 71.12 (2016), pp. 43–47. DOI: `10.1515/zna-2016-0313`.

[Ols98] M. Olshanii. "Atomic Scattering in the Presence of an External Confinement and a Gas of Impenetrable Bosons." In: *Physical Review Letters* 81.5 (1998), pp. 938–941. DOI: `10.1103/PhysRevLett.81.938`.

[Ott10] T. B. Ottenstein. "Few-body physics in ultracold Fermi gases." PhD thesis. Ruperto-Carola University of Heidelberg, 2010.

[PB08] B. Paredes and I. Bloch. "Minimum instances of topological matter in an optical plaquette." In: *Physical Review A* 77.2 (2008), p. 023603. DOI: `10.1103/PhysRevA.77.023603`.

[Par+15] M. F. Parsons et al. "Site-resolved Imaging of Fermionic Li in an Optical Lattice." In: *Physical Review Letters* 114.21 (2015), p. 213002. DOI: `10.1103/PhysRevLett.114.213002`.

[Par+16] M. F. Parsons et al. “Site-resolved measurement of the spin-correlation function in the Fermi-Hubbard model.” In: *Science* 353.6305 (2016), pp. 1253–1256. DOI: 10.1126/science.aag1430.

[Per96] A. Peres. “Separability Criterion for Density Matrices.” In: *Physical Review Letters* 77.8 (1996), pp. 1413–1415. DOI: 10.1103/PhysRevLett.77.1413.

[PS95] M. E. Peskin and D. V. Schroeder. *An introduction to quantum field theory*. Westview Press, 1995.

[Pou10] A. D. Poularikas, ed. *Transforms and Applications Handbook*. 3rd ed. CRC Press, 2010.

[Rav+17] D. Raventós et al. “Cold bosons in optical lattices: a tutorial for exact diagonalization.” In: *Journal of Physics B: AMO Physics* 50.11 (2017), p. 113001. DOI: 10.1088/1361-6455/aa68b1.

[Rec+03] A Recati et al. “Fermi one-dimensional quantum gas: Luttinger liquid approach and spin-charge separation.” In: *Journal Of Optics B-Quantum And Semiclassical Optics* 5.2 (2003), S55–S64. DOI: 10.1088/1464-4266/5/2/359%7D.

[Rie+15] M. G. Ries et al. “Observation of Pair Condensation in the Quasi-2D BEC-BCS Crossover.” In: *Physical Review Letters* 114.23 (2015), p. 230401. DOI: 10.1103/PhysRevLett.114.230401.

[RDO08] M. Rigol, V. Dunjko, and M. Olshanii. “Thermalization and its mechanism for generic isolated quantum systems.” In: *Nature* 452.7189 (2008), pp. 854–8. DOI: 10.1038/nature06838.

[Rom+06] T Rom et al. “Free fermion antibunching in a degenerate atomic Fermi gas released from an optical lattice.” In: *Nature* 444.7120 (2006), pp. 733–736. DOI: 10.1038/nature05319.

[Rom09] T. Rom. “Bosonische und fermionische Quantengase in dreidimensionalen optischen Gittern.” In: (2009), p. 389.

[Rüe+08] C. Rüegg et al. “Quantum Magnets under Pressure: Controlling Elementary Excitations in TlCuCl3.” In: *Physical Review Letters* 100.20 (2008), p. 205701. DOI: 10.1103/PhysRevLett.100.205701.

[Sac08] S. Sachdev. “Quantum magnetism and criticality.” In: *Nature Physics* 4.3 (2008), pp. 173–185. DOI: 10.1038/nphys894.

[Sac11] S. Sachdev. *Quantum Phase Transitions*. Cambridge University Press, 2011, p. 517. DOI: `10.1017/CBO9780511973765`.

[SSC13] M. S. Safronova, U. I. Safronova, and C. W. Clark. "Magic wavelengths for optical cooling and trapping of lithium." In: *Physical Review A - AMO Physics* 87.5 (2013), pp. 1–7. DOI: `10.1103/PhysRevA.86.042505`.

[Sca16] R. T. Scalettar. "An Introduction to the Hubbard Hamiltonian." In: *Quantum Materials: Experiments and Theory*. Vol. 6. 2016.

[SHL10] L. Schermelleh, R. Heintzmann, and H. Leonhardt. "A guide to super-resolution fluorescence microscopy." In: *Journal of Cell Biology* 190.2 (2010), pp. 165–175. DOI: `10.1083/jcb.201002018`.

[Sch+05] C. H. Schunck et al. "Feshbach resonances in fermionic Li6." In: *Physical Review A - Atomic, Molecular, and Optical Physics* 71.4 (2005), pp. 1–4. DOI: `10.1103/PhysRevA.71.045601`.

[Sch+99] U Schunemann et al. "Simple scheme for tunable frequency offset locking of two lasers." In: *Review Of Scientific Instruments* 70.1 (1999), pp. 242–243. DOI: `10.1063/1.1149573`.

[Sch08] F. Schwabl. *Quantenmechanik für Fortgeschrittene (QM II)*. Springer Berlin Heidelberg, 2008. DOI: `10.1007/978-3-540-85076-2`.

[SMF12] F. Schwarz, T.-O. Müller, and H. Friedrich. "Near-threshold Feshbach resonances in interatomic collisions and spectra." In: *Physical Review A* 85.5 (2012), p. 052703. DOI: `10.1103/PhysRevA.85.052703`.

[Ser+11] F Serwane et al. "Deterministic Preparation of a Tunable Few-Fermion System." In: *Science* 332.6027 (2011), pp. 336–338. DOI: `10.1126/science.1201351`.

[Ser11] F. Serwane. "Deterministic preparation of a tunable few-fermion system." PhD thesis. Ruperto-Carola University of Heidelberg, 2011.

[SSW51] C. G. Shull, W. A. Strauser, and E. O. Wollan. "Neutron Diffraction by Paramagnetic and Antiferromagnetic Substances." In: *Physical Review* 83.2 (1951), pp. 333–345. DOI: `10.1103/PhysRev.83.333`.

[Ste16] T. Steinle. "Implementation of Simultaneously Imaging two Hyperfine States of Ultracold 6Li Atoms in a Magnetic Field." Bachelor's Thesis. Ruperto-Carola University of Heidelberg, 2016.

[Sud63] E. C. G. Sudarshan. "Equivalence of semiclassical and qu. mechanical descriptions of statistical light beams." In: *Physical Review Letters* 10.7 (1963), pp. 277–279. DOI: `10.1103/PhysRevLett.10.277`.

[Tan04] S. Tan. "Short Range Scaling Laws of Quantum Gases With Contact Interactions." In: *arXiv* 02.18 (2004), p. 4.

[Tas98] H. Tasaki. "The Hubbard model - an introduction and selected rigorous results." In: *Journal of Physics: Condensed Matter* 10.20 (1998), pp. 4353–4378. DOI: `10.1088/0953-8984/10/20/004`.

[Tho16] L. J. Thormählen. "Implementation of a Versatile Digital Laser Lock for Imaging Ultracold Lithium." Bachelor's Thesis. Ruperto-Carola University of Heidelberg, 2016.

[Tre+06] S. Trebst et al. "d-Wave Resonating Valence Bond States of Fermionic Atoms in Optical Lattices." In: *Physical Review Letters* 96.25 (2006), p. 250402. DOI: `10.1103/PhysRevLett.96.250402`.

[Tro+08] S. Trotzky et al. "Time-Resolved Observation and Control of Superexchange Interactions with Ultracold Atoms in Optical Lattices." In: *Science* 319.5861 (2008), pp. 295–299. DOI: `10.1126/science.1150841`.

[TSG82] D. C. Tsui, H. L. Stormer, and A. C. Gossard. "Two-Dimensional Magnetotransport in the Extreme Quantum Limit." In: *Physical Review Letters* 48.22 (1982), pp. 1559–1562. DOI: `10.1103/PhysRevLett.48.1559`.

[Tul10] S. M. Tulloch. "Optimisation of an EMCCD." In: *Munich DFA Conference* (2010).

[UG15] S. Uchino and T. Giamarchi. "Two-leg fermionic Hubbard ladder system in the presence of state-dependent hopping." In: *Physical Review A* 91.1 (2015), pp. 1–9. DOI: `10.1103/PhysRevA.91.013604`.

[Ved03] V. Vedral. "Entanglement in the second quantization formalism." In: *Open Physics* 1.2 (2003), p. 11. DOI: `10.2478/BF02476298`.

[WV03] H. M. Wiseman and J. A. Vaccaro. "Entanglement of Indistinguishable Particles Shared between Two Parties." In: *Physical Review Letters* 91.9 (2003), p. 097902. DOI: `10.1103/PhysRevLett.91.097902`.

[Woo98] W. K. Wootters. "Entanglement of Formation of an Arbitrary State of Two Qubits." In: *Physical Review Letters* 80.10 (1998), pp. 2245–2248. DOI: `10.1103/PhysRevLett.80.2245`.

[YSF14] M. Yamanaka, N. I. Smith, and K. Fujita. “Introduction to super-resolution microscopy.” In: *Microscopy* 63.3 (2014), pp. 177–192. DOI: `10.1093/jmicro/dfu007`.

[Yan+96] Z.-C. Yan et al. “Variational calculations of dispersion coefficients for interactions among H, He, and Li atoms.” In: *Physical Review A* 54.4 (1996), pp. 2824–2833. DOI: `10.1103/PhysRevA.54.2824`.

[Zaj+84] W. A. Zajc et al. “Two-pion correlations in heavy ion collisions.” In: *Physical Review C* 29.6 (1984), pp. 2173–2187. DOI: `10.1103/PhysRevC.29.2173`.

[Zan02] P. Zanardi. “Quantum entanglement in fermionic lattices.” In: *Physical Review A* 65.4 (2002), p. 042101. DOI: `10.1103/PhysRevA.65.042101`.

[Zor95] P. Zorabedian. “Tunable External-Cavity Semiconductor Lasers.” In: *Tunable Lasers Handbook*. 1995, pp. 349–442.

[Zür12a] G. Zürn. “Few-fermion systems in one dimension.” PhD thesis. Ruperto-Carola University of Heidelberg, 2012.

[Zür12b] G. Zürn. *Personal Communication*. 2012.

[Zwe16] W. Zwerger. “Strongly Interacting Fermi Gases.” In: *Proceedings of the Int. School of Physics "Enrico Fermi", Volume 191: Qu. Matter at Ultralow Temperatures*. 2016, pp. 63–141. DOI: `10.3254/978-1-61499-694-1-63`.

DANKSAGUNG

Nun ist meine Doktorarbeit zu Ende — sie wäre mir nicht gelungen ohne die Hilfe und Unterstützung meiner Kollegen, Freunde und Familie.

Zu allererst möchte ich mich bei Selim bedanken. Du warst nicht nur ein Supervisor, der mir immer mit Rat zur Seite stand, sondern ein echter Leader. Du hast mich nicht nur mit seiner Begeisterung motiviert, sondern auch mit deinen physikalischen Einsichten und deiner praktischen Erfahrung im Labor weitergebracht.

Ein ganz besonderer Dank geht dabei an Andrea, Simon, Thomas, Gerhard, Philipp, Jan-Hendrik und neuerdings Ralf, mit denen ich am Few-Fermion Experiment fast alle erdenklichen Höhen und Tiefen [Ber17] durchlebt habe (zum Glück blieb uns das Vakuum erspart, aller meiner Unkenrufe zum Trotz). Auf euch war immer Verlass, und ohne euch würde im Labor nichts laufen. Auch danke an Andrea, Philipp und Ralf für das Korrekturlesen dieser Arbeit.

Mein Dank geht auch an meine weiteren, teils langjährigen, Kollegen, Friedhelm, Andre, Martin, Mathias, Puneet, Luca, Dhruv, Marvin, Michael und Justin, und an die Neuen, Lukas und Antonia. Die gemeinsamen Kicker-Runden, Uni-Shop-Besuche und Diskussionen haben den Alltag stets angenehm gestaltet, und wir haben bei Ausflügen und bei mancher Nacht-und-Nebel-Aktion viel Spaß gehabt.

Nicht vergessen möchte ich die vielen Studenten und HiWis, mit denen ich über die Jahre zusammengearbeitet habe. Ich möchte mich hier bei Marius, Arnulf, Daniel, Jonathan, Benjamin, Alexander, Peter, Lennert, Ram-Janik, Paul, Rodrigo und Philine bedanken, eure Arbeit hat wesentliche Verbesserungen und Fortschitte zum Experiment beigetragen. Vor allem schätze ich, dass ihr bereit wart, euch auch über das Ende eurer Bachelorarbeit hinaus zu engagieren.

Ich möchte mich auch für die Zusammenarbeit bei den Theoretikern bedanken, vor allem bei Frank Deuretzbacher und Dörte Blume, für eure Arbeit und Diskussionen, die mein Verständnis unserer Experimente wesentlich vorangebracht haben.

Außerdem möchte ich mich bei den technischen Abteilungen bedanken, unter anderem bei Herrn Dr. Angelov, Herrn Schumacher und Frau Kupfer. Besonderer Dank geht an den Leiter der Werkstatt, Ralf Ziegler, der immer dafür sorgt, dass es im Institut rund läuft und dass Aufträge schnell, sauber und unbürokratisch erledigt werden. Und natürlich bedanke ich mich außerordentlich bei Esther Danzeisen, die zusammen mit mir etliche Feshbach-Spulen geplant und gebaut hat und ohne ihrer hervorragenden Arbeit es heute kein funktionierendes Few-Fermion Experiment geben würde. Vielen Dank!

Für die Zeit, die ich außerhalb des Labors verbracht habe, möchte ich mich bei allen meinen Freunden bedanken. Mit euch Ausflüge zu machen, Fußball zu schauen, Tanzen zu gehen, Sprachen zu lernen, oder auch einfach nur gemeinsam etwas essen zu gehen, hat mit immer große Freude bereitet. Besonders schön war es immer mit meinen alten Schulfreunden, mit euch ist immer was los!

Ein großer Dank geht auch an meine Familie, insbesondere meine Eltern und Großeltern. Auch wenn ich euch nicht so oft gesehen habe, wie ihr und ich es gerne gehabt hätten, wart ihr immer für mich da und habt mich immer unterstützt.

Zu guter Letzt möchte ich meiner Kasia danken — hast du vor fast vier Jahren gewusst, worauf du dich da einlässt? Ich bin trotzdem überglücklich, dass du es getan hast, und ich freue mich Woche für Woche, dich endlich wieder zu sehen. Danke, dass du während dieser langen Zeit mir immer zur Seite gestanden bist.

Erklärung:

Ich versichere, dass ich diese Arbeit selbstständig verfasst habe und keine anderen als die angegebenen Quellen und Hilfsmittel benutzt habe.

Heidelberg, den ....